

---

Electronic Thesis and Dissertation Repository

---

8-27-2014 12:00 AM

## Wind-Induced Pressures in Air Permeable, Double-Layer Roof Systems in Regions of Separated Flow

Jeong Hee Oh, *The University of Western Ontario*

Supervisor: Dr. Gregory Kopp, *The University of Western Ontario*

A thesis submitted in partial fulfillment of the requirements for the Doctor of Philosophy degree in Civil and Environmental Engineering

© Jeong Hee Oh 2014

Follow this and additional works at: <https://ir.lib.uwo.ca/etd>



Part of the [Architectural Engineering Commons](#), [Architectural Technology Commons](#), [Civil Engineering Commons](#), and the [Structural Engineering Commons](#)

---

### Recommended Citation

Oh, Jeong Hee, "Wind-Induced Pressures in Air Permeable, Double-Layer Roof Systems in Regions of Separated Flow" (2014). *Electronic Thesis and Dissertation Repository*. 2344.  
<https://ir.lib.uwo.ca/etd/2344>

This Dissertation/Thesis is brought to you for free and open access by Scholarship@Western. It has been accepted for inclusion in Electronic Thesis and Dissertation Repository by an authorized administrator of Scholarship@Western. For more information, please contact [wlsadmin@uwo.ca](mailto:wlsadmin@uwo.ca).

**WIND-INDUCED PRESSURES IN AIR PERMEABLE, DOUBLE-LAYER ROOF  
SYSTEMS IN REGIONS OF SEPARATED FLOW**

(Thesis format: Integrated Article)

by

Jeong Hee Oh

Graduate Program in Civil and Environmental Engineering

A thesis submitted in partial fulfillment  
of the requirements for the degree of  
Doctor of Philosophy

The School of Graduate and Postdoctoral Studies  
The University of Western Ontario  
London, Ontario, Canada

© Jeong Hee Oh 2014

## Abstract

This thesis is concerned with the wind-induced pressure distribution acting on air permeable, double-layer roof systems placed on low-rise buildings. Because of the pressure transmission into the cavity between layers, the pressure difference in the double-layer systems differs significantly from that in a single layer. The interior pressures (in the cavity between layers) are highly correlated with external pressures at the openings on the external surface of the outer layer and thereby, the net wind load for the design of the outer layer is considerably reduced by the pressure equalization between the external and internal surfaces of the outer layer. Examples of the outer layer in practice are loose-laid roof pavers and solar panel arrays on roofs, and rainscreen walls. The objective of this thesis is to characterize and model how the cavity pressures between layers are related to the external pressures and the outer layer and cavity geometries.

First, experimental studies were conducted to investigate the detailed cavity pressure distributions, the correlation with external pressures and effects of geometric parameters within the double-layer system. Wind tunnel experimental data on a model of a low-rise building in an open country terrain were used and in total, 39 configurations consisting of six different heights of the panels above the roof surface ( $H$  which is the gap between layers), six different gaps between panels ( $G$ ) and three additional configurations with a larger panel size ( $L$ ) were examined. It was found in these experiments that the pressure distributions on the internal surface of panels are significantly affected by the geometric parameters. Higher values of the non-dimensional parameters,  $\left[\frac{G}{H}\right]^2 \left[\frac{fL/H}{C_L}\right]$ , take greater advantage of the double layer system, so that the pressures between the external and internal surfaces of panels are more highly equalized.

An analytical model was developed to simulate one-dimensional pressure distributions ( $Cp_i$ ) in the cavity between the layers in a double-layer system, given pressure data on the external surface ( $Cp_e$ ) and the geometric parameters. The model was derived considering the pressure drops associated with the flow through the gaps between panels, which is like an orifice flow, and the cavity flow between parallel plates. Thus, the model uses two primary equations: the unsteady discharge equation and the equation

for unsteady flow between two parallel plates. The model accounts for several geometric parameters including the gap ( $G$ ) between the panels, the height ( $H$ ) of the cavity between the layers, the length ( $L$ ) of the panels and the thickness ( $l_o$ ) of the panels, as well as the loss coefficients for the orifice and cavity flows. The proposed model is able to capture the fluctuations of  $Cp_i$  and a good agreement is found between the numerical and experimental results for the mean, RMS and peak coefficients, to a great extent, when spanwise-averaged external pressure coefficients are used as input.

The analytical model was further validated with wind tunnel test data on a more practical problem which consists of 12 rows of photovoltaic panels placed within all roof zones, from the separation region, the reattachment point, up to the leeward region of the roof. The model captures fluctuations of the cavity pressure, although there are slight differences between the numerical and experimental data, in particular, on panels at the leading edge and in the reattachment regions. Lastly, the thesis discusses how the analytical model can be used as a tool to design compartments for such air permeable, double-layer systems.

**Key words:** pressure distribution; wind loads; low-rise buildings; aerodynamics; discharge equation; double layer cladding; pressure equalization; cavity pressure

## Co-Authorship Statement

Two articles (Chapter 2 and Chapter 3) used in this integrated article thesis are co-authored by my supervisor, Dr. Gregory Kopp and myself. For these articles, all the experiments, the analyses, and the preparation of the manuscripts were carried out by me under the supervision of Dr. Gregory Kopp. The co-authorship is as follows:

Chapter 2: “An experimental study of pressure distributions within a double-layered roof system in a region of separated flow”

**Jeong Hee Oh** and Gregory Kopp

submitted to *Journal of Wind Engineering & Industrial Aerodynamics* for possible publication in March, 2014.

In this paper, I was primarily responsible for the design of the wind tunnel model, the wind tunnel testing, the analyses of the test data, and the preparation of the manuscripts. Dr. Gregory Kopp initiated the research, supervised the design of the model and the experiments, and provided invaluable advice and comments in the preparation of this article.

Chapter 3: “One-dimensional modelling of the flow in pressure equalizing, double-layer, roof systems in regions of separated flow”

**Jeong Hee Oh** and Gregory Kopp

submitted to *Building and Environment* for possible publication in June, 2014.

In this paper, I was primarily responsible for the development of the analytical model, the Matlab coding, the analyses of the data, and the preparation of the manuscripts. Dr. Gregory Kopp assisted in developing the analytical model and interpreting the results from numerical simulations, and provided significant instruction and feedback in the preparation of this article.

*To my wife Anna and my son Jonathan.*

## Acknowledgements

A number of people are to be thanked for their direct and indirect contributions to this thesis. First of all, I would like to thank my supervisor, Dr. Gregory Kopp, for giving me the opportunity to pursue this research and instilling ideas that greatly enhanced this thesis. He took me on as a master student in 2003 and has worked with me on several research projects when I was a research engineer for the Boundary Layer Wind Tunnel Laboratory. The continuous works with him and his special interests on pressures on solar panels drove me to start my PhD degree. He has always welcomed me on matters I brought throughout the PhD work. In addition, I appreciate that he gave me the opportunities to attend international conferences and to be involved in other interesting projects during the course of this thesis.

I extend my special thanks to Dr. Eric Ho. He has taught me, from beginning to end, how a wind tunnel project is done and provided me with the opportunities to get involved in various projects during times in the PhD pursuit. Thanks also go to my colleagues of the staff of the laboratory, in particular, Gerry Dafoe and Anthony Burggraaf who helped me to carry out the wind tunnel tests whose results appear in Chapters 2 and 3, and Steve Farquhar for supplying experimental data used in Chapter 4. The wind tunnel model was constructed by Chris Vandelaar, a staff of the University Machine Shop. His genius advice during the design of the model is truly appreciated. I would like to thank all fellow graduate students of the laboratory for the lengthy conversations, collaboration and friendship along the long journey.

Financial support for this work was provided by NSERC through the Discovery Grants program. This work is also, in part, supported by the Alexander Graham Bell Canada Graduate Scholarships provided by NSERC. These financial supports are truly acknowledged.

I am heartily thankful to my family and friends for their love, support and encouragement. Most of all, for my loving, supportive, encouraging, and patient wife Anna and my lovely son Jonathan whose faithful support during the journey of this PhD is so appreciated.

# Table of Contents

|   |              |
|---|--------------|
| <b>CERTIFICATE OF EXAMINATION .....</b>   | <b>i</b>     |
| <b>Abstract.....</b>  | <b>ii</b>    |
| <b>Co-Authorship Statement .....</b>  | <b>iv</b>    |
| <b>Acknowledgements .....</b>   | <b>vi</b>    |
| <b>Table of Contents .....</b>  | <b>vii</b>   |
| <b>List of Tables .....</b>   | <b>x</b>     |
| <b>List of Figures.....</b>   | <b>xi</b>    |
| <b>List of Appendices.....</b>  | <b>xvii</b>  |
| <b>List of Symbols .....</b>  | <b>xviii</b> |
| <b>Chapter 1 Introduction.....</b>  | <b>1</b>     |
| <b>1.1 Background .....</b>   | <b>1</b>     |
| <b>1.1.1 Experimental studies in the literature.....</b>  | <b>3</b>     |
| <b>1.1.2 Analytical models in the literature .....</b>  | <b>6</b>     |
| <b>1.2 Motivations of Thesis.....</b>   | <b>8</b>     |
| <b>1.3 Objectives of Thesis .....</b>   | <b>10</b>    |
| <b>1.4 Organization of Thesis.....</b>  | <b>10</b>    |
| <b>1.5 Original Contributions .....</b>   | <b>11</b>    |
| <b>References .....</b>   | <b>12</b>    |
| <b>Chapter 2 An Experimental Study of Pressure Distributions within a Pressure<br/>Equalizing, Double-Layer, Roof System in Regions of Separated Flow .....</b> | <b>18</b>    |
| <b>2.1 Introduction.....</b>  | <b>18</b>    |
| <b>2.2 Experimental Setup .....</b>   | <b>19</b>    |
| <b>2.3 Results .....</b>  | <b>25</b>    |
| <b>2.3.1 Assessment of two-dimensional mean flow .....</b>  | <b>25</b>    |
| <b>2.3.2 Mean pressure distributions .....</b>  | <b>27</b>    |
| <b>2.3.3 RMS pressure distributions .....</b>   | <b>31</b>    |
| <b>2.3.4 Instantaneous pressure distributions .....</b>   | <b>35</b>    |
| <b>2.3.5 Peak pressure distributions.....</b>   | <b>38</b>    |
| <b>2.4 Discussion of Pressure Distribution .....</b>  | <b>41</b>    |



|   |           |
|---|-----------|
| 2.4.1 Mechanisms of external and cavity pressure distributions.....   | 41        |
| 2.4.2 Dimensional analysis of mean pressure distribution .....  | 43        |
| 2.5 Conclusions.....  | 47        |
| References .....  | 48        |
| <b>Chapter 3 One-dimensional modelling of the flow in pressure equalizing, double-layer, roof systems in regions of separated flow.....</b> | <b>51</b> |
| 3.1 Introduction.....   | 51        |
| 3.2 Governing Equations .....   | 53        |
| 3.2.1 Governing equation for flows through an orifice.....  | 53        |
| 3.2.2 Governing equation for flows between two parallel plates .....  | 55        |
| 3.2.3 Analytical model for one-dimensional flows in the cavity between layers in a double layer system.....                                 | 57        |
| 3.3 Numerical Simulation Details .....  | 59        |
| 3.3.1 Numerical solution .....  | 59        |
| 3.3.2 Numerical parameters .....  | 60        |
| 3.3.3 Pressure coefficients.....  | 61        |
| 3.4 Comparison of Simulation Results with Experimental Data .....   | 62        |
| 3.4.1 Time histories and spectra .....  | 62        |
| 3.4.2 Mean and RMS point pressure distributions .....   | 67        |
| 3.4.3 Use of spanwise-averaged external pressure coefficients as input .....  | 71        |
| 3.4.4 Peak pressures .....  | 77        |
| 3.5 Numerical Simulations from Cpe using Bare Roof Data.....  | 81        |
| 3.6 Contributions of the Terms in the Analytical Model.....   | 83        |
| 3.7 Conclusions.....  | 86        |
| Reference .....   | 87        |
| <b>Chapter 4 Pressure Distributions on Photovoltaic Arrays Mounted on Large Flat-Roofs: A Case Study .....</b>                              | <b>91</b> |
| 4.1 Introduction.....   | 91        |
| 4.2 Non-Dimensional Form of Governing Equations .....   | 92        |
| 4.3 Numerical Simulation Details .....  | 94        |
| 4.3.1 Numerical model .....   | 94        |

|   |     |
|---|-----|
| 4.3.2 Pressure model .....  | 96  |
| 4.3.3 Pressure measurements .....   | 99  |
| 4.4 Results and Comparison with Experimental Data .....   | 99  |
| 4.4.1 Spanwise correlation in mean two-dimensional flows .....                                      | 99  |
| 4.4.2 Basic statistics of area-averaged pressures on photovoltaic panels.....                       | 102 |
| 4.4.3 Time histories and spectra of area-averaged pressures on photovoltaic panels.....             | 105 |
| 4.4.4 Point pressure distributions along the midplane .....   | 113 |
| 4.5 Numerical Simulations of Compartmentalization in a Photovoltaic Array .....                     | 119 |
| 4.5.1 Compartmentalization of cavity in different number of rows .....                              | 119 |
| 4.5.2 Compartmentalization of cavity in different locations of the roof .....                       | 121 |
| 4.5.3 Compartmentalization of cavity between edge and intermediate rows .....                       | 122 |
| 4.5.4 Compartmentalization of cavity between modules .....  | 126 |
| 4.6 Summary and Conclusions .....   | 129 |
| References .....  | 131 |
| Chapter 5 Summary, Conclusions and Recommendations.....   | 133 |
| 5.1 General.....  | 133 |
| 5.2 Pressure Distributions within a Double-Layer Roof System in Regions of Separated Flow.....      | 133 |
| 5.3 Development of One-Dimensional Modelling of Flows in Double-Layer Systems .....                 | 135 |
| 5.4 Pressure Distributions on Roof-Mounted Photovoltaic Arrays .....                                | 137 |
| 5.5 Recommendations for Future Research .....   | 140 |
| Appendix A Numerical Method.....  | 141 |
| Appendix B Spanwise Correlation and Area-Averaged Pressures on Photovoltaic Arrays for 0° wind..... | 142 |
| Appendix C Point Pressures on Photovoltaic Arrays for All Spanwise-Averaged C <sub>pe</sub> .....   | 146 |
| Appendix D Preliminary Study on Two-Dimensional Modelling of the Flow in the Cavity .....           | 165 |
| Curriculum Vitae .....  | 169 |

## **List of Tables**

|   |     |
|---|-----|
| Table 1.1 Summary of numerical models for internal pressures .....              | 9   |
| Table 2.2 Experimental details of wind tunnel tests .....                       | 24  |
| Table 3.1 Numerical values used in numerical computations.....                  | 61  |
| Table 4.1 Mean area-averaged pressures on Module 6 for 180° wind.....           | 104 |
| Table 4.2 RMS area-averaged pressures on Module 6 for 180° wind .....           | 104 |
| Table 4.3 Peak (minimum) area-averaged pressures on Module 6 for 180° wind..... | 105 |
| Table B.1 Mean area-averaged pressures on Module 6 for 0° wind .....            | 144 |
| Table B.2 RMS area-averaged pressures on Module 6 for 0° wind.....              | 144 |
| Table B.3 Peak (minimum) area-averaged pressures on Module 6 for 0° wind .....  | 145 |

## List of Figures

|   |    |
|---|----|
| Figure 1.1 Examples of double-layer system.....   | 2  |
| Figure 1.2 Section view of double-layer system and sketch of pressure equalization. ....  | 2  |
| Figure 1.3 Section view of compartmentalized cavities in double-layer systems. ....   | 3  |
| Figure 2.1 Wind tunnel model: (a) sketch of the building model with locations of panels and definition of the coordinate system; (b) details of panels and pressure tap layout. ...   | 21 |
| Figure 2.2 Photographs of (a) the upstream terrain in the wind tunnel with the model for the panel and tap region built from Plexiglas, (b) a close-up of the model. ....   | 22 |
| Figure 2.3 Vertical profile of mean wind velocity and longitudinal turbulence intensity simulated in the wind tunnel. ....  | 23 |
| Figure 2.4 Distribution of mean and RMS pressure coefficients: a) along the x-direction, b) along the y-direction, and c) comparison with NIST data. Cpe were obtained from three different pressure tap lines (Left, Middle and Right, as shown in Figure 2.1b) and Cpi from 591 pressure taps on the top surface of the inner layer. The configuration with $G = 2.5$ mm and $H = 2.5$ mm were used to compare with data obtained from the midplane of a bare-roofed building from the NIST aerodynamic database for low-rise buildings.. | 26 |
| Figure 2.5 Mean pressure distributions for the pressure taps in the middle row: (a) two gaps ( $G = 2.5$ mm at $x/h = 0.11$ and $G = 3.5$ mm at $x/h = 0.74$ ) with $H$ variations; (b) five gaps of $G = 1$ mm with $H$ variations; and (c) five gaps with $H = 1.2$ mm and with $G$ variations.....   | 29 |
| Figure 2.6 RMS pressure distributions for the pressure taps in the middle row: (a) two gaps ( $G = 2.5$ mm at $x/h = 0.11$ and $G = 3.5$ mm at $x/h = 0.74$ ) with $H$ variations; (b) five gaps of $G = 1$ mm with $H$ variations; and (c) five gaps with $H = 1.2$ mm and with $G$ variations.....  | 33 |
| Figure 2.7 Instantaneous pressure distributions for the pressure taps in the middle row: (a) two gaps ( $G = 2.5$ mm at $x/h = 0.11$ and $G = 3.5$ mm at $x/h = 0.74$ ) with $H$ variations; (b) five gaps of $G = 1$ mm with $H$ variations; and (c) five gaps with $H = 1.2$ mm and with $G$ variations.....  | 36 |
| Figure 2.8 Peak pressure distributions for $G = 1$ mm with $H$ variations: (a) minima; (b) maxima. (The vertical hidden lines indicate locations of the gaps.).....   | 39 |

|   |    |
|---|----|
| Figure 2.9 Peak pressure distributions for $H = 1.2$ mm with $G$ variations: (a) minima; (b) maxima.....  | 40 |
| Figure 2.10 Idealization of the flow and pressure distribution mechanisms on external and internal surfaces of panels: (a) mean flow; (b) mean; (c) RMS; (d) minima; and (e) maxima.....  | 42 |
| Figure 2.11 Idealization of the flow and pressure distribution mechanisms on external and internal surfaces of panels for the separated underside space: (a) mean flow; (b) mean..  | 43 |
| Figure 2.12 Pressures and flows on two gaps of the double layer system.....   | 46 |
| Figure 3.1 Flow and pressure model for the double layer system: (a) two gaps; (b) five gaps on the air-permeable layer. ....  | 53 |
| Figure 3.2 Time series and spectra of area averaged pressure coefficients for $G = 1$ mm and $H = 15$ mm: (a) $C_{pe}$ ; (b) $C_{pi}$ ; (c) power spectra on Panel 1; (d) $C_{pe}$ ; (e) $C_{pi}$ ; and (f) power spectra on Panel 4. ....  | 64 |
| Figure 3.3 Time series and spectra of area averaged pressure coefficients for $G = 1$ mm and $H = 2.5$ mm: (a) $C_{pe}$ ; (b) $C_{pi}$ ; (c) power spectra on Panel 1; (d) $C_{pe}$ ; (e) $C_{pi}$ ; and (f) power spectra on Panel 4. ....   | 65 |
| Figure 3.4 Time series and spectra of area averaged pressure coefficients for $G = 1$ mm and $H = 0.5$ mm: (a) $C_{pe}$ ; (b) $C_{pi}$ ; (c) power spectra on Panel 1; (d) $C_{pe}$ ; (e) $C_{pi}$ ; and (f) power spectra on Panel 4. ....   | 66 |
| Figure 3.5 Mean pressure distributions for the pressure taps in the middle row with numerical simulation from the point external pressure coefficients: (a) $G = 1$ mm with $H$ variations; and (b) $H = 1.2$ mm and with $G$ variations. ....  | 68 |
| Figure 3.6 RMS pressure distributions for the pressure taps in the middle row with numerical simulation from the point external pressure coefficients: (a) $G = 1$ mm with $H$ variations; and (b) $H = 1.2$ mm and with $G$ variations. ....   | 69 |
| Figure 3.7 Distribution of the ratio of the numerical to the experimental results of $C_{pi}$ for $G = 1$ mm with $H$ variations (numerical simulation from the point external pressure coefficients): (a) mean; and (b) RMS. ....  | 70 |
| Figure 3.8 Correlation of pressure data in the y-direction with respect to the pressure tap in the middle row: (a) along the gap between Panels 1 and 2 (i.e., $G_2$ ); and (b) along the midplane of Panel 2. Straight lines are used to connect data points, for clarity only. .... | 73 |

|  |     |
|--|-----|
| Figure 3.9 Mean pressure distributions for the pressure taps in the middle row with numerical simulation from the average external pressure coefficients: (a) $G = 1$ mm with $H$ variations; and (b) $H = 1.2$ mm and with $G$ variations. ....   | 74  |
| Figure 3.10 RMS pressure distributions for the pressure taps in the middle row with numerical simulation from the average external pressure coefficients: (a) $G = 1$ mm with $H$ variations; and (b) $H = 1.2$ mm and with $G$ variations. ....   | 75  |
| Figure 3.11 Distribution of the ratio of the numerical to the experimental results of $C_{pi}$ for $G = 1$ mm with $H$ variations (numerical simulation from the average external pressure coefficients): (a) mean; and (b) RMS. ....  | 76  |
| Figure 3.12 Instantaneous pressure distributions for the pressure taps in the middle row with numerical simulation from the average external pressure coefficients for $G = 1$ mm with $H$ variations: (a) $H = 15$ mm and 5 mm; (a) $H = 2.5$ mm and 1.2 mm; and (c) $H = 0.5$ mm. .... | 78  |
| Figure 3.13 Peak (minima) pressure distributions for the pressure taps in the middle row with numerical simulation from the average external pressure coefficients: (a) $G = 1$ mm with $H$ variations; and (b) $H = 1.2$ mm and with $G$ variations. ....                               | 80  |
| Figure 3.14 Pressure distributions of the numerical results from the average external pressure data with $G = 0$ mm and $H = 0$ mm: (a) mean; and (b) RMS for $G = 1$ mm with $H$ variations. ....   | 82  |
| Figure 3.15 Time series, mean and RMS values of pressure drops by the unsteady, discharge and friction terms in the analytical model for $G = 1.5$ mm and $H = 1.2$ mm: (a) pressure drop through the gap ( $G_2$ ); and (b) pressure drop through the cavity in Panel 2.85              | 85  |
| Figure 4.1 Wind tunnel model: (a) sketch of the building model with a photovoltaic panel array and definition of the coordinate system; (b) details of dimension and pressure tap layout, and photovoltaic module and row layout. ....   | 97  |
| Figure 4.2 Pressure model photographs: (a) overview; (b) side view (photographs courtesy of Farquhar and Kopp, 2009). ....   | 98  |
| Figure 4.3 Correlation of pressure data in the $y$ -direction with respect to the pressure taps in the midplane (i.e., Module 6), for $180^\circ$ wind: (a) $C_{pe}$ ; (b) $C_{pi}$ . Straight lines are used to connect data points, for clarity only. ....                             | 101 |

|  |     |
|--|-----|
| Figure 4.4 Time series and spectra of area-averaged pressure coefficients ( $C_{pe}$ and $C_{pi}$ ) on Module 6 for 12 different rows, for 180° wind: (a) Rows 1 and 2; (b) Rows 3 and 4; (c) Rows 5 and 6; (d) Rows 7 and 8; (e) Rows 9 and 10; (f) Rows 11 and 12..... | 107 |
| Figure 4.5 Mean point pressure distributions for the pressure taps along the midplane (Module 6): (a) for 180°; (b) for 0° wind. ....  | 115 |
| Figure 4.6 RMS point pressure distributions for the pressure taps in the midplane (Module 6): (a) for 180°; (b) for 0° wind. ....  | 116 |
| Figure 4.7 Peak (minimum) point pressure distributions for the pressure taps in the midplane: (a) for 180°; (b) for 0° wind.....   | 117 |
| Figure 4.8 (a) Flow separation, reattachment and vertex-generated backward flow on roof and (b) local flow separation mechanisms on panels before and after the reattachment point. ....   | 118 |
| Figure 4.9 Configurations examined numerically to investigate effects of compartmentalization of the cavity in different number of rows. ....  | 120 |
| Figure 4.10 Effects of compartmentalization of cavity in different number of rows, as shown in Figure 4.9, on mean cavity pressures for 180° wind. ....  | 120 |
| Figure 4.11 Configurations examined numerically to investigate cavity pressures on a two panel array for different locations.....  | 121 |
| Figure 4.12 Effects of compartmentalization of cavity in different locations of the roof, as shown in Figure 4.11, on mean cavity pressures for 180° wind .....  | 122 |
| Figure 4.13 Compartmentalization between rows 3 & 4 and between 9 & 10 to numerically investigate cavity pressures. ....   | 123 |
| Figure 4.14 External, cavity and net pressure distributions from compartmentalization of cavities as shown in Figure 4.13, for 180° wind: (a) mean; (b) RMS; (c) peak values. .  | 124 |
| Figure 4.15 Compartmentalization below Module 6 to numerically investigate cavity pressures.....   | 127 |

|   |     |
|---|-----|
| Figure 4.16 External, cavity and net pressure distributions from compartmentalization of cavities as shown in Figure 4.15, for 180° wind: (a) mean; (b) RMS; (c) peak values. .   | 127 |
| Figure B.1 Correlation of pressure data in the y-direction with respect to the pressure taps in the midplane (i.e., Module 6), for 0° wind: (a) $C_{pe}$ ; (b) $C_{pi}$ . Straight lines are used to connect data points, for clarity only..... | 143 |
| Figure C.1 Mean point pressure distributions for the pressure taps along the midplane (Module 6): (a) for 180°; (b) for 0° wind. – single tap for spanwise-averaged $C_{pe}$ –.....   | 147 |
| Figure C.2 RMS point pressure distributions for the pressure taps in the midplane (Module 6): (a) for 180°; (b) for 0° wind. – single tap for spanwise-averaged $C_{pe}$ –.....   | 148 |
| Figure C.3 Peak (minimum) point pressure distributions for the pressure taps in the midplane (Module 6): (a) for 180°; (b) for 0° wind. – single tap for spanwise-averaged $C_{pe}$ –.....  | 149 |
| Figure C.4 Mean point pressure distributions for the pressure taps along the midplane (Module 6): (a) for 180°; (b) for 0° wind. – three taps for spanwise-averaged $C_{pe}$ –.....   | 150 |
| Figure C.5 RMS point pressure distributions for the pressure taps in the midplane (Module 6): (a) for 180°; (b) for 0° wind. – three taps for spanwise-averaged $C_{pe}$ –.....   | 151 |
| Figure C.6 Peak (minimum) point pressure distributions for the pressure taps in the midplane (Module 6): (a) for 180°; (b) for 0° wind. – three taps for spanwise-averaged $C_{pe}$ –.....  | 152 |
| Figure C.7 Mean point pressure distributions for the pressure taps along the midplane (Module 6): (a) for 180°; (b) for 0° wind. – five taps for spanwise-averaged $C_{pe}$ –.....  | 153 |
| Figure C.8 RMS point pressure distributions for the pressure taps in the midplane (Module 6): (a) for 180°; (b) for 0° wind. – five taps for spanwise-averaged $C_{pe}$ –.....  | 154 |
| Figure C.9 Peak (minimum) point pressure distributions for the pressure taps in the midplane (Module 6): (a) for 180°; (b) for 0° wind. – five taps for spanwise-averaged $C_{pe}$ –.....   | 155 |



|   |     |
|---|-----|
| Figure C.10 Mean point pressure distributions for the pressure taps along the midplane<br>(Module 6): (a) for 180°; (b) for 0° wind. – seven taps for spanwise-averaged $Cp_e$ –....            | 156 |
| Figure C.11 RMS point pressure distributions for the pressure taps in the midplane<br>(Module 6): (a) for 180°; (b) for 0° wind. – seven taps for spanwise-averaged $Cp_e$ –....                | 157 |
| Figure C.12 Peak (minimum) point pressure distributions for the pressure taps in the<br>midplane (Module 6): (a) for 180°; (b) for 0° wind. – seven taps for spanwise-averaged<br>$Cp_e$ –..... | 158 |
| Figure C.13 Mean point pressure distributions for the pressure taps along the midplane<br>(Module 6): (a) for 180°; (b) for 0° wind. – nine taps for spanwise-averaged $Cp_e$ –.....            | 159 |
| Figure C.14 RMS point pressure distributions for the pressure taps in the midplane<br>(Module 6): (a) for 180°; (b) for 0° wind. – nine taps for spanwise-averaged $Cp_e$ –.....                | 160 |
| Figure C.15 Peak (minimum) point pressure distributions for the pressure taps in the<br>midplane (Module 6): (a) for 180°; (b) for 0° wind. – nine taps for spanwise-averaged $Cp_e$<br>–.....  | 161 |
| Figure C.16 Mean point pressure distributions for the pressure taps along the midplane<br>(Module 6): (a) for 180°; (b) for 0° wind. – 12 taps for spanwise-averaged $Cp_e$ –.....              | 162 |
| Figure C.17 RMS point pressure distributions for the pressure taps in the midplane<br>(Module 6): (a) for 180°; (b) for 0° wind. – 12 taps for spanwise-averaged $Cp_e$ –.....                  | 163 |
| Figure C.18 Peak (minimum) point pressure distributions for the pressure taps in the<br>midplane (Module 6): (a) for 180°; (b) for 0° wind. – 12 taps for spanwise-averaged $Cp_e$ –<br>.....   | 164 |
| Figure D.1 Plan view of panels with pressures at the gaps and in the cavity beneath the<br>panels. ....   | 165 |
| Figure D.2 Plan view of panels with flow velocities at the gaps and in the cavity beneath<br>the panels. ....   | 165 |

## **List of Appendices**

|  |            |
|--|------------|
| <b>Appendix A Numerical Method.....</b>  | <b>141</b> |
| <b>Appendix B Spanwise Correlation and Area-Averaged Pressures on Photovoltaic<br/>Arrays for 0° wind.....</b> | <b>142</b> |
| <b>Appendix C Point Pressures on Photovoltaic Arrays for All Spanwise-Averaged<br/>Cpe .....</b>               | <b>146</b> |
| <b>Appendix D Preliminary Study on Two-Dimensional Modelling of the Flow in the<br/>Cavity .....</b>           | <b>165</b> |

## List of Symbols

|                  |  |
|------------------|--|
| $a$              | = the area of the opening ( $\text{m}^2$ )                               |
| $C_L$            | = loss coefficient ( $=1/k^2$ )  |
| $C'_p$           | = pressure fluctuation   |
| $\tilde{C}_p$    | = RMS (i.e., standard deviation) pressure                                |
| $C_{pe}$         | = (external) pressure coefficient on external surface of the outer layer |
| $\bar{C}_{pe}$   | = mean external pressure coefficient                                     |
| $\tilde{C}_{pe}$ | = RMS external pressure coefficient                                      |
| $\check{C}_{pe}$ | = minimum external pressure coefficient                                  |
| $\hat{C}_{pe}$   | = maximum external pressure coefficient                                  |
| $C_{pi}$         | = (cavity) pressure coefficient on interior surface of the outer layer   |
| $\bar{C}_{pi}$   | = mean cavity pressure coefficient                                       |
| $\tilde{C}_{pi}$ | = RMS cavity pressure coefficient  |
| $\check{C}_{pi}$ | = minimum peak cavity pressure coefficient                               |
| $\hat{C}_{pi}$   | = maximum peak cavity pressure coefficient                               |
| $\dot{C}_{pi}$   | = first time derivative of cavity pressure coefficient                   |
| $\ddot{C}_{pi}$  | = second time derivative of cavity pressure coefficient                  |
| $C_{pn}$         | = net pressure coefficient from $C_{pe} - C_{pi}$                        |
| $\bar{C}_{pn}$   | = mean net pressure coefficient  |
| $\tilde{C}_{pn}$ | = RMS net pressure coefficient   |
| $\check{C}_{pn}$ | = minimum peak net pressure coefficient                                  |
| $\hat{C}_{pn}$   | = maximum peak net pressure coefficient                                  |
| $c$              | = flow coefficient   |
| $d$              | = time step  |
| $f$              | = friction factor  |
| $f_B$            | = body force   |
| $G$              | = gap between panels on the outer layer                                  |
| $H$              | = height of the cavity between layers                                    |

|               |   |
|---------------|---|
| $h$           | = eave height of the building   |
| $K_A$         | = the bulk modulus of air   |
| $k$           | = discharge coefficient   |
| $L$           | = length of the panel on the outer layer                              |
| $L^*$         | = non-dimensional length  |
| $L_m^*$       | = non-dimensional length in model scale                               |
| $L_f^*$       | = non-dimensional length in model scale                               |
| $l_e$         | = effective length of the fluid passing through the gap, $G$          |
| $l_o$         | = thickness of the panel (plate) on the outer layer                   |
| $l_u$         | = turbulence intensity of approaching wind                            |
| $n$           | = number of taps within the area of the panel, pressure exponent      |
| $P_e$         | = external pressure (Pa)  |
| $P_i$         | = cavity (interior) pressure (Pa)                                     |
| $P_o$         | = static pressure (Pa)  |
| $p$           | = pressure (Pa)   |
| $\dot{P}$     | = first time derivative of pressure                                   |
| $Q$           | = flow rate   |
| $Q_o$         | = flow rate through the area of the orifice ( $\text{m}^3/\text{s}$ ) |
| $Q_i$         | = flow rate through the area of the cavity ( $\text{m}^3/\text{s}$ )  |
| $R$           | = gas constant  |
| $Re_i$        | = Reynolds number for flow in the cavity                              |
| $Re_g$        | = Reynolds number for flow through the gap                            |
| $Re_h$        | = Reynolds number of building   |
| $R(\Delta y)$ | = correlation coefficient   |
| $T$           | = absolute temperature  |
| $t$           | = time (second)   |
| $t^*$         | = non-dimensional time, $\frac{t\bar{V}_h}{l_e}$                      |
| $U$           | = average velocity in the cavity, $H$ (m/s)                           |
| $\dot{U}$     | = first time derivative of $U$  |
| $U_g$         | = average velocity of flow in the gap, $G$ (m/s)                      |

|                  |   |
|------------------|---|
| $\dot{U}_g$      | = first time derivative of $U_g$                                      |
| $U_i$            | = average velocity of Couette flow per unit width in the cavity (m/s) |
| $u$              | = x-component velocity (m/s)  |
| $V^*$            | = non-dimensional velocity  |
| $V_m^*$          | = non-dimensional velocity in model scale                             |
| $V_f^*$          | = non-dimensional velocity in full scale                              |
| $\bar{V}_h$      | = mean velocity at eave height, $h$ (m/s)                             |
| $\bar{V}_{ref}$  | = mean velocity at reference height above wind tunnel floor (m/s)     |
| $V_o$            | = internal volume (m <sup>3</sup> )                                   |
| $v$              | = y-component velocity (m/s)  |
| $W$              | = area of the panel   |
| $w$              | = tributary area of the pressure tap, z-component velocity (m/s)      |
| $x$              | = x-coordinate variable   |
| $y$              | = y-coordinate variable   |
| $z$              | = z-coordinate variable   |
| $\Delta C_p$     | = pressure coefficient variation                                      |
| $\Delta C_{p_e}$ | = external pressure coefficient variation                             |
| $\Delta C_{p_i}$ | = cavity pressure coefficient variation                               |
| $\Delta P$       | = pressure variation (Pa)   |
| $\Delta P_e$     | = external pressure variation (Pa)                                    |
| $\Delta P_i$     | = pressure drop in the cavity (Pa)                                    |
| $\Delta P_o$     | = pressure drop in the orifice (Pa)                                   |
| $\Delta y$       | = distance from the midplane (m)                                      |
| $\gamma$         | = heat capacity ratio   |
| $\mu$            | = air viscosity (N·s/m <sup>2</sup> )                                 |
| $\nu$            | = kinematic viscosity of air (m <sup>2</sup> /s)                      |
| $\rho$           | = air density (kg/m <sup>3</sup> )                                    |
| $\dot{\rho}$     | = first time derivative of $\rho$                                     |
| $\tau_0, \tau_H$ | = wall shear stress (N/m <sup>2</sup> )                               |

## Chapter 1 Introduction

### 1.1 Background

Double-layer systems installed on building envelopes are widely employed by designers for many purposes. Examples of double-layer systems in practice are loose-laid roof pavers, solar panel arrays, and multi-layer wall claddings for rain and sun screens, as shown in Figure 1.1. Within the double-layer system on building envelopes, the inner layer (such as the roof or wall) is often (nominally) sealed to provide thermal insulation and water proofing (in case of the roof), while the outer layer (such as pavers, solar panels and rain screens) is essentially air-permeable. In structural design, extreme wind is often a significant concern pertaining to the structural safety of the outer layers because they are typically light-weight. Thus, the proper understanding of how wind-induced pressures are formed on the outer layer is important in design. Since the outer layer is porous, external pressures are transmitted into the cavity between the inner and outer layers. If the external pressures are completely transmitted and local flows are resisted, then the pressures on both external and internal surfaces of the outer layer can be nearly perfectly equalized resulting in close to zero net pressure on the outer layer for small panels, as illustrated in Figure 1.2. A recent review of pressure equalization concepts can be found in Kumar (2000).

Pressure equalization is defined as a process whereby the cavity pressure is partially equalized with the external pressure. It has been widely used in the wind engineering and the building science communities (Kumar, 2000; Shi and Burnett, 2013). Although “perfect” equalization does not occur in reality, pressure equalization does play a vital role in reducing the wind loads for the design of the outer layer (Bienkiewicz and Endo, 2009; Kopp, 2014). Kramer et al. (1979), Kind and Wardlaw (1982) and Bienkiewicz and Sun (1992 and 1997) found from studies on loose-laid roof pavers that the net wind pressures on the outer layer of double-layer system are often less than those on a bare roof due to the pressure equalization between the external and internal surfaces across the outer layer. In the literature, a number of works concerning pressure equalization have

been published from experimental studies as well as theoretical approaches. These are discussed below.

Solar panels on rooftop of building



Loose-laid roof pavers



Vinyl siding



Multi-layer wall claddings



Figure 1.1 Examples of double-layer system.

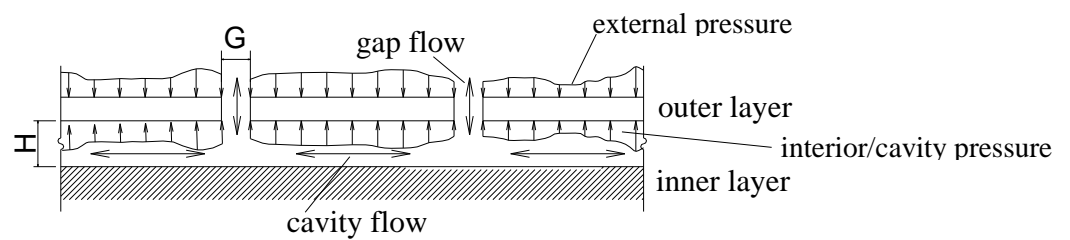


Figure 1.2 Section view of double-layer system and sketch of pressure equalization.

### 1.1.1 Experimental studies in the literature

Kramer et al. (1979) presented studies on the wind loading mechanism of roof pavers with mean external, internal and net pressure distributions. The net pressure was found to be reduced with higher resistance to flow in the cavity. Other studies, such as Gerhardt and Kramer (1983), Chino et al. (1991) and Gerhardt and Janser (1994), further investigated how the flow resistance within double-layer systems plays a role in determining pressure equalization. For instance, for a given geometry of double-layer system, higher flow resistance (by installing wire nets or batten) in the cavity flow between layers caused greater pressure equalization, resulting in lower net pressures on the outer layer. The concept of flow resistance is similar to the compartmentalization effects in double-layer system, which was examined in other publications (e.g., Inculet, 1990; Kumar, 2000). A schematic sketch of the compartmentalized cavities in air permeable double-layer systems is shown in Figure 1.3.

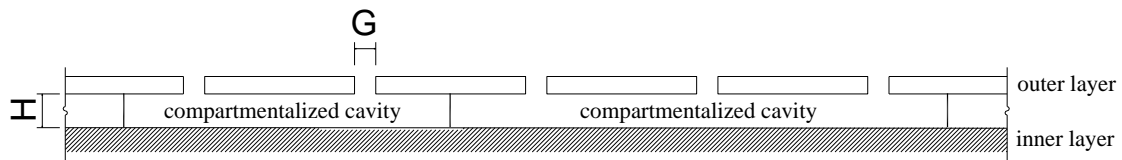


Figure 1.3 Section view of compartmentalized cavities in double-layer systems.

Other experimental studies described pressure equalization on roof pavers or asphalt shingles on roof and concluded that the pressure equalization depends on the gap ( $G$ ) between roof pavers and the height ( $H$ ) of the cavity. Failure model tests were carried out by Kind and Wardlaw (1982) to investigate lifting and overturning of roof pavers. They observed that blow-off of roof pavers could be prevented by the presence of gaps between roof paver elements, compared with tightly fitting joints between paver elements. Based on the failure model tests, a correlation model was developed by Kind et al. (1988) for predicting the wind speeds causing failure of roof pavers. Failure wind speed investigations on roof pavers were also conducted by Okada and Okabe (1991) with 1:50 models to examine the effects of two different heights of the cavity underneath the roof pavers; one loose-laid and the other raised to a certain height. The roof pavers from the raised configuration were blown off at lower wind speeds (due to poor pressure



equalization). Peterka et al. (1997) found that, from field measurements and wind tunnel tests, uplift net loads on asphalt shingles is significantly lower than typical design loads specified by building codes.

On the other hands, researchers such as Cheung and Melbourne (1988), Bienkiewicz and Sun (1992 and 1997), O'Brien et al. (2004) and Bienkiewicz and Endo (2009) conducted parametric studies of how the geometry of double-layer system (the size of opening (i.e., gap between panels,  $G$ ) in outer layer, and the height ( $H$ ) of the cavity, as shown in Figure 1.2) alters pressure equalization. For example, for a given external pressure, the level of pressure equalization depends on the gap-to-cavity size ratio, in such a way that the higher the ratio, the greater the pressure equalization. One of the most recent studies on pressure equalization on roof pavers were carried out by Mooneghi et al. (2014) in a large-scale testing facility at Florida International University. The results showed that higher gap-to-height ratio ( $G/H$ ) and the parapet height reduce the net loads, which is similar to the results from wind tunnel tests.

Many studies on pressure equalization of double-layer systems have been published pertaining to building facade and rainscreen systems, since Garden (1964) introduced the principle of the rain penetration control on multilayer walls. Gerhardt and Kramer (1983) presented experimental results of external and net pressures on building facades, while adjusting the permeability of the cladding systems and the resistance of the cavity flow. The results showed that increasing the permeability in the outer layer and the resistance of the cavity leads to a decrease of net loads. Similar results on the effects of the gap size ( $G$ , i.e., the permeability) and the cavity height ( $H$ , i.e., the resistance) on pressure equalization in rainscreen walls can be found in other experimental studies, such as Fazio and Kontopidis (1988), Gerhardt and Janser (1994), Burgess (1995a), and Van Schijndel and Schols (1998). A study carried out by Killip and Cheetham (1984) on rainscreen walls also investigated the effect of air-permeability of the outer layer and the inner layer, as well. They concluded that 99% pressure equalization occurred when the permeability ratio of the outer layer to the inner layer (i.e., the ratio of total opening areas between the outer layer and the inner layer) is 25 – 40. However, the study did not fully take into account the effect of unsteadiness and other significant factors (e.g., external pressure

gradients and the geometry of the double-layer system), which were examined later by Inculet and Davenport (1994).

Some experimental studies quantified the degree of pressure equalization on rainscreen walls. Ganguli and Dalglish (1988) measured the cavity pressure in full-scale for a rainscreen wall system of an existing building and reported significant reductions of net loads on the rainscreen and found as much as a 75 % reduction compared to the external pressures in cases where the gaps in the inner layer and compartments in the cavity are particularly effective. Baskaran and Brown (1992) found that, from model-scale experiments on a pressure equalized rainscreen wall, the equalization between the external and cavity pressures is at least 50% and the air-permeability of the outer layer should be at least 1%.

Gerhardt and Janser (1994) investigated differences of the pressure equalization performance between model scale and full scale and found that the net loads in full scale tend to be greater. This is due to the fact that the pressure losses in the cavity flow for the laminar model scale flow is greater than those for the turbulent full scale flow (i.e., the friction factor for the laminar model scale flow is greater than that for the turbulent full scale flow (Potter et al. (2012)). They suggested that the model scale cavity height ( $H$ ) should be larger than the full scale cavity height by a factor of 1.24 for the equivalent flow condition in the model scale and full scale.

Choi and Wang (1998) conducted full-scale experiments with aluminum-curtain-wall systems to investigate effects of the flexibility of the inner layer on pressure equalization performance. Although the tests were limited to sinusoidal external pressure fluctuations, the study concluded that the flexibility of the inner layer disrupts the pressure equalization of the outer layer (i.e., it increases the net wind loads on the outer layer). Other research concerning the flexibility of the inner layer can be found in Shi et al. (2006) and Shi and Burnett (2008 and 2013).

Kumar et al. (2003) concluded from field measurements of wind loads on rainscreen walls that the cavity pressure can be equalized to the external pressure for mean and quasi-steady pressures, but they are less equalized for highly fluctuating external pressures. Design and construction guidelines to improve pressure equalization on stone wall claddings were addressed by Mar et al. (2011) in terms of the size and shape of the

gap, the cavity volume and the compartment seals. Recently, pressure equalization performance of wall systems with sheathing and siding was investigated by Kopp and Gavanski (2012), Cope et al. (2013) and Kochkin et al. (2013). The studies showed that the pressure equalization is an important parameter in determining the wind loads on both the sheathing and siding.

More recently, the concept of pressure equalization has been examined for roofs with solar panels, such as O'Brien et al. (2004), Bienkiewicz and Endo (2009), Kopp et al. (2012), Geurts and Blackmore (2013), Banks (2013), Cao et al. (2013), and Kopp (2014). O'Brien et al. (2004), Bienkiewicz and Endo (2009) conducted wind tunnel experiments to characterize effects of the gap-to-cavity size ratio ( $G/H$ ) on pressure equalization. Wind tunnel research has been conducted by Kopp et al. (2012), Banks (2013), Cao et al. (2013), and Kopp (2014) to determine wind load design procedures for photovoltaic arrays, covering a wide range of tilt angles, mounted on typical low-rise buildings with flat roofs. Experiments on a stand-off photovoltaic system mounted on a full-scale, pitched roof carried out by Geurts and Blackmore (2013) have shown that there is significant reduction of net uplift loads on the photovoltaic panels due to the correlation of pressures on the upper and lower surfaces of the panel, i.e., pressure equalization.

### **1.1.2 Analytical models in the literature**

Experimental studies in the literature have shown that pressure equalization largely depends on how the cavity pressures respond to the external pressures, while the cavity pressure is formed through the gap flow and the cavity flow. The fluid motions involved in the gap and cavity flows, in turn, are related to various parameters, e.g., the external pressure variations, the gap-to-cavity size ratio, the air-permeability ratio of the outer layer to the inner layer, the outer layer's panel size and thickness, and the locations of compartment boundaries. Some flow equations used to simplify modelling of wind loads on rainscreen walls have been introduced in the literature. The basic equations employed to simulate the flows in double-layer systems are either the power law equation, i.e., the discharge equation for flow through openings (ASHRAE, 2009),

$$Q = ca(\Delta P)^n \approx ka \sqrt{\frac{2\Delta P}{\rho}} \quad (1.1)$$

or the unsteady discharge equation i.e., the Helmholtz resonator model (Holmes, 1979; Vickery, 1986),

$$\rho l_e \dot{U} + C_L \frac{\rho}{2} U|U| = \Delta P \quad (1.2)$$

along with the continuity equation, where  $Q$  is the flow rate through the area of opening,  $a$ ,  $c$  is the flow coefficient,  $\Delta P$  is pressure difference across opening,  $n$  is the pressure exponent,  $k$  is the discharge coefficient,  $C_L$  is the loss coefficient,  $\rho$  is the air density,  $l_e$  is the effective length of opening,  $U$  is the flow velocity.

In 1980s and early 1990s (e.g., Killip and Cheetham, 1984; Fazio and Kontopidis, 1988; Baskaran and Brown, 1992; Xie et al, 1992), analytical models were developed from Eq. (1.1), assuming incompressible air. Burgess (1995b) and Van Schijndel and Schols (1998) developed models based on Eq. (1.1) and the ideal gas law (Potter et al., 2012),

$$p = \rho RT \quad (1.3)$$

where  $p$  is the absolute pressure,  $R$  is the gas constant and  $T$  is the absolute temperature. Inculet and Davenport (1994), Choi and Wang (1998), and Kumar and Van Schijndel (1999) employed Eq. (1.2) to take into account the effect of unsteadiness. The predicted net pressures on the outer layer simulated by the analytical models above were well matched with experimental data. However, the models were limited to a particular condition of spatially uniform external pressure, which means a single external pressure. The uniform external pressure can be achieved in rainscreen walls with compartmentalization within which the external pressure is assumed to be spatially uniform.

However, compartments are not always used with double-layer systems, for instance, loose-laid roof pavers whose cavity is required for the drainage of rainwater. To model the cavity pressures which are spatially varying, resulting in longitudinal flow in the cavity, Amano et al. (1988), Trung et al. (2010) and Lou et al. (2012) used Eq.(1.2) for flows in the cavity between the layers, perceiving the cavity flow as the orifice

(discharge) flow, as well. The discharge equation has been widely employed in wind engineering to model the flow through an opening (Holmes, 1979; Vickery, 1986; Sharma and Richards, 1997; Oh et al., 2007; Kopp et al., 2008; Ginger et al. 2010). However, it may not be sufficient to describe a fluid motion in the cavity because there should be significant viscous effects involved in the cavity flow, in particular, in the case that the cavity is thin and long. On the other hand, Sun and Bienkiewicz (1993) developed an analytical model to compute pressure distributions in the cavity underneath loose-laid roof pavers. In this model they assumed steady flows in gap and cavity and used Darcy's law to model the mean flow, while the assumption for this analytical model is limited to the flow at low Reynolds Number. The significant studies on numerical models for internal and cavity pressures are summarized in Table 1.1, along with model dimensions (in space and time), the type of model employed, as well as the intended applications.

## **1.2 Motivations of Thesis**

Although there has been invaluable research on many aspects of pressure equalization for double-layer systems, this problem has not been completely solved. For example, most building codes of practice do not currently provide exclusive guidance for the design of double-layer systems (e.g., ASCE 7-10 allows for reductions on design loads for air-permeable cladding only if test data or literature approve lower loads), while wind tunnel testing remains a significant challenge because of scale effects. This may be attributed to the lack of understanding mechanisms of pressure equalization and insufficient studies. Further investigations on pressure equalization on double-layer systems are needed in specific areas, such as detailed cavity pressure distributions and modelling of flows involved in air permeable, double-layer systems in regions of separated flow. The analytical models developed in past years have focused on modelling the local cavity pressure within the compartment, while modelling of spatially and temporally varying cavity pressures in double-layer systems has not yet been performed.

Table 1.1 Summary of numerical models for internal pressures

| Author                      | Year | Dimensions<br>in space | Dimensions<br>in time          | Model   | Application                 |  |
|-----------------------------|------|------------------------|--------------------------------|---|-----------------------------|--|
| Killip and Cheetham         | 1984 | uniform<br>pressure    | steady                         | power law<br>equation<br>(i.e.,discharge<br>equation) | Rainscreen<br>walls         |  |
| Fazio and Kontopidis        | 1988 |                        |                                |   |                             |  |
| Baskaran and Brown          | 1992 |                        | 1-dimensional<br>(fluctuating) | power law<br>equation +<br>ideal gas law              |                             |  |
| Xie et al.                  | 1992 |                        |                                |   |                             |  |
| Burgess                     | 1995 |                        |                                |   |                             | Helmholtz<br>resonator<br>(i.e.,unsteady<br>discharge<br>equation) |
| Van Schijndel and<br>Schols | 1998 |                        |                                |   |                             |  |
| Inculet and Davenport       | 1994 |                        |                                |   |                             |  |
| Choi and Wang               | 1998 |                        |                                |   |                             |  |
| Kumar and Van<br>Schijndel  | 1999 |                        |                                |   |                             |  |
| Holmes                      | 1979 |                        |                                | Building<br>internal<br>pressure                      |                             |  |
| Vickery                     | 1986 |                        |                                |   |                             |  |
| Sharma and Richards         | 1997 |                        |                                |   |                             |  |
| Oh et al.                   | 2007 |                        |                                |   |                             |  |
| Ginger et al.               | 2010 |                        |                                |   |                             |  |
| Lou et al.                  | 2012 | 1-dimensional          | 1-dimensional<br>(fluctuating) | Darcy’s law   | Double-skin<br>facades      |  |
| Amano et al.                | 1988 | 2-dimensional          |                                |   | Roof pavers                 |  |
| Trung et al.                | 2010 |                        |                                |   | Porous roof<br>cover sheets |  |
| Sun and Bienkiewicz         | 1993 |                        |                                |   | Roof pavers                 |  |
| Current study               | 2014 | 1-dimensional          | 1-dimensional<br>(fluctuating) | Unsteady<br>discharge<br>equation +<br>Couette flow   | Double-<br>layer roof       |  |

### 1.3 Objectives of Thesis

The major goal of this study is to characterize and model how the cavity pressures beneath the outer layer are related to the external pressures on the external surface of the outer layer in air permeable, double-layer, roof systems in regions of separated flow. To attain the goal of the study, wind tunnel models and an analytical model are developed and the model is validated with the experimental data.

Experiments with the wind tunnel models were intended to investigate the detailed cavity pressure distributions and the correlation with external pressures, rather than design wind loads on double-layer roof systems. The effects of geometric parameters (gap between panels,  $G$ , height of cavity,  $H$ , and length of panel,  $L$ ) on the cavity pressure were also examined (with 39 different wind tunnel model configurations).

Development of the analytical model aimed to (i) model the flow involved in double-layer systems, and thus, (ii) predict time histories of the cavity pressures on double-layer system, in terms of external pressure time histories with the panel and cavity geometric parameters.

Numerical investigations on photovoltaic panel arrays were undertaken to (i) determine whether the analytical model is applicable to a practical problem which consist of 12 photovoltaic rows placed at the entire roof zones from the separation, the reattachment point, up to the leeward zone, and (ii) discuss how this analytical model can be used as a tool to design compartments for pressure equalizing, double-layer systems.

### 1.4 Organization of Thesis

This thesis is prepared in the Integrated-Article Format as specified by the School of Graduate and Postdoctoral Studies at The University of Western Ontario. Except for the first and last chapters, each chapter is presented in a manuscript format without an abstract. Although this is an Integrated-Article Thesis, Chapters 2, 3 and 4 are linked. Chapter 2 presents experimental results which are used to validate numerical results presented in Chapter 3. The analytical model developed in Chapter 3 is used to investigate photovoltaic panel arrays and compartmentalization presented in Chapter 4.

Chapter 2 describes the analysis of the cavity pressure distributions on a double-layer roof system while the gap ( $G$ ) between panels and the height ( $H$ ) of cavity are varied, along with the result of the external pressure distributions. Wind tunnel data for the variation of the gaps and heights are obtained from 39 different configurations. Wind perpendicular to the building edge is investigated so that the mean flow on the double-layer roof system is approximately two-dimensional.

Chapter 3 presents the development of a one-dimensional analytical model to simulate fluctuating cavity pressures on a double-layer roof system for perpendicular wind, along with its validation by comparing with experimental data presented in Chapter 2. The numerical model is developed based on considering two primary types of flow equation: the unsteady discharge equation for the gap flow and the unsteady equation of Couette flow for the cavity flow.

Chapter 4 discusses an investigation of the cavity and external pressure distributions on a photovoltaic panel array mounted on a large flat rooftop, with numerical results simulated by the analytical model developed in Chapter 3. The wind tunnel data obtained by Kopp (2014) are used for this study. In addition, numerical investigations on different configurations of compartmentalization of the cavity in the photovoltaic array are carried out to investigate the compartment effects on the cavity pressure distributions and the net loads.

Finally, Chapter 5 discusses the conclusions obtained from this study and recommendations for future studies.

## 1.5 Original Contributions

This study confirms that the cavity pressures on double-layer systems depend on the gap-to-cavity size ratio ( $G/H$ ), as well as the ratio of the loss coefficients (i.e., resistance to flow) between the gap and cavity flows. Detailed cavity pressure distributions are revealed by a fine resolution of pressure taps, which are varied in the cavity either fairly linearly or uniformly for two-dimensional flow. The linear pressure gradient results from the friction losses in the cavity flow, while the uniform pressure gradient is caused by the



significant pressure drop through the gap flow, which is comparable to the (building) internal pressure problem (Chapter 2).

A one-dimensional analytical model is developed to predict temporal cavity pressures as a function of (i) external pressure, (ii) gap ( $G$ ) between panels, (iii) height ( $H$ ) of cavity, (iv) length of panel, (v) thickness of panel, and (vi) the loss coefficients. The current analytical model captures time histories of one-dimensional cavity pressures to a great extent (Chapters 3 and 4) and provides a necessary basis to solve two-dimensional cavity pressures for the future studies.

## References

- Amano, T., Fujii, K. and Tazaki, S. (1988). Wind loads on permeable roof-blocks in roof insulation systems. *Journal of Wind Engineering and Industrial Aerodynamics*, 29: 39-48.
- ASCE 7 -10. (2010). Minimum design loads for buildings and other structures. *American Society of Civil Engineers*, 2010.
- ASHRAE HANDBOOK. (2009). Fundamentals, SI Edition, American Society of Heating Refrigeration and Air-conditioning Engineers, Chapter 16: 16.1-16.36.
- Banks, D. (2013). The role of corner vortices in dictating peak wind loads on tilted flat solar panels mounted on large, flat roofs. *Journal of Wind Engineering and Industrial Aerodynamics*, 123: 192-201.
- Baskaran, B.A. and Brown, W.C. (1992). Performance of pressure equalized rainscreen walls under cyclic loading. *Journal of Thermal Insulation and Building Envelopes*, 16: 183-193.
- Bienkiewicz, B. and Sun, Y. (1992). Wind-tunnel study of wind loading on loose-laid roofing systems. *Journal of Wind Engineering and Industrial Aerodynamics*, 41-44: 1817-1828.
- Bienkiewicz, B. and Sun, Y. (1997). Wind loading and resistance of loose-laid roof paver systems. *Journal of Wind Engineering and Industrial Aerodynamics*, 77: 401-410.

- Bienkiewicz, B. and Endo, M. (2009). Wind considerations for loose-laid and photovoltaic roofing systems. *Proceedings of the 2009 Structures Congress*, Austin, Texas, April 30-May 2, 2009, pp. 2578-2587.
- Burgess J.C. (1995a). Air pressure equalization in rainscreened joints by geometric alteration. *Building and Environment*, 30(1): 13-18.
- Burgess J.C. (1995b). Pressure equalised rainscreen joint modelling with the numerical model PERAM. *Building and Environment*, 30(1): 385-389.
- Cheung, J.C.K. and Melbourne, W.H. (1988). Wind loading on a porous roof. *Journal of Wind Engineering and Industrial Aerodynamics*, 29: 19-28.
- Chino, N., Iwasa, Y., Mataka, Y., Hagiwara, T. and Sato, H. (1991). Internal pressure of double composite exteriors. *Journal of Wind Engineering and Industrial Aerodynamics*, 38: 381-391.
- Choi, E.C.C. and Wang, Z. (1998). Study on pressure-equalization of curtain wall systems. *Journal of Wind Engineering and Industrial Aerodynamics*, 73:251-266.
- Cope, A.D., Crandell, J.H., Johnston, D., Kochkin, V., Liu, Z., Stevig, L., and Reinhold, T.A. (2013). Wind Loads on Components of Multi-Layer Wall Systems with Air-Permeable Exterior Cladding. *Proceedings of ATC & SEI Conference on Advances in Hurricane Engineering*, Miami, Florida, October 24-26, 2012, pp. 238-257.
- Fazio, P. and Kontopidis, T. (1988). Cavity pressure in rain screen walls. *Building and Environment*, 23(2): 137-143.
- Ganguli, U. and Dalgliesh, W.A. (1988). Wind pressures on open rain screen walls: place air Canada. *Journal of Structural Engineering*, 114(3): 642-656
- Garden, G.K. (1964). Glazing design. *Canadian Building Digest*, No. 55 (CBD-55), National Research Council, Canada.
- Gerhardt, H.J. and Janser, F. (1994). Wind loads on wind permeable facades. *Journal of Wind Engineering and Industrial aerodynamics*, 53:37-48.
- Gerhardt, H.J. and Kramer, C. (1983). Wind loads on wind-permeable building facades. *Journal of Wind Engineering and Industrial Aerodynamics*, 11: 1-20.

- Geurts, C.P.W. and Blackmore, P. (2013). Wind loads on stand-off photovoltaic systems on pitched roofs. *Journal of Wind Engineering and Industrial Aerodynamics*, 123: 239-249.
- Ginger, J.D., Holmes, J.D. and Kim, P.Y. (2010). Variation of internal pressure with varying sizes of dominant openings and volumes. *Journal of Structural Engineering*, 136(9): 1319-1326.
- Holmes, J.D. (1979). Mean and fluctuating internal pressure induced by wind. *Proceedings of the 5<sup>th</sup> International Conference on Wind Engineering*, Colorado State University, Fort Collins, Colorado, USA, July, 1979, pp.435-450.
- Inculet, D.R. (1990). Pressure-equalization of rainscreen cladding. *M.E.Sc. Thesis*, The University of Western Ontario, Canada, 1990.
- Inculet, D.R. and Davenport, A.D. (1994). Pressure-equalized rainscreens: A study in the frequency domain. *Journal of Wind Engineering and Industrial Aerodynamics*, 53: 63-87.
- Killip, L.R. and Cheetham, D.W. (1984). The prevention of rain penetration through external walls and joints by means of pressure equalization. *Building and Environment*, 19(2): 81-91.
- Kind, R.J. and Wardlaw, R.L. (1982). Failure mechanism of loose-laid roof-insulation systems. *Journal of Wind Engineering and Industrial Aerodynamics*, 9: 325-341.
- Kind, R.J. Savage, M.G. and Wardlaw, R.L. (1988). Prediction of wind-induced failure of loose laid roof cladding systems. *Journal of Wind Engineering and Industrial Aerodynamics*, 29: 29-37.
- Kochkin, V., Davies, R. and DeRenzis, A. (2013). Evaluation of the wind pressure performance of walls with exterior rigid foam sheathing. *Proceedings of ATC & SEI Conference on Advances in Hurricane Engineering*, Miami, Florida, October 24-26, 2012, pp. 258-269.
- Kopp, G.A. (2014). Wind loads on Low-Profile, Tilted, Solar Arrays Placed on Large, Flat, Low-Rise Building Roofs. *Journal of Structural Engineering*, 140 (2): 04013057.

- Kopp, G.A., Farquhar, S. and Morrison, M.J. (2012). Aerodynamic mechanisms for wind load on tilted, roof-mounted solar arrays. *Journal of Wind Engineering and Industrial Aerodynamics*, 111: 40-52.
- Kopp, G.A. and Gavanski, E. (2012). Effects of pressure equalization on the performance of residential wall systems under extreme wind loads. *Journal of Structural Engineering*, 138 (4): 526-538.
- Kopp, G.A., Oh, J.H. and Inculet, D.R. (2008). Wind-induced internal pressures in houses. *Journal of Structural Engineering*, 134 (7): 1129-1138.
- Kramer, C., Gerhardt, H.J. and Kuster, H.W. (1979). On the wind-loading mechanism of roofing elements. *Journal of Industrial Aerodynamics*, 4: 415-427.
- Kumar, K.S. (2000). Pressure equalization of rainscreen walls: a critical review. *Building and Environment*, 35: 161-179.
- Kumar, K.S., Stathopoulos, T. and Wisse, J.A. (2003). Field measurement data of wind loads on rainscreen walls. *Journal of Wind Engineering and Industrial Aerodynamics*, 128: 22-36. 91:1401-1417.
- Kumar, K.S. and Van Schijndel, A.W.M. (1999). Prediction of pressure equalization performance of rainscreen walls. *Wind and Structures*, 2(4): 325- 345.
- Lou, W., Huang, M., Zhang, M. and Lin, N. (2012). Experimental and zonal modeling for wind pressures on double-skin facades of a tall building. *Energy and Buildings*, 54:179-191.
- Mas, A., Gutierrez, J. Gil, E, Gil, A. and Galvan, V. (2011). Design and construction recommendations to improve impermeability in rainscreen walls built with natural stone coverings. *Construction and Building Materials*, 25: 1753-1761.
- Mooneghi, M.A., Irwin, P. and Chowdhury, A.G. (2014). Large-scale testing on wind uplift of roof pavers. *Journal of Wind Engineering and Industrial Aerodynamics*, 128: 22-36.

- O'Brien, C., Neff, D.E., Bienkiewicz, B. and Dinwoodie, T. (2004). Optimization of wind resistance of photovoltaic roofing system. *Proceedings of the 2004 Structures Congress*, Nashville, Tennessee, May 22-26, 2004, pp. 1-8.
- Oh, J.H., Kopp, G.A., and Inculet, D. R. (2007). The UWO contribution to the NIST aerodynamic database for wind loads on low buildings: Part 3. Internal Pressures. *Journal of Wind Engineering and Industrial Aerodynamics*, 95: 755-779.
- Okada, H. and Okabe, M. (1991). Wind tunnel tests to determine the wind forces on roof blocks for existing buildings. *Journal of Wind Engineering and Industrial Aerodynamics*, 38: 393-403.
- Peterka, J.A., Cermak, J.E., Cochran, L.S., Cochran, B.C., Hosoya, N., Derickson, R.G., Harper, C., Jones, J. and Metz, B. (1997). Wind uplift model for asphalt shingles. *Journal of Architectural Engineering*, 3(4): 147-155.
- Potter, M.C., Wiggert, D.C. and Rmadan, B.H. (2012). *Mechanics of fluids*. 4<sup>th</sup> Edition, Cengage Learning, 2012.
- Sharma, R.N. and Richards, P.J. (1997). Computational modelling of transient response of building internal pressures to a sudden opening. *Journal of Wind Engineering and Industrial Aerodynamics*, 72: 149-161.
- Shi, X. and Burnett, E. (2008). Mechanics and test study of flexible membranes ballooning in three dimensions. *Building and Environment*, 43: 1871-1881.
- Shi, X. and Burnett, E. (2013). Effect of membrane ballooning on screen pressure equalization: A short literature review. *Journal of Building Physics*, 37(2): 185-199.
- Shi, X., Liang, J. and Burnett, E. (2006). Mechanics and test study of two-dimensional flexible membranes. *Journal of Architectural Engineering*, 12(2): 93-99.
- Sun, Y. and Bienkiewicz, B. (1993). Numerical simulation of pressure distributions underneath roofing paver systems. *Journal of Wind Engineering and Industrial Aerodynamics*, 46-47: 517-626.
- Trung, V.T., Tamura, Y. and Yoshida, A. (2010). Numerical computation for lower surface pressures on a porous sunshade roof cover sheet. *Proceedings of the 5<sup>th</sup> International*

*Symposium on Computational Wind Engineering*, Chapel Hill, North Carolina, USA, May 23-27, 2010.

- Van Schijndel, A.W.M. and Schols, S.F.C. (1998). Modeling pressure equalization in cavities. *Journal of Wind Engineering and Industrial Aerodynamics*, 74-76:641-649.
- Vickery, B.J. (1986). Gust factors for internal pressures in low-rise buildings. *Journal of Wind Engineering and Industrial Aerodynamics*, 23: 259-271.
- Xie, J., Schuyler, G.D. and Resar, H.R. (1992). Prediction of net pressure on pressure equalized cavities. *Journal of Wind Engineering and Industrial Aerodynamics*, 41-44: 2449-2460.

## **Chapter 2**

### **An Experimental Study of Pressure Distributions within a Pressure Equalizing, Double-Layer, Roof System in Regions of Separated Flow**

#### **2.1 Introduction**

The wind-induced external pressure distributions and the building internal pressures are well defined in many current building codes, while the net wind loads used for building envelop design are often significantly different because of the significance of the building internal pressure. In the same vein, the net wind pressures on the outer (air-permeable) layer of double-layer system should be taken into account with the interior pressure in the cavity (cavity pressure) between layers.

Past studies on double-layer roof system in the literature showed that the application of the building codes to the design of the outer layer results in a considerably conservative estimate of wind loads in most of regions of roof, due to the fact that the effects of pressure equalization are not taken into account (Kind and Wardlaw, 1982; Gerhardt and Kramer, 1983; Chino et al., 1991; Bienkiewicz and Sun, 1992 and 1997; O'Brien et al., 2004; Bienkiewicz and Endo, 2009; Geurts and Blackmore, 2013; Kopp, 2014).

As discussed earlier in Chapter 1, pressure equalization is dependent on the geometric parameters of the double-layer system (Bienkiewicz and Sun, 1992, 1997; and Bienkiewicz and Endo, 2009). The geometric parameters of double-layer system include the gap ( $G$ ) between panels, the height ( $H$ ) of the cavity between panels and the roof, and the panel size ( $L$ ), as defined in Figure 2.1. However, the foregoing research has focused on characterizing the pressure equalization on double-layer system and the effect of the gap-to-cavity size ratio ( $G/H$ ) on the cavity pressure. Investigations on the detailed cavity pressure distributions obtained from fine resolution of pressure taps, changes in external and cavity pressure distributions by various  $G/H$  ratios, and mechanisms of pressure

distributions have not been extensively carried out in the literature. The detailed pressure measurements in the cavity characterize how the pressures transmitted through two adjacent gaps are modified through the cavity flow.

In this chapter, the effects of the geometric parameters ( $G$ ,  $H$  and  $L$ ) on the detailed cavity pressure distribution, and the correlation with the external pressures, are examined by using wind tunnel data as described in the next section. A non-dimensional parameters involved in mechanism of generating the cavity pressures are described based on some of flow equations.

## 2.2 Experimental Setup

A rigid wind tunnel model of the double-layer roof system placed on a low-rise building was designed and equipped with pressure measurement instrumentation, as shown in Figure 2.1a. The model size was selected to allow reasonably accurate construction of the gaps and cavity depths, and is consistent with the building sizes used for previous experiments on roof-mounted solar arrays (Kopp et al., 2012). The maximum nominal blockage was 4.8% from the geometry of the test building, which was 323 mm high  $\times$  805 mm wide  $\times$  955 mm long. The roof height Reynolds Number was  $2 \times 10^5$ . One of the goals of the experiments was to investigate pressure distributions in a two-dimensional internal flow, simplifying the problem. Thus, the pressure data were collected only from the region in the middle of the front (windward) portion of the roof, as shown in Figure 2.1a, where there is little impact from the vortex generated by the side edge of the roof so that the mean flow is approximately two-dimensional. The panel and tap region in Figure 2.1a was built from Plexiglas and equipped with pressure measurement instrumentation, while the rest of the building mass was constructed from Styrofoam, as shown in the photograph in Figure 2.2b.

Four panels representing the outer layer were arranged as shown in Figure 2.1b, and embedded in the top surface of the model so that the pressure underneath the panels are only influenced by the pressures at the gaps between the panels. The panels were



equipped with pressure taps on the external and internal surfaces; each surface with 48 taps. The PVC tubes connecting the 96 pressure taps with pressure scanners were designed to pass through the openings located outside the interior volume (i.e., the cavity between the layers) so that the tubes do not disrupt the cavity flows at all, as shown in Figure 2.1b.

The gaps ( $G$ ) between panels were set by sliding the panels and screw-fastening. The positions of the screw holes were machined to maintain dimensional precision for the different gaps. When the gap is reduced, the gap at the end between the last panel and the roof increases. Thus, a dummy panel was added to make this end gap into the same size. The height ( $H$ ) of the cavity between panels and the roof surface was altered by lowering the inner layer so that the external surface of the panel is always flush with roof, as shown in Figure 2.1b. The edges of the inner layer were machined and grease-sealed to allow sliding and to ensure air-tightness. In order to investigate a larger panel size, the four panels were placed together and the gaps between panels were sealed by tape. In total, 39 configurations were examined including 36 configurations from six different  $G$  (0, 0.5, 1, 1.5, 2.5 and 15 mm) and six different  $H$  (0, 0.5, 1.2, 2.5, 5 and 15 mm) based on  $L=50$  mm. As well, three additional  $H$  (0.5, 5 and 15 mm) with  $L=200$  mm were included. 591 pressure taps were installed on the upper surface of the inner layer to provide a fine resolution of the pressure underneath the panel. The pressure tap layout is depicted in Figure 2.1b.

The tests were carried out in Boundary Layer Wind Tunnel II at the University of Western Ontario (UWO). The wind tunnel has a test section 3.4 m wide by 2.5 m high at the turntable, with an upstream fetch of 39 m. A photograph of the upstream terrain in the wind tunnel is shown in Figure 2.2a and a close-up view of the model in Figure 2.2b. The upstream terrain was designed to match an open country terrain with identical profiles as those used by Kopp et al. (2012). Figure 2.3 depicts the measured mean longitudinal velocity and turbulence intensity profiles. The mean velocity in the profile was normalized to the eave height of 323 mm.

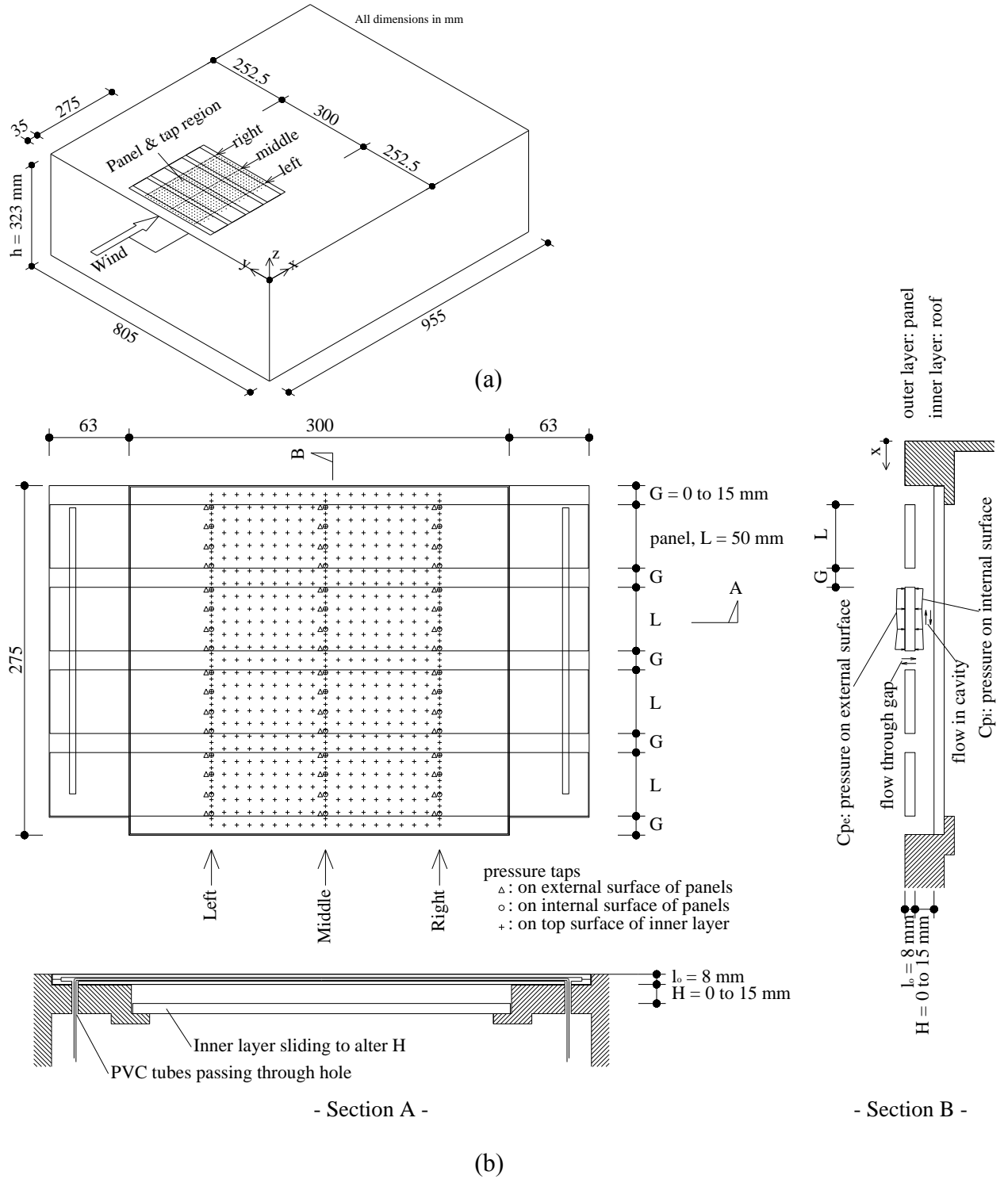


Figure 2.1 Wind tunnel model: (a) sketch of the building model with locations of panels and definition of the coordinate system; (b) details of panels and pressure tap layout.



(a)



(b)

Figure 2.2 Photographs of (a) the upstream terrain in the wind tunnel with the model for the panel and tap region built from Plexiglas, (b) a close-up of the model.

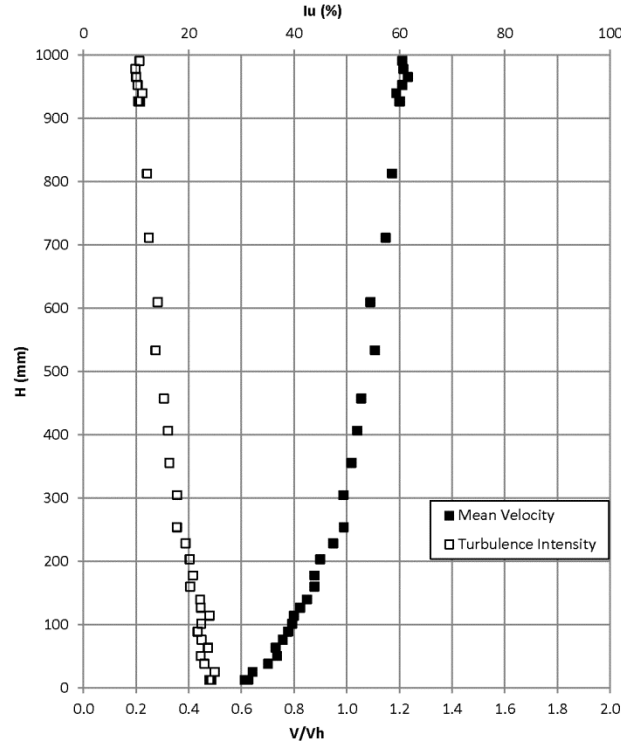


Figure 2.3 Vertical profile of mean wind velocity and longitudinal turbulence intensity simulated in the wind tunnel.

Pressures measurements were conducted at a roof height wind speed of approximately 10.7 m/s for a wind direction perpendicular to the leading edge of the roof, as shown in Figure 2.1a. For each configuration, pressures were sampled essentially simultaneously at a rate of 400 Hz for 160 seconds, equivalent to other wind tunnel studies of low-rise buildings (Kopp et al., 2005, 2012). The sampled data were digitally low-pass filtered at 200 Hz. Experimental details can be found in Table 2.1. The measured pressure coefficient data were referenced to the mean dynamic pressure at the reference height of about 1.4 m above the tunnel floor, and then re-referenced to the mean dynamic pressure at the eave height,  $h$ , using the mean velocity profile depicted in Figure 2.3.

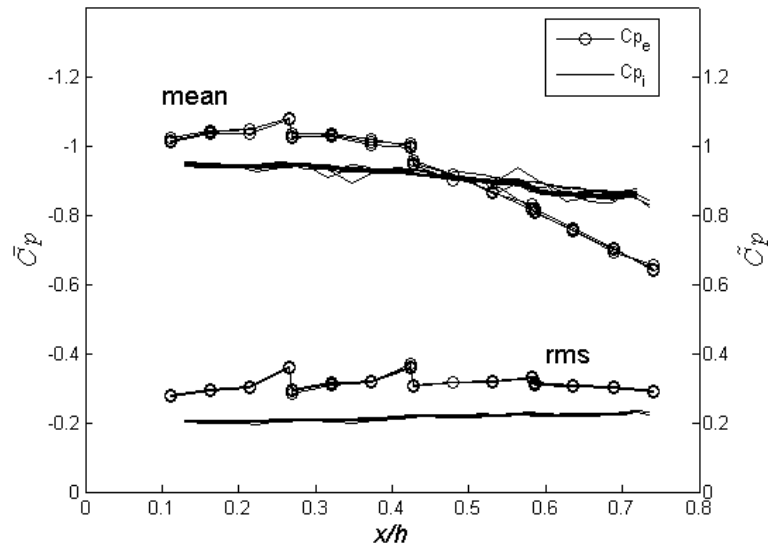
Table 2.2 Experimental details of wind tunnel tests

| Parameter                         | Pressure tests              |
|-----------------------------------|-----------------------------|
| eave height, $h$                  | 323 mm                      |
| gap between panels, $G$           | 0, 0.5, 1, 1.5, 2.5 & 15 mm |
| gap between layers, $H$           | 0, 0.5, 1.2, 2.5, 5 & 15 mm |
| thickness of panel, $l_o$         | 8 mm                        |
| upstream terrain                  | open country                |
| number of taps                    | 687                         |
| sampling frequency                | 400 Hz                      |
| low pass filter cut-off frequency | 200 Hz                      |
| sampling time                     | 160 sec                     |
| roof height wind speed            | 10.7 m/s                    |

## 2.3 Results

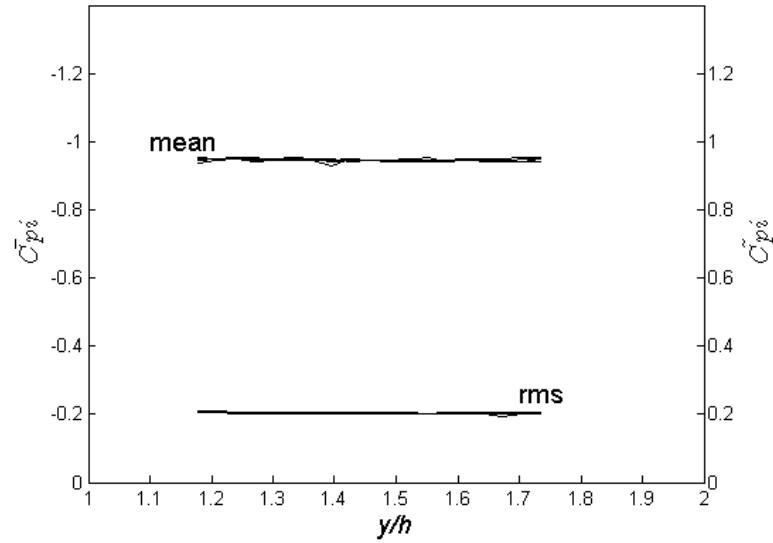
### 2.3.1 Assessment of two-dimensional mean flow

Wind-induced pressures on the double-layer roof system were analyzed to check the two-dimensionality of the mean flow. In order to demonstrate that the panel and tap region is in two-dimensional mean flow, the pressure distributions were compared from all lines of taps. Figures 2.4a and 2.4b show mean and RMS (obtained with the mean removed, i.e., standard deviation) pressure coefficient distribution plots along the x-direction and the y-direction, respectively. Pressure coefficients on the external surface of panels,  $C_{p_e}$ , were obtained from three different pressure tap lines (Left, Middle and Right, as shown in Figure 2.1b), while  $C_{p_i}$ , the interior pressure coefficients in the cavity (i.e., cavity pressure) were obtained from the 591 pressure taps. If the data for each line of taps in the x-direction overlay, and the data for each line in the y-direction overlay and are horizontal, the mean flow is essentially two-dimensional. Although there are some deviations, it is reasonable to state that the mean flow can be considered as two-dimensional based on these plots.

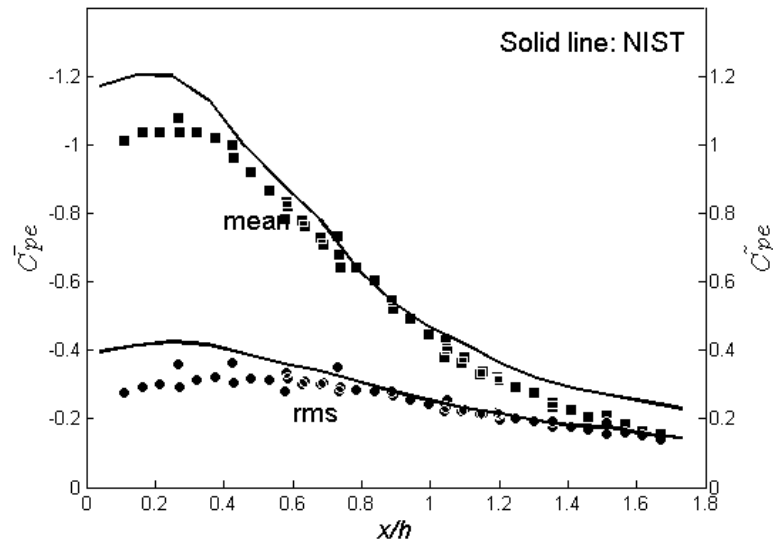


(a)

See caption on p.16.



(b)



(c)

Figure 2.4 Distribution of mean and RMS pressure coefficients: a) along the x-direction, b) along the y-direction, and c) comparison with NIST data.  $C_{pe}$  were obtained from three different pressure tap lines (Left, Middle and Right, as shown in Figure 2.1b) and  $C_{pi}$  from 591 pressure taps on the top surface of the inner layer. The configuration with  $G = 2.5$  mm and  $H = 2.5$  mm were used to compare with data obtained from the midplane of a bare-roofed building from the NIST aerodynamic database for low-rise buildings.

To validate the test results,  $Cp_e$  was also compared with data from published literatures. The NIST aerodynamic pressures were used for this purpose, and data were obtained from the midplane of a bare-roofed low building (Ho et.al, 2005), as shown in Figure 2.4c.  $Cp_e$  close to the leading edge from the current results are similar to the NIST data, although differences may be due to different building dimensions, scaling differences, and (potentially) modification of the flow near the roof surface, as shown in detail below.

### 2.3.2 Mean pressure distributions

Mean pressure coefficient distributions on both the external ( $\bar{C}p_e$ ) and internal surfaces ( $\bar{C}p_i$ ) of the panels are shown in Figure 2.5. The pressure coefficients presented in the plot were obtained from the pressure taps along the middle row of the panel, as shown in Figure 2.1b. Figure 2.5a depicts the pressure distribution between two gaps (i.e.,  $L = 200$  mm); one ( $G = 2.5$  mm) located at  $x/h = 0.11$  and the other ( $G = 3.5$  mm) at  $x/h = 0.74$ , where  $x$  is defined in Figure 2.1 and  $h$  is the eave height. Figures 2.5b and 2.5c depict cases with five gaps, as illustrated in the insets. It should be noted that the gaps of  $G = 1$  mm and  $H = 1.2$  mm in the plots were chosen for comparison as the effects of the  $G$  and  $H$  variations were best described by these two sizes. Effects of the entire ranges of  $G$  and  $H$  are presented later. Several observations can be made:

1. For pressures on the external surface, the  $\bar{C}p_e$  from six different experiments are similar with a variation of  $\pm 5\%$ , which is within the experimental measurement uncertainty bounds (Diaz, 2006). The  $\bar{C}p_e$  do not vary monotonically or linearly and show the classic separated bubble pressure distribution, noting that the reattachment point is around  $x/h = 1$  (Pratt and Kopp, 2013); thus, there are large suction near  $x/h \leq 0.4$ , reducing towards  $x/h \rightarrow 1$ . It should be noted that the  $\bar{C}p$  in Figure 2.5c are plotted versus panel sizes instead of  $x/h$ , because  $G$  varies for these different configurations so that the total length,  $x$ , is larger when  $G$  is larger. Thus, the curves of  $\bar{C}p_e$  appear to be discontinuous for  $G = 15$  mm, in particular.



2. For cavity pressures on the internal surface, the  $\bar{C}p_i$  are different and depend on  $G$  and  $H$ , and the panel size,  $L$  (see the observation 5). For small  $H$ , say  $H = 0.5$  mm, the  $\bar{C}p_i$  vary in a nearly linear manner in the  $x$ -direction between the gaps, with a pressure gradient such that mean flow direction is from larger  $x/h$  to smaller  $x/h$ . The  $\bar{C}p_i$  for this  $H$  are clearly affected by the (orifice) flow at the gaps and vary monotonically between the two ends in Figure 2.5a and in each segment in Figure 2.5b. Thus, for  $H = 0.5$  mm the  $\bar{C}p_i$  are quite similar to  $\bar{C}p_e$  in Figure 2.5b with the four panels (it is approximately piecewise linear), but is quite different in Figure 2.5a when a single panel spans the same external pressure gradient.
3. For  $H = 1.2$  mm, one can see in Figure 2.5b that the  $\bar{C}p_i$  do not follow  $\bar{C}p_e$  quite so well as for  $H = 0.5$  mm.
4. The  $\bar{C}p_i$  are fairly uniform for  $H = 5$  mm and  $G = 1$  mm, but have a slight non-uniformity (i.e., approximately linear variation) when  $H = 2.5$  mm. Thus, the boundary for the change in phenomena, from linear variation of  $\bar{C}p_i$  to uniform  $\bar{C}p_i$ , is at about  $G/H = 0.2$  to  $0.4$  for this building size, panel size and wind direction.
5. For  $H \geq 5$  mm with  $G = 1$  mm, the  $\bar{C}p_i$  is uniform over almost all of the underside with the entire pressure drop accounted for at the location of the gaps. The gaps (see the inset in plots in Figure 2.5 for the direction of the mean flow in and out) play an interesting role here though, because  $\bar{C}p_i$  for a single panel (Figure 2.5a) is not equal to  $\bar{C}p_i$  for the four panels (Figure 2.5b). Depending on the locations of the gaps, the magnitude of  $\bar{C}p_i$  can be shifted. For instance, more gaps (in Figure 2.5b) result in lowering the magnitude of  $\bar{C}p_i$ , compared to one panel (in Figure 2.5a).
6. In Figure 2.5c,  $G = 0$  mm indicates a single layer system with  $\bar{C}p_i \approx 0$ . This shows that the panel edges were quite flat, providing a remarkably good seal. Equalization begins rapidly, as the  $G = 0.5$  mm results indicate, once gaps are present.

Figure 2.5 indicates that the  $\bar{C}p_i$  distribution is directly affected by  $\bar{C}p_e$  at the gaps between panels and by  $H$ . Overall, the  $\bar{C}p_e$ 's for different  $H$  are closely distributed as might be expected, within the experimental measurement uncertainty. However, the  $\bar{C}p_i$  distribution when  $H = 0.5$  mm varies monotonically, indicating that the pressure drop is broadly similar to a developing two-dimensional flow between parallel plates. On the other hand,  $\bar{C}p_i$ 's for the larger values of  $H$  are more uniform, which can be interpreted as being similar to what happens for internal pressures within a building volume, i.e., the pressure drops occur mostly through the (orifice) gaps,  $G$ , with uniform pressures in between.

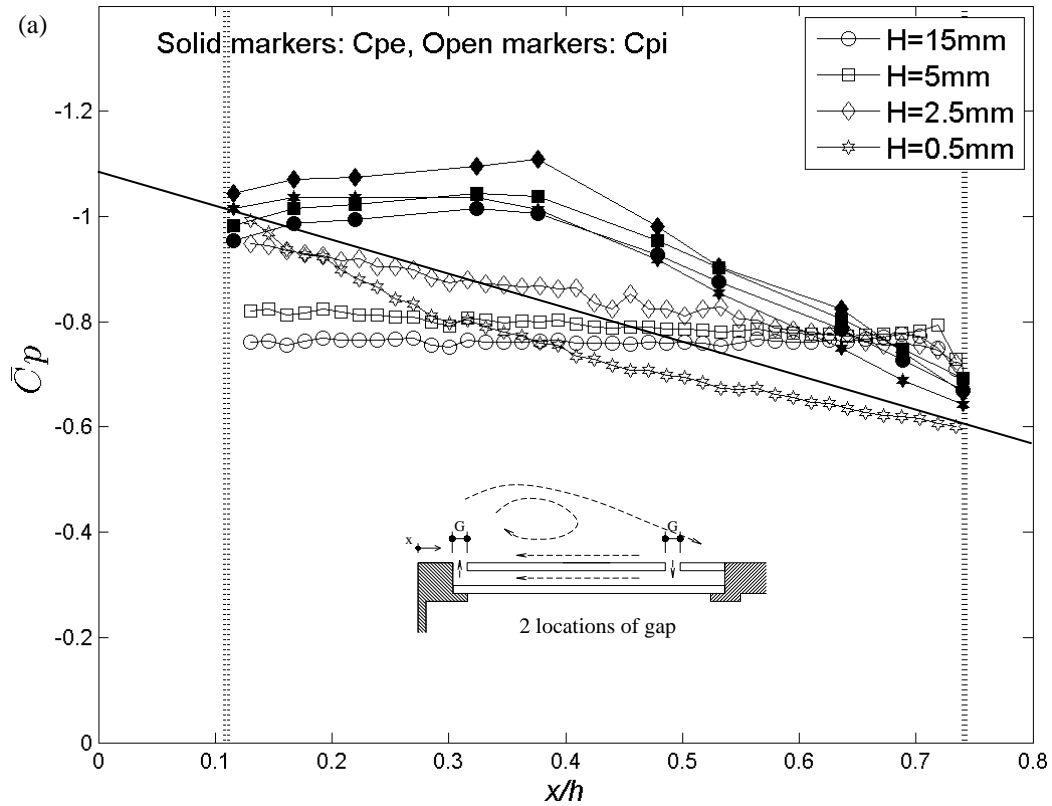


Figure 2.5 Mean pressure distributions for the pressure taps in the middle row: (a) two gaps ( $G = 2.5$  mm at  $x/h = 0.11$  and  $G = 3.5$  mm at  $x/h = 0.74$ ) with  $H$  variations; (b) five gaps of  $G = 1$  mm with  $H$  variations; and (c) five gaps with  $H = 1.2$  mm and with  $G$  variations.

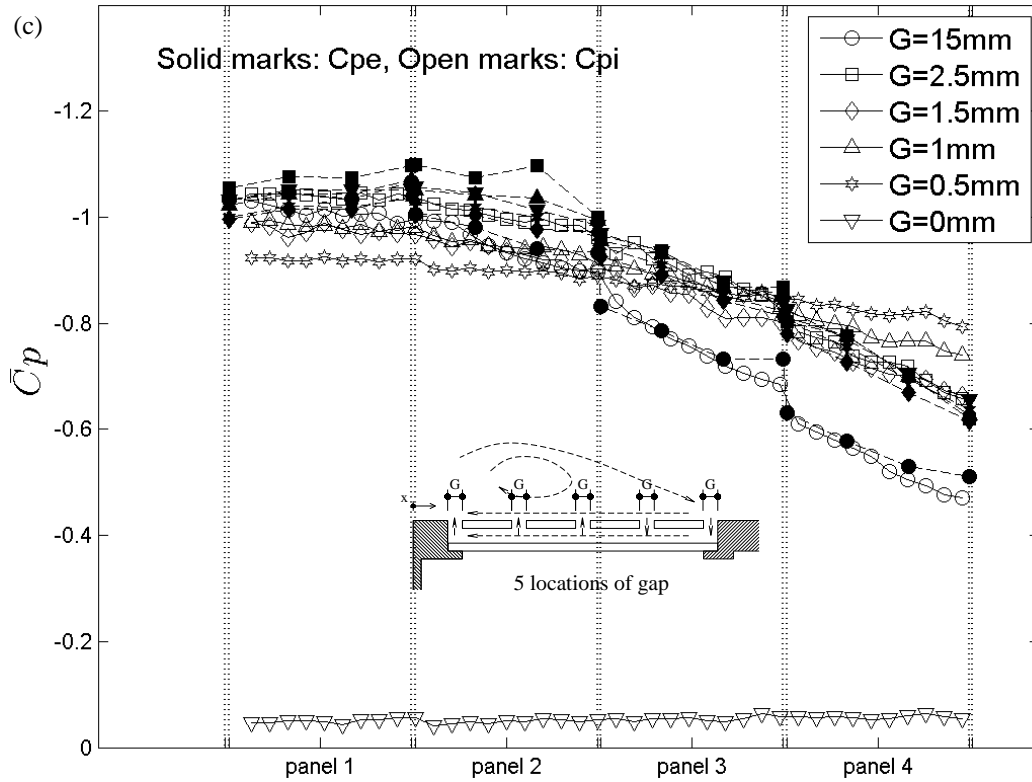
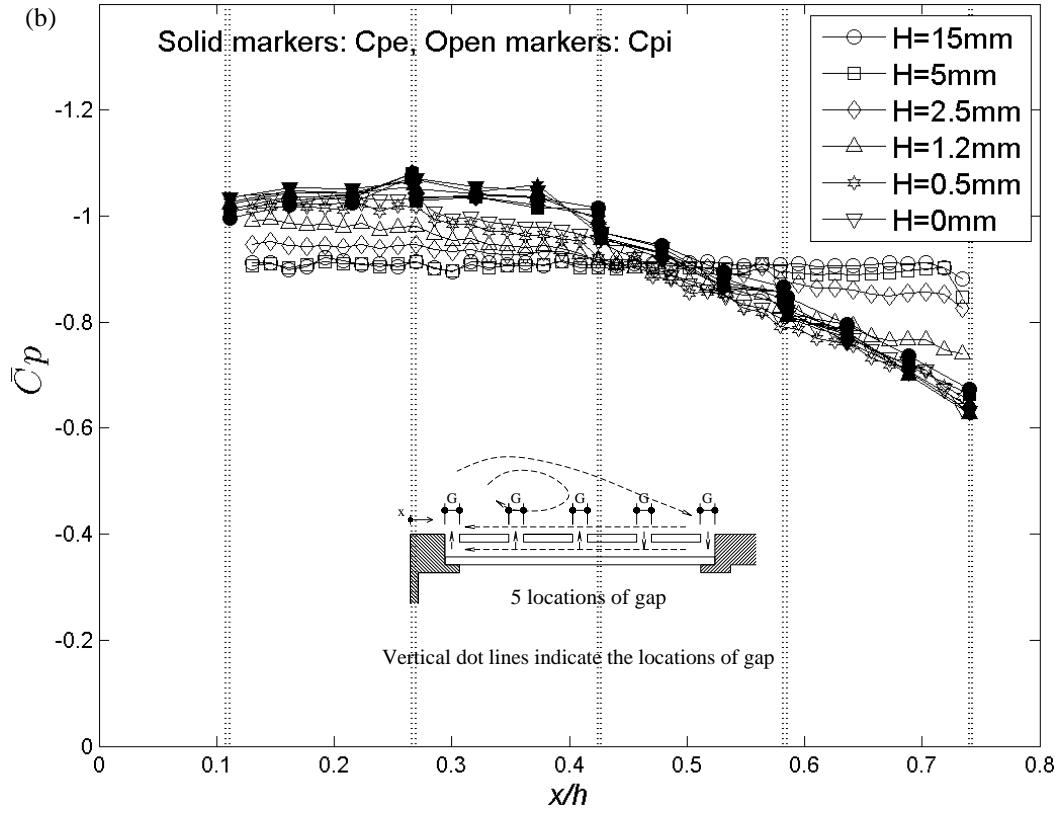


Figure 2.5: continued.

### 2.3.3 RMS pressure distributions

Figure 2.6 shows the RMS pressure distributions on the external ( $\tilde{C}p_e$ ) and internal surfaces ( $\tilde{C}p_i$ ) of the panels, corresponding to the mean pressure seen in Figure 2.5. It can be seen that the  $\tilde{C}p_i$  distributions are dramatically altered by  $G$  and  $H$ . Observations are described below:

1. The  $\tilde{C}p_e$  are quite similar overall but there are some differences between them. For example, Figures 2.6b and 2.6c show that the gap between panels clearly alters the pressure fluctuations on the external surface, comparable to results found by Kopp et al. (2012) and by Pratt and Kopp (2013) for tilted solar arrays on large, flat roofs.
2. The  $\tilde{C}p_i$  are clearly attenuated compared to  $\tilde{C}p_e$  although they tend to increase significantly near the gaps and are more highly attenuated near the interior of panel. The smallest  $H$  and the largest  $G$  have the least attenuation at the gap, with high fluctuations which occur further into the interior. It should be noted that the least height of the cavity (i.e.,  $H = 0$  mm) is not precisely zero but is only nominally zero because of manufacturing tolerances. Oh et al. (2007) found a similar result from their internal pressure experiments for building internal volumes, that is, less attenuation of  $Cp_e$  with a larger opening size (which is comparable to the larger  $G/H$ ). The equation of the motion of the air mass moving in and out of the opening of area,  $a$ , (Holmes, 1979) can explain the phenomena,

$$\frac{\rho l_e}{\gamma P_o} \left( \frac{V_o}{a} \right) \ddot{C}p_i + \left( \frac{\rho \bar{V}_h}{2k\gamma P_o} \right)^2 \left( \frac{V_o}{a} \right)^2 \dot{C}p_i |\dot{C}p_i| + C_{pi} = C_{pe} \quad (2.1)$$

The interior volume with a larger  $H$  (i.e., internal volume,  $V_o$ ) and a smaller  $G$  (i.e., opening area,  $a$ ) is relatively larger so that the larger  $V_o/a$  (i.e., smaller  $G/H$ ) tends to provide greater attenuation of the dynamic component of the air mass motion due to the higher resistance of the volume (induced by the 1<sup>st</sup> and 2<sup>nd</sup> terms in the equation). On the other hand, the smaller  $V_o/a$  (i.e., larger  $G/H$ ) has less resistance; thus, the  $Cp_i$  fluctuates close to the  $Cp_e$  fluctuations at the opening (gap) although it is gradually attenuated near the interior of panel.

3. Figure 2.6a shows that, for the single large panel,  $\tilde{C}p_i$  in the interior of panel eventually becomes independent of  $H$  at distances further from the gap. It is also observed that  $\tilde{C}p_i$  is not symmetric at the two ends of the panel due to the slightly different gap sizes (2.5 mm and 3.5 mm) for this case and the different external flow conditions at either end.
4. Comparing Figures 2.6a and 2.6b, for  $H > 2.5$  mm, the number of panels does not alter  $\tilde{C}p_i$ . However, for  $H < 2.5$  mm, with the shorter panels in Figure 2.6b, the attenuation begins to diminish so that larger fluctuations are observed everywhere as  $H$  is reduced. This is likely to help PE by allowing external pressure fluctuations into the underside.

For  $G = 0$  mm in Figure 2.6c, the fluctuations are not fully attenuated so some  $\tilde{C}p_e$  are transmitted through the gap even though  $\tilde{C}p_i \approx 0$ .

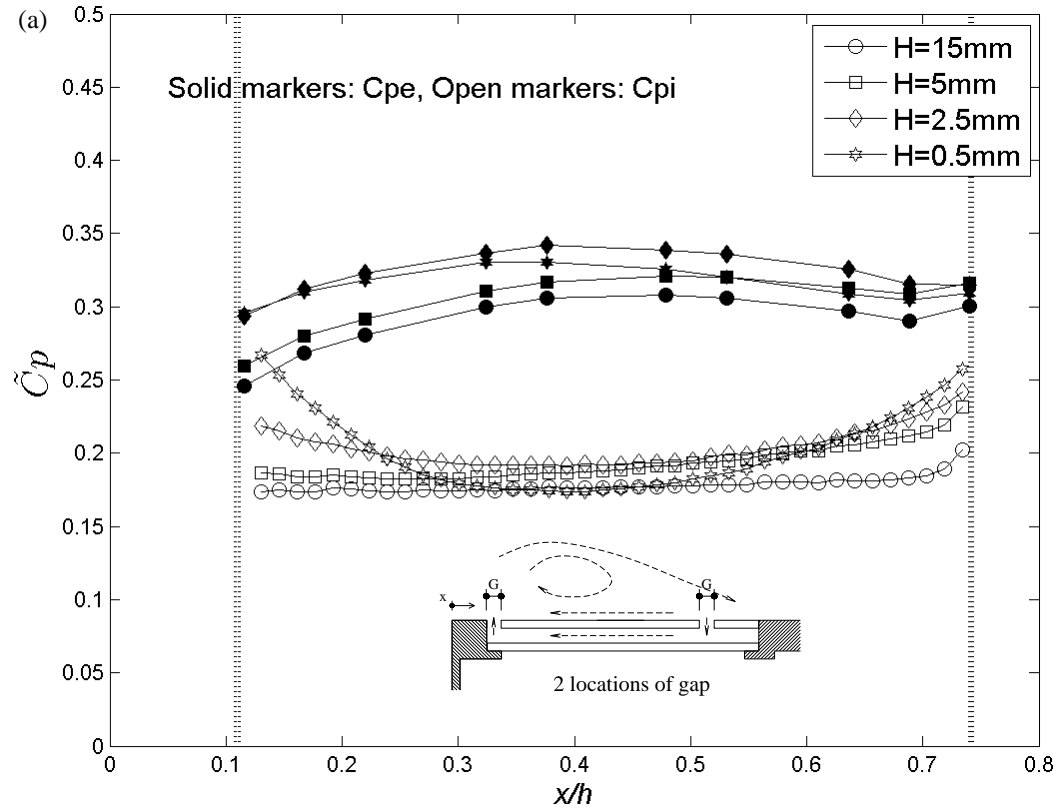


Figure 2.6 RMS pressure distributions for the pressure taps in the middle row: (a) two gaps ( $G = 2.5$  mm at  $x/h = 0.11$  and  $G = 3.5$  mm at  $x/h = 0.74$ ) with  $H$  variations; (b) five gaps of  $G = 1$  mm with  $H$  variations; and (c) five gaps with  $H = 1.2$  mm and with  $G$  variations.

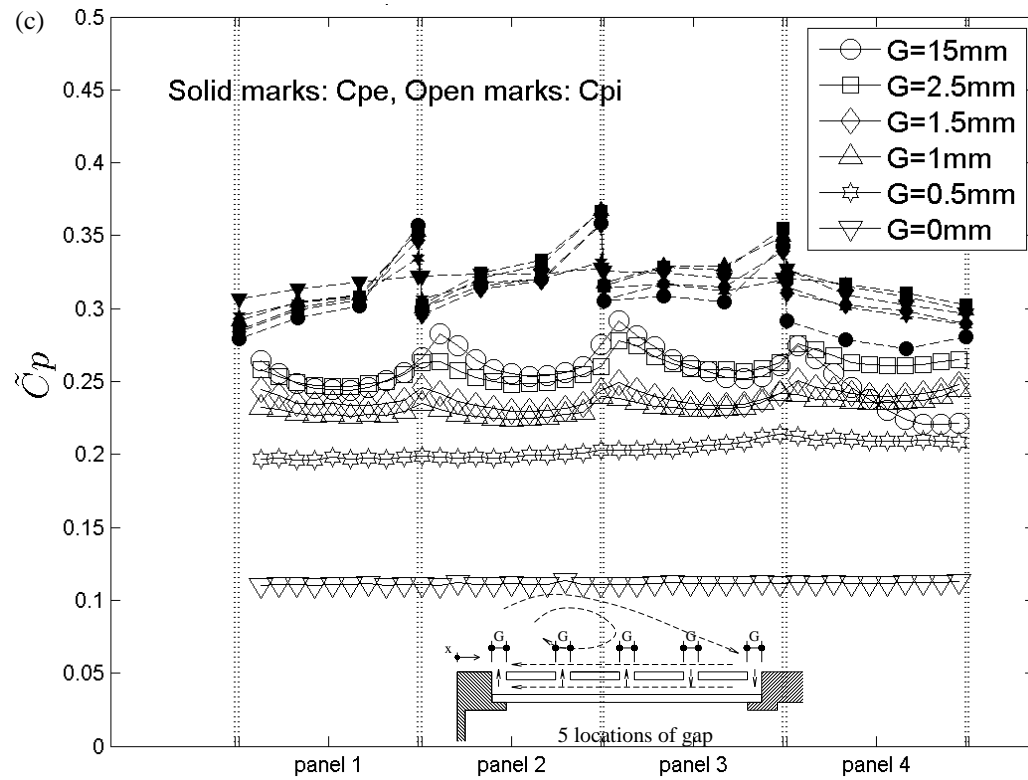
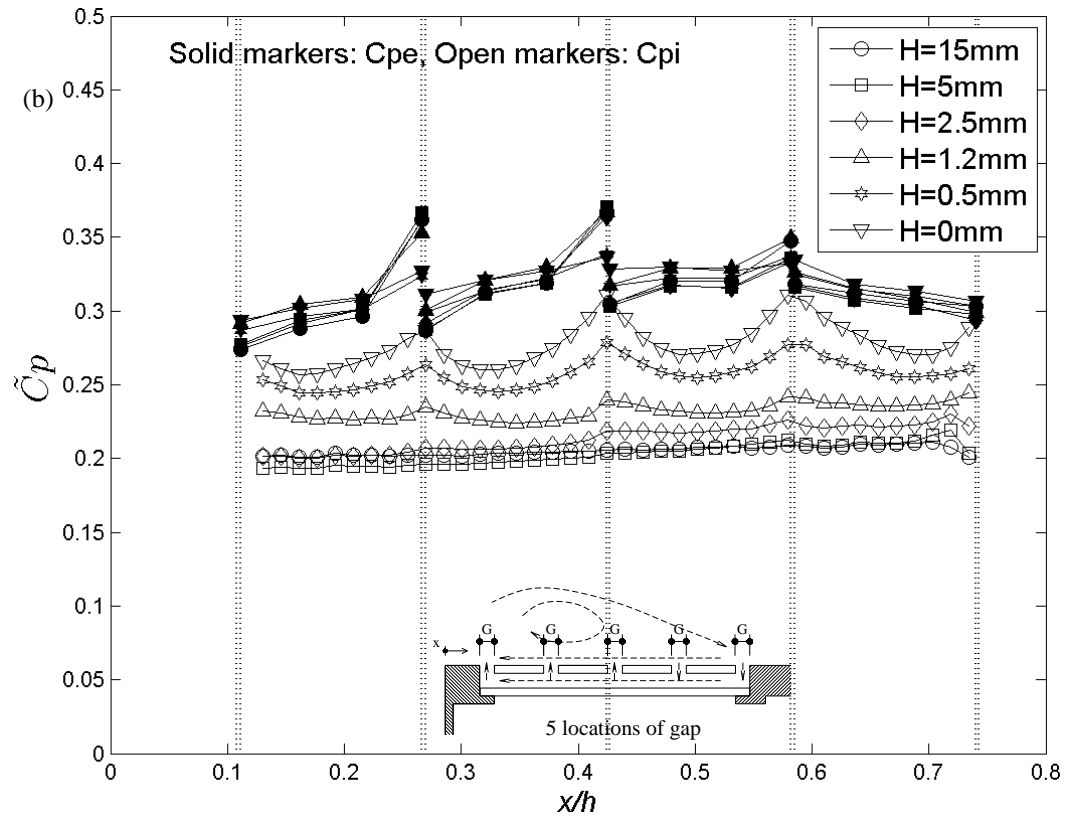


Figure 2.6: continued.

### 2.3.4 Instantaneous pressure distributions

Figure 2.7 depicts the pressure distributions of  $Cp_e$  and  $Cp_i$  at the instant time when one of the pressure taps near the gap on the first panel is at its peak magnitude. In Figure 2.7a, uniform cavity pressure coefficient,  $Cp_i$ , are observed only for  $H = 15$  mm. Thus, the uniform cavity pressure depends on the magnitude of  $\Delta Cp_e$  with larger  $\Delta Cp_e$  driving more flow through the openings and making uniform pressure between the layers less likely. In fact, the flow field in the cavity between layers is like unsteady flow between parallel plates (i.e., unsteady Couette flow) rather than an internal building pressure type of flow where there is little (or no) net flow through the volume and all of the air flow is confined to that moving in and out of gaps (i.e., orifice) between the panels of the outer layer. When  $\Delta Cp_e$  is smaller, the pressure drops are only at the gaps and flow is similar to building internal pressures, that is, flow is localized at the opening, moving in and out, but not through the cavity (to any significant extent). For the other  $H$ , pressure is monotonically changing and is nearly linear, again consistent with Couette flow.

Figures 2.7b and 2.7c illustrate that, even with the very large pressure differences at adjacent gaps, the smaller panels tend to have locally uniform pressures. The  $Cp_i$  do not respond locally or immediately to  $Cp_e$  during the peak event, except for  $H = 0$  mm, although even this is limited. The actual flow and the height ( $H$ ) of the cavity between the parallel layers may be playing a large role here so that the  $Cp_i$  is not completely controlled by the local  $Cp_e$ . This would be an “unsteady” effect so that models based on quasi-steady theory may be challenged in such computations.



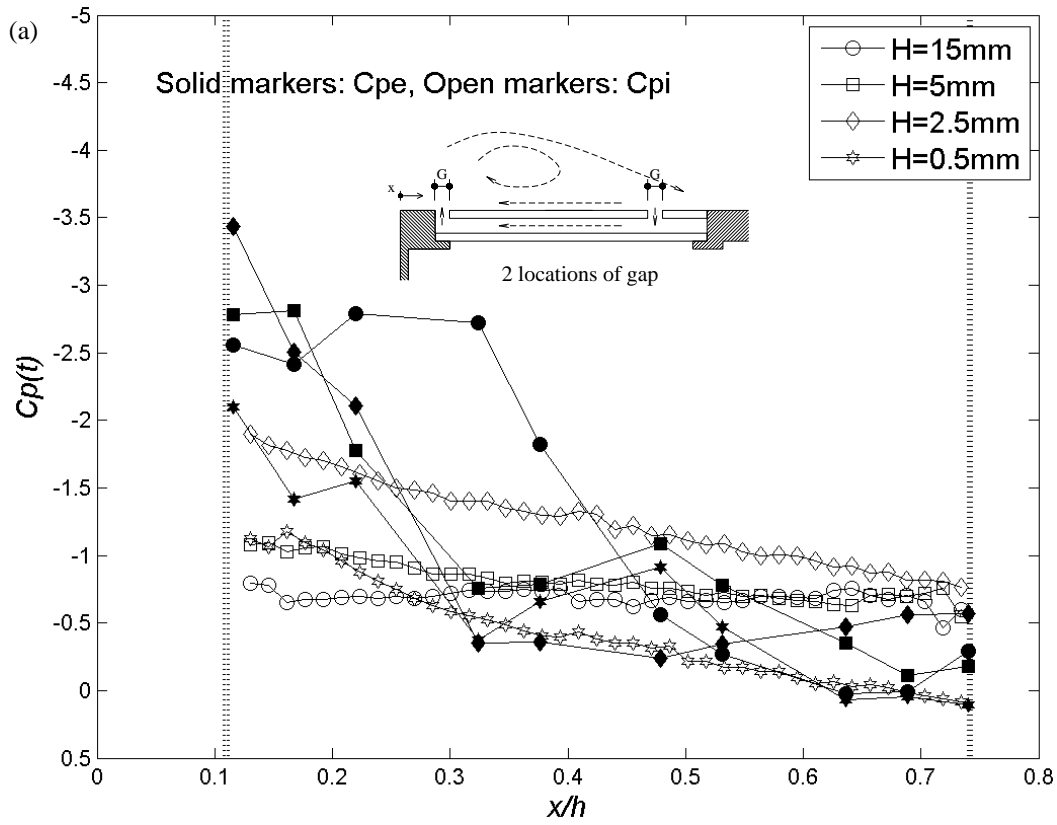


Figure 2.7 Instantaneous pressure distributions for the pressure taps in the middle row: (a) two gaps ( $G = 2.5\text{ mm}$  at  $x/h = 0.11$  and  $G = 3.5\text{ mm}$  at  $x/h = 0.74$ ) with  $H$  variations; (b) five gaps of  $G = 1\text{ mm}$  with  $H$  variations; and (c) five gaps with  $H = 1.2\text{ mm}$  and with  $G$  variations.

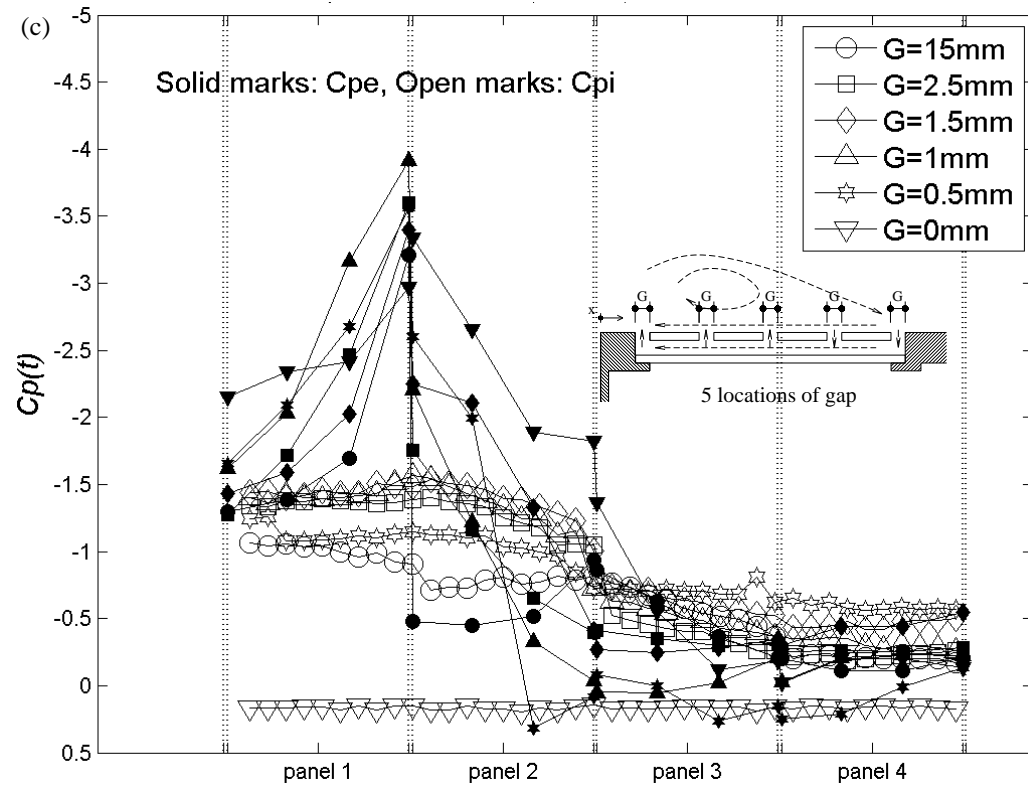
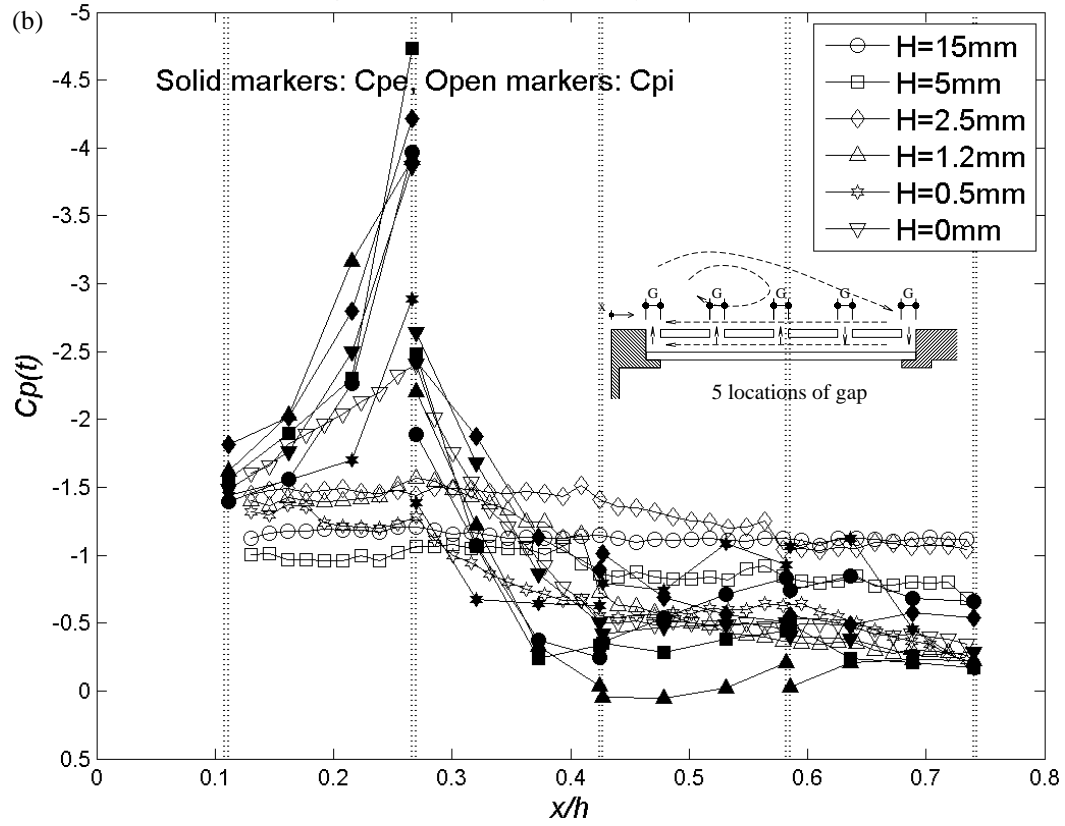
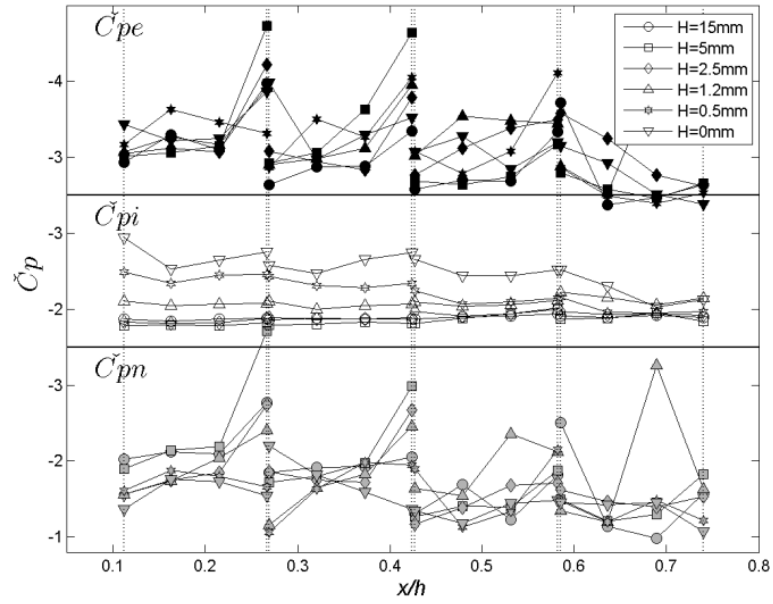


Figure 2.7: continued.

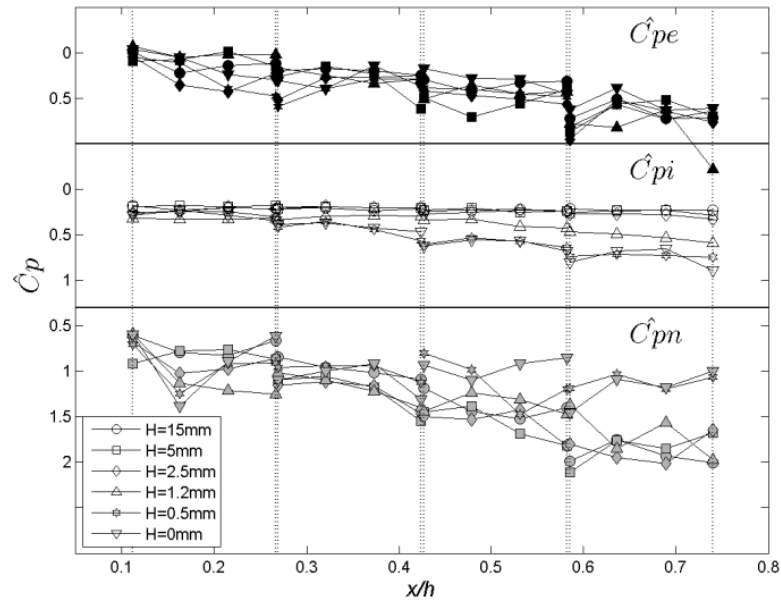
### 2.3.5 Peak pressure distributions

Figures 2.8 and 2.9 depict minimum and maximum peak pressure distributions for the external ( $\check{C}p_e, \hat{C}p_e$ ) and internal ( $\check{C}p_i, \hat{C}p_i$ ) surfaces of the panels. Peak net pressure coefficients ( $\check{C}p_n, \hat{C}p_n$ ) are simply defined as the peak of the time series of  $(Cp_e - Cp_i)$  at the same location. Several observations can be made when examining the figures:

1. The  $\check{C}p_e$  distributions show generally higher suctions near the leading edge ( $x/h = 0.11$ ), tending to decrease as  $x/h$  increases. Similar to the  $\bar{C}p_e$  distribution, the presence of gaps between the panels definitely alters  $\check{C}p_e$ , especially right adjacent to the gaps. The range of  $\check{C}p_e$  among the six configurations is higher at the locations of the gaps than at the middle of the panels. This is likely due to a local flow such as secondary separations at the edge of the gaps of the panel (Pratt and Kopp, 2013). The  $\hat{C}p_e$  distribution shows a similar pattern as  $\check{C}p_e$  but the “gap effects” vanish almost completely for the maximum peak pressure distribution.
2. The  $\check{C}p_i$  and  $\hat{C}p_i$  distributions are much smoother compared to  $\check{C}p_e$  indicating that large external fluctuations due to the “gap effects” are not transmitted to the underside since they originate from the underside (Pratt and Kopp, 2013). It is clearly observed that  $\check{C}p_i$  and  $\hat{C}p_i$  increase with smaller  $H$  and larger  $G$ , except at the last panel and the first panel respectively. This implies that the effects of  $G$  and  $H$  on the interior pressures also depend on the external flow conditions, to some extent.
3. The magnitudes of  $\check{C}p_n$  drop to about 50-70 % of the external pressures, depending on the configurations. For the positive pressures, the  $\hat{C}p_n$  increases significantly, compared to the external pressures, and the magnitudes are almost of the same order of  $\check{C}p_n$ .

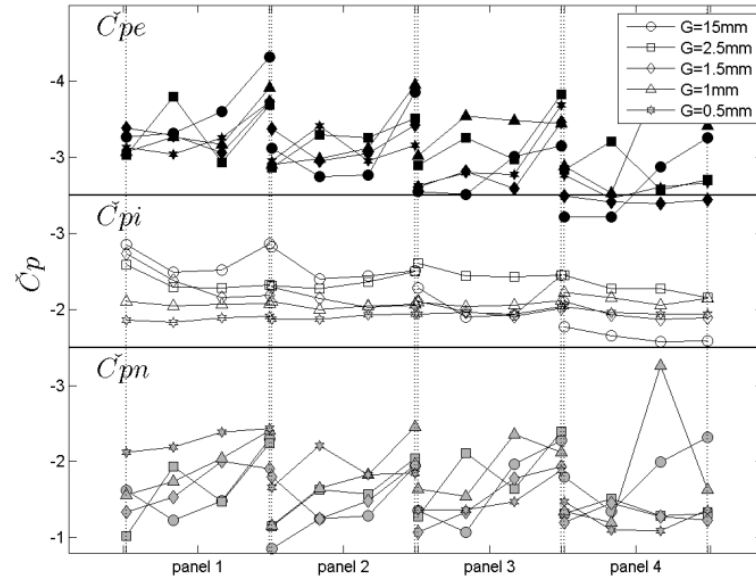


(a)

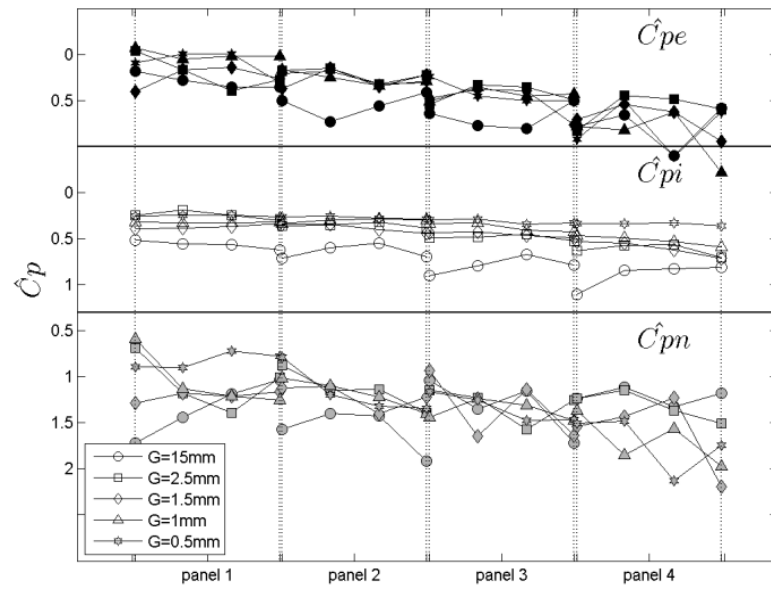


(b)

Figure 2.8 Peak pressure distributions for  $G = 1$  mm with  $H$  variations: (a) minima; (b) maxima. (The vertical hidden lines indicate locations of the gaps.)



(a)



(b)

Figure 2.9 Peak pressure distributions for  $H = 1.2$  mm with  $G$  variations: (a) minima; (b) maxima.

## 2.4 Discussion of Pressure Distribution

### 2.4.1 Mechanisms of external and cavity pressure distributions

Figure 2.10 illustrates the mean, RMS and peak pressure distributions on the external and internal surfaces of panels. In these plots, the pressure distributions are idealized to better explain the mechanism; for instance,  $\bar{C}p_e$  is depicted as a solid straight line, simplifying the curve in the separation zone. Figure 2.10a shows the panel geometry while Figure 2.10b depicts the mean pressure distributions on the external and internal surfaces of the panels. The  $\Delta\bar{C}p_i$  follow  $\Delta\bar{C}p_e$  but the gradient of  $\bar{C}p_i$  depends on  $G/H$ , being closer to  $\Delta\bar{C}p_e$  with the higher  $G/H$ . As described earlier in Section 2.3.2, for the larger  $G$  and smaller  $H$ , the pressure drop is linear and similar to a developing two-dimensional flow between parallel plates (Couette Flow). For the smaller  $G$  and larger  $H$ , the cavity pressure coefficients,  $\bar{C}p_i$ , are more uniform and the pressure drops occur primarily through the gaps between panels. These different gradients for  $\bar{C}p_e$  and  $\bar{C}p_i$  on the double layer system under the roof separation bubble results in three different pressure zones on the panels: mean upward pressures (i.e., suctions) in the “higher suction zone”, mean downward pressures in the “lower suction zone”, and approximately zero pressures in the “neutral pressure line”, where the higher suction zone occurs when  $\bar{C}p_e < \bar{C}p_i$ , the lower suction zone when  $\bar{C}p_e > \bar{C}p_i$ , and the neutral pressure line when  $\bar{C}p_e = \bar{C}p_i$ .

The external and cavity pressure distributions generate flows through the gaps between panels and in the cavity between the layers, as illustrated in Figure 2.10a for a given  $G$  and  $H$ . The external pressure difference from  $\Delta\bar{C}p_e$  between the gaps is a driving force to generate these internal flows. The lower external pressures,  $\bar{C}p_e$ , at the gaps 1, 2 and 3 (i.e., the differential pressures due to  $\bar{C}p_i > \bar{C}p_e$ ) initiate to orifice (discharge) flow through the gaps between the panels. This discharged flow drives the leftward flow in the horizontal cavity between the layers and the inlet flows, subsequently, at the gaps 4 and 5. By restricting or disturbing the interior horizontal flow, the cavity pressure distribution can be manipulated. For instance, if the length of the underside cavity is separated into two volumes (i.e., there is no flow between the two volumes) as shown in

Figure 2.11a, the cavity pressure distribution is also divided into the two volumes as depicted in Figure 2.11b, which results in lowering net pressures. Thus, for a given  $\Delta\bar{C}p_e$ , a shorter horizontal length of the underside space has a greater advantage to reduce net pressures, assuming that  $\Delta\bar{C}p_i$  remain identical.

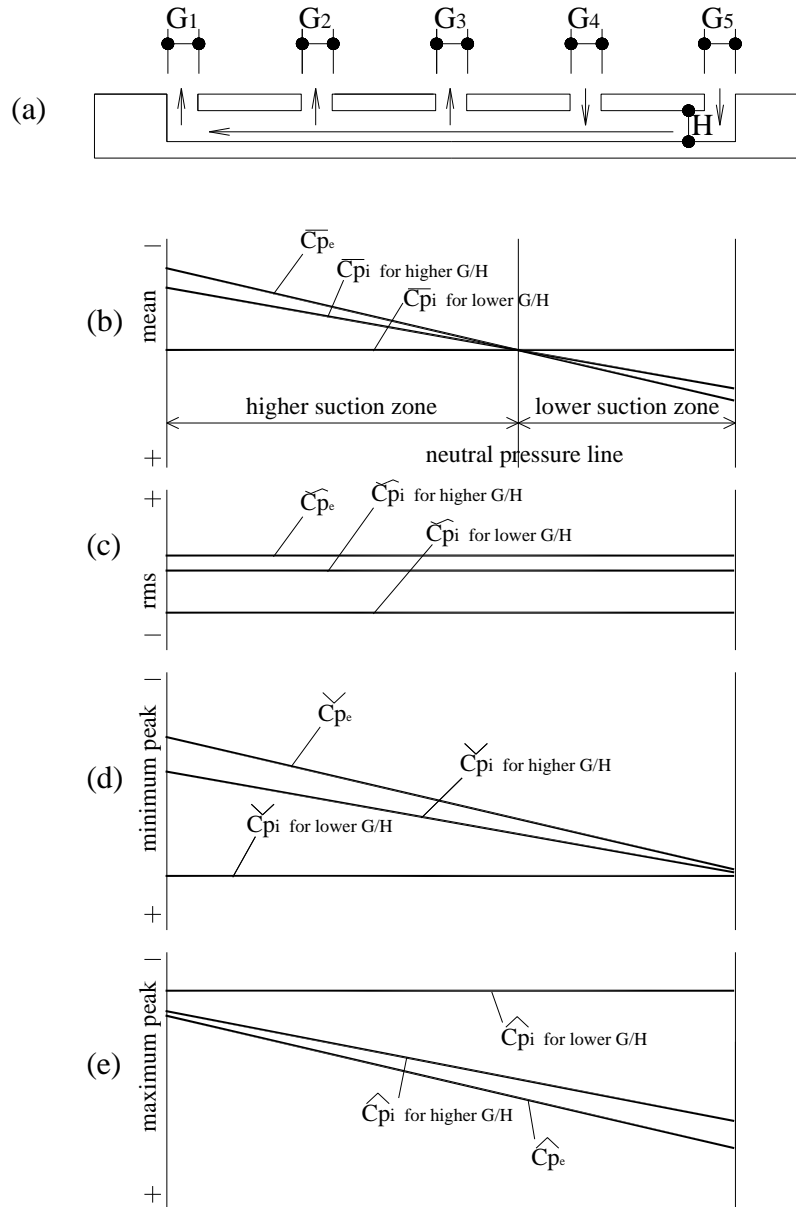


Figure 2.10 Idealization of the flow and pressure distribution mechanisms on external and internal surfaces of panels: (a) mean flow; (b) mean; (c) RMS; (d) minima; and (e) maxima.

The RMS pressure coefficients, shown in Figure 2.10c, are relatively uniform. The magnitude of  $\check{C}p_i$  is reduced compared to  $\check{C}p_e$ , and depends on  $G/H$ , being larger with the higher  $G/H$ . This implies that the fluctuating component of external pressures can be transmitted more efficiently with the higher  $G/H$ .

The peak pressure distributions ( $\check{C}p$  and  $\hat{C}p$ ), depicted in Figures 2.10d and 2.10e, result from the combination of  $\bar{C}p$  and  $\check{C}p$ . They are shifted from the mean by the RMS value times some peak factor. Thus, the  $\check{C}p_e$  and  $\hat{C}p_e$  are altered up and down the most since the RMS value is greatest, while the  $\Delta\check{C}p_i$  and  $\Delta\hat{C}p_i$  are shifted less. As a result, the neutral pressure line is also moved to the last and first panels for  $\check{C}p$  and  $\hat{C}p$ , respectively.

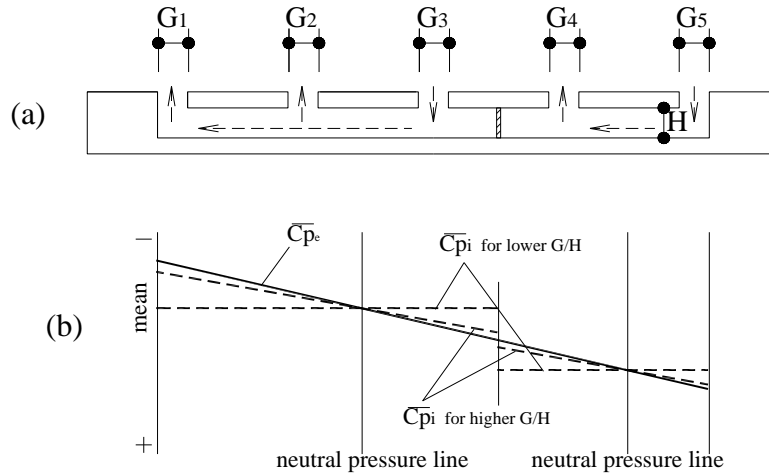


Figure 2.11 Idealization of the flow and pressure distribution mechanisms on external and internal surfaces of panels for the separated underside space: (a) mean flow; (b) mean.

## 2.4.2 Dimensional analysis of mean pressure distribution

The experimental data, as shown in Figure 2.5, show that geometric and flow parameters are involved in setting the pressure distributions on the internal surface ( $\bar{C}p_i$ )



of the panels. Here we use analysis to determine the dependence of the pressure drop on the parameters involved and establish the non-dimensional groups. The problem involves two well-known flow equations: the Discharge equation and one-dimensional Couette flow.

Considering the driving forces to generate the flows, the flow from the orifice 2, through the channel, and through the orifice 1 has

$$\Delta P_e = P_{e2} - P_{e1} \quad (2.2)$$

where  $P_{e1}$  and  $P_{e2}$  are external pressures at the orifices 1 and 2. Similarly, the driving force for discharge through orifices 1 and 2 can be expressed as

$$\Delta P_{o1} = P_{i1} - P_{e1} \quad (2.3a)$$

$$\Delta P_{o2} = P_{e2} - P_{i2} \quad (2.3b)$$

where  $P_{i1}$  and  $P_{i2}$  are internal pressures at orifices 1 and 2, as shown in Figure 2.12. Then, the driving force for the Couette flow through the horizontal cavity between the layers is

$$\Delta P_i = P_{i2} - P_{i1} \quad (2.4)$$

Thus,

$$\Delta P_{o1} + \Delta P_i + \Delta P_{o2} = \Delta P_e \quad (2.5)$$

For a given  $\Delta P_e$ , the magnitudes of the internal pressure drops ( $\Delta P_o$  and  $\Delta P_i$ ) are determined by the flow and geometric parameters. If  $\Delta P_o$  is negligible, the pressure drop mostly occurs for the Couette flow between the layers and  $\Delta P_i$  is proportional to  $\Delta P_e$ . In the case that  $\Delta P_o$  dominates and  $\Delta P_i$  is negligible, resulting in uniform pressure in the cavity between layers. This is equivalent to  $\frac{\Delta P_o}{\Delta P_i} \gg 1$ .

The orifice pressure drop,  $\Delta P_o$ , can be expressed by the discharge equation, i.e.,

$$\Delta P_{o1} = \frac{\rho}{2} \frac{1}{k^2} \frac{1}{G^2} Q_{o1}^2 \text{ and } \Delta P_{o2} = \frac{\rho}{2} \frac{1}{k^2} \frac{1}{G^2} Q_{o2}^2 \quad (2.6)$$

where  $\rho$  is the air density,  $k$  is the discharge coefficient, and  $Q_o$  is the flow rate through the area of the orifice,  $G$ . The equation for the Couette flow between the layers is

$$\Delta P_i = \frac{12\mu L}{H^3} Q_i \quad (2.7)$$

where  $\mu$  is the air viscosity,  $L$  is the length of the panel, and  $Q_i$  is the flow rate between the layers,  $H$ . Employing the continuity equation for incompressible flow,

$$Q_{o1} - Q_i = 0, Q_i - Q_{o2} = 0, Q_{o1} - Q_{o2} = 0$$

$$Q_{o1} = Q_{o2} = Q_i = HU_i \quad (2.8)$$

Eqs. (2.6) and (2.7) become

$$\Delta P_o = \frac{\rho}{2} C_L \left(\frac{H}{G}\right)^2 U_i^2 \quad (2.9)$$

$$\Delta P_i = \frac{12\mu L}{H^2} U_i \quad (2.10)$$

where  $C_L$  is the loss coefficient ( $=1/k^2$ ),  $U_i$  is the average velocity of the Couette flow with  $\Delta P_o = \Delta P_{o1} = \Delta P_{o2}$  for a given  $G$ .

Therefore, the ratio  $\frac{\Delta P_i}{\Delta P_o}$  can be obtained from (2.9) and (2.10) as

$$\frac{\Delta P_i}{\Delta P_o} \approx \frac{\frac{12\mu L}{H^2} U_i}{\frac{\rho}{2} C_L \left(\frac{H}{G}\right)^2 U_i^2} \approx \left(\frac{G}{H}\right)^2 \left(\frac{L}{H}\right) \left(\frac{\mu}{\rho H U_i}\right) \left(\frac{24}{C_L}\right) \propto \left[\frac{G}{H}\right]^2 \left[\frac{L}{H}\right] \left[\frac{1}{Re_i}\right] \left[\frac{1}{C_L}\right] \propto \left[\frac{G}{H}\right]^2 \left[\frac{fL/H}{C_L}\right] \quad (2.11)$$

where  $f = \frac{24}{Re}$  is the friction factor for laminar Couette flow between parallel plates. Since the friction loss coefficient is  $fL/H$ , one can write  $\frac{\Delta P_i}{\Delta P_o} \propto \left[\frac{G}{H}\right]^2 \left[\frac{fL/H}{C_L}\right]$ .

Thus, the critical geometric parameters which determine the interior pressure distribution are the height of the cavity between panels and roof surface, the gap between the panels, and the length of the panels. Bienkiewicz and Sun (1992, 1997) pointed out the importance of the  $G/H$  ratio, which is confirmed here. In addition, the panel size,  $L$ ,

plays a role which arises in the ratio of the loss coefficient,  $\frac{fL/H}{c_L}$ , for the flow in the cavity and the orifice gap flow.

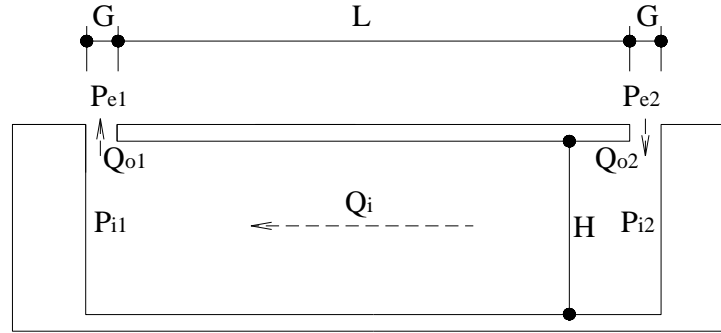


Figure 2.12 Pressures and flows on two gaps of the double layer system.

Figures 2.8 and 2.9 indicate that the greatest pressure equalization occurs when  $G/H$  is larger (or  $H/G$  is smaller), implying that  $\frac{\Delta P_i}{\Delta P_o}$  is relatively large. Large values of  $\frac{\Delta P_i}{\Delta P_o}$  also arise for relatively large panels, i.e., when  $L/H$  is large, consistent with the experimental results. It is also important to emphasize the role of  $\Delta P_e$ . When  $\frac{\Delta P_i}{\Delta P_o}$  is relatively large, Eq. (2.5) indicates that  $\Delta P_i \approx \Delta P_e$ , which is why the degree of pressure equalization along the length of the panel is maximized.

The friction factor also plays a subtle role as indicated by the differences between instantaneous pressure distributions in Figure 2.7 compared to Figure 2.5, with higher flow rates reducing  $f$ . This has the same effect as reducing  $G$ , i.e., the potential to reduce the pressure equalization. However, if the cavity Reynolds number,  $Re_i$ , increases sufficiently, the flow will be in transition to turbulence increasing the friction factor,  $f$ . These factors may explain some of the “unsteady” effects observed with respect to the instantaneous flow fields leading to the pressure distributions in Figure 2.7. This merits further investigation, which will be examined in future work.

## 2.5 Conclusions

The objective of the present chapter was to: (i) investigate the net, aerodynamic pressure coefficients and the pressure equalization on a double-layer roof system in a two-dimensional mean flow, and ii) examine effects of the gaps ( $G$  and  $H$ ). In total, 39 configurations consisting of six different gaps between panels ( $G$ ), six different height of the panels above the roof surface ( $H$ ) and three additional configurations with different panel sizes were examined. The main conclusions are:

1. The presence of gaps between the panels alters the pressure distribution on the external surface ( $Cp_e$ ) near the locations of the gaps. This is likely due to the local flow through the gap, including “secondary” flow separations at the edge of the gaps of the panel, as previously shown by Pratt and Kopp (2013) for low tilt angle solar arrays.
2. The mean pressure distribution on the internal surface ( $Cp_i$ ) of the panel is significantly altered by  $G/H$  and  $\frac{f_{L/H}}{c_L}$ . It is fairly uniform for smaller  $G/H$  ratios but varies linearly along the panel for larger  $G/H$  ratios. The uniform cases result from the significant pressure drop through the gaps ( $G$ ), which is comparable to the (building) internal pressure problem where there is insignificant net flow through the cavity between the panel and the roof surface. The linear case is caused by the friction losses in the flow in the cavity. The boundary for the change in phenomena is about  $G/H = 0.2$  to  $0.4$  for the current building size, panel size and shape, and wind direction.
3. The RMS pressure coefficients,  $\tilde{Cp}_i$ , are relatively uniform in the cavity compared to the mean coefficients,  $\bar{Cp}_i$ . The magnitude of  $\tilde{Cp}_i$  increases with larger  $G/H$  and with shorter panels. This helps pressure equalization by allowing fluctuations into the cavity flow region.
4. The instantaneous  $Cp_i$  do not respond locally or immediately to  $Cp_e$  during strong peak events. This would be an “unsteady” effect so that models based on quasi-steady theory may be challenged in such computations, a point which will be explained in Chapter 3.

5. The peak internal pressures,  $\check{p}_i$ , also increase with larger  $G/H$  but they are relatively independent of the effects of  $G/H$  at the panels nearer the reattachment point, implying that the effects of  $G$  and  $H$  on pressure equalization is not consistent across all panels. This is due to relative differences in the external and internal pressures causing the presence of adjacent upward and downward net loads.
6. The pressure distribution in the cavity depends on two dimensionless parameters,  $G/H$  and  $\frac{fL/H}{c_L}$ . The smaller the parameters the more uniform the cavity pressure distribution is. The non-dimensional parameter controlling the cavity pressure distribution is  $\left[\frac{G}{H}\right]^2 \left[\frac{fL/H}{c_L}\right]$ , given external pressure gradient,  $\Delta P_e$ , and the panel thickness,  $l_o$ .

## References

- Bienkiewicz, B. and Sun, Y. (1992). Wind-tunnel study of wind loading on loose-laid roofing systems. *Journal of Wind Engineering and Industrial Aerodynamics*, 41-44: 1817-1828.
- Bienkiewicz, B. and Sun, Y. (1997). Wind loading and resistance of loose-laid roof paver systems. *Journal of Wind Engineering and Industrial Aerodynamics*, 77: 401-410.
- Bienkiewicz, B. and Endo, M. (2009). Wind considerations for loose-laid and photovoltaic roofing systems. *Proceedings of the 2009 Structures Congress*, Austin, Texas, April 30-May 2, 2009, pp. 2578-2587.
- Chino, N., Iwasa, Y., Mataka, Y., Hagiwara, T. and Sato, H. (1991). Internal pressure of double composite exteriors. *Journal of Wind Engineering and Industrial Aerodynamics*, 38: 381-391.
- Gerhardt, H.J. and Kramer, C. (1983). Wind loads on wind-permeable building facades. *Journal of Wind Engineering and Industrial Aerodynamics*, 11: 1-20.
- Geurts, C.P.W. and Blackmore, P. (2013). Wind loads on stand-off photovoltaic systems on pitched roofs. *Journal of Wind Engineering and Industrial Aerodynamics*, 123: 239-249.

- Ho, T.C.E., Surry, D., Morrish, D. and Kopp, G.A. (2005). The UWO contribution to the NIST aerodynamic database for wind loads on low buildings: Part 1. Archiving format and basic aerodynamic data. *Journal of Wind Engineering and Industrial Aerodynamics*, 93: 1-30.
- Holmes, J.D. (1979). Mean and fluctuating internal pressure induced by wind. *Proceedings of the 5<sup>th</sup> International Conference on Wind Engineering*, Colorado State University, Fort Collins, Colorado, USA, July, 1979, pp.435-450.
- Kind, R.J. and Wardlaw, R.L. (1983). Failure mechanism of loose-laid roof-insulation systems. *Journal of Wind Engineering and Industrial Aerodynamics*, 9: 325-341.
- Kopp, G.A., Surry, D. and Mans, C. (2005). Wind effects of parapets on low buildings: Part 1. Basic aerodynamics and local loads. *Journal of Wind Engineering and Industrial Aerodynamics*, 93: 817-841.
- Kopp, G.A., Farquhar, S. and Morrison, M.J. (2012). Aerodynamic mechanisms for wind load on tilted, roof-mounted solar arrays. *Journal of Wind Engineering and Industrial Aerodynamics*, 111: 40-52.
- Kopp, G.A. (2014). Wind loads on Low-Profile, Tilted, Solar Arrays Placed on Large, Flat, Low-Rise Building Roofs. *Journal of Structural Engineering*, 140 (2): 04013057.
- O'Brien, C., Neff, D.E., Bienkiewicz, B. and Dinwoodie, T. (2004). Optimization of wind resistance of photovoltaic roofing system. *Proceedings of the 2004 Structures Congress*, Nashville, Tennessee, May 22-26, 2004, pp. 1-8.
- Oh, J. H., Kopp, G. A., and Inculet, D. R. (2007). The UWO contribution to the NIST aerodynamic database for wind loads on low buildings: Part 3. Internal Pressures. *Journal of Wind Engineering and Industrial Aerodynamics*, 95: 755-779.
- Pratt, R. and Kopp, G. (2013). Velocity measurements around low-profile, tilted, solar arrays mounted on large flat-roofs, for wall normal wind directions. *Journal of Wind Engineering and Industrial Aerodynamics*, Online published in October 2013.
- Trung, V., Tamura, Y. and Yoshida, A. (2009). Study on wind loading on porous roof cover sheets on a low-rise building: effects of parapet height and underneath volume. *Proceedings of the 11<sup>th</sup> Americas Conference on Wind Engineering*, San Juan, Puerto Rico, June 22-26, 2009.

Diaz, P.S.Q. (2006). Uncertainty analysis of surface pressure measurements on low-rise buildings. *Master Thesis*, The University of Western Ontario, Canada, 2006.

## Chapter 3

### One-dimensional modelling of the flow in pressure equalizing, double-layer, roof systems in regions of separated flow

#### 3.1 Introduction

Analytical modeling of internal pressures has been well established since Holmes (1979) introduced the Helmholtz resonator model. While there are still various issues being resolved, such as the appropriate loss coefficients (Kim and Ginger, 2012; Bhangoo, 2013) or the effects of multiple interior volumes, it is generally possible to compute the internal pressure time histories if the external pressure time history at the opening and the geometry of the opening and internal volume are known (e.g., Oh et al., 2007). This is not the case for pressure equalizing systems such as roof-mounted solar arrays (Bienkiewicz and Endo, 2009; Kopp, 2014) or multi-layer wall cladding (Cope, et al., 2013), although the approach of using the external pressures with an analytical model has been considered, as discussed below.

Amano et al. (1988) and Trung et al. (2010) modeled flows and pressures in double-layer roof systems (i.e., permeable roof-blocks and porous sunshade roof cover sheets) by using the discharge equation. They treated the cavity pressure between the layers as being similar to building internal pressure with multiple openings, which is also described by Oh et al. (2007). In this model, the cavity volume between the layers is divided into a finite number of “rooms” to apply the discharge equation to the flow through an opening into a single room. Then, the pressure in the room, which is uniform (similar to the building internal pressure), is transmitted to adjacent rooms by differential pressure between rooms. The flow between rooms is also modeled by the discharge equation. Although the model works for a particular case, it is too simple to define flows and pressure gradients within the air-permeable layer, especially when the panel length ( $L$ ) is large or the height ( $H$ ) of the cavity between the air-permeable layer and the inner layer is relatively small. Results from experimental studies, as described in Chapter 2, indicate



that the cavity pressures in a relatively thin cavity (i.e., small  $H$ ) vary approximately linearly, rather than step changes from one internal room to an adjacent room. In other words, the pressure drops are due to friction and not due to orifice-like pressure drops.

Sun and Bienkiewicz (1993) employed Darcy's law to model the mean flow between and underneath roof pavers on a low-rise building. They assumed the gaps between and underneath pavers are small so that flows are steady with low Reynolds Number. However, the use of the model is limited to crack size gaps where Darcy's law is preserved, and effects of pressure fluctuations from the external flow were not examined.

Results from the experimental study described in Chapter 2 indicate that the cavity pressure distribution in a double layer system depends on two non-dimensional parameters,  $G/H$  and  $\frac{fL/H}{C_L}$ , where  $f$  is the friction factor for the cavity flow between the layers, and  $C_L$  is the loss coefficient for the flow through the gap between panels. The dimensional parameter,  $\frac{fL/H}{C_L}$  represents the ratio between the friction losses for the (cavity) flow between the layers to the losses for the discharge through the gap and clarifies the important role of the panel length for this problem. These two parameters control the pressure drops through the gap flow and the cavity flow so that the pressure distribution in the cavity is determined.

When considering the flows involved in a double layer system, there are two primary types of flow: (i) flow through the openings on the air-permeable layer and (ii) flow in the cavity between the layers as illustrated in Figure 3.1a. Since the flows are continuous, this problem can be solved simultaneously by combining the discharge equation and the equation for flow between parallel plates (i.e., Couette flow). Thus, in the combined model, the pressure drop through the gap ( $G$ ) between panels is governed by the discharge equation and the pressure distribution between the layers ( $H$ ) is governed by the equation for Couette flow. This model can be extended to solve for multiple panels, as illustrated in Figure 3.1b. The objective of this study is to develop a numerical model to predict the unsteady pressure distribution within a double-layer roof system using this concept of sequential pressure drops with the unsteady discharge equation for the flow through the gaps in the air permeable layer and Couette Flow for the flow through the

cavity. A one-dimensional model is developed and validated using the experimental data discussed in Chapter 2. The intent is that the model uses external pressure time histories with the panel and cavity geometry to estimate the pressure time histories within the cavity of a double-layer roof system.

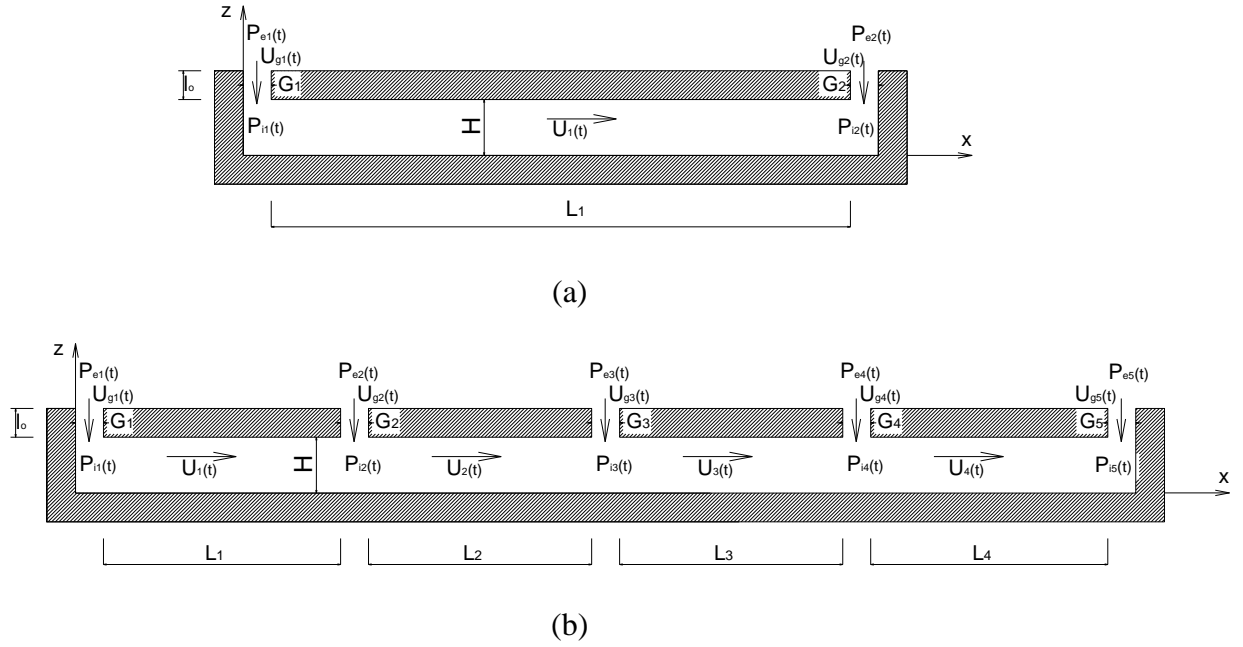


Figure 3.1 Flow and pressure model for the double layer system: (a) two gaps; (b) five gaps on the air-permeable layer.

## 3.2 Governing Equations

### 3.2.1 Governing equation for flows through an orifice

The governing equation for the fluid flow through an opening can be derived from the Navier-Stokes equations for incompressible flow,

$$\rho \frac{\partial u_j}{\partial t} + \rho u_k \frac{\partial u_j}{\partial x_k} = -\frac{\partial p}{\partial x_j} + \mu \frac{\partial^2 u_j}{\partial x_j \partial x_j} + \rho f_{bj} \quad (3.1)$$

where  $\rho$  and  $\mu$  are density and viscosity of the fluid,  $u$  is (componential) velocity,  $p$  is the pressure,  $f_b$  is the body force, and the summation notation is used. Eq. (3.1) can be reduced to Euler's equations, when the fourth (i.e., viscous) term is negligibly small, i.e.,

$$\rho \frac{\partial u_j}{\partial t} + \rho u_k \frac{\partial u_j}{\partial x_k} = -\frac{\partial p}{\partial x_j} + \rho f_{bj} \quad (3.2)$$

Integrating Eq. (3.2) along the streamline,

$$\int_s \left( \rho \frac{\partial U}{\partial t} + \rho U \frac{\partial U}{\partial s} + \frac{\partial p}{\partial s} - \rho f_b \right) ds = 0 \quad (3.3a)$$

$$\rho \int_1^2 \frac{dU}{dt} ds + \rho \int_1^2 U \frac{dU}{ds} ds + \int_1^2 \frac{dp}{ds} ds - \int_1^2 \rho f_b ds = 0 \quad (3.3b)$$

$$\rho \int_1^2 ds \frac{dU}{dt} + \rho \int_1^2 U dU + \int_1^2 dp - \int_1^2 \rho f_b ds = 0 \quad (3.3c)$$

Eq. (3.2) becomes the unsteady Bernoulli equation (Currie, 2003),

$$\rho \int_1^2 \frac{\partial U}{\partial t} ds + \rho \frac{U_2^2 - U_1^2}{2} + \int_1^2 dp - \rho g(z_2 - z_1) = 0 \quad (3.4)$$

Considering unsteady flow along a streamtube through an opening from  $x_1$ , just outside the opening where the pressure is  $P_1$ , to  $x_2$ , just inside the opening where the pressure is  $P_2$ , Eq. (3.4) becomes (Vickery, 1986; Oh et al., 2007)

$$\rho l_e \dot{U} + C_L \frac{\rho}{2} U |U| + \frac{12\mu l_o}{G^2} U = \Delta P \quad (3.5)$$

where,  $U$  is the average velocity through the area of the opening,  $l_e$  is the effective length of the fluid passing through the orifice ( $\int_1^2 ds = x_2 - x_1$ ),  $l_o$  is the plate thickness and  $G$  is the opening width of the orifice,  $\dot{U} = dU/dt$  is assumed constant along the streamtube, and  $\Delta P$  is the differential pressure ( $P_1 - P_2$ ). The third term in Eq. (3.5) represents the viscous losses and assumes one-dimensional laminar flow through the opening.

The unsteady discharge equation has been used for numerical models of internal pressures within building volumes (e.g., Holmes (1979), Vickery (1986) and Oh et al. (2007)) to estimate time-varying internal pressures,  $P_i(t)$  ( $=P_2(t)$ ), given known external

pressures,  $P_e(t)$  ( $=P_1(t)$ ), at the opening. There are two unknowns in the case of a single opening into an otherwise sealed volume, the velocity of flow through the opening,  $U(t)$ , and the internal pressure,  $P_i(t)$ . These can be calculated from Eq. (3.5) and the continuity equation,

$$\rho Q(t) = V_o \dot{\rho}(t) \quad (\text{i.e., mass flux} = \text{change of mass within the internal volume, } V_o) \quad (3.6a)$$

$$\rho a U(t) = V_o \frac{\rho}{K_A} \dot{P}(t) \quad (3.6b)$$

$$\dot{P}(t) = \frac{\gamma P_o a U(t)}{V_o} \quad (3.6c)$$

where  $\dot{P} = \frac{dP}{dt}$ ,  $K_A$  is the bulk modulus of air, which is equivalent to the heat capacity ratio,  $\gamma$ , times the static pressure,  $P_o$ , while  $a$  is the area of the opening. To sum up, the discharge equation models the flow of air into or out of the opening and the internal pressure obtained from this model represents the single (i.e., uniform) pressure for the entire volume when there is a single opening into the volume. However, when there are multiple openings, the assumptions in Eq. (3.6) may not hold and the pressure may vary spatially within the internal volume as discussed in Chapter 2 and in the literature such as Bienkiewicz and Sun (1992 and 1997) and Karava et al. (2011), and as discussed below.

### 3.2.2 Governing equation for flows between two parallel plates

The experimental results of Bienkiewicz and Sun (1992, 1997) and from Chapter 2 suggest that, for relatively small distances between the layers of a multi-layer system, the flow in the cavity between the layers can be modeled as the unsteady flow between parallel plates, i.e., unsteady Couette Flow. In contrast, the experiments of Karava et al. (2011) indicate that when the distances between layers are large (such as the distance between walls in a building) compared to the dimension of the opening, the interior flow field may be fully three-dimensional. For the case of Couette Flow, the pressure gradient along the  $x$ -direction drives flow between two parallel plates when there are no body forces acting on fluid, where the  $x$  co-ordinate is defined in Figure 3.1. The governing equation for this problem can be obtained from the Navier-Stokes equations, Eq. (3.1)

when the flow is taken to be in the x-direction, one-dimensional, and incompressible (i.e.,  $v = w = 0$  and  $\partial u / \partial x = 0$ ) as follows,

$$\rho \frac{\partial u}{\partial t} = -\frac{\partial p}{\partial x} + \mu \frac{\partial^2 u}{\partial z^2} \quad (3.7)$$

Integrating Eq. (3.7) with respect to  $z$ , between 0 and  $H$ ,

$$\rho \frac{dQ}{dt} = -\frac{\partial p}{\partial x} H + \tau_H - \tau_0 \quad (3.8)$$

where  $Q = \int_0^H u dz$ , is the flow rate per unit width, and  $\tau_0 = \mu \left[ \frac{\partial u}{\partial z} \right]_{z=0}$  and  $\tau_H = \mu \left[ \frac{\partial u}{\partial z} \right]_{z=H}$  are the wall shear stresses. Since  $Q/H = U$ , the average velocity, and  $\tau_0 = \frac{6\mu U}{H}$  and  $\tau_H = -\frac{6\mu U}{H}$  for laminar flow, Eq. (3.8) can be rearranged as

$$\rho \frac{dU}{dt} = -\frac{\partial p}{\partial x} - \frac{12\mu U}{H^2} \quad (3.9)$$

Similar to the derivation of Bernoulli's equation, integrating Eq. (3.9) along the streamtube between the parallel plates (i.e., in the cavity flow)

$$\rho \int_1^2 ds \frac{dU}{dt} + \frac{12\mu}{H^2} \int_1^2 ds U + \int_1^2 dp = 0 \quad (3.10a)$$

$$\rho L \frac{dU}{dt} + \frac{12\mu L}{H^2} U = \Delta P \quad (3.10b)$$

where  $L = \int_1^2 ds = x_2 - x_1$  (i.e., the length of the plate) and  $U$  is the average velocity per unit area between the panel and the solid surface. Therefore, for a given flow ( $U$ ), the pressure gradient ( $\Delta P$ ) along the cavity between the parallel plates depends on geometric parameters,  $L$  and  $H$ .

### 3.2.3 Analytical model for one-dimensional flows in the cavity between layers in a double layer system

As discussed in the introduction to this chapter, the one-dimensional flow through a double layer system with two openings (Figure 3.1a) may be modeled by combining Eqs. (3.5) and (3.10) such that,

$$\rho l_{e1} \dot{U}_{g1}(t) + C_{L1} \frac{\rho}{2} U_{g1}(t) |U_{g1}(t)| + \frac{12\mu l_{o1}}{G_1^2} U_{g1}(t) = P_{e1}(t) - P_{i1}(t) \quad (3.11a)$$

$$\rho L_1 \dot{U}_1(t) + \frac{12\mu L_1}{H^2} U_1(t) = P_{i1}(t) - P_{i2}(t) \quad (3.11b)$$

$$\rho l_{e2} \dot{U}_{g2}(t) + C_{L2} \frac{\rho}{2} U_{g2}(t) |U_{g2}(t)| + \frac{12\mu l_{o2}}{G_2^2} U_{g2}(t) = P_{e2}(t) - P_{i2}(t) \quad (3.11c)$$

where  $U_g$  is the average velocity through the gap ( $G$ ) between adjacent panels, and  $U$  is the average velocity per unit width in the cavity between the panel and the inner surface. The numbers in the subscripts (i.e., 1 or 2) for  $l_e$ ,  $l_o$ ,  $C_L$ ,  $U_g$ ,  $G$ ,  $L$ ,  $U$ ,  $P_e$  and  $P_i$  denote the number of the location of the gaps as depicted in Figure 3.1a. Eqs. (3.11a) and (3.11c) represent the pressure drop through the orifice-like gaps between the panels while Eq. (3.11b) describes the pressure drop through the cavity between layers. Applying the Continuity equation ( $G_1 U_{g1} = H U_1 = -G_2 U_{g2}$ ) for incompressible flow, Eqs. (3.11) can be rearranged as

$$\rho l_{e1} \frac{H}{G_1} \dot{U}_1(t) + C_{L1} \frac{\rho}{2} \left(\frac{H}{G_1}\right)^2 U_1(t) |U_1(t)| + \frac{12\mu l_{o1} H}{G_1^3} U_1(t) = P_{e1}(t) - P_{i1}(t) \quad (3.12a)$$

$$\rho L_1 \dot{U}_1(t) + \frac{12\mu L_1}{H^2} U_1(t) = P_{i1}(t) - P_{i2}(t) \quad (3.12b)$$

$$\rho l_{e2} \frac{H}{G_2} \dot{U}_1(t) + C_{L2} \frac{\rho}{2} \left(\frac{H}{G_2}\right)^2 U_1(t) |U_1(t)| + \frac{12\mu l_{o2} H}{G_2^3} U_1(t) = P_{e2}(t) - P_{i2}(t) \quad (3.12c)$$

These three equations can be combined into a single equation by eliminating  $P_{i1}(t)$  and  $P_{i2}(t)$  showing that it is the external pressure gradient,  $\Delta P_e(t) = P_{e1}(t) - P_{e2}(t)$ , which drives the flow through the openings between panels and in the cavity between the layers.

Using the same concept when there are multiple panels, additional equations are required in the analytical model to handle the flows through the multiple gaps between panels and between layers. For instance, five Discharge equations and four equations for Couette flow are required to solve the problem with four panels illustrated by Figure 3.1b. Applying the Continuity equations for incompressible flows in Figure 3.1b,

$$G_1 U_{g1} = H U_1, \text{ for the 1}^{\text{st}} \text{ gap} \quad (3.13a)$$

$$G_2 U_{g2} = H(U_2 - U_1), \text{ for the 2}^{\text{nd}} \text{ gap} \quad (3.13b)$$

$$G_3 U_{g3} = H(U_3 - U_2), \text{ for the 3}^{\text{rd}} \text{ gap} \quad (3.13c)$$

$$G_4 U_{g4} = H(U_4 - U_3), \text{ for the 4}^{\text{th}} \text{ gap} \quad (3.13d)$$

$$G_5 U_{g5} = -H U_4, \text{ for the 5}^{\text{th}} \text{ gap} \quad (3.13e)$$

the analytical model for one-dimensional flows in the cavity with four panels can be expressed by,

$$\rho l_{e1} \frac{H}{G_1} \dot{U}_1(t) + C_{L1} \frac{\rho}{2} \left( \frac{H}{G_1} \right)^2 U_1(t) |U_1(t)| + \frac{12\mu l_{o1} H}{G_1^3} U_1(t) = P_{e1}(t) - P_{i1}(t) \quad (3.14a)$$

$$\rho L_1 \dot{U}_1(t) + \frac{12\mu L_1}{H^2} U_1(t) = P_{i1}(t) - P_{i2}(t) \quad (3.14b)$$

$$\begin{aligned} \rho l_{e2} \frac{H}{G_2} (\dot{U}_2(t) - \dot{U}_1(t)) + C_{L2} \frac{\rho}{2} \left( \frac{H}{G_2} \right)^2 (U_2(t) - U_1(t)) |U_2(t) - U_1(t)| + \\ \frac{12\mu l_{o2} H}{G_2^3} (U_2(t) - U_1(t)) = P_{e2}(t) - P_{i2}(t) \end{aligned} \quad (3.14c)$$

$$\rho L_2 \dot{U}_2(t) + \frac{12\mu L_2}{H^2} U_2(t) = P_{i2}(t) - P_{i3}(t) \quad (3.14d)$$

$$\begin{aligned} \rho l_{e3} \frac{H}{G_3} (\dot{U}_3(t) - \dot{U}_2(t)) + C_{L3} \frac{\rho}{2} \left( \frac{H}{G_3} \right)^2 (U_3(t) - U_2(t)) |U_3(t) - U_2(t)| + \\ \frac{12\mu l_{o3} H}{G_3^3} (U_3(t) - U_2(t)) = P_{e3}(t) - P_{i3}(t) \end{aligned} \quad (3.14e)$$

$$\rho L_3 \dot{U}_3(t) + \frac{12\mu L_3}{H^2} U_3(t) = P_{i3}(t) - P_{i4}(t) \quad (3.14f)$$

$$\rho l_{e4} \frac{H}{G_4} (\dot{U}_4(t) - \dot{U}_3(t)) + C_{L4} \frac{\rho}{2} \left( \frac{H}{G_4} \right)^2 (U_4(t) - U_3(t)) |U_4(t) - U_3(t)| + \frac{12\mu l_{o4} H}{G_4^3} (U_4(t) - U_3(t)) = P_{e4}(t) - P_{i4}(t) \quad (3.14g)$$

$$\rho L_4 \dot{U}_4(t) + \frac{12\mu L_4}{H^2} U_4(t) = P_{i4}(t) - P_{i5}(t) \quad (3.14h)$$

$$\rho l_{e5} \frac{H}{G_5} \dot{U}_4(t) + C_{L5} \frac{\rho}{2} \left( \frac{H}{G_5} \right)^2 U_4(t) |U_4(t)| + \frac{12\mu l_{o5} H}{G_5^3} U_4(t) = P_{e5}(t) - P_{i5}(t) \quad (3.14i)$$

### 3.3 Numerical Simulation Details

#### 3.3.1 Numerical solution

Exact solutions to Eqs. (3.14) cannot be established but they can be solved at each time step by employing a numerical method. Here, a 2<sup>nd</sup> order, backward differencing, numerical scheme (Chapra and Canale, 2006) is applied using a given set of time series data for the external pressures on the outer surfaces near the locations of the gaps. Details of the numerical method are provided in the Appendix A.

The validation cases for the numerical model were obtained from wind tunnel data of a double layer system on the roof of a low-rise building as presented in Chapter 2. The wind tunnel model of the building, with dimensions and pressure measurement locations is shown in Figure 2.1. Further experimental details, along with a detailed analysis of the data, can be found in Chapter 2.

Again, pressure distributions for a mean, one-dimensional cavity flow were investigated in this study. In total, 10 configurations were utilized here including five different  $G$  (0.5, 1, 1.5, 2.5 and 15 mm) with  $H = 1.2$  mm, and five different  $H$  (0.5, 1.2, 2.5, 5 and 15 mm) with  $G = 1$  mm. The length of the panels (i.e., the cavities),  $L$ , is 50 mm.



### 3.3.2 Numerical parameters

Numerical simulations in this study are based on the assumption that the cavity flow remains laminar using the wind tunnel model dimensions. The Reynolds number for the laminar flow in the cavity between the parallel plates ( $H$ ), derived from the equation for Couette flow, for a given mean pressure drop,  $\Delta\bar{C}p_i$ , and panel length ( $L$ ) can be approximated by,

$$Re_i = \frac{UH}{\nu} = \frac{H^3 \bar{V}_h^2 \Delta\bar{C}p_i}{24\nu^2 L} \quad (3.15)$$

where  $\bar{V}_h$  is mean wind velocity at the building roof height ( $h$ ) and  $\nu$  is the kinematic viscosity of air. The estimated Reynolds numbers from Eq. (3.15) for the flow between the layers from the model dimensions are 160, 110, 37 and 4 for  $H = 5$  mm, 2.5 mm, 1.2 mm and 0.5 mm, respectively, indicating  $Re_i$  is below the critical Reynolds number and the flow remains laminar. It should be noted that  $H$  of 15 mm is not included herein due to the small value of  $\Delta\bar{C}p_i$  (close to zero), which means that, because of the sensitivity to  $\Delta\bar{C}p_i$ , the uncertainty inherent in the Reynolds number calculation is too large. Numerical values used in the computations are summarized in Table 3.1. The effective length,  $l_e$ , is defined as  $l_e = l_o + 0.89G$  (Vickery, 1986) or  $l_o + H$ , whichever is smaller. The latter takes into account a decrease in the effective length due to a smaller  $H$  when  $H/G < 1$ . The loss coefficient,  $C_L$ , was 2.5 which has been used for studies on orifice flow models, such as Vickery (1986).

Predictions from the numerical model are compared and validated with the experimental measurements of the pressure coefficients on the interior surface of the four panels ( $Cp_i$ ) obtained from the pressure taps along the middle row of the panel on a double-layer roof system in an approximately two-dimensional mean flow, as shown in Figure 2.1, for the single wind direction considered herein.

Table 3.1 Numerical values used in the model calculations

| Parameter and value   | Definition   |
|---|--|
| $l_o = 8 \text{ mm}$  | panel thickness  |
| $L = 50 \text{ mm}$   | panel length   |
| $G = 0.5, 1, 1.5, 2.5 \text{ and } 15 \text{ mm}$                       | gap between panels                                       |
| $H = 0.5, 1.2, 2.5, 5 \text{ and } 15 \text{ mm}$                       | height of cavity between layers                          |
| $V_h = 10.7 \text{ m/s}$  | mean velocity at roof height (h)                         |
| $l_e = l_o + 0.89G$ (Vickery, 1986) or $l_o + H$ , whichever is smaller | effective length of the fluid passing through the gap, G |
| $C_L = 2.5$ (Vickery, 1986)   | loss coefficient   |
| $\nu = 1.5 \times 10^{-5} \text{ m}^2/\text{s}$                         | kinematic viscosity of air                               |

### 3.3.3 Pressure coefficients

The pressure time series obtained from both the numerical computations and the experimental measurements are referenced to the mean dynamic velocity pressure at roof height,  $h$ , such that

$$C_{pe}(t) = \frac{P_e(t) - P_o}{\frac{1}{2}\rho\bar{V}_h^2} \quad (3.13)$$

where  $C_{pe}(t)$  is the time-varying pressure coefficient on the external surface of the panel,  $P_o$  is the static (thermodynamic) pressure and  $\bar{V}_h$  is the mean velocity at roof height. Analogously, the time-varying pressure coefficient on the interior surface of the panel,  $C_{pi}(t)$ , is defined by

$$C_{pi}(t) = \frac{P_i(t) - P_o}{\frac{1}{2}\rho\bar{V}_h^2} \quad (3.14)$$

Area-averaged pressure coefficients are obtained along the middle line of pressure taps by integrating the pressures simultaneously over the panel areas, such that

$$C_{p,area-averaged}(t) = \sum_{j=1}^n C_{pj}(t) \frac{w_j}{W} \quad (3.15)$$

where  $n$  is the number of taps within the area of the panel,  $W$ , being examined;  $C_{pj}(t)$  is the pressure coefficient at location  $j$ ; and  $w_j$  is the tributary area of the pressure tap at location  $j$ . The peak (minima and maxima) pressure coefficients presented in the current study are the absolute minimum and maximum coefficients within the time history.

### 3.4 Comparison of Simulation Results with Experimental Data

#### 3.4.1 Time histories and spectra

Three different configurations ( $H = 15$  mm,  $H = 2.5$  mm and  $H = 0.5$  mm with a gap of  $G = 1$  mm) with four panels (Figure 3.1b) were chosen to validate the numerical model. The numerical model requires the time histories of the external pressures at the gaps between the panels as input. The experiments had data for 3 rows of external pressure taps. Here the “middle row”, as indicated in Figure 2.1, is used for the input. As discussed in Chapter 2, the mean pressure coefficients on the internal surface of the panels ( $\bar{C}p_i$ ) are fairly uniform for  $H = 15$  mm,  $G = 1$  mm, but vary linearly between the gaps when  $H = 0.5$  mm,  $G = 1$  mm.  $H = 2.5$  mm is the approximate boundary between uniform and linear pressure variations when  $G = 1$  mm. Thus, changes in  $Cp_i$  behavior are clearly delineated by these three configurations.

Area-averaged pressure coefficients along the middle line of taps for Panels 1 and 4 (see Figure 2.1 for the panel layout) were formed and the time histories and corresponding spectra are presented in Figures 3.2 to 3.4. Segments of the time histories of 2 sec duration (between 10 to 12 seconds) were chosen arbitrarily. The numerical simulations of  $Cp_i$  computed from the measured time history data of  $Cp_e$  are compared with the experimental values of  $Cp_i$ . It is clear from the figures that the numerical model can capture the temporal variations of  $Cp_i$ , as well as the mean and standard deviation (i.e., root-mean-square, RMS) values. The time history plots of  $Cp_i$ , and the corresponding mean and RMS values, are almost undistinguishable for both Panels 1 and

4 when  $H = 15$  mm, as shown in Figure 3.2. As found in Chapter 2,  $Cp_i(t)$  is uniform beneath all of the panels such that the discharge equations in Eqs. (3.14a; 3.14c; 3.14e; 3.14g; 3.14i) dominate the pressure difference between the external and internal flows. Because of this, the  $Cp_i(t)$  do not follow  $Cp_e(t)$  from either Panel 1 or 4 but are formed by the combination of all the  $Cp_e(t)$ , much like the case for internal building pressures.

For Panels 1 and 4 there are significant differences in the  $Cp_i(t)$  time histories when  $H = 0.5$  mm, as shown in Figure 3.4. In this case, they are more localized such that  $Cp_i(t) \approx Cp_e(t)$  at the same  $x$  location. For this gap and height combination, the cavity (Couette) flow dominates the pressure drop, meaning that relatively less of the pressure gradient occurs for the flow through the orifices. This leads to a higher level of pressure equalization and consequently this should lead to lower net wind loads. Figure 3.3 shows behavior between these two bounds, with the numerical model again capturing the fluctuating behavior.

The fluctuating components are further investigated with the plots of spectra. The power spectral density (PSD) of the  $Cp_i$  are attenuated, relative to  $Cp_e$ , to a larger extent when  $H = 15$  mm (Figure 3.2) compared to those for  $H = 0.5$  mm (Figure 3.4). When this attenuation occurs, the external and internal pressures are less equalized because the internal pressure cannot track the external pressure fluctuations to the same extent. Comparing the spectra between the numerical and experimental results, the numerical simulations yield slightly higher fluctuations, particularly at the higher frequencies, but match the data well up to about 20 Hz in these simulations using the model dimensions, below which 90% of fluctuating energy is contained.

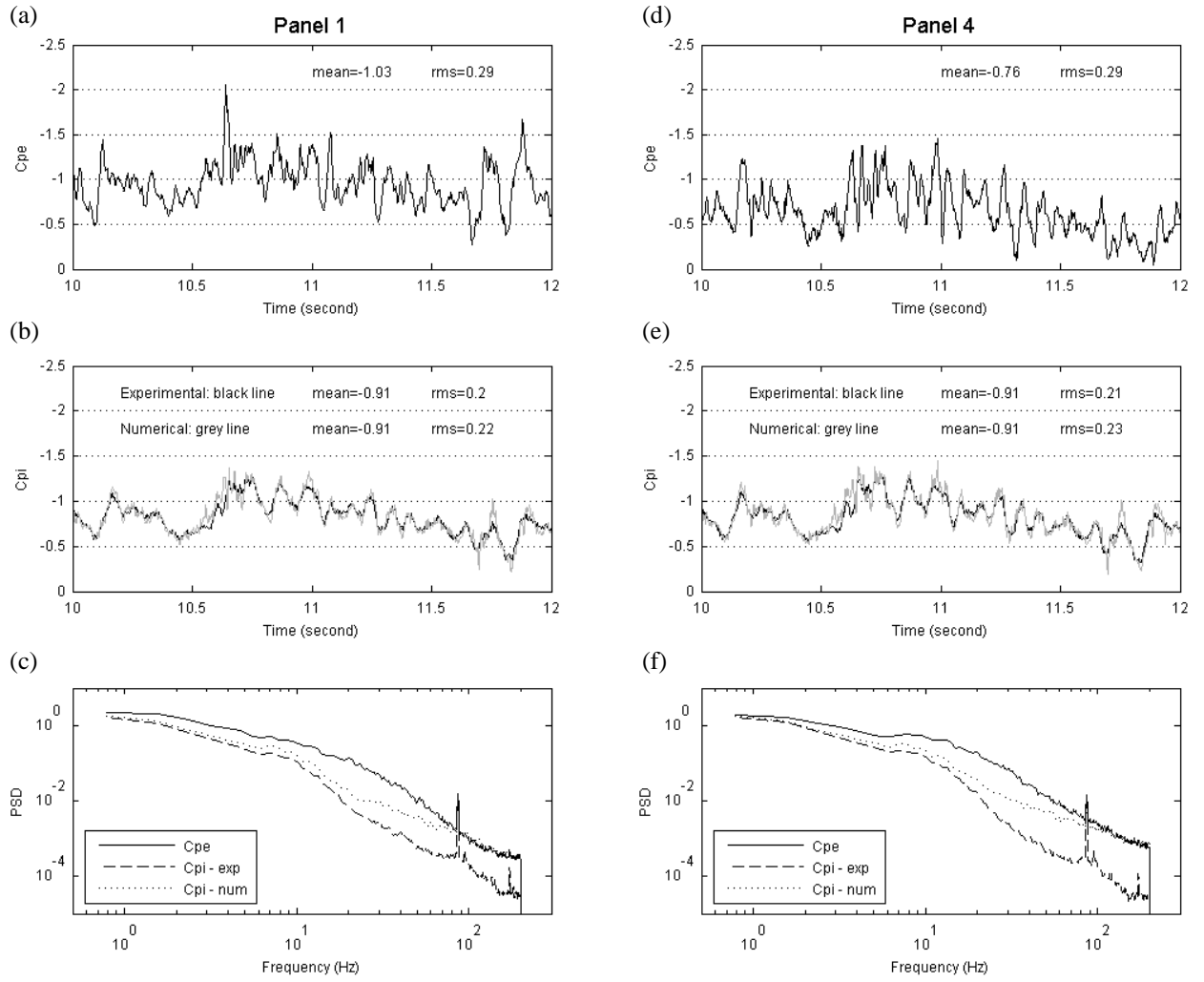


Figure 3.2 Time series and spectra of area averaged pressure coefficients for  $G = 1$  mm and  $H = 15$  mm: (a)  $C_{pe}$ ; (b)  $C_{pi}$ ; (c) power spectra on Panel 1; (d)  $C_{pe}$ ; (e)  $C_{pi}$ ; and (f) power spectra on Panel 4.

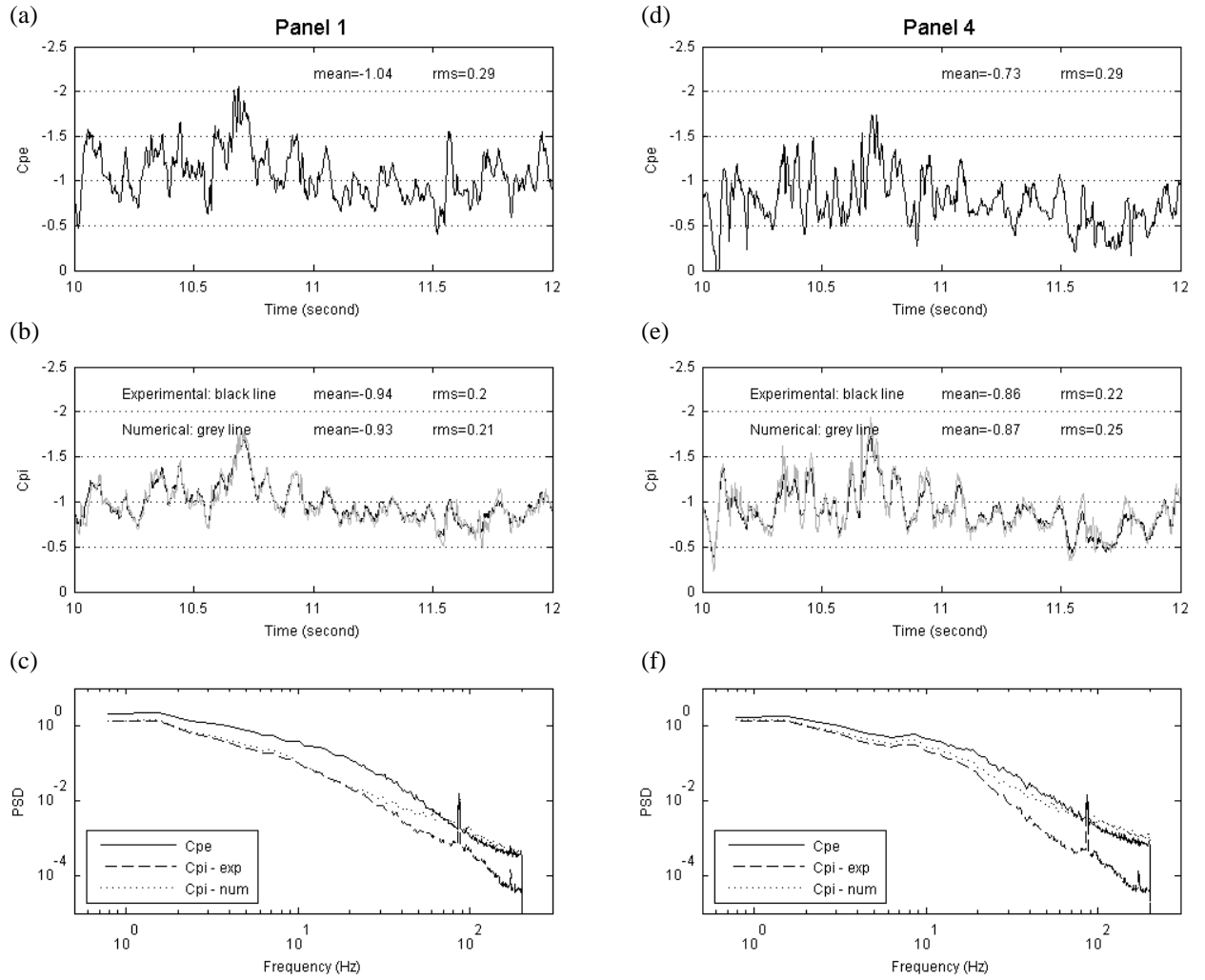


Figure 3.3 Time series and spectra of area averaged pressure coefficients for  $G = 1 \text{ mm}$  and  $H = 2.5 \text{ mm}$ : (a)  $C_{pe}$ ; (b)  $C_{pi}$ ; (c) power spectra on Panel 1; (d)  $C_{pe}$ ; (e)  $C_{pi}$ ; and (f) power spectra on Panel 4.

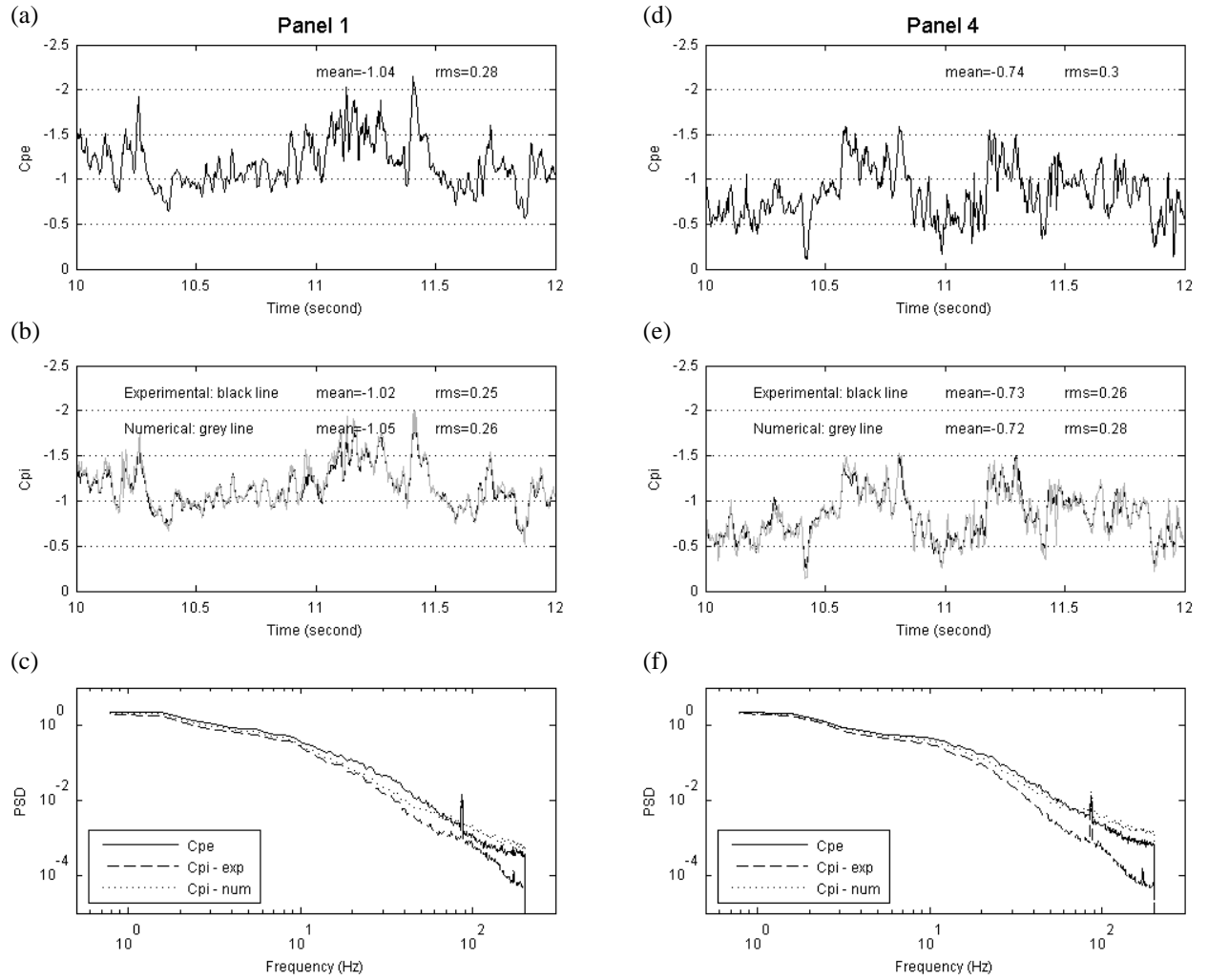


Figure 3.4 Time series and spectra of area averaged pressure coefficients for  $G = 1 \text{ mm}$  and  $H = 0.5 \text{ mm}$ : (a)  $C_{pe}$ ; (b)  $C_{pi}$ ; (c) power spectra on Panel 1; (d)  $C_{pe}$ ; (e)  $C_{pi}$ ; and (f) power spectra on Panel 4.

### 3.4.2 Mean and RMS point pressure distributions

Figures 3.5 and 3.6 depict mean and RMS point pressure coefficient distributions on the external and interior surfaces of the panels,  $Cp_e$  and  $Cp_i$ , comparing the experimental and numerical results. Figure 3.5a shows that when  $H$  is varied, the  $\bar{Cp}_i$  distributions have different shapes, as discussed in detail in Chapter 2. The numerical model, represented by the grey markers in the plot, captures the shape of the mean pressure distributions quite well, although there are some discrepancies between the numerical and experimental results. Similarly, the numerical model captures the  $\bar{Cp}_i$  variations as  $G$  is altered, as depicted in Figure 3.5b.

RMS values,  $\tilde{Cp}_i$ , on the internal surface of the panels are attenuated significantly depending on the  $H$  and  $G$ , compared to the  $\tilde{Cp}_e$  distributions, as shown in Figure 3.6. Again, the numerical model is able to capture the shape of the RMS pressure coefficient distributions when both  $H$  and  $G$  are varied, although the magnitudes between the results do not match perfectly with the numerical model leading to higher levels of fluctuations.

To better describe the discrepancies between the numerical and experimental results, the ratios of the numerical to experimental values are plotted in a histogram, as shown in Figure 3.7. In these a perfect match is indicated when the ratio is unity. The histograms for the mean values, as shown in Figure 3.7a, indicate no bias with the range of average discrepancies between about  $\pm 5\%$ . In contrast, RMS values have some bias and thus, the numerical results are always higher, in the range from  $+5\%$  to  $+15\%$ , as seen in Figure 3.7b. This is consistent with the time histories and spectra in Figures 3.2 to 3.4, where the numerical model was found to have high levels of fluctuations, particularly at the higher frequencies. This may be due to the use of point external pressures as the input, which may not perfectly represent the driving force for the cavity flow in the numerical computations. This point is examined next.



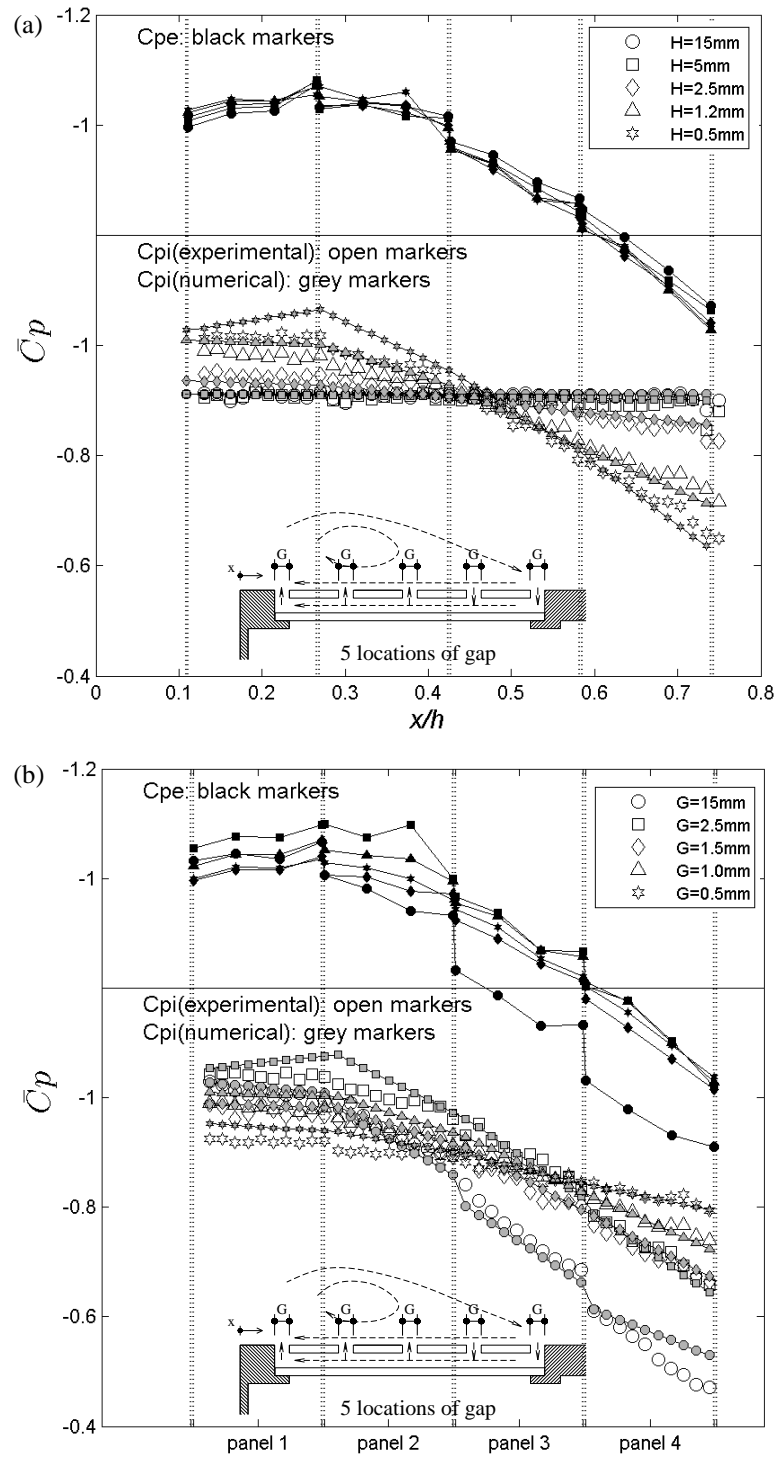


Figure 3.5 Mean pressure distributions for the pressure taps in the middle row with numerical simulation from the point external pressure coefficients: (a)  $G = 1$  mm with  $H$  variations; and (b)  $H = 1.2$  mm and with  $G$  variations.

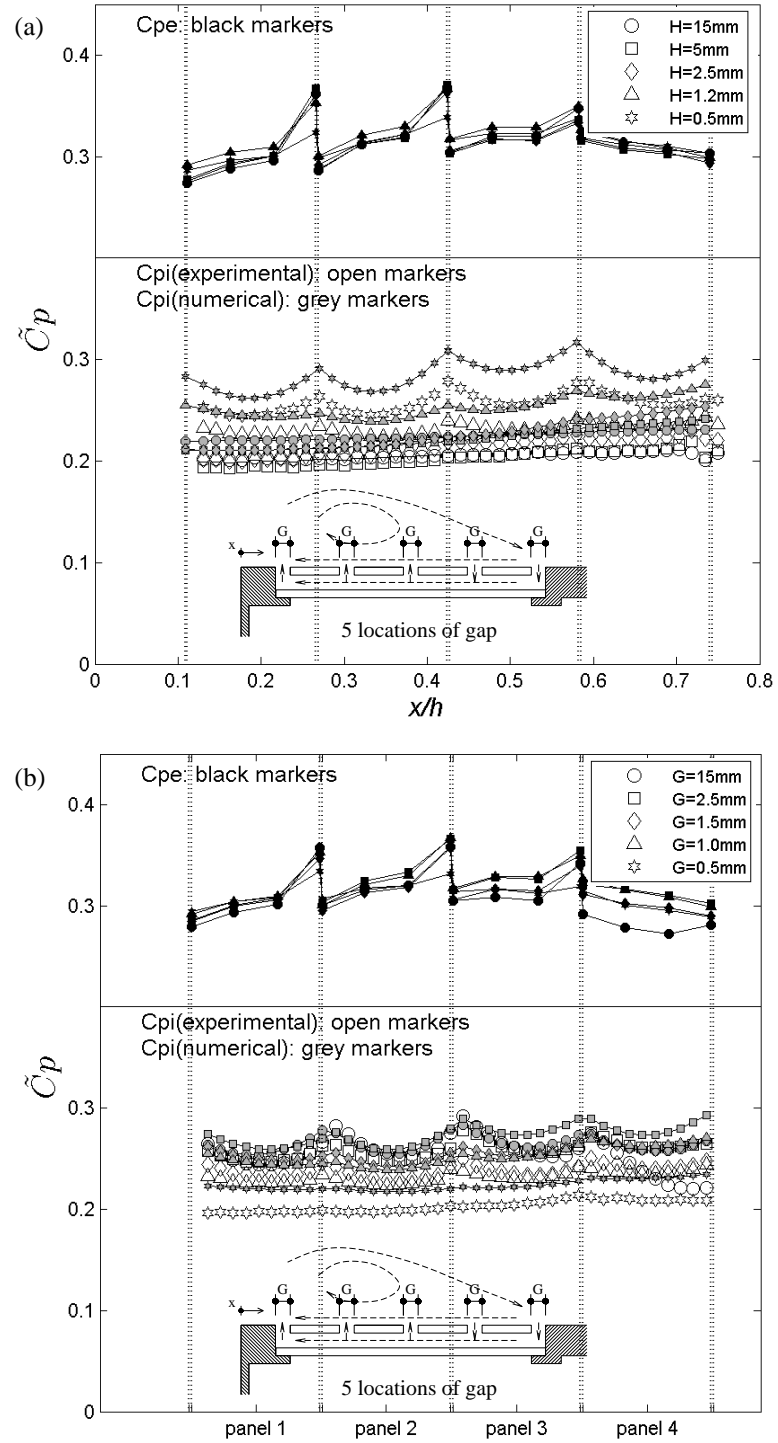
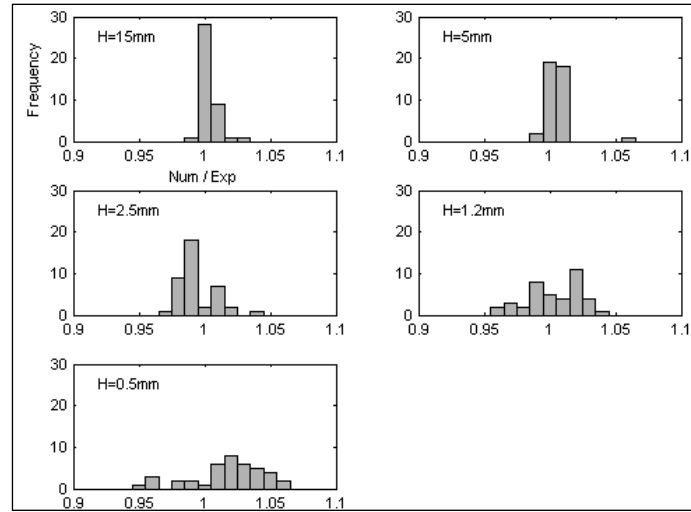
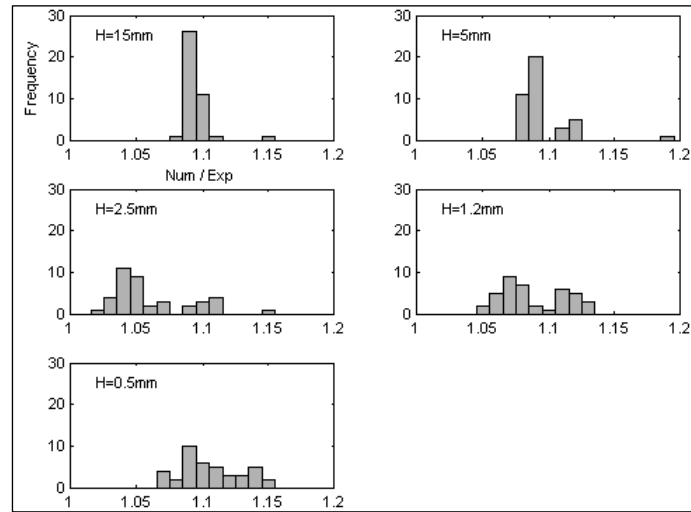


Figure 3.6 RMS pressure distributions for the pressure taps in the middle row with numerical simulation from the point external pressure coefficients: (a)  $G = 1 \text{ mm}$  with  $H$  variations; and (b)  $H = 1.2 \text{ mm}$  and with  $G$  variations.



(a)



(b)

Figure 3.7 Distribution of the ratio of the numerical to the experimental results of  $C_{pi}$  for  $G = 1$  mm with  $H$  variations (numerical simulation from the point external pressure coefficients): (a) mean; and (b) RMS.

### 3.4.3 Use of spanwise-averaged external pressure coefficients as input

Figure 3.8a depicts spanwise correlations coefficients,

$$R(\Delta y) = \frac{\frac{1}{T} \int_0^T C_p'(x, y, t) C_p'(x, y + \Delta y, t) dt}{\tilde{C}_p(x, y) \tilde{C}_p(x, y + \Delta y)} \cong \frac{\frac{1}{T} \int_0^T C_p'(x, y, t) C_p'(x, y + \Delta y, t) dt}{[\tilde{C}_p(x, y)]^2} \quad (3.16)$$

where  $C_p'(x, y, t)$  is the pressure fluctuation at location  $(x, y)$  and time,  $t$ ,  $\tilde{C}_p(x, y)$  is the RMS (i.e., standard deviation) value, and  $R(\Delta y)$  is the correlation coefficient. Here,  $(x, y)$  is set to be the midspan of panels 1 and 2. The correlation is assessed along the span in the  $y$ -direction (using the taps along the gap ( $G_2$ ) between Panels 1 and 2, with respect to the pressure tap in the middle row. Figure 3.8 shows that the degree of correlation is quite distinct between  $Cp_e$  and  $Cp_i$ , and for the  $Cp_i$ 's with different  $G/H$  values. First, the spanwise correlation of  $Cp_e$ , denoted by a dot line for clarity only, is less correlated than for any  $Cp_i$  case. The correlation coefficient for the external pressures drops to about 0.7 for a spanwise separation of about  $0.3h$ . In contrast, when the cavity (interior) pressures are nearly uniform, as they are for large values of  $H$  (or small values of  $G/H$ ),  $R(\Delta y) \approx 1$  for the cavity pressure. This is exactly what occurs for building internal pressures with a single dominant opening except that here,  $Cp_i$  depends on the combination of all the spanwise  $Cp_e$  values, instead of following a single (point)  $Cp_e$ . The spanwise correlation of  $Cp_i$  is gradually reduced as  $G/H$  is increased. For  $G/H = 12.5$ , the spanwise correlation coefficients are similar for  $Cp_e$  and  $Cp_i$ , which means  $Cp_i$  is close to following the single  $Cp_e$ . The spanwise correlation of the pressure data along the middle of Panel 2, as seen in Figure 3.8b, shows similar trends but  $Cp_i$  are more highly correlated in this case, compared to the  $Cp_i$  along the gap. This implies that the pressures in the cavity located away from the gap tend to be more uniform.

The analysis of the spanwise correlation of pressure data suggests that using spanwise-averaged external pressures is appropriate. For example, for low values of  $G/H$ , when  $Cp_i$  is uniform, the most appropriate values for  $Cp_e$  would be the average along the entire gap, since  $Cp_i$  does not respond to the local variations of  $Cp_e$  along the gap. However, for high  $G/H$  values, for a particular panel size,  $Cp_e$  values averaged over a portion of the span would be more appropriate. Since there are limited numbers of

external pressure taps in the current wind tunnel data, only a complete span average (of 3 taps) is examined here.

Results from numerical simulation by employing the spanwise-averaged  $Cp_e$  are presented in Figure 3.9 for mean values and in Figure 3.10 for RMS pressure distributions. Several observations can be made from the plots, comparing them with Figure 3.5 and 3.6. First, the mean pressure distributions are nearly identical between Figure 3.5 and Figure 3.9, implying that the spanwise-averaged  $Cp_e$  does not alter the mean  $Cp_i$  due to the fact that mean pressures are one-dimensional, as demonstrated in Chapter 2. However, the RMS pressure distributions, as shown in Fig 3.10a, are dramatically shifted, approximately overlying on the experimental results. The numerical RMS values obtained from the spanwise-averaged  $Cp_e$  are smaller than those from local (point) external pressures, indicating that fluctuating components of the local  $Cp_e$  are attenuated during area-averaging, i.e., the simulated interior pressures are not affected by the highly fluctuating local external pressures. Thus, the cavity flow is able to resist changes due to the short duration local of external pressure fluctuations and the  $Cp_i$  depend on the combination of the spanwise  $Cp_e$  values, which results in eliminating sharp peaks in the time history of the interior pressures. As a result, the numerical model better captures  $\tilde{Cp}_i$  for larger  $H$  (or smaller  $G/H$  values), as depicted in Figure 3.10. However, as expected, the numerical results are not always better using the spanwise-averaged  $Cp_e$  when  $G/H$  is larger. In particular, it becomes worse for the configuration of  $G = 15$  mm and  $H = 1.2$  mm, indicating that the spanwise-averaged  $Cp_e$  (from the three pressure tap locations) is not appropriate for this large  $G/H$  and, thus,  $Cp_e$  should be spanwise-averaged over a narrower section. To evaluate this further, higher external pressure tap resolution would be required, which is not available from the current wind tunnel data. Figure 3.11 shows the ratio of the numerical to experimental results, analogous to Figure 3.7, confirmed the improved accuracy for the fluctuations using the spanwise-averaged  $Cp_e$ , as the input for these simulations.

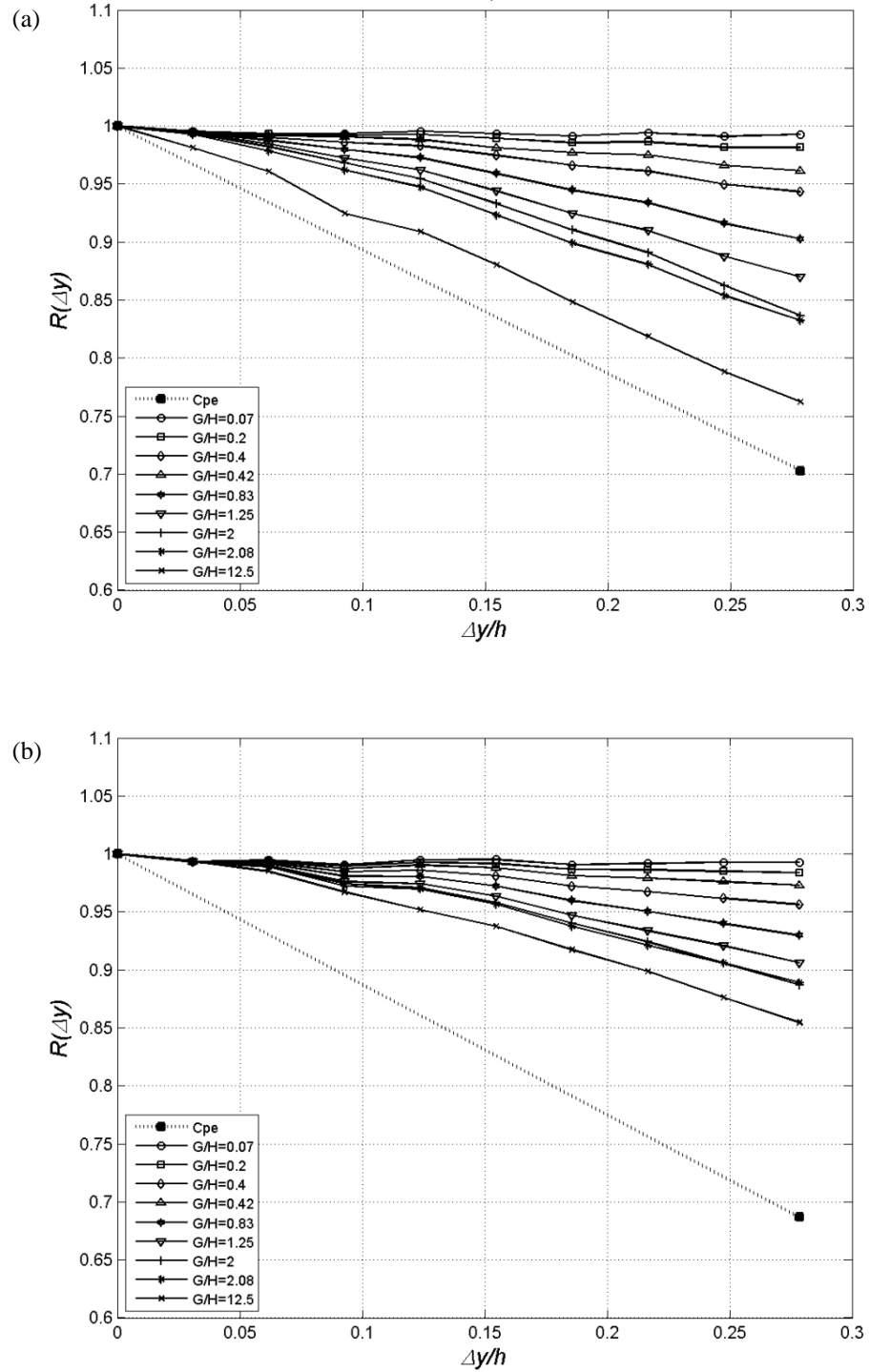


Figure 3.8 Correlation of pressure data in the y-direction with respect to the pressure tap in the middle row: (a) along the gap between Panels 1 and 2 (i.e.,  $G_2$ ); and (b) along the midplane of Panel 2. Straight lines are used to connect data points, for clarity only.

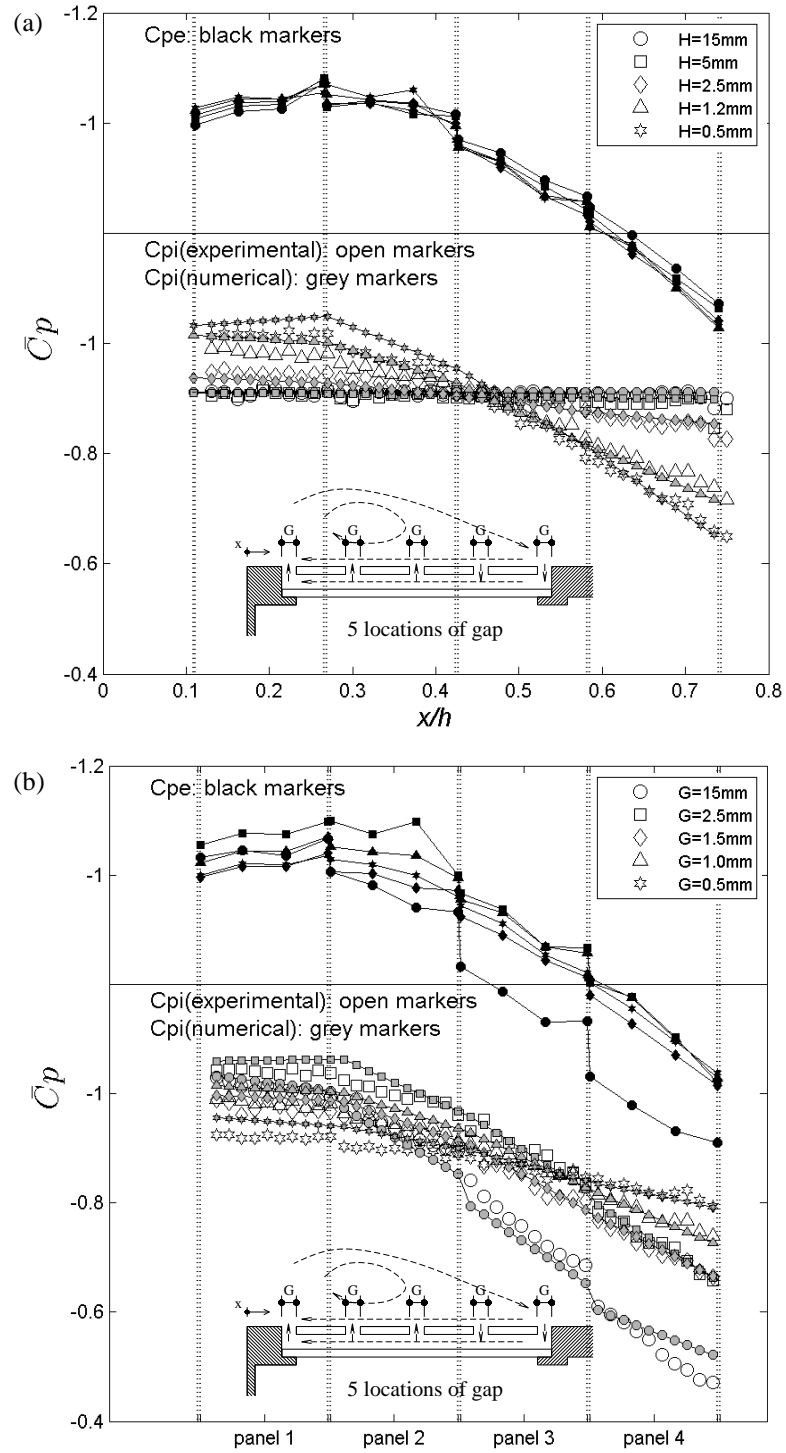


Figure 3.9 Mean pressure distributions for the pressure taps in the middle row with numerical simulation from the average external pressure coefficients: (a)  $G = 1$  mm with  $H$  variations; and (b)  $H = 1.2$  mm and with  $G$  variations.

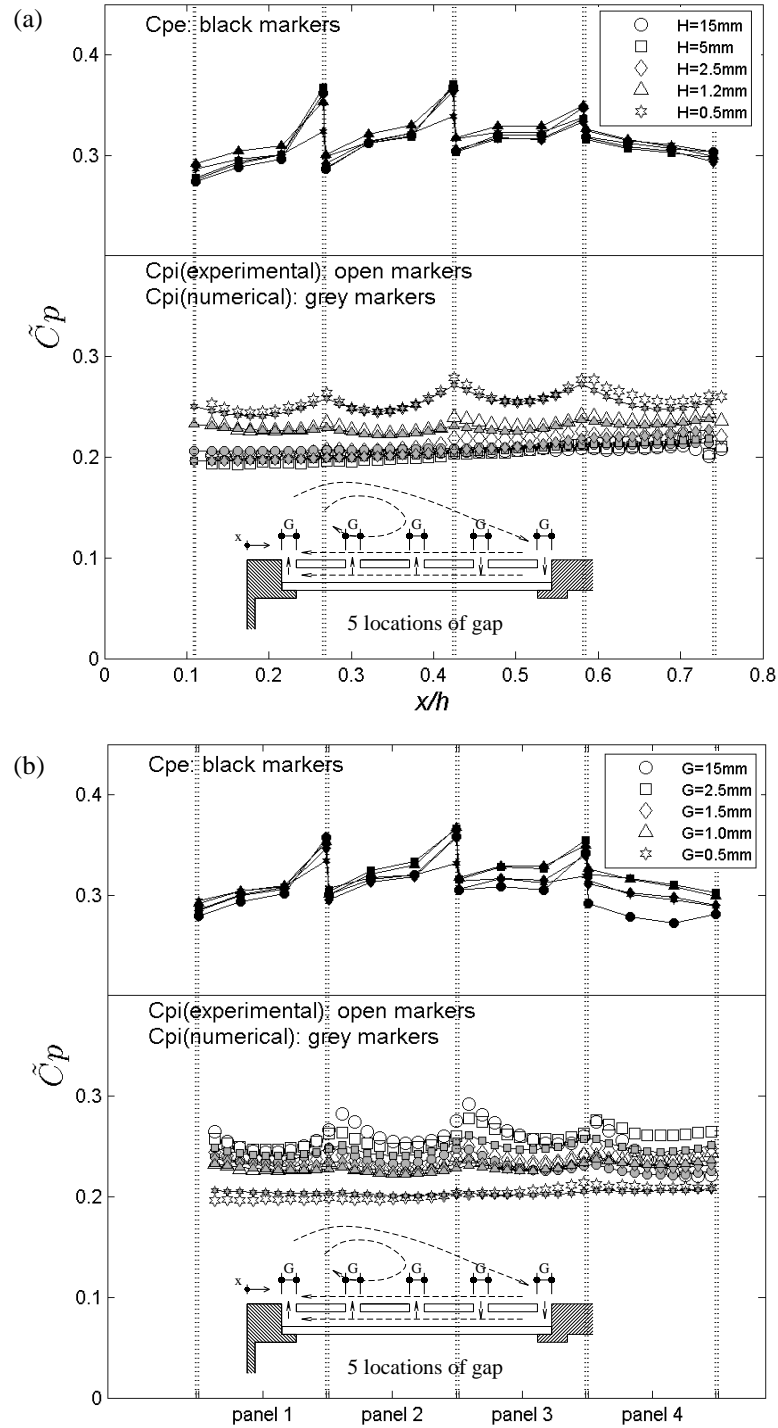
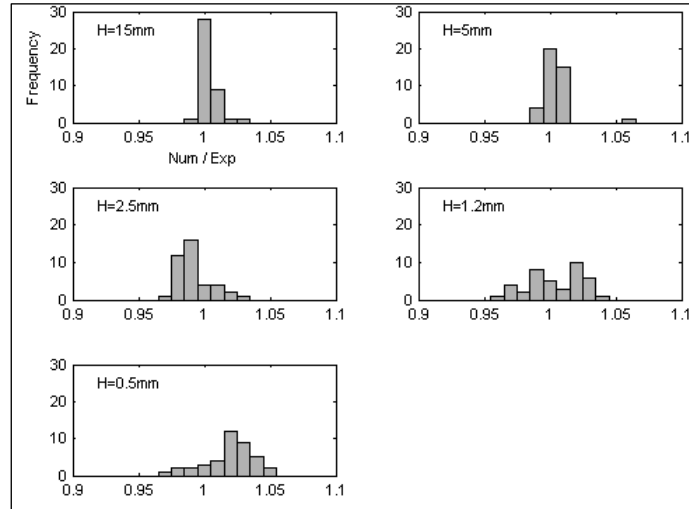
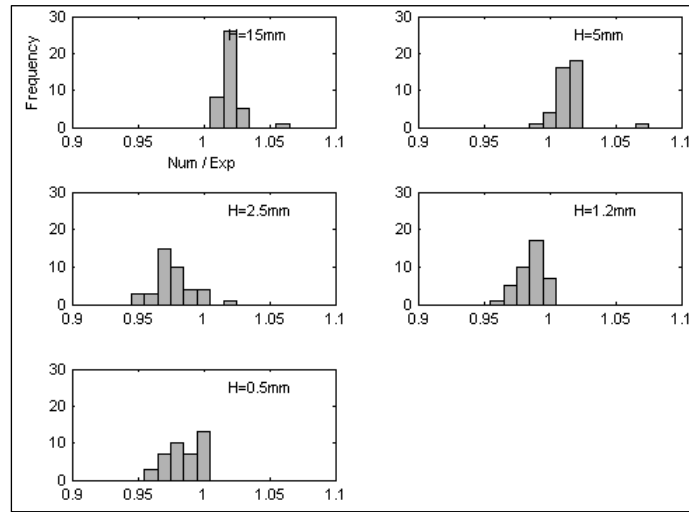


Figure 3.10 RMS pressure distributions for the pressure taps in the middle row with numerical simulation from the average external pressure coefficients: (a)  $G = 1$  mm with  $H$  variations; and (b)  $H = 1.2$  mm and with  $G$  variations.





(a)



(b)

Figure 3.11 Distribution of the ratio of the numerical to the experimental results of  $C_{pi}$  for  $G = 1 \text{ mm}$  with  $H$  variations (numerical simulation from the average external pressure coefficients): (a) mean; and (b) RMS.

### 3.4.4 Peak pressures

Figure 3.12 illustrates instantaneous local pressure coefficient distributions of  $Cp_e$  and  $Cp_i$  at the time when the pressure tap near the second gap ( $G_2$ ) on the second panel is at its peak (minimum) value. Figure 3.12a depicts both  $Cp_e$  and  $Cp_i$  for the numerical and experimental results with  $G = 1$  mm and  $H = 15$  mm and 5 mm using the spanwise-averaged  $Cp_e$  for the input to the simulation. As shown in the figure, the  $Cp_e$  at the gaps vary from 0 to -3 for  $H = 15$  mm, while the experimentally measured  $Cp_i$  is nearly uniform. The numerical model captures the instantaneous pressure distributions of  $Cp_i$ , which is represented by grey markers. It is similar for  $H = 5$  mm but the discrepancy between the numerical and experimental coefficients is slightly greater.

When  $H$  becomes smaller, e.g.,  $H$  of 2.5 mm and 1.2 mm, as shown in Figure 3.12b, the instantaneous  $Cp_i$  are not uniform, but are rather piecewise linearly distributed. The numerical simulation captures the shape of this, although the experimental coefficients are not varying in a perfectly linear manner. For an even smaller  $H$ , e.g.,  $H = 0.5$  mm, as shown in Figure 3.12c, the instantaneous  $Cp_i$  tend to follow the  $Cp_e$  at the gaps. There seems no significant pressure drop for the flow through the gap at the first, third, fourth and fifth gaps ( $G_1$ ,  $G_3$ ,  $G_4$ , and  $G_5$ ). However, the  $Cp_e$  at the second gap ( $G_2$ ) is significantly attenuated from -2.3 to -1.3. The numerical results for these configurations are not as accurate when compared to those for smaller  $G/H$ , as discussed above. The model does not fully capture the attenuation at the second gap while it over or underestimates instantaneous  $Cp_i$  at the other gaps. It is thought that one could improve the accuracy by area-averaging  $Cp_e$  over a narrower span for large  $G/H$  ratios. Further experimental and analytical work would be required to assess this since it is possible that the current model would not be able to fully capture a “sudden” pressure drop during a peak of the local external pressure that may be caused by “unsteady” effects, as discussed in Chapter 2.

Figure 3.13 depicts minimum peak distributions of the cavity pressure coefficients, comparing between the numerical and experimental results. There are several distinct points that arise when examining the figures. The numerical model predicts the shape of

peak pressure distributions to a great extent, while the magnitudes of peak pressures gradually increase as  $G/H$  increases. For  $H = 15$  mm from Figure 3.13a and  $G = 0.5$  mm from Figure 3.13b, which are the lowest  $G/H$  in each figure, the agreement between the numerical and experimental peaks is excellent. However, with larger  $G/H$  values, the accuracy of the numerical prediction is not good as that for smaller  $G/H$ . In particular, for  $G = 15$  mm from Figure 3.13b, the error reaches about 25 % of the peak value. Using the single (local)  $Cp_e$  in the simulation partially improves this accuracy, as presented in Figure 3.13b by black markers for  $G = 15$  mm. Thus, the spanwise averaging works well for these one-dimensional flow fields for  $G/H < \sim 2$  (for this particular panel size). Further work is required to fully assess these boundaries, as well as impacts of two-dimensional cavity flow.

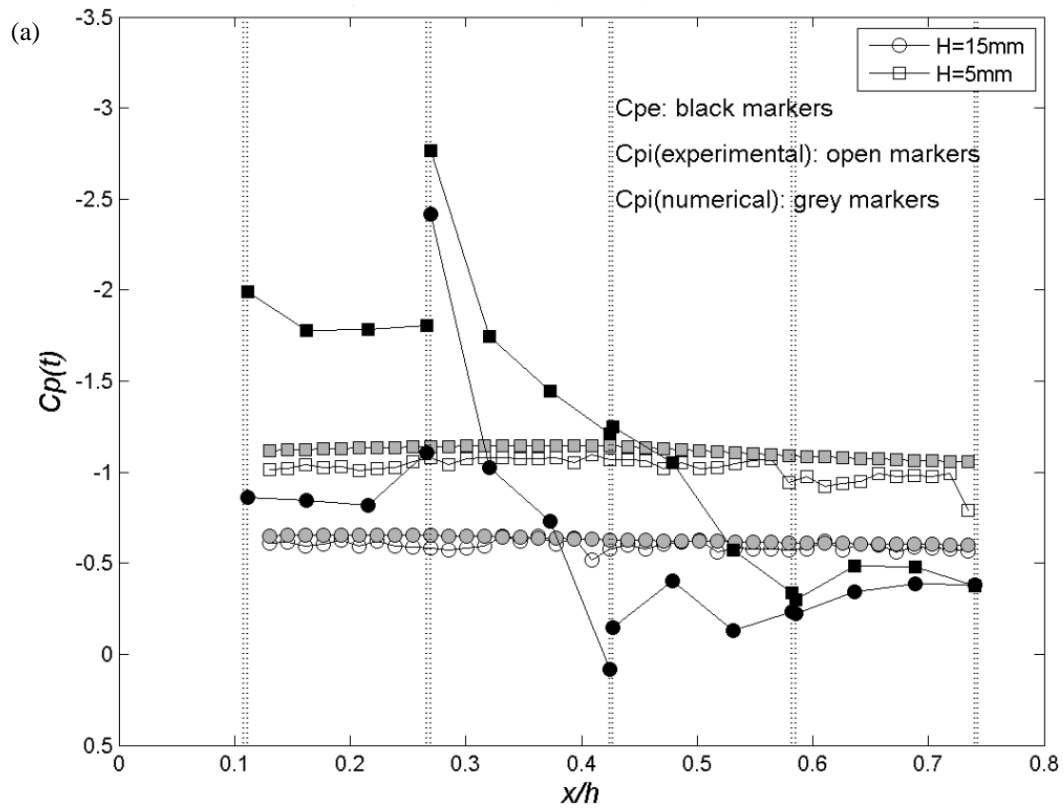


Figure 3.12 Instantaneous pressure distributions for the pressure taps in the middle row with numerical simulation from the average external pressure coefficients for  $G = 1$  mm with  $H$  variations: (a)  $H = 15$  mm and 5 mm; (a)  $H = 2.5$  mm and 1.2 mm; and (c)  $H = 0.5$  mm.

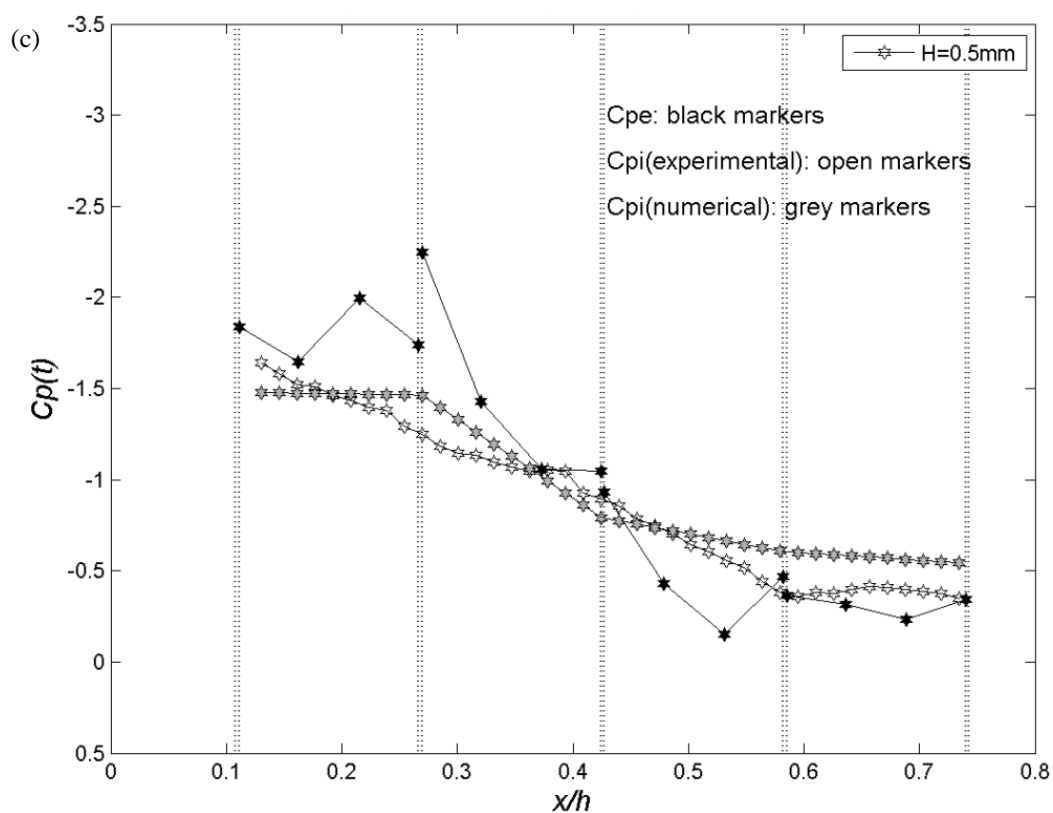
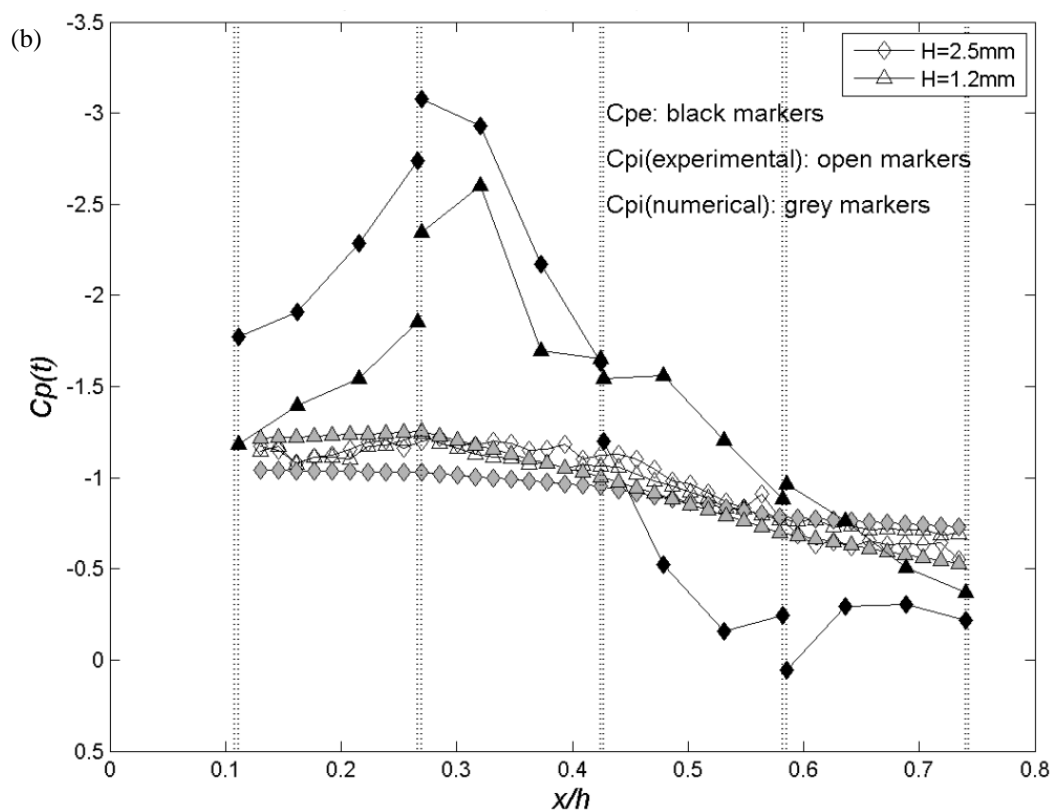


Figure 3.12: continued.

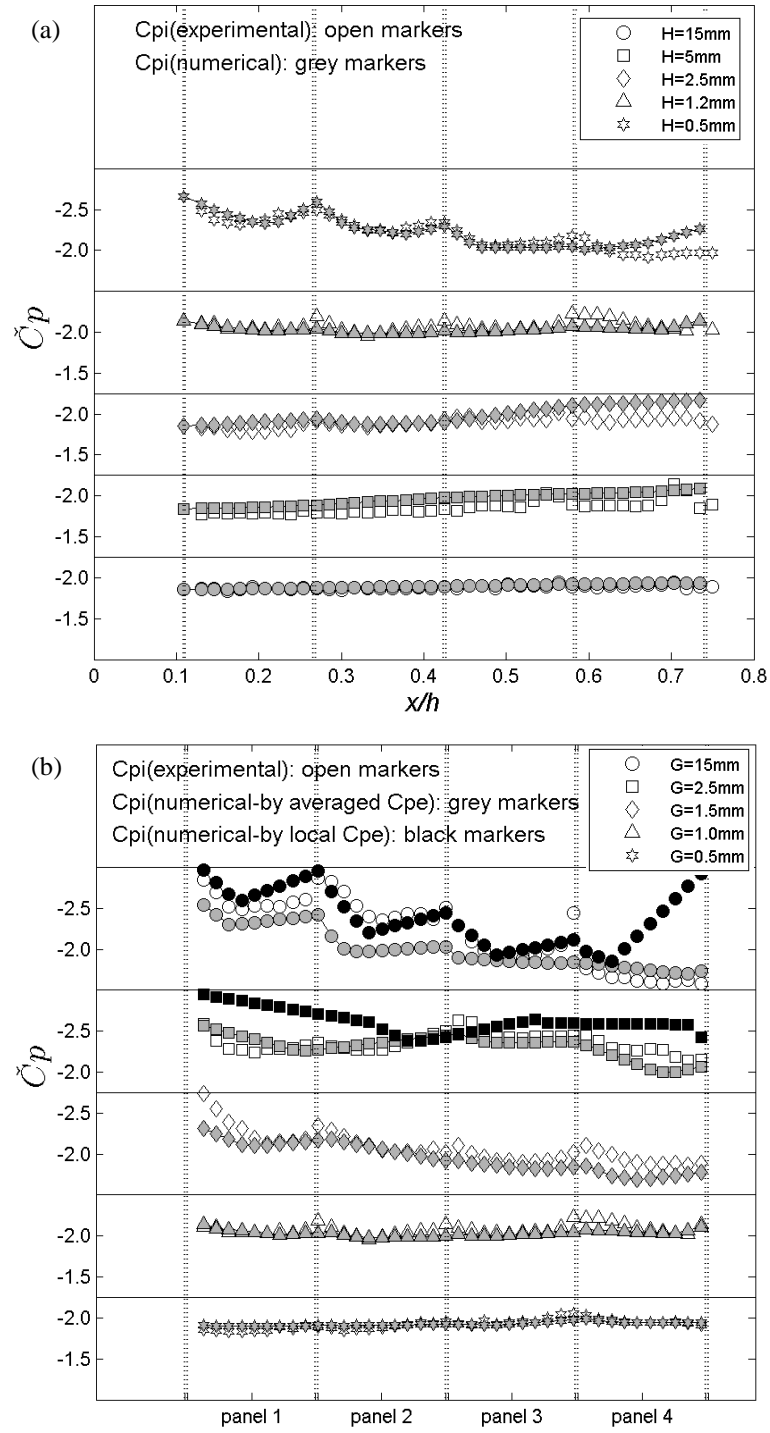


Figure 3.13 Peak (minima) pressure distributions for the pressure taps in the middle row with numerical simulation from the average external pressure coefficients: (a)  $G = 1$  mm with  $H$  variations; and (b)  $H = 1.2$  mm and with  $G$  variations.

### 3.5 Numerical Simulations from $Cp_e$ using Bare Roof Data

In the previous section, the numerical model exhibited good prediction of  $Cp_i$  from external pressure data on the gaps where the gaps actually existed on the wind tunnel model. In this section, an external pressure time history measured without the presence of the gaps (i.e., similar to a bare, single layer roof) is applied to the numerical model and the numerical results are validated with experimental results which are obtained with the presence of the multi-layer system. In this case, time-histories cannot be directly compared; however, statistical results can be examined. The configuration of  $G = 0$  mm and  $H = 0$  mm from the current wind tunnel data set presented in Chapter 2 is chosen to be the external pressure data for the simulation because this configuration is most similar to a bare roof case.

The results are depicted in Figure 3.14 with mean and RMS pressure distributions shown for  $H$  variations with  $G = 1$  mm.  $Cp_e$  data are depicted in the upper part of the plots, with the numerical results represented by the grey markers, plotted at the lower part of the figure when  $H$  varies. It should be noted that  $H$  is the only variable in the numerical model to be varied to determine the mean and RMS distributions of  $Cp_i$ . Comparing with the experimental results, the numerical predictions are very similar to those simulated from  $Cp_e$  with the presence of the gaps as shown in the plots in Figs 3.9a and 3.10a. Thus, this result indicates that similar mean and RMS cavity pressure coefficients can be obtained from  $Cp_e$  on a bare (single layer) roof.

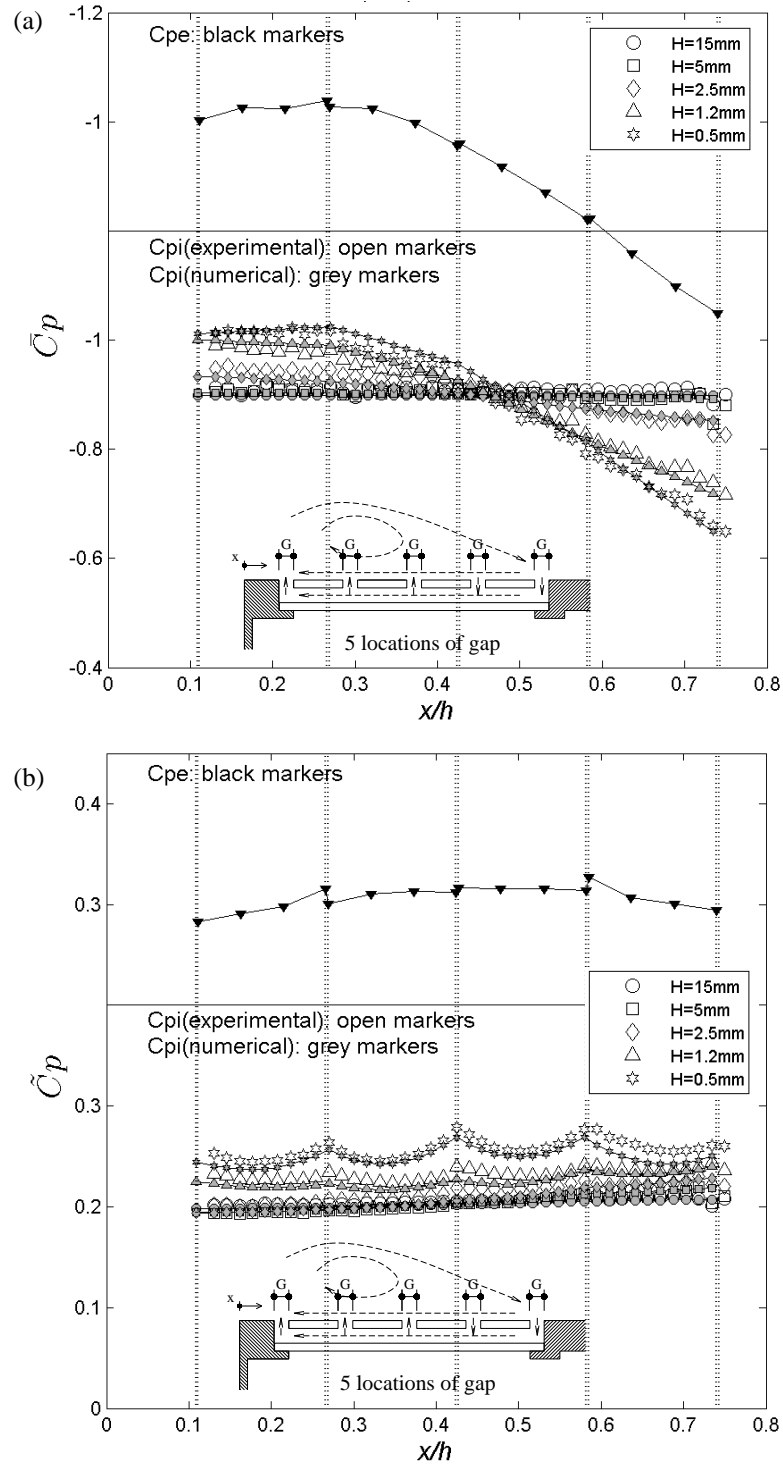


Figure 3.14 Pressure distributions of the numerical results from the average external pressure data with  $G = 0$  mm and  $H = 0$  mm: (a) mean; and (b) RMS for  $G = 1$  mm with  $H$  variations.

### 3.6 Contributions of the Terms in the Analytical Model

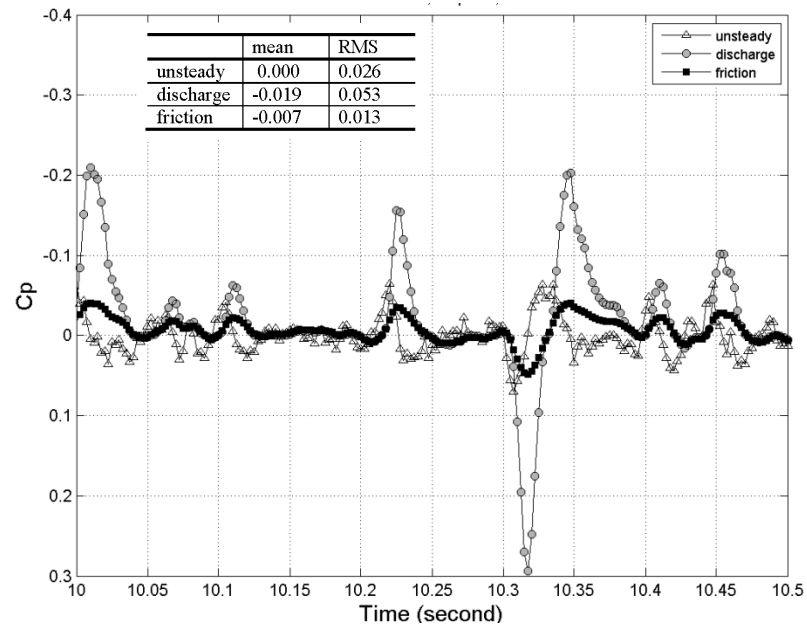
The analytical model in Eq. (3.14) consists of three different terms describing the pressure losses by the unsteady, discharge and friction effects for the one-dimensional flow through a double-layer system. Thus, the sum of pressure drops from unsteady, discharge and friction terms at the 2<sup>nd</sup> gap ( $G_2$ ) is equal to  $\Delta Cp = Cp_{e2} - Cp_{i2}$ , whereas those from unsteady and friction terms within the second cavity is identical to  $\Delta Cp = Cp_{i2} - Cp_{i3}$ . The unsteady terms are the first terms in Eqs. (3.14a – 3.14i) and the discharge terms are the second terms in Eqs. (3.14a; 3.14c; 3.14e, 3.14g; 3.14i), while the friction terms are the third terms in Eqs. (3.14a; 3.14c; 3.14e, 3.14g; 3.14i) and the second terms in Eq. (3.14b; 3.14d; 3.14f; 3.14h). Variations of the three terms to pressure drops through the second gap ( $G_2$ ), and in the cavity beneath the second panel, is presented in Figure 3.15 for  $G = 1.5$  mm,  $H = 1.2$  mm. Figure 3.15a illustrates time series, mean and RMS values of pressure drops through the gap, while Figure 3.15b shows pressures drops through the cavity below the second panel. Several observations can be drawn from the figures.

As expected, the mean pressure drops by the unsteady terms are zero, as shown in the tables within the Figure 3.15. Thus, the mean pressure drops through the gap and the cavity are governed by the discharge and friction terms. The mean pressure drop by the friction through the gap is about 25 % of the discharge loss at the gap, which is significant, especially considering the small length of the gap (i.e.,  $l_o = 8$  mm) relative to the panel (i.e.,  $L = 50$  mm). Comparing mean flows between the gap (Figure 3.15a) and the cavity (Figure 3.15b), 74 % of total mean pressure loss occurs by the friction in the cavity for this  $G/H$  ratio. The unsteady term plays a role in the pressure drop when the pressures are fluctuating as RMS values show.

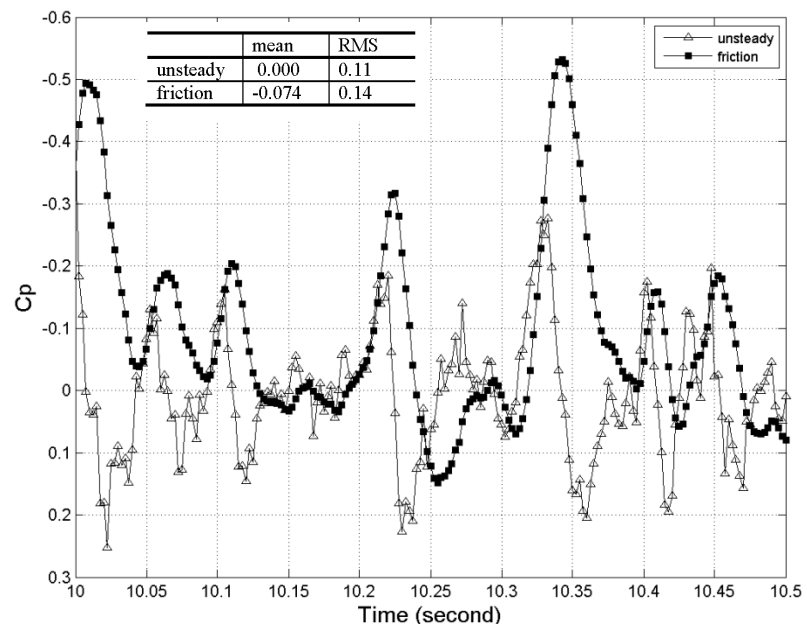
In the time series plots, it is observed that, again, the discharge term at the gap and the friction term in the cavity govern the pressure drop. The segments of the time series in Figure 3.15 were arbitrary chosen. For the gap flow, depicted in Figure 3.15a, the friction term acts in the same direction as the discharge term, following the wave of the discharge term. These two terms damp the external pressure, resulting in a larger  $\Delta Cp$ . However,



the unsteady term does not always act in the same direction with the discharge and friction terms. The unsteady term also contributes the pressure drop when it acts in the same direction (e.g.,  $t = \sim 10.22$  seconds). However, when the magnitude of the unsteady term is larger (e.g.,  $t = \sim 10.03$  seconds) than that from the discharge and friction and its direction is opposite, the pressure is increasing (rather than dropping) through the gap by the inertia effect, which implies that  $Cp_i$  could be larger than  $Cp_e$  at that moment. Therefore, the results indicate that the discharge effect at the gap flow and the friction in the cavity flow are the main cause of the pressure drop. However, the unsteady term plays a role in determining fluctuating and peak pressures.



(a)



(b)

Figure 3.15 Time series, mean and RMS values of pressure drops by the unsteady, discharge and friction terms in the analytical model for  $G = 1.5$  mm and  $H = 1.2$  mm: (a) pressure drop through the gap ( $G_2$ ); and (b) pressure drop through the cavity in Panel 2.

### 3.7 Conclusions

This chapter describes the development of a one-dimensional analytical model to simulate pressure distributions within a double-layer roof system, along with its validation by comparing with wind tunnel data. The numerical model is derived from the unsteady Bernoulli equation and the equation for the flow between parallel plates (Couette flow) assuming laminar flow in the cavity. The approach for the numerical model requires as input the external pressure time histories at the openings so that the cavity (interior) pressure time histories can be obtained. The numerical simulations were conducted with two different approaches using the external pressure time histories at the gaps as the input: (i)  $Cp_e(t)$  from point pressure taps along the middle row, and (ii) spanwise-averaged  $Cp_e(t)$ . The numerical results obtained by using the point pressure  $Cp_e(t)$  are compared with  $Cp_i(t)$  obtained from experiments in plots of time history, spectra and distributions of mean and RMS pressure coefficients. The results indicate that the numerical model captures the variations of the pressure distribution of  $Cp_i$ , although there are some discrepancies (i.e., about  $\pm 5$  % for mean and  $+5 \sim +15$  % for RMS) in magnitude. The bias in RMS values was found to be due to the use of point external pressures as the input, which may not perfectly represent the driving force for the cavity flow in the numerical computations. The analysis of the spanwise correlation of pressure data shows that, depending on  $G/H$ , the spanwise  $Cp_i$  are closely correlated, indicating that  $Cp_i$  depends on the spanwise-averaged  $Cp_e$  values, instead of following a single  $Cp_e$ . Results from numerical simulation by employing the spanwise-averaged  $Cp_e$  indicate that the pressure distributions of both the mean and RMS  $Cp_i$  are within a range of numerical error of about  $\pm 5$  % (when  $G/H < \sim 2$  for the panel size examined herein). This implies that the spanwise-averaged  $Cp_e$  does not alter the mean  $Cp_i$  due to the fact that mean flow is two-dimensional. However, the numerical RMS values are decreased and much closer to the experimental results, which means that fluctuating components of the local  $Cp_e$  are attenuated during area-averaging and that the simulated cavity pressures are not affected by the highly fluctuating, but localized, external pressures. As a result, the numerical model better captures  $\tilde{Cp}_i$ , especially for larger  $H$  (or smaller  $G/H$  values).

Minimum peak distributions of the cavity pressure coefficients are compared between the numerical and experimental results, as well as instantaneous local pressure coefficient distributions. The numerical simulation results using the spanwise-averaged  $Cp_e$  for the input indicate that the numerical model is able to predict the shape of peak and instantaneous pressure distributions except for relatively large  $G/H$  (e.g.,  $G = 15\text{mm}$  and  $H = 1.2\text{mm}$ ) while the magnitudes of peak pressures gradually increase as  $G/H$  increases. However, with larger  $G/H$  values, the accuracy of the numerical prediction is not as good as that for smaller  $G/H$ . The current work indicates that the spanwise averaging works well for these two-dimensional flow fields when  $G/H < \sim 2$  (for this particular panel size).

The numerical computations from two different  $Cp_e$  data sets were compared, one with and the other without the presence of the gaps and cavities. The numerical predictions were found to be very similar, indicating that experiments conducted without panels may be used to estimate the cavity pressures and net panel wind loads.

Variations of the unsteady, discharge and friction terms in the analytical model to pressure drops through the second gap ( $G_2$ ) and in the cavity underneath the second panel were investigated with the mean and RMS values and the time history plots for  $G = 1.5\text{ mm}$ ,  $H = 1.2\text{ mm}$ . The results indicate that the discharge effect at the gap flow and the friction in the cavity flow are the main cause of the pressure drop. However, the unsteady term plays a role in determining fluctuating and peak pressures.

## Reference

Amano, T., Fujii, K. and Tazaki, S. (1988). Wind loads on permeable roof-blocks in roof insulation systems. *Journal of Wind Engineering and Industrial Aerodynamics*, 29: 39-48.

- Bhangoo, A. (2013). A study of the ill-defined parameters of the internal pressure dynamics of a low-rise building. *Master Thesis*, University of Auckland, New Zealand, 2013.
- Bienkiewicz, B. and Endo, M. (2009). Wind considerations for loose-laid and photovoltaic roofing systems. *Proceedings of the 2009 Structures Congress*, Austin, Texas, April 30-May 2, 2009, pp. 2578-2587.
- Bienkiewicz, B. and Sun, Y. (1992). Wind-tunnel study of wind loading on loose-laid roofing systems. *Journal of Wind Engineering and Industrial Aerodynamics*, 41-44: 1817-1828.
- Bienkiewicz, B. and Sun, Y. (1997). Wind loading and resistance of loose-laid roof paver systems. *Journal of Wind Engineering and Industrial Aerodynamics*, 77: 401-410.
- Chapra, S.C. and Canale, R.P. (2006). Numerical methods for engineers. 5<sup>th</sup> Edition, *McGraw-Hill*, pp. 632-634.
- Cope, A.D., Crandell, J.H., Johnston, D., Kochkin, V., Liu, Z., Stevig, L., and Reinhold, T.A. (2013). Wind Loads on Components of Multi-Layer Wall Systems with Air-Permeable Exterior Cladding. *Proceedings of ATC & SEI Conference on Advances in Hurricane Engineering*, Miami, Florida, October 24-26, 2012, pp. 238-257.
- Currie, I.G. (2003). Fundamental mechanics of fluids. 3<sup>rd</sup> Edition, *Marcel Dekker*, 2003.
- Holmes, J.D. (1979). Mean and fluctuating internal pressure induced by wind. *Proceedings of the 5<sup>th</sup> International Conference on Wind Engineering*, Colorado State University, Fort Collins, Colorado, USA, July, 1979, pp.435-450.

- Karava, P., Stathopoulos, T., and Athienitis, A.K. (2011). Airflow assessment in cross-ventilated buildings with operable façade elements. *Building and Environment*, 46: 266-279.
- Kim, P.Y. and Ginger, J.D. (2012). Discharge coefficients for a dominant opening in a building. *Proceedings of the 15<sup>th</sup> Australasian Wind Engineering Society Workshop*, Sydney, Australia, February 23-24, 2012.
- Kopp, G.A. (2014). Wind loads on Low-Profile, Tilted, Solar Arrays Placed on Large, Flat, Low-Rise Building Roofs. *Journal of Structural Engineering*, 140(2): 04013057.
- Oh, J.H. (2004). Wind-induced internal pressures in low-rise buildings. *Master Thesis*, The University of Western Ontario, Canada, 2004.
- Oh, J.H., Kopp, G.A., and Inculet, D. R. (2007). The UWO contribution to the NIST aerodynamic database for wind loads on low buildings: Part 3. Internal Pressures. *Journal of Wind Engineering and Industrial Aerodynamics*, 95: 755-779.
- Oosthuizen, P.H. and Naylor, D. (1999). Introduction to convective heat transfer analysis. *McGraw-Hill*, 1999.
- Potter, M.C., Wiggert, D.C. and Rmadan, B.H. (2012). Mechanics of fluids. 4<sup>th</sup> Edition, *Cengage Learning*, 2012.
- Sun, Y. and Bienkiewicz, B. (1993). Numerical simulation of pressure distributions underneath roofing paver systems. *Journal of Wind Engineering and Industrial Aerodynamics*, 46-47: 517-626.
- Trung, V.T., Tamura, Y. and Yoshida, A. (2010). Numerical computation for lower surface pressures on a porous sunshade roof cover sheet. *Proceedings of the 5<sup>th</sup>*

*International Symposium on Computational Wind Engineering*, Chapel Hill, North Carolina, USA, May 23-27, 2010.

Vickery, B.J. (1986). Gust factors for internal pressures in low-rise buildings. *Journal of Wind Engineering and Industrial Aerodynamics*, 23: 259-271.

## Chapter 4

### Pressure Distributions on Photovoltaic Arrays Mounted on Large Flat-Roofs: A Case Study

#### 4.1 Introduction

The solar energy industry has been growing rapidly (35-40% per year (Razykov *et al.*, 2011)), ranging from residential houses, commercial buildings, to solar farms. Wind is a critical issue for the design and maintenance of these light-weight structures. However, there has been little published research on this problem and codes of practice do not currently provide exclusive guidance, although some standards are emerging (e.g., NEN 7250:2013, SEAOC-PV2-2012 and AS/NZS5033:2012). ASCE 7-10 allows for reductions on design wind loads for air-permeable cladding (i.e., double-layer systems) if approved test data or the recognized literature demonstrate lower loads. However, there are still many assumptions and uncertainties to determine the wind loads for the design of solar panel system in practice. Recently, proprietary research has been conducted by Kopp *et al.* (2012), Banks (2013) and others to determine a wind load design procedure for photovoltaic arrays, covering a wide range of tilt angles, mounted on typical low-rise buildings. Although this research has provided invaluable experimental results, the detailed pressure distributions in the cavity on photovoltaic arrays have not been analyzed.

In this chapter, therefore, an investigation of (external and cavity) pressure distributions on 2° tilted photovoltaic panel arrays mounted on a large flat rooftop are discussed, with numerical results simulated from the analytical model which was developed in Chapter 3. The first objective of the study is to determine how accurately the analytical model predicts the interior pressure coefficients in the cavity ( $C_{pi}$ ) of the photovoltaic panels, applying it to a practical problem which consists of 12 photovoltaic rows spanning all roof zones from the separation point, to the reattachment point, and up to the leeward zone. One set of existing wind tunnel test data was selected for the current study, which was conducted by Kopp (2014). The current author did not contribute to the



model design and wind tunnel tests. As in Chapters 2 and 3, the current study again focuses on only one-dimensional pressure distributions for wind perpendicular to the photovoltaic panel array and building edges.

The second objective of the study is to demonstrate how this analytical model can be used as a tool to design compartments for pressure equalizing, double-layer systems. Effects of compartmentalization from different configurations in the photovoltaic array are examined numerically to investigate changes in the cavity pressures and eventually, in the upward net wind loads.

## 4.2 Non-Dimensional Form of Governing Equations

It is most common that the differential equations used to describe fluid flows are expressed in non-dimensional form (Potter et. al., 2012). It is noted that the dimension of each term in Eqs. 3.11 is pressure. The differential governing equations in Eqs. (3.11) can be non-dimensionalized by dividing the terms by the mean velocity pressure at roof height,  $\frac{1}{2}\rho\bar{V}_h^2$ , where  $\bar{V}_h$  is velocity at roof height of building, such that

$$\frac{2l_{e1}}{\bar{V}_h^2} \dot{U}_{g1} + \frac{C_{L1}}{\bar{V}_h^2} U_{g1} |U_{g1}| + \frac{24\nu l_{o1}}{\bar{V}_h^2 G_1^2} U_{g1} = C_{pe1} - C_{pi1} \quad (4.1a)$$

$$\frac{2L_1}{\bar{V}_h^2} \dot{U}_1 + \frac{24\nu L_1}{\bar{V}_h^2 H^2} U_1 = C_{pi1} - C_{pi2} \quad (4.1b)$$

$$\frac{2l_{e2}}{\bar{V}_h^2} \dot{U}_{g2} + \frac{C_{L2}}{\bar{V}_h^2} U_{g2} |U_{g2}| + \frac{24\nu l_{o2}}{\bar{V}_h^2 G_2^2} U_{g2} = C_{pe2} - C_{pi2} \quad (4.1c)$$

where  $U_g$  is the average velocity through the gap ( $G$ ) between adjacent panels,  $U$  is the average velocity per unit width in the cavity between the panel and the inner surface, and  $C_p$  is the pressure coefficient,  $\frac{P}{\frac{1}{2}\rho\bar{V}_h^2}$ . The subscripts, 1 and 2, denote the number of the location of the gaps as depicted in Figure 3.1a. It should be noted that  $U_g$ ,  $U$ , and  $C_p$  are a function of time but the expression of ( $t$ ) is omitted in the equations for simplicity.

Eqs. (4.1) can be re-written, when applying the continuity equations ( $G_1 U_{g1} = H U_1 = -G_2 U_{g2}$ ) for incompressible flow, such that

$$\frac{2l_{e1}}{\bar{V}_h^2} \frac{H}{G_1} \dot{U}_1 + \frac{C_{L1}}{\bar{V}_h^2} \left(\frac{H}{G_1}\right)^2 U_1 |U_1| + \frac{24\nu l_{o1} H}{\bar{V}_h^2 G_1^3} U_1 = C_{pe1} - C_{pi1} \quad (4.2a)$$

$$\frac{2L_1}{\bar{V}_h^2} \dot{U}_1 + \frac{24\nu L_1}{\bar{V}_h^2 H^2} U_1 = C_{pi1} - C_{pi2} \quad (4.2b)$$

$$\frac{2l_{e2}}{\bar{V}_h^2} \frac{H}{G_2} \dot{U}_1 + \frac{C_{L2}}{\bar{V}_h^2} \left(\frac{H}{G_2}\right)^2 U_1 |U_1| + \frac{24\nu l_{o2} H}{\bar{V}_h^2 G_2^3} U_1 = C_{pe2} - C_{pi2} \quad (4.2c)$$

In order to further investigate non-dimensional parameters, Eqs. (4.2) are rearranged as:

$$2 \left(\frac{H}{G_1}\right) \frac{d\left(\frac{U_1}{\bar{V}_h}\right)}{dt^*} + C_{L1} \left(\frac{H}{G_1}\right)^2 \left(\frac{U_1}{\bar{V}_h}\right) \left|\frac{U_1}{\bar{V}_h}\right| + 24 \left(\frac{1}{Re_{g1}}\right) \left(\frac{l_{o1}}{G_1}\right) \left(\frac{H}{G_1}\right)^2 \left(\frac{U_1}{\bar{V}_h}\right)^2 = C_{pe1} - C_{pi1} \quad (4.3a)$$

$$2 \left(\frac{L_1}{l_e}\right) \frac{d\left(\frac{U_1}{\bar{V}_h}\right)}{dt^*} + 24 \left(\frac{1}{Re_{i1}}\right) \left(\frac{L_1}{H}\right) \left(\frac{U_1}{\bar{V}_h}\right)^2 = C_{pi1} - C_{pi2} \quad (4.3b)$$

$$2 \left(\frac{H}{G_2}\right) \frac{d\left(\frac{U_1}{\bar{V}_h}\right)}{dt^*} + C_{L2} \left(\frac{H}{G_2}\right)^2 \left(\frac{U_1}{\bar{V}_h}\right) \left|\frac{U_1}{\bar{V}_h}\right| + 24 \left(\frac{1}{Re_{g1}}\right) \left(\frac{l_{o2}}{G_2}\right) \left(\frac{H}{G_2}\right)^2 \left(\frac{U_1}{\bar{V}_h}\right)^2 = C_{pe2} - C_{pi2} \quad (4.3c)$$

where  $t^*$  is the non-dimensional time which is equal to  $\frac{t\bar{V}_h}{l_e}$ . All the dimensionless parameters in Eqs. (4.3) can be classified into five groups: (i) dimensionless length,  $L^*$ , (i.e.,  $\frac{H}{G}$ ,  $\frac{l_o}{G}$  and  $\frac{L}{H}$ ), (ii) dimensionless velocity,  $V^*$ , (i.e.,  $\frac{U}{\bar{V}_h}$ ), (iii) the Reynolds numbers (i.e.,  $Re_g = \frac{U_g G}{\nu}$  for the gap flow and  $Re_i = \frac{UH}{\nu}$  for the cavity flow), (iv) the loss coefficients,  $C_L$ , and (v) the pressure coefficients,  $C_{pe}$  and  $C_{pi}$ . The dimensionless length,  $L^*$ , are parameters which describe the geometry of double-layer system and play a role in determining the cavity pressure coefficient,  $C_{pi}$ , as the building geometry affect  $C_{pe}$ . The Reynolds numbers for the gap flow and the cavity flow appear at the friction terms in Eq. 4.3, which is actually part of the loss coefficients under the assumption of laminar flow. These Reynolds numbers affect the cavity pressures in a double-layer system as the Reynolds number of building ( $\frac{\bar{V}_h h}{\nu}$ ) does on the building aerodynamics.

Because of geometric similarity between model scale and full scale,  $\frac{L_m^*}{L_f^*} = 1$ , where  $m$  and  $f$  in subscripts denote the model and full scales. Similarly,  $\frac{V_m^*}{V_f^*} = 1$  due to the velocity ratio similarity between the model and full scales. Because the Reynolds numbers between model and full scales are different and the loss coefficients may also be different, the quantities of interior pressures,  $C_{pi}$ , on a double layer system, which are obtained in a model scale, could be different to those obtained in a full scale. However, the Reynolds number in the friction terms in Eq. 4.3 only arises because of the friction coefficient, i.e.,  $f = \frac{\text{constant}}{Re_i}$  for laminar flow. If the cavity flow in full scale is turbulent, the friction coefficient is less dependent on the Reynolds number so that the differences of the cavity pressure between model scale and full scale might not be significant. The investigation of the Reynolds number effects and the loss coefficients are not dealt with in this work and need to be examined in the future. Thus, in this chapter, the normalized, non-dimensional governing equations in Eqs. (4.2) are applied to the wind tunnel data, focusing on the model scale, in order to simulate one-dimensional flows in the cavity between the photovoltaic panel arrays and the roof surface.

## 4.3 Numerical Simulation Details

### 4.3.1 Numerical model

As described in Section 3.2.3, 13 discharge equations and 12 equations for the cavity flow are required to solve the problem with the 12 photovoltaic panel array as depicted in Figure 4.1, adding equations to Eqs. 4.1. Applying the Continuity equations for incompressible flows, using the sign convention in Figure 4.1 and 3.1,

$$G_1 U_{g1} = H U_1 \text{ for the side gap on the leading edge of the 1<sup>st</sup> row} \quad (4.4a)$$

$$G_2 U_{g2} = H(U_2 - U_1) \text{ for gap 1 as depicted in 4.1b} \quad (4.4b)$$

$$G_3 U_{g3} = H(U_3 - U_2) \text{ for gap 2 as depicted in 4.1b} \quad (4.4c)$$

⋮

$$G_{12}U_{g12} = H(U_{12} - U_{11}) \text{ for gap 11 as depicted in 4.1b} \quad (4.4d)$$

$$G_{13}U_{g13} = -HU_{12} \text{ for the side gap on the trailing edge of the 12}^{\text{th}} \text{ row} \quad (4.4e)$$

the analytical model for the flows through the thirteen gaps and twelve cavities becomes:

$$\frac{2l_{e1}}{\bar{V}_h^2} \frac{H}{G_1} \dot{U}_1 + \frac{C_{L1}}{\bar{V}_h^2} \left(\frac{H}{G_1}\right)^2 U_1 |U_1| + \frac{24vl_{o1}H}{\bar{V}_h^2 G_1^3} U_1 = C_{pe1} - C_{pi1} \quad (4.5a)$$

$$\frac{2L_1}{\bar{V}_h^2} \dot{U}_1 + \frac{24vL_1}{\bar{V}_h^2 H^2} U_1 = C_{pi1} - C_{pi2} \quad (4.5b)$$

$$\frac{2l_{e2}}{\bar{V}_h^2} \frac{H}{G_2} (\dot{U}_2 - \dot{U}_1) + \frac{C_{L2}}{\bar{V}_h^2} \left(\frac{H}{G_2}\right)^2 (U_2 - U_1) |U_2 - U_1| + \frac{24vl_{o2}H}{\bar{V}_h^2 G_2^3} (U_2 - U_1) = C_{pe2} - C_{pi2} \quad (4.5c)$$

$$\frac{2L_2}{\bar{V}_h^2} \dot{U}_2 + \frac{24vL_2}{\bar{V}_h^2 H^2} U_2 = C_{pi2} - C_{pi3} \quad (4.5d)$$

$$\frac{2l_{e3}}{\bar{V}_h^2} \frac{H}{G_3} (\dot{U}_3 - \dot{U}_2) + \frac{C_{L3}}{\bar{V}_h^2} \left(\frac{H}{G_3}\right)^2 (U_3 - U_2) |U_3 - U_2| + \frac{24vl_{o3}H}{\bar{V}_h^2 G_3^3} (U_3 - U_2) = C_{pe3} - C_{pi3} \quad (4.5e)$$

$$\frac{2L_3}{\bar{V}_h^2} \dot{U}_3 + \frac{24vL_3}{\bar{V}_h^2 H^2} U_3 = C_{pi3} - C_{pi4} \quad (4.5f)$$

⋮

$$\frac{2l_{e11}}{\bar{V}_h^2} \frac{H}{G_{11}} (\dot{U}_{11} - \dot{U}_{10}) + \frac{C_{L11}}{\bar{V}_h^2} \left(\frac{H}{G_{11}}\right)^2 (U_{11} - U_{10}) |U_{11} - U_{10}| + \frac{24vl_{o11}H}{\bar{V}_h^2 G_{11}^3} (U_{11} - U_{10}) = C_{pe11} - C_{pi11} \quad (4.5g)$$

$$\frac{2L_{11}}{\bar{V}_h^2} \dot{U}_{11} + \frac{24vL_{11}}{\bar{V}_h^2 H^2} U_{11} = C_{pi11} - C_{pi12} \quad (4.5h)$$

$$\frac{2l_{e12}}{\bar{V}_h^2} \frac{H}{G_{12}} (\dot{U}_{12} - \dot{U}_{11}) + \frac{C_{L12}}{\bar{V}_h^2} \left(\frac{H}{G_{12}}\right)^2 (U_{12} - U_{11}) |U_{12} - U_{11}| + \frac{24vl_{o12}H}{\bar{V}_h^2 G_{12}^3} (U_{12} - U_{11}) = C_{pe12} - C_{pi12} \quad (4.5i)$$

$$\frac{2L_{12}}{\bar{V}_h^2} \dot{U}_{12} + \frac{24vL_{12}}{\bar{V}_h^2 H^2} U_{12} = C_{pi12} - C_{pi13} \quad (4.5j)$$

$$\frac{2l_{e13}}{\bar{V}_h^2} \frac{H}{G_{13}} \dot{U}_{12} + \frac{C_{L13}}{\bar{V}_h^2} \left(\frac{H}{G_{13}}\right)^2 U_{12} |U_{12}| + \frac{24vl_{o13}H}{\bar{V}_h^2 G_{13}^3} U_{12} = C_{pe13} - C_{pi13} \quad (4.5k)$$

Again, the 2<sup>nd</sup> order, backward differencing, numerical scheme (Chapra and Canale, 2006) is applied to solve the 25 simultaneous differential equations in Eqs. 4.5, using a given set of time series data for the external pressures on the upper surfaces of the panel near the locations of the gaps. Details of the numerical method are provided in Appendix A. The effective length ( $l_e$ ), the loss coefficient ( $C_L$ ) and the kinematic viscosity of air ( $\nu$ ) used in the computations are the same as described in Table 3.1.

#### 4.3.2 Pressure model

The pressure model design and wind tunnel experiments on photovoltaic panel arrays mounted on a large flat rooftop were conducted in Boundary Layer Wind Tunnel II at the University of Western Ontario in 2009. The current author was not involved in any performance of tests but analyzed pressure data for this study. Results and experimental details concerning wind simulations (e.g., wind profiles, turbulent intensity and spectrum) are reported Kopp et al. (2012) and Kopp (2014). The geometry of the low-rise building, at a scale of 1:30, is shown in Figure 4.1a. The building has model-scale dimensions of 750 mm x 535 mm with a roof height of 245 mm. The model has 12 rows of photovoltaic modules. The photovoltaic modules are all tilted 2° towards the south, as shown in Figure 4.1b. The 2° tilt angle was neglected in the numerical analysis.

Figure 4.1b shows a plan view of the test building, as well as details of the photovoltaic panel dimension and pressure tap layout. Figure 4.2 shows photographs of the wind tunnel model. Each panel has a 33.5 mm panel length ( $L$ ) with a 3.76 mm gap ( $G$ ) between panels. The height ( $H$ ) of the panels above the roof surface is 3.5 mm, which is the mean value due to the tilted panel slope. The external pressure data used in this study were obtained from 36 pressure taps installed on the upper surface of each panel (432 pressure taps in total for all 12 photovoltaic rows), while the interior pressures in the cavity between the panel and the roof surface were obtained from 300 pressure taps placed on the roof surface, as shown in Figure 4.1b. There are no pressure taps representing external pressures for the openings located at the leading edge of the first panel and the trailing edge of the twelfth panel. Thus, the closest pressure taps located on

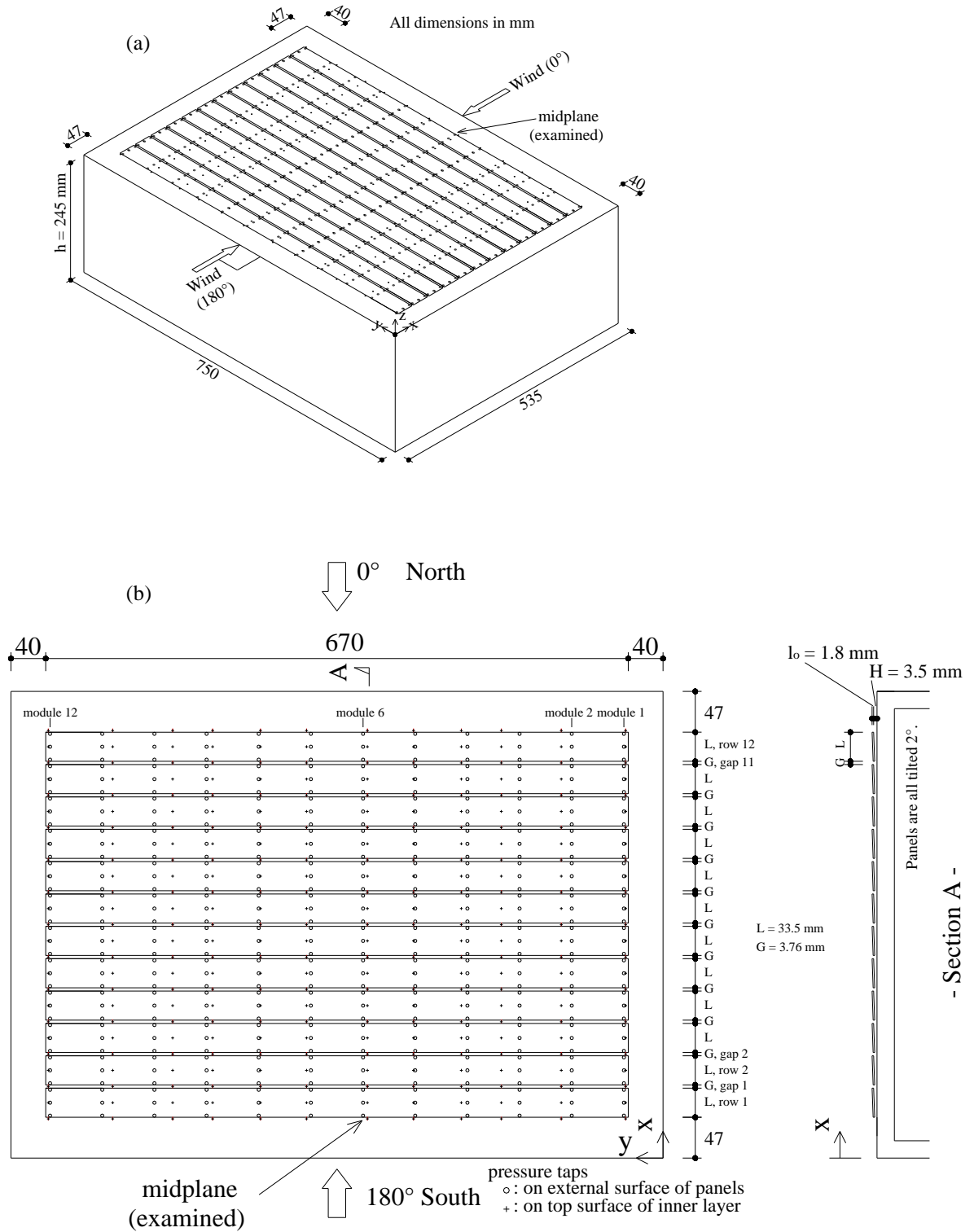
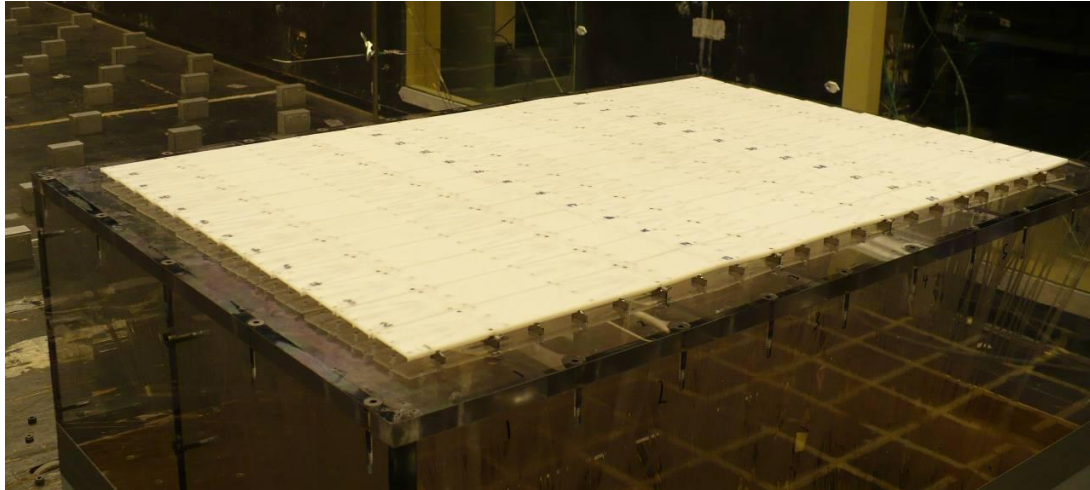


Figure 4.1 Wind tunnel model: (a) sketch of the building model with a photovoltaic panel array and definition of the coordinate system; (b) details of dimension and pressure tap layout, and photovoltaic module and row layout.



(a)



(b)

Figure 4.2 Pressure model photographs: (a) overview; (b) side view (photographs courtesy of Farquhar and Kopp, 2009).

the upper surface of the panels were used for numerical simulation as the next best option, although they did not capture exact aerodynamic behavior for these side openings.

### 4.3.3 Pressure measurements

The experiments were conducted with an open country terrain characterized by a roughness length,  $z_o$ , of 0.03m and at a roof height wind speed of approximately 11.6 m/s. The pressure data from all pressure taps were sampled at 400 Hz for 160 seconds, essentially simultaneously. The sampled data were digitally low-pass filtered at 200 Hz. Further details for pressure measurements can be found in Farquhar and Kopp (2009) and Kopp et al. (2012). All measured pressure coefficients were referenced to the mean velocity pressure ( $\frac{1}{2}\rho\bar{V}_{ref}^2$ ) at the reference height of about 1.4 m above the tunnel floor. Then, these were re-referenced to the mean velocity pressure at roof height,  $h = 245$  mm, such that

$$C_p = \frac{P_e - P_o}{\frac{1}{2}\rho\bar{V}_{ref}^2} \left( \frac{\bar{V}_{ref}}{\bar{V}_h} \right)^2 = \frac{P_e - P_o}{\frac{1}{2}\rho\bar{V}_h^2} \quad (4.5)$$

Only wind directions ( $0^\circ$  and  $180^\circ$ ) perpendicular to the leading edge of the roof, as shown in Figure 4.1a, are analyzed in this study because, like for Chapter 3, only one-dimensional pressure distributions are considered for the current analytical model.

## 4.4 Results and Comparison with Experimental Data

### 4.4.1 Spanwise correlation in mean two-dimensional flows

This study considers the approximately two-dimensional mean flows on the external surface of photovoltaic panels and the resulting, approximately one-dimensional mean pressures in the cavity between photovoltaic panels and roof surface. Such mean flows are achievable within the middle region of the roof where there is little influence of the side edges of the roof, as discussed in Section 2.3.1. However, the instantaneous turbulent flows are not two-dimensional, even though they are correlated along the span (in the y-



direction), as described in Section 3.4.3. The spanwise correlations of the external and cavity pressure data in the y-direction are assessed by Eq. 3.16 with respect to the pressure taps in the midplane (i.e., Module 6). Figure 4.3a shows the correlation coefficients of external pressure coefficient ( $C_{pe}$ ) data for the 11 different gaps (from gap 1 to gap 11) between photovoltaic panels, noting that the gap 1 is the closest to the leading edge of the roof for  $180^\circ$  wind. The degree of the correlation of  $C_{pe}$  is reduced with the distance ( $\Delta y$ ) from the midplane and the distance ( $x/h$ ) from the leading edge of the roof. This trend is similar to the results presented in Figure 3.8 and found in the literature (e.g., Matsumoto et al., 2003). Compared to the magnitude of the correlation coefficient (i.e.,  $R(\Delta y) \approx 0.7$  when  $\Delta y/h = 0.28$ ,  $x/h = 0.27$ ) of  $C_{pe}$  in Figure 3.8,  $R(\Delta y)$  from the first gap (gap 1, i.e., when  $\Delta y/h = 0.25$ ,  $x/h = 0.33$ ), as shown in Figure 4.3a, is about 0.76. This difference could be due to the measurement uncertainty, the different shape of panels mounted on the roof (one flush with roof and  $0^\circ$  tilt, and the other above the roof surface with  $2^\circ$  tilt), and the size of the buildings (noting that the ratio of the width to the roof height is  $w/h = 2.5$  in Figure 3.8 and  $w/h = 3$  in Figure 4.3a).

The degree of spanwise correlation of the cavity pressure ( $C_{pi}$ ) data is also reduced with  $\Delta y$  and  $x/h$ , as shown in Figure 4.3b. However, compared to the external pressures, the pressures in the cavity between the panels and the roof are more highly correlated. Comparing to the results presented in Figure 3.8,  $R(\Delta y) = 0.92$  from the first gap (gap 1, i.e., when  $\Delta y/h = 0.25$ ,  $x/h = 0.33$ ), as shown in Figure 4.3b, is slightly larger than  $R(\Delta y) = 0.87$  from  $G/H = 1.25$  in Figure 3.8a, which is the closest corresponding gap-to-height ratio. The correlation coefficients of  $C_{pi}$  drop up to 0.5 to 0.6 when  $\Delta y/h = 0.5$ , especially  $x/h > 1$  (where  $x/h \approx 1$  is approximately the reattachment point). Spanwise correlation coefficients for  $0^\circ$  wind are presented in Figure B.1 in Appendix B, which show similar trends as for the  $180^\circ$  wind. However, the cavity pressures for this wind appear to be slightly less correlated in the y-direction, in particular, at the gaps after the reattachment point.

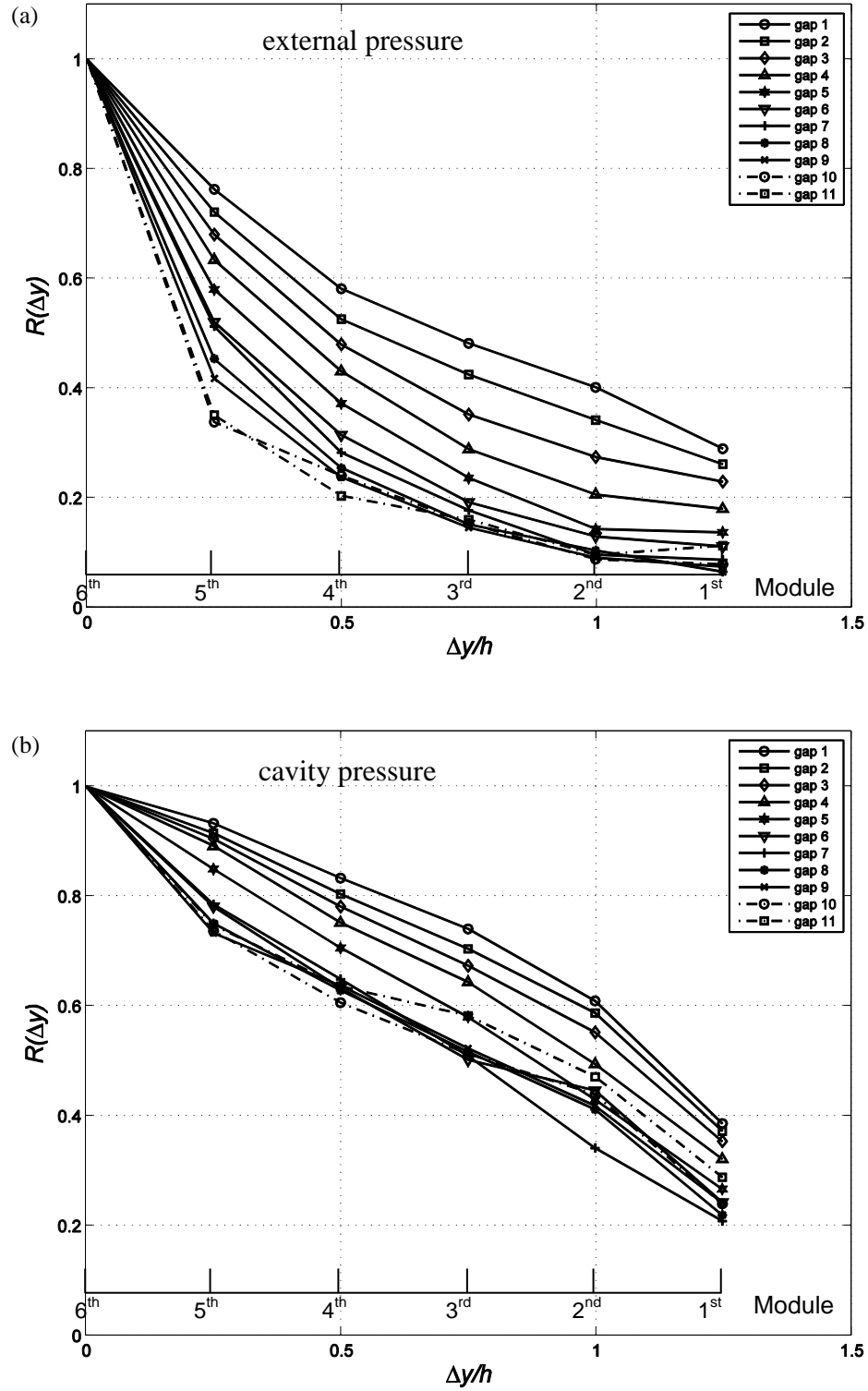


Figure 4.3 Correlation of pressure data in the y-direction with respect to the pressure taps in the midplane (i.e., Module 6), for 180° wind: (a)  $Cp_e$ ; (b)  $Cp_i$ . Straight lines are used to connect data points, for clarity only.

#### 4.4.2 Basic statistics of area-averaged pressures on photovoltaic panels

Time histories of point pressure coefficients in the cavity ( $Cp_i$ ) beneath the 12 photovoltaic panels along the midplane (i.e., Module 6) are simulated by solving the simultaneous differential equations (Eqs. 4.5) with time histories of spanwise-averaged  $Cp_e$  at the gaps between photovoltaic panels as input. The time histories of the point cavity pressure coefficients are, then, area-averaged from three taps which are allotted to each panel, in order to obtain time histories of  $Cp_i$  acting on each individual photovoltaic panel along the midplane. The time histories of the measured external pressure coefficients and the measured cavity pressure coefficients on the photovoltaic panels are also area-averaged in the same manner.

Mean, RMS and peak values of the time histories of the area-averaged cavity pressure coefficients obtained experimentally and numerically for  $180^\circ$  wind are summarized in Tables 4.1 to 4.3, along with of the measured external pressure coefficients. The mean pressure coefficients presented in Table 4.1 indicate a significant level of equalization between the measured  $\bar{Cp}_e$  and  $\bar{Cp}_i$ . The result is small net upward loads on panels (i.e., Module 6) in Rows 1 to 6 and small net downward loads in Rows 7 to 12, similar to the results discussed in the foregoing chapters. The numerically predicted  $\bar{Cp}_i$  were obtained using six different cases of spanwise-averaged  $Cp_e$  from a single tap, three taps (from Modules 5, 6 & 7), up to 12 pressure taps, in order to examine how spanwise-averaging, as input, alters the numerical results. The predicted  $\bar{Cp}_i$  from the six spanwise-averaged  $Cp_e$  are nearly identical due to the two-dimensional mean flow but they are slightly reduced when including input from the edges of the panels, such as Modules 1, 2, 10 and 12. Compared to the measured  $\bar{Cp}_i$ , the magnitudes of predicted  $\bar{Cp}_i$  are slightly higher, except for the 1<sup>st</sup> and 2<sup>nd</sup> rows.

The RMS pressure coefficients ( $\tilde{Cp}_i$ ) in the cavity, shown in Table 4.2, are dramatically attenuated, relative to the external pressure coefficients ( $\tilde{Cp}_e$ ). In contrast with the mean values, predicted  $\tilde{Cp}_i$  are significantly altered by the number of taps used for the input in the spanwise-averaged  $Cp_e$ . However, the magnitudes of predicted  $\tilde{Cp}_i$  are higher than those of measured  $\tilde{Cp}_i$ , especially, in rows near the reattachment point.

The differences between predicted and measured  $\tilde{C}p_i$  are decreased when the number of pressure taps for spanwise-averaged  $Cp_e$  are increased. The cells with grey in the table indicate that predicted  $\tilde{C}p_i$  are within  $\pm 5\%$  of the measured  $\tilde{C}p_i$ . Results for  $0^\circ$  wind presented in Tables B.1 to B.3 in Appendix B indicate similar tendency with those for  $180^\circ$  wind. However, the measured RMS pressure coefficients show smaller attenuations, perhaps due to effects of the tilt panel (noting that all panels tilt toward the south), implying that fluctuating pressures are transmitted in this slope of photovoltaic panels. The numerical model does not capture this because the effect of the tilt panel was not considered in numerical computations and thus, the predicted  $\tilde{C}p_i$  are similar to those for  $180^\circ$  wind. Similar to  $\tilde{C}p_i$ , the peak pressure coefficients ( $\check{C}p_i$ ) are also attenuated and altered by the number of pressure taps for spanwise-averaged  $Cp_e$ , as presented in Table 4.3.

The results suggest that to capture the RMS values within  $\pm 5\%$  of the measured values requires external pressure data from a span of 3 - 5 modules (i.e.,  $\Delta y/h \approx 1$ ), for  $180^\circ$  wind, at least for this size building and panels. For  $0^\circ$  wind, the span used for external pressure data is reduced to 1 - 3 modules because of effects of the tilt panels. However, for the peak values more modules are required with the full span. This indicates that unsteady effects on the loss coefficients may not be fully accounted for; a point which merits further investigation.

Table 4.1 Mean area-averaged pressures on Module 6 for 180° wind

| Row | Measured     |              | Numerical                                     |       |       |       |       |       |
|-----|--------------|--------------|---|-------|-------|-------|-------|-------|
|     | $\bar{C}p_e$ | $\bar{C}p_i$ | $\bar{C}p_i^*$                                |       |       |       |       |       |
|     |              |              | No. of taps for spanwise-averaged $Cp_e^{**}$ |       |       |       |       |       |
|     |              |              | 1   | 3     | 5     | 7     | 9     | 12    |
| 1   | -1.16        | -0.97        | -0.92   | -0.92 | -0.92 | -0.92 | -0.91 | -0.9  |
| 2   | -1.02        | -0.88        | -0.87   | -0.86 | -0.87 | -0.86 | -0.85 | -0.84 |
| 3   | -0.84        | -0.73        | -0.77   | -0.77 | -0.77 | -0.76 | -0.75 | -0.73 |
| 4   | -0.67        | -0.6         | -0.67   | -0.66 | -0.66 | -0.65 | -0.64 | -0.62 |
| 5   | -0.53        | -0.49        | -0.58   | -0.57 | -0.56 | -0.56 | -0.54 | -0.53 |
| 6   | -0.42        | -0.41        | -0.49   | -0.49 | -0.48 | -0.47 | -0.46 | -0.45 |
| 7   | -0.35        | -0.36        | -0.42   | -0.42 | -0.41 | -0.4  | -0.39 | -0.38 |
| 8   | -0.29        | -0.32        | -0.36   | -0.36 | -0.35 | -0.35 | -0.34 | -0.33 |
| 9   | -0.25        | -0.29        | -0.32   | -0.32 | -0.31 | -0.31 | -0.3  | -0.3  |
| 10  | -0.23        | -0.27        | -0.29   | -0.29 | -0.28 | -0.28 | -0.28 | -0.27 |
| 11  | -0.21        | -0.27        | -0.27   | -0.27 | -0.27 | -0.27 | -0.26 | -0.26 |
| 12  | -0.22        | -0.28        | -0.26   | -0.27 | -0.26 | -0.26 | -0.26 | -0.26 |

\*: Numerical  $Cp_i$  are calculated from six different cases of spanwise-averaged  $Cp_e$ .

\*\*: The numbers indicate the number of pressure taps used to obtain spanwise-averaged  $Cp_e$  which are input for numerical computations. (e.g., 1: tap from Module 6 only, 3: taps from Modules 5, 6 & 7, and 12: taps from all Modules from 1 to 12)

Table 4.2 RMS area-averaged pressures on Module 6 for 180° wind

| Row | Measured       |                | Numerical                                     |      |      |      |      |      |
|-----|----------------|----------------|---|------|------|------|------|------|
|     | $\tilde{C}p_e$ | $\tilde{C}p_i$ | $\tilde{C}p_i^*$                              |      |      |      |      |      |
|     |                |                | No. of taps for spanwise-averaged $Cp_e^{**}$ |      |      |      |      |      |
|     |                |                | 1   | 3    | 5    | 7    | 9    | 12   |
| 1   | 0.33           | 0.23           | 0.23  | 0.21 | 0.2  | 0.19 | 0.18 | 0.18 |
| 2   | 0.33           | 0.21           | 0.22  | 0.21 | 0.2  | 0.19 | 0.18 | 0.17 |
| 3   | 0.3            | 0.18           | 0.22  | 0.2  | 0.19 | 0.18 | 0.17 | 0.16 |
| 4   | 0.27           | 0.16           | 0.21  | 0.19 | 0.18 | 0.17 | 0.16 | 0.15 |
| 5   | 0.24           | 0.14           | 0.2   | 0.18 | 0.17 | 0.16 | 0.15 | 0.13 |
| 6   | 0.21           | 0.12           | 0.18  | 0.16 | 0.15 | 0.14 | 0.13 | 0.11 |
| 7   | 0.18           | 0.11           | 0.15  | 0.14 | 0.12 | 0.12 | 0.11 | 0.1  |
| 8   | 0.16           | 0.1            | 0.13  | 0.11 | 0.11 | 0.1  | 0.09 | 0.08 |
| 9   | 0.14           | 0.09           | 0.11  | 0.1  | 0.09 | 0.09 | 0.08 | 0.07 |
| 10  | 0.13           | 0.08           | 0.1   | 0.09 | 0.08 | 0.08 | 0.07 | 0.07 |
| 11  | 0.12           | 0.08           | 0.09  | 0.08 | 0.08 | 0.07 | 0.07 | 0.06 |
| 12  | 0.11           | 0.08           | 0.09  | 0.08 | 0.07 | 0.07 | 0.06 | 0.06 |

\*: Numerical  $Cp_i$  are calculated from six different cases of spanwise-averaged  $Cp_e$ .

\*\*: The numbers indicate the number of pressure taps used to obtain spanwise-averaged  $Cp_e$  which are input for numerical computations.

■ : indicates that numerical  $Cp_i$  are within  $\pm 5\%$  of the measured  $Cp_i$ .

Table 4.3 Peak (minimum) area-averaged pressures on Module 6 for 180° wind

| Row | Measured       |                | Numerical                                     |       |       |       |       |       |
|-----|----------------|----------------|---|-------|-------|-------|-------|-------|
|     | $\check{C}p_e$ | $\check{C}p_i$ | $\check{C}p_i^*$                              |       |       |       |       |       |
|     |                |                | No. of taps for spanwise-averaged $Cp_e^{**}$ |       |       |       |       |       |
|     |                |                | 1   | 3     | 5     | 7     | 9     | 12    |
| 1   | -3.08          | -2.25          | -1.99   | -1.86 | -1.81 | -1.71 | -1.68 | -1.64 |
| 2   | -2.73          | -1.81          | -1.82   | -1.72 | -1.71 | -1.64 | -1.6  | -1.56 |
| 3   | -2.48          | -1.54          | -1.75   | -1.62 | -1.59 | -1.51 | -1.5  | -1.47 |
| 4   | -2.1           | -1.36          | -1.82   | -1.52 | -1.44 | -1.43 | -1.44 | -1.39 |
| 5   | -1.91          | -1.16          | -1.69   | -1.61 | -1.48 | -1.43 | -1.35 | -1.32 |
| 6   | -1.9           | -1.02          | -1.72   | -1.45 | -1.41 | -1.35 | -1.25 | -1.14 |
| 7   | -1.56          | -1.01          | -1.37   | -1.34 | -1.28 | -1.22 | -1.14 | -0.98 |
| 8   | -1.59          | -0.89          | -1.38   | -1.22 | -1.14 | -1.08 | -0.99 | -0.86 |
| 9   | -1.32          | -0.82          | -1.25   | -1.15 | -1.06 | -0.93 | -0.86 | -0.74 |
| 10  | -0.99          | -0.74          | -1.12   | -1.02 | -0.93 | -0.82 | -0.77 | -0.64 |
| 11  | -1.01          | -0.68          | -0.91   | -0.84 | -0.8  | -0.75 | -0.7  | -0.6  |
| 12  | -0.96          | -0.69          | -0.95   | -0.79 | -0.75 | -0.71 | -0.66 | -0.55 |

\*: Numerical  $Cp_i$  are calculated from six different cases of spanwise-averaged  $Cp_e$ .

\*\* : The numbers indicate the number of pressure taps used to obtain spanwise-averaged  $Cp_e$  which are input for numerical computations.

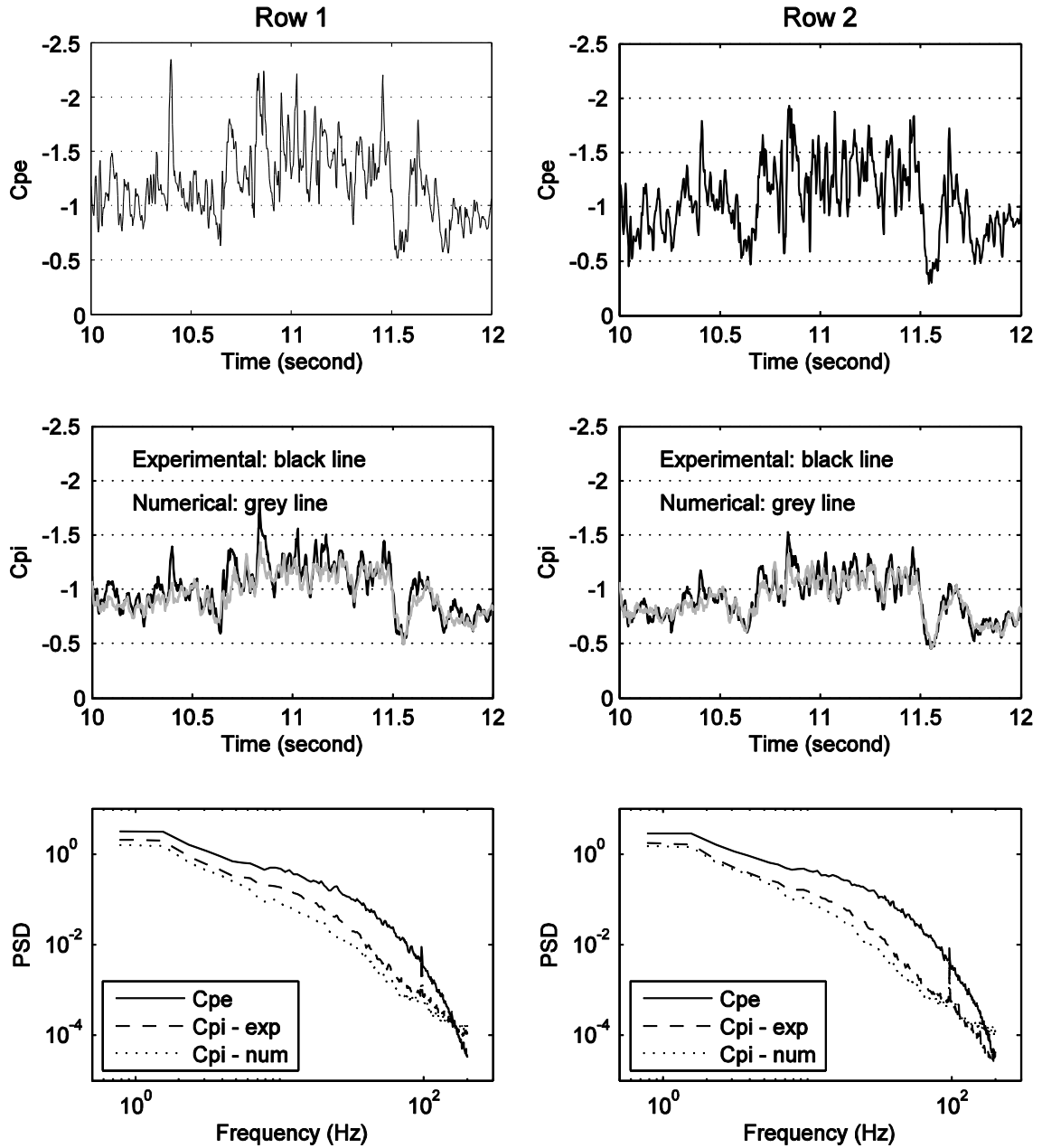
■ : indicates that numerical  $Cp_i$  are within  $\pm 5\%$  of the measured  $Cp_i$ .

#### 4.4.3 Time histories and spectra of area-averaged pressures on photovoltaic panels

Time histories of area-averaged external and interior pressures on the 12 different photovoltaic rows for 180° wind are shown in Figures 4.4. Segments of the time histories of 2 seconds (between 10 and 12 seconds) were chosen arbitrarily. A time history of the measured external pressure coefficients are presented at the top, while the measured cavity pressure coefficients are shown in the middle, along with the predicted cavity pressure coefficients for comparison. The numerical results presented in the plots are based on input time histories of the spanwise-averaged  $Cp_e$  from the seven pressure taps (from Modules 3, 4, 5, 6, 7, 8 and 9), or  $\Delta y/h \approx 1.5$ . Although this spanwise-averaging is not perfect for all the rows as shown in Tables 4.1 to 4.3, it would be the best to estimate fluctuating pressures on most rows.

Several observations can be made from the time history plots. Comparing time histories between the measured external and cavity pressure coefficients, the cavity pressure coefficients on each panel tend to follow the local external pressure fluctuations on that panel although the fluctuations are significantly attenuated in the cavity between the panel and the roof. Numerical simulation presented with grey lines captures the fluctuations of localized, attenuated cavity pressure coefficients to a great extent. The magnitude of predicted cavity pressure coefficients underneath row 1, shown in Figure 4.4a, tends to be lower and less fluctuating than the experimental data, which may be due to the input of  $Cp_e$  measured on the upper surface of the panel, instead of  $Cp_e$  measured at the side edge of the panel at the opening. (It should be noted that row 1 is located near the leading edge of roof, while row 12 is placed at the trailing edge of roof for this  $180^\circ$  wind, as shown in Figure 4.1.) The numerical simulations on rows 3 and 4 are fairly similar to the experimental data, while the magnitudes from numerical results become slightly higher at rows 5 and 6 where the separated flow becomes reattached. Beyond the reattachment point, for Rows 7 – 12, the numerical model predicts the temporal variations of  $Cp_i$  with considerable accuracy.

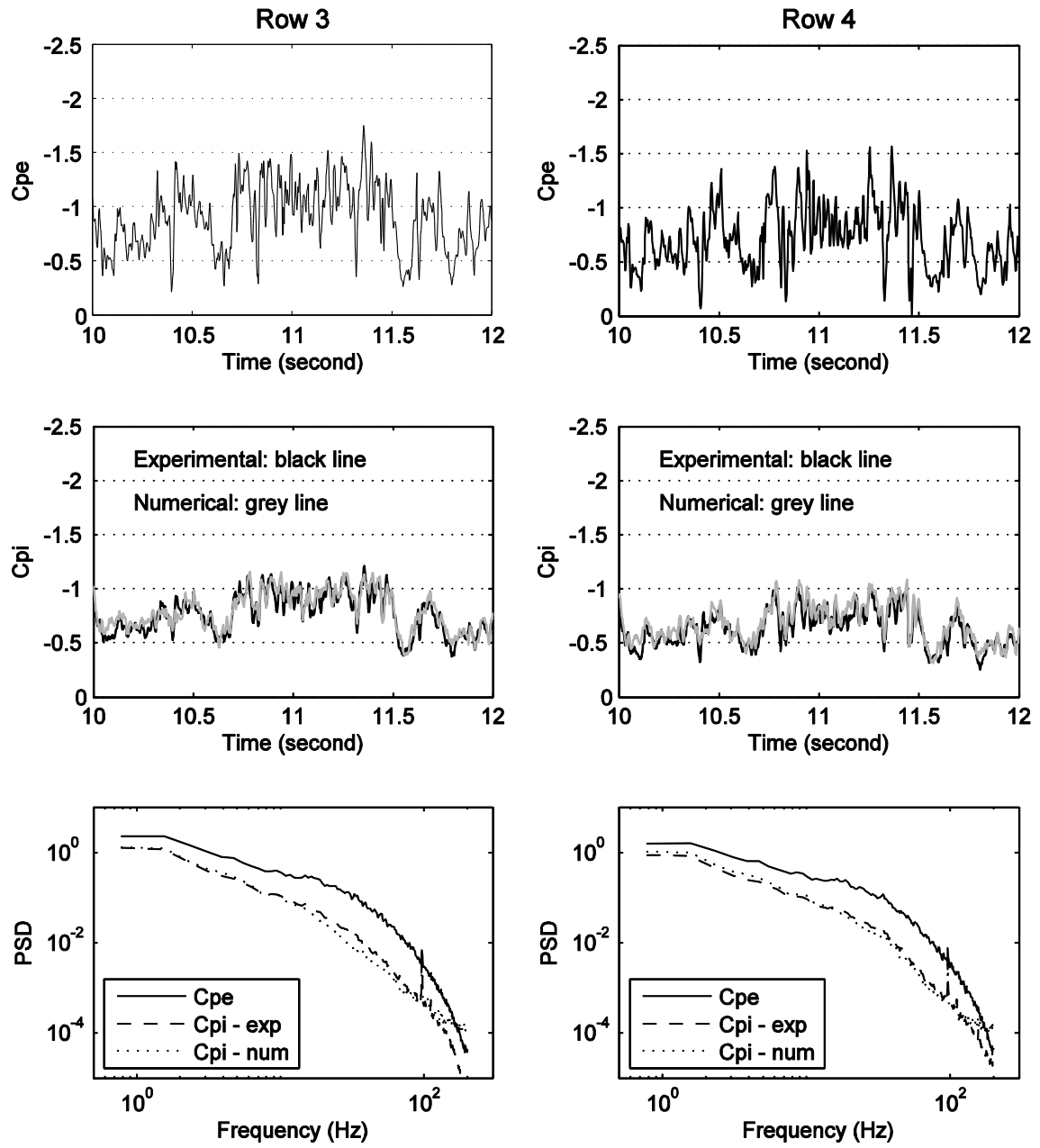
The fluctuating  $Cp_i$  are also presented with the power spectral density plots for each panel in Figure 4.4. Comparing the spectra for  $Cp_e$  and  $Cp_i$  and for both the numerical and experimental  $Cp_i$ 's, it is observed that the power spectral densities (PSD) of  $Cp_i$  are attenuated, compared to those of  $Cp_e$ . Similar to the observations from the time history plots, the predicted spectra of  $Cp_i$  show that the PSD are lower than the experimental results on rows 1 and 2, slightly higher on the rows (5, 6 and 7) in regions of the reattachment point, and fairly well estimated for the rest of the rows.



(a)

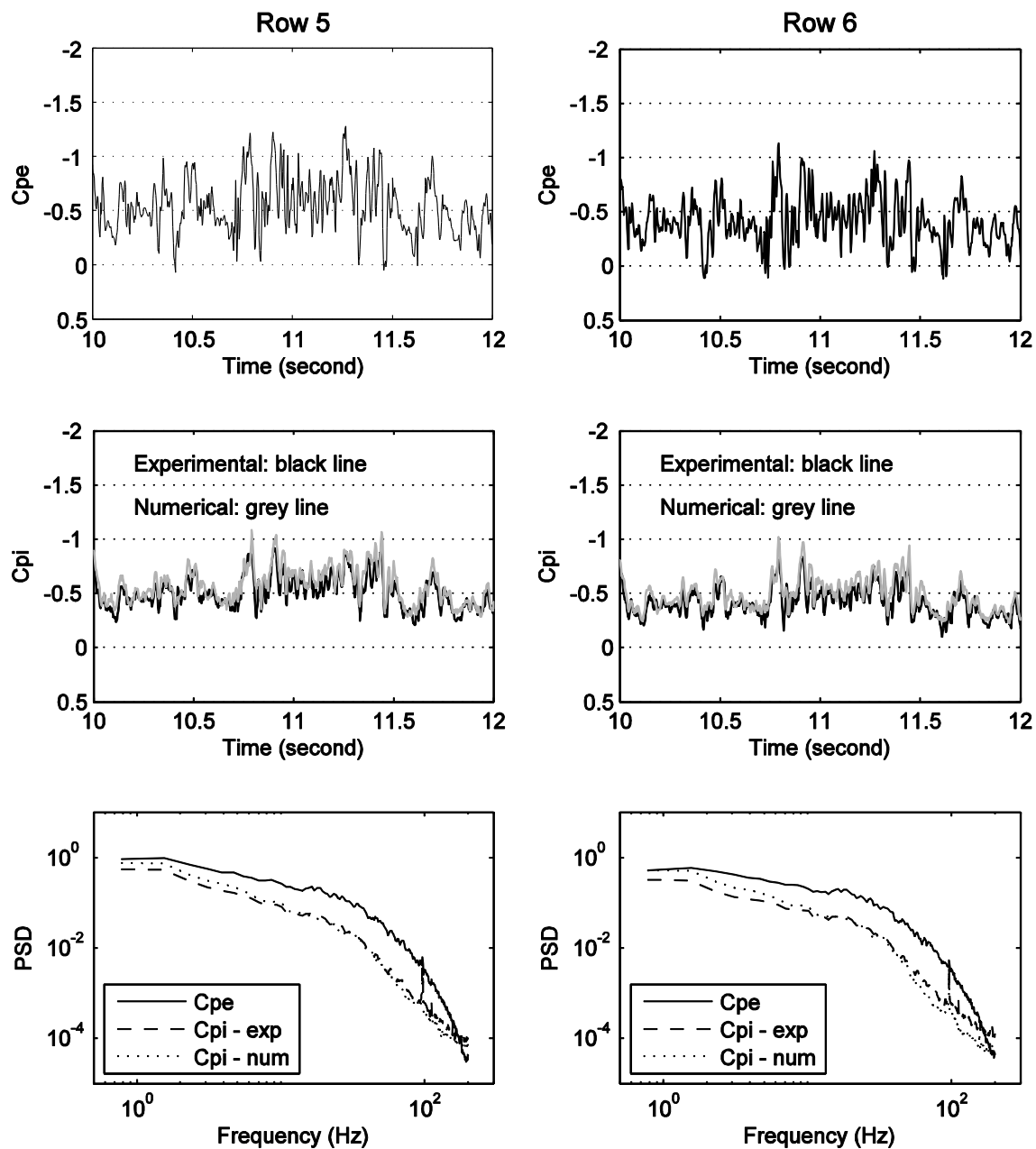
Figure 4.4 Time series and spectra of area-averaged pressure coefficients ( $C_{pe}$  and  $C_{pi}$ ) on Module 6 for 12 different rows, for  $180^\circ$  wind: (a) Rows 1 and 2; (b) Rows 3 and 4; (c) Rows 5 and 6; (d) Rows 7 and 8; (e) Rows 9 and 10; (f) Rows 11 and 12.





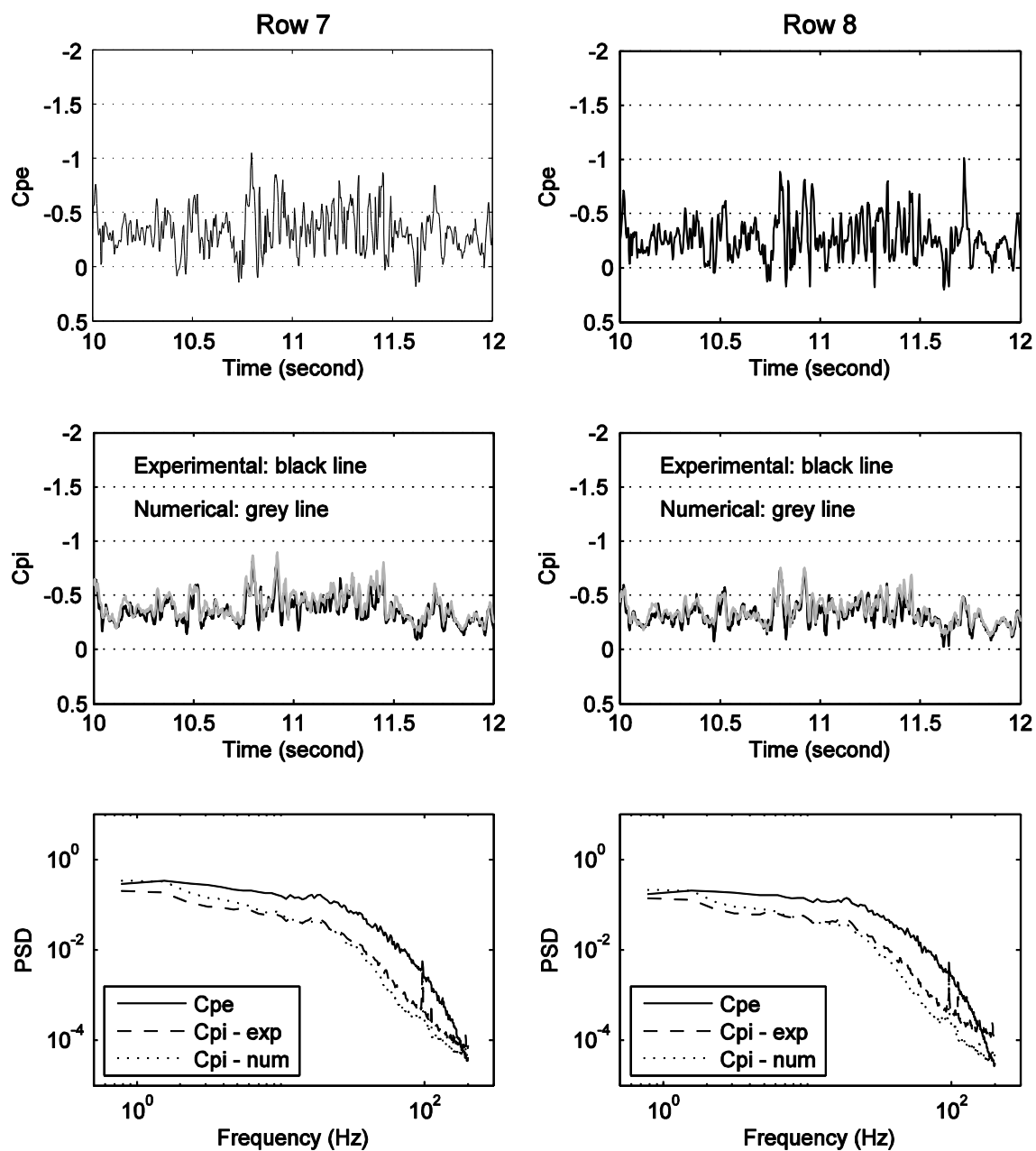
(b)

Figure 4.4: continued.



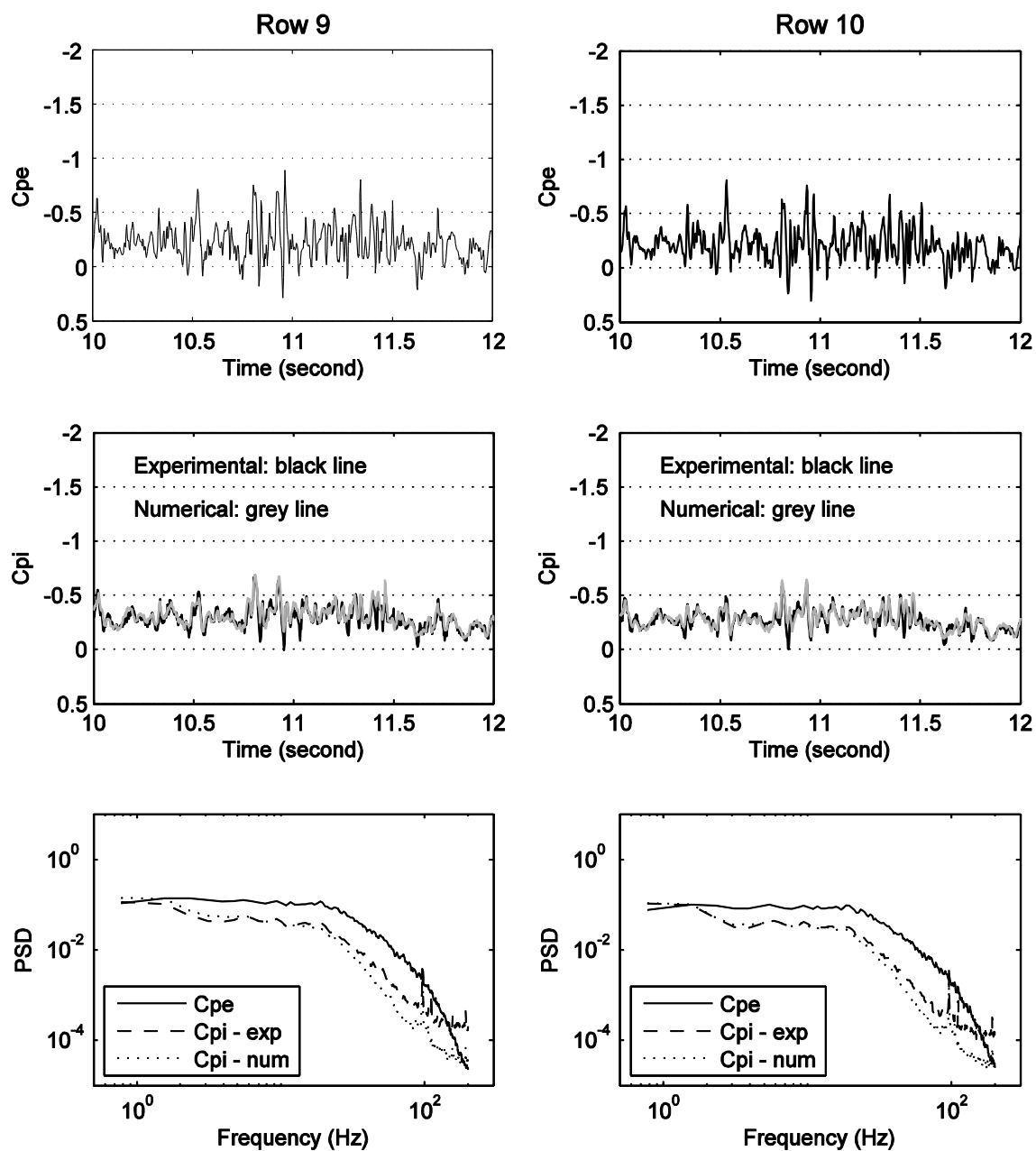
(c)

Figure 4.4: continued.



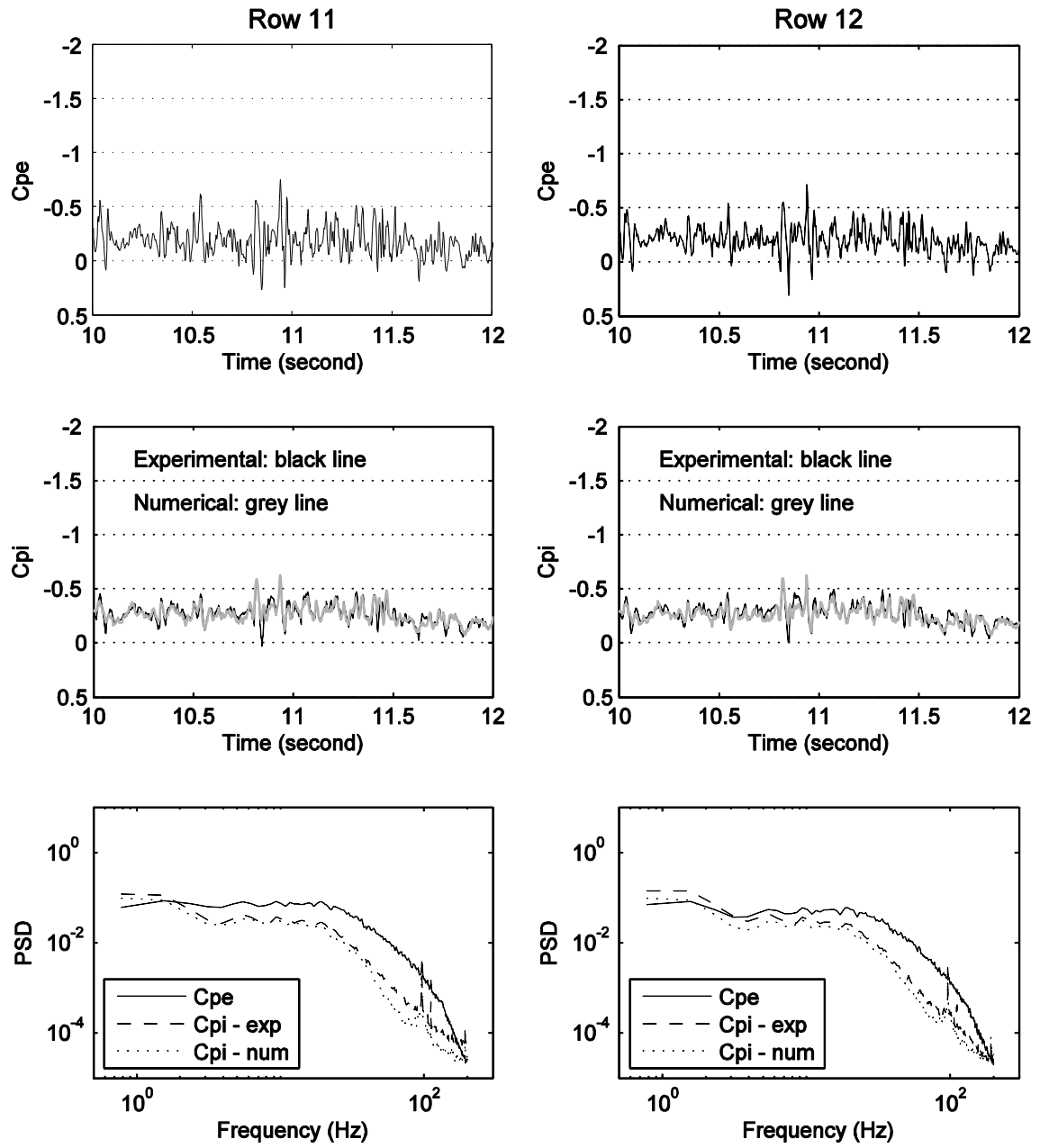
(d)

Figure 4.4: continued.



(e)

Figure 4.4: continued.



(f)

Figure 4.4: continued.

#### 4.4.4 Point pressure distributions along the midplane

The point pressure distributions along the midplane are investigated with basic statistics, e.g., mean, RMS and peak (minimum) pressure coefficients for  $0^\circ$  and  $180^\circ$  winds, as depicted in Figures 4.5 to 4.6. It is observed that the mean external and cavity pressure coefficients ( $\bar{C}p_e$  and  $\bar{C}p_i$ ), shown in Figure 4.5, are reversely distributed between the  $0^\circ$  and  $180^\circ$  winds and fairly similar in magnitude. As discussed in Chapter 2 and by Pratt and Kopp (2013),  $\bar{C}p_e$  are altered by the local flows generated by photovoltaic panels, although the changes are greater for the  $180^\circ$  wind, where the panels tilt towards the south. The mean cavity pressure coefficients,  $\bar{C}p_i$ , are quite similar to the external coefficients,  $\bar{C}p_e$ , for this photovoltaic panel arrays, leading to a direction of mean cavity flow from the trailing edge to the leading edge of the roof. The mean cavity flow between the panels and the roof dominates the mean pressure drop, although there are small mean pressure gradients across the gaps between panels indicating flow. The numerical results calculated from input time histories of  $Cp_e$  are presented in the plots with grey markers. The numerical model captures the shape of the point cavity pressure distributions quite well, although the magnitudes of predicted  $\bar{C}p_i$  are a bit greater than the measured values between  $x/h = 0.7$  and  $1.2$ , which is in the region of the reattachment point.

Figure 4.6 shows the RMS point pressure coefficients ( $\tilde{C}p$ ) along the midplane, both  $\tilde{C}p_e$  and  $\tilde{C}p_i$  and for the numerical and experimental results. The numerical results presented in Figures 4.6 and 4.7 were calculated from spanwise-averaged  $Cp_e$  obtained from seven pressure taps (i.e.,  $\Delta y/h \approx 1.5$ ) for  $180^\circ$  wind and three pressure taps (i.e.,  $\Delta y/h \approx 0.5$ ) for  $0^\circ$  wind. These spans,  $\Delta y/h$ , for spanwise-averaging were selected because both the predicted RMS and peak values are the closest equivalent to the experimental data. Numerical results from other spanwise-averaged  $Cp_e$  are presented in Appendix C. The spanwise-averaged  $\tilde{C}p_e$  are included for comparison. It is again observed that  $\tilde{C}p_e$  are affected by the presence of the gaps, while there is an interesting observation of how the  $\tilde{C}p_e$  are altered, depending on the distance ( $x/h$ ) from the leading edge of the roof. The  $\tilde{C}p_e$  are magnified at the trailing edge when  $x/h$  is relatively small until  $x/h \approx 0.9$

which is near the reattachment point. Beyond this point, on the other hand, the amplifications of  $\tilde{C}p_e$  by the gaps occur at the leading edge. The mechanism that is associated with effects of the gaps can be explained by Figure 4.8. Because of the bluff body flow separation, the recirculation, and the reattachment in a region of separated flows, the flow on external surface of panels is backward within the recirculation region before the reattachment point (as discussed by Pratt and Kopp, 2013) and forward beyond the reattachment point. So with the flow directions on external surface, the local separations are formed either on the trailing edge or the leading edge of photovoltaic panels, which amplify  $\tilde{C}p_e$ . The local flow-driven aspects of  $\tilde{C}p_e$  are not transmitted into the cavity because they are due to exit flow at the gaps. As a result, the external pressures as input should be carefully selected. In this study, the lower values of RMS external pressures between two adjacent pressure taps at gaps (i.e., pressure taps at the trailing edge of photovoltaic panels before reattachment point and pressure taps at the leading edge of photovoltaic panels after reattachment point) are used for  $Cp_e$  as input because they are expected to represent more reliable pressures at gaps between panels for modelling the cavity pressures. Compared to  $\tilde{C}p_e$  measured at the midplane,  $\tilde{C}p_i$  are attenuated quite significantly, indicating that a certain portion of fluctuating external pressures are diminished through the gap between panels and in the cavity. The RMS cavity pressure coefficients are predicted with considerable accuracy by the numerical model, although there are some differences, especially for panels in the region of the leading edge and the reattachment point on roof. It seems that the current model cannot compute the fluctuating flows in the cavity near the leading edge particularly well.

Minimum, peak point pressure coefficients are depicted in Figure 4.7. The peak cavity pressure coefficients ( $\tilde{C}p_i$ ) are significantly decreased when compared to  $\tilde{C}p_e$ , relative to  $\bar{C}p_i$ . The numerical model can capture the trend of this pressure drop

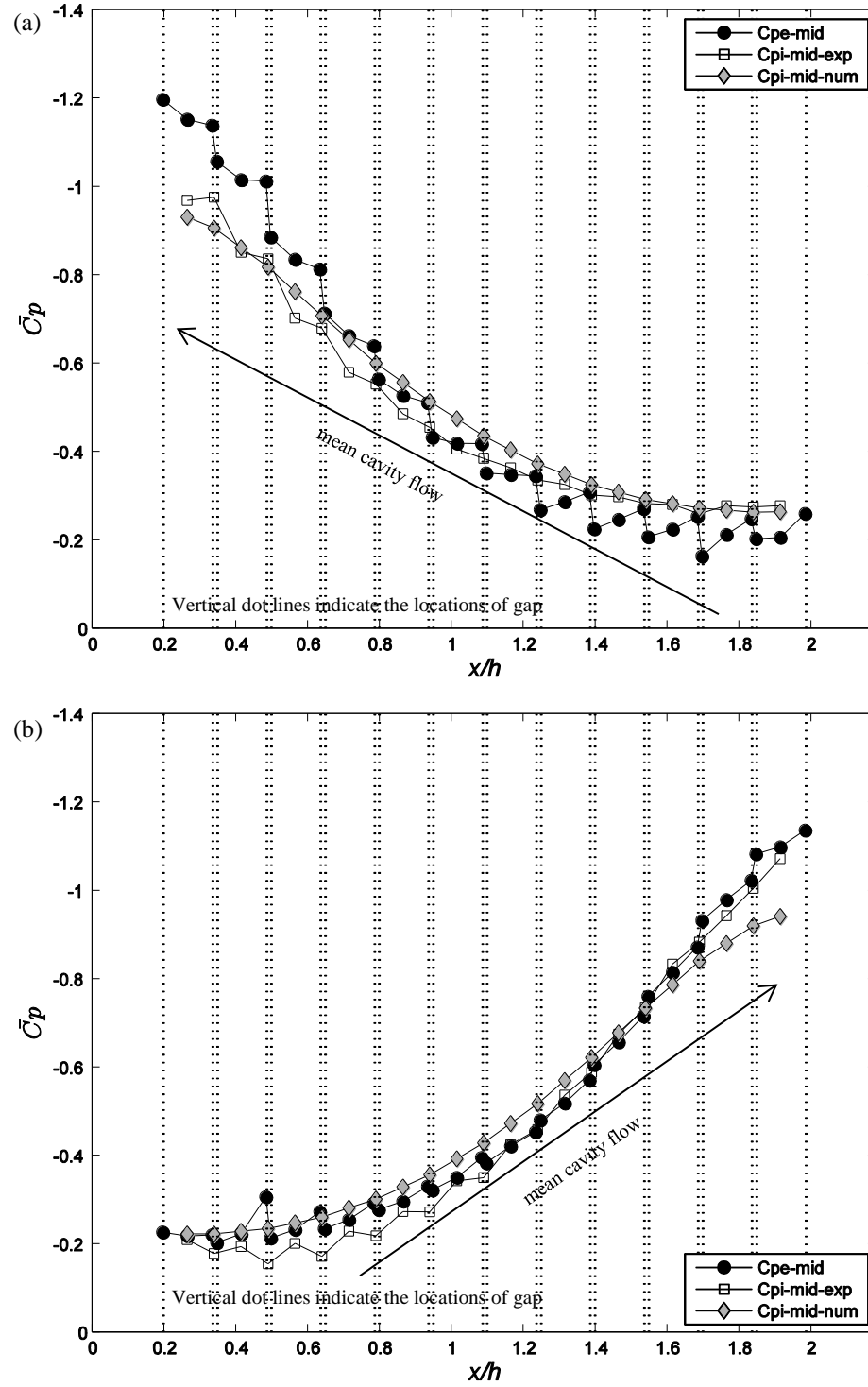


Figure 4.5 Mean point pressure distributions for the pressure taps along the midplane (Module 6): (a) for 180°; (b) for 0° wind.



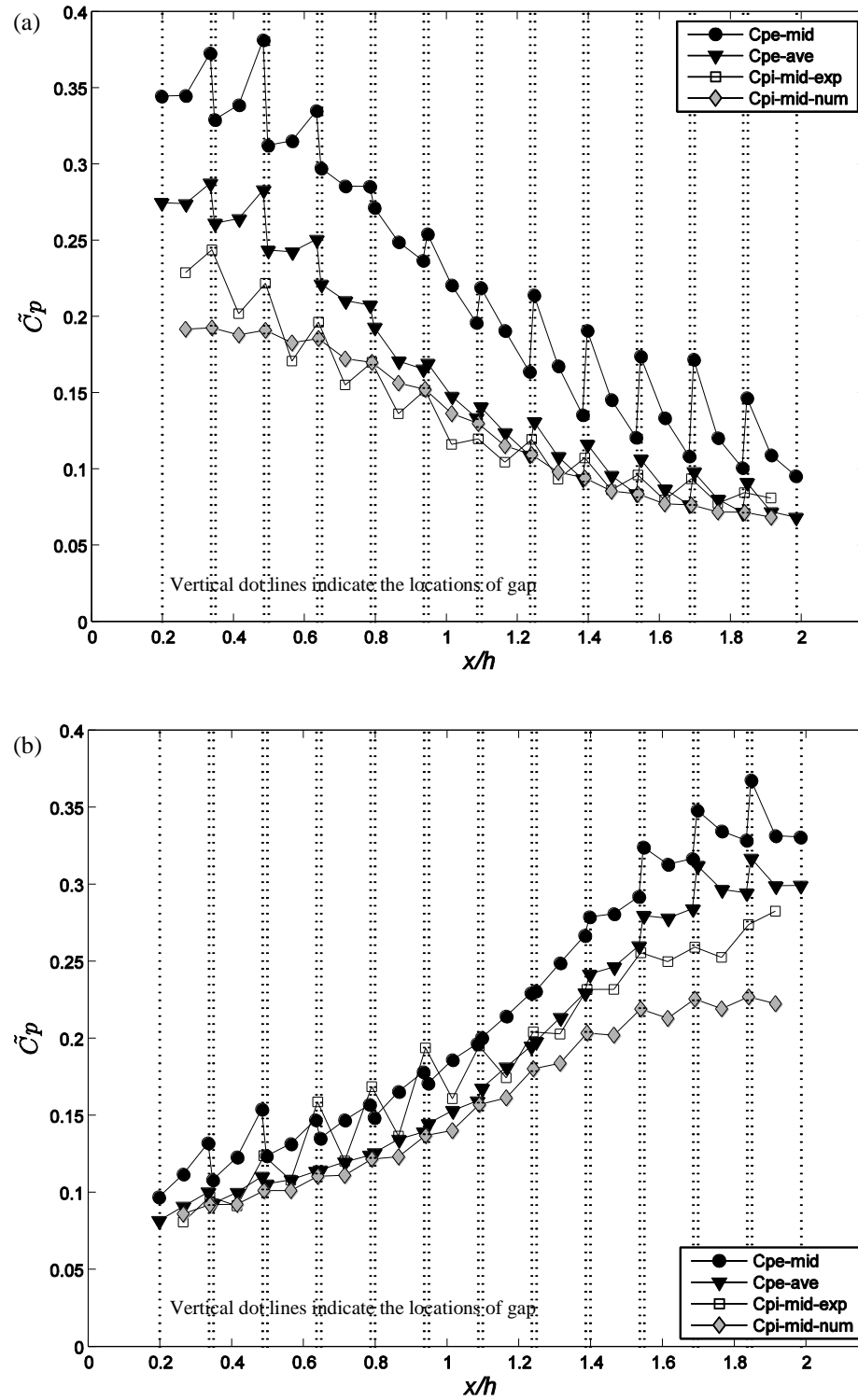


Figure 4.6 RMS point pressure distributions for the pressure taps in the midplane (Module 6): (a) for 180°; (b) for 0° wind.

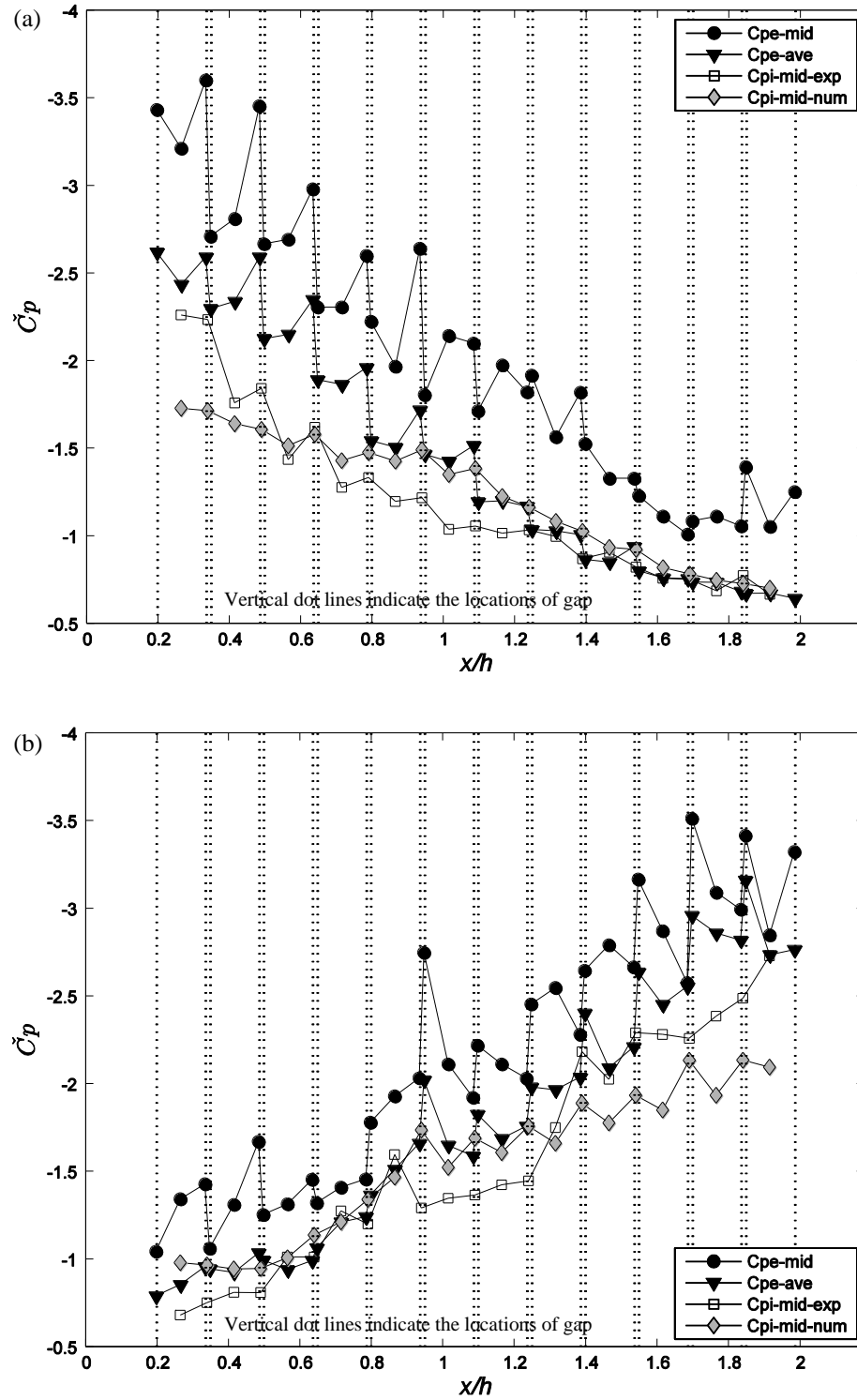


Figure 4.7 Peak (minimum) point pressure distributions for the pressure taps in the midplane: (a) for 180°; (b) for 0° wind.

but again, it tends to predict lower magnitudes of the cavity pressure coefficients on panels near the leading edge of roof and higher magnitudes on panels in the intermediate zone. This might be due to the effect of the side opening on the panels in both side edges of roof or unknown factors in the flow within the reattachment region. This needs to be investigated further in the future.

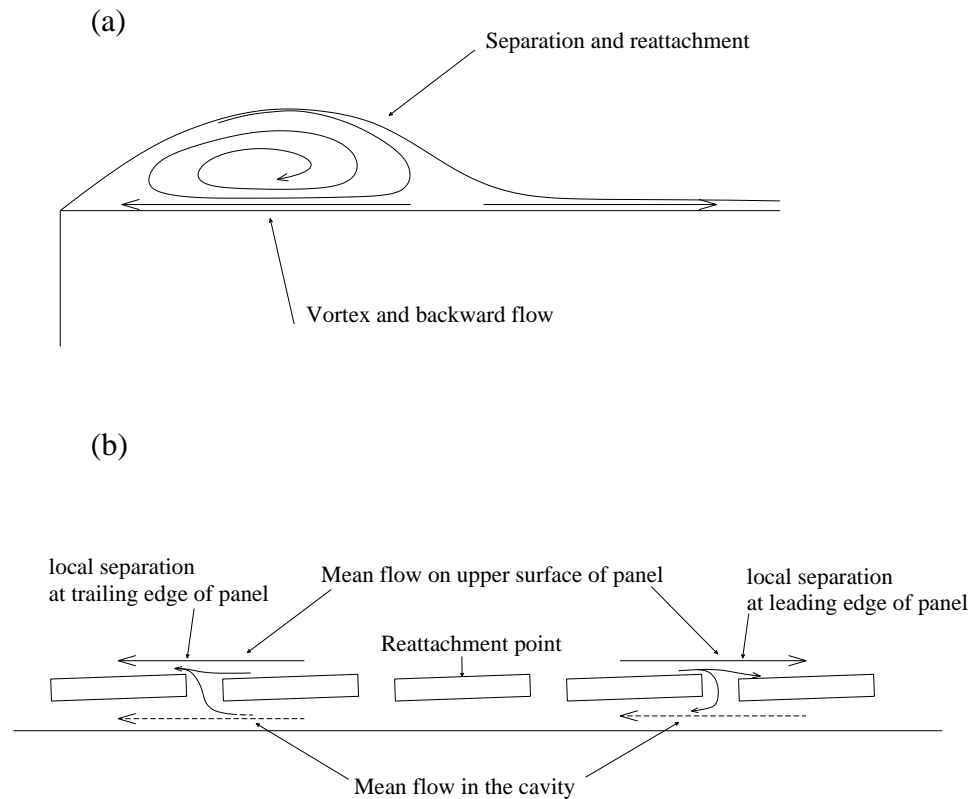


Figure 4.8 (a) Flow separation, reattachment and vortex-generated backward flow on roof and (b) local flow separation mechanisms on panels before and after the reattachment point.

## 4.5 Numerical Simulations of Compartmentalization in a Photovoltaic Array

In this section, an investigation on compartment effects of the cavity in a photovoltaic panel array is discussed with results from numerical simulations on various compartmentalization of the cavity. The experimental data of external pressure time histories obtained from the photovoltaic array described in Section 4.3 were used as input to compute cavity pressures and upward net loads.

### 4.5.1 Compartmentalization of cavity in different number of rows

Six configurations illustrated in Figure 4.9 are intended to investigate the effects of compartmentalization of the cavity in different number of rows. With the full length of the 12 panel array, 10, 8, 6, 4 and 2 panel arrays are examined, removing two rows, one from each side of the array so that the compartmentalized cavity for the two panel array are beneath the rows 6 and 7. Time histories of point cavity pressure coefficients ( $\bar{C}p_i$ ) are computed using the analytical model (Eqs. 4.5) for the 6 different compartment configurations, assuming that external pressure coefficients ( $Cp_e$ ) as input are of the same magnitude for all the configurations.

The numerical results of mean point cavity pressure distributions from the six configurations for 180° wind are plotted in Figure 4.10, comparing with the measured  $\bar{C}p_e$ . The mean cavity pressure coefficients,  $\bar{C}p_i$ , beneath panels are found to vary significantly with the compartmentalization in different number of rows. For instance, the compartmentalization between rows 2 and 11 shows that the magnitude of  $\bar{C}p_i$  on leading edge of the second row is reduced from -0.92 to -0.82. The reduction is greater when the number of rows is decreased, e.g., the compartmentalization of the six panel array between rows 4 and 9 shows that the magnitude of  $\bar{C}p_i$  on leading edge of the fourth row drops from -0.72 to -0.56. Overall, for a given gap-to-cavity ratio,  $G/H$ , the mean cavity pressure gradients ( $\Delta\bar{C}p_i$ ) decrease while the number of rows within the compartment

decreases. This should be due to the smaller external pressure gradient ( $\Delta\bar{C}_p$ ) and the shorter length of the cavity ( $L$ ) when decreasing the number of rows.

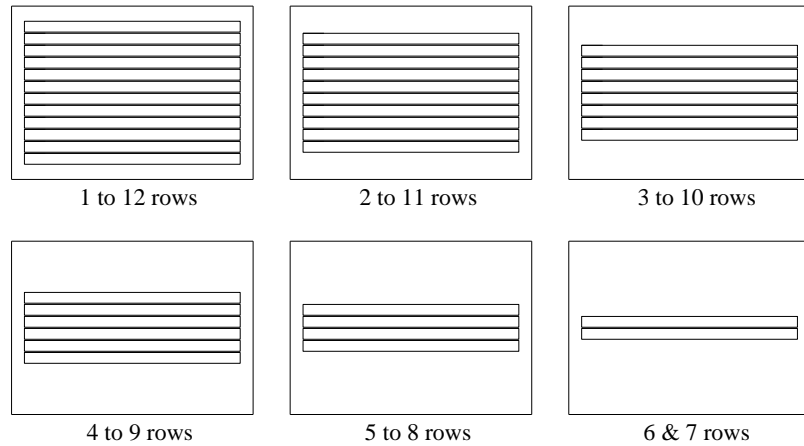


Figure 4.9 Configurations examined numerically to investigate effects of compartmentalization of the cavity in different number of rows.

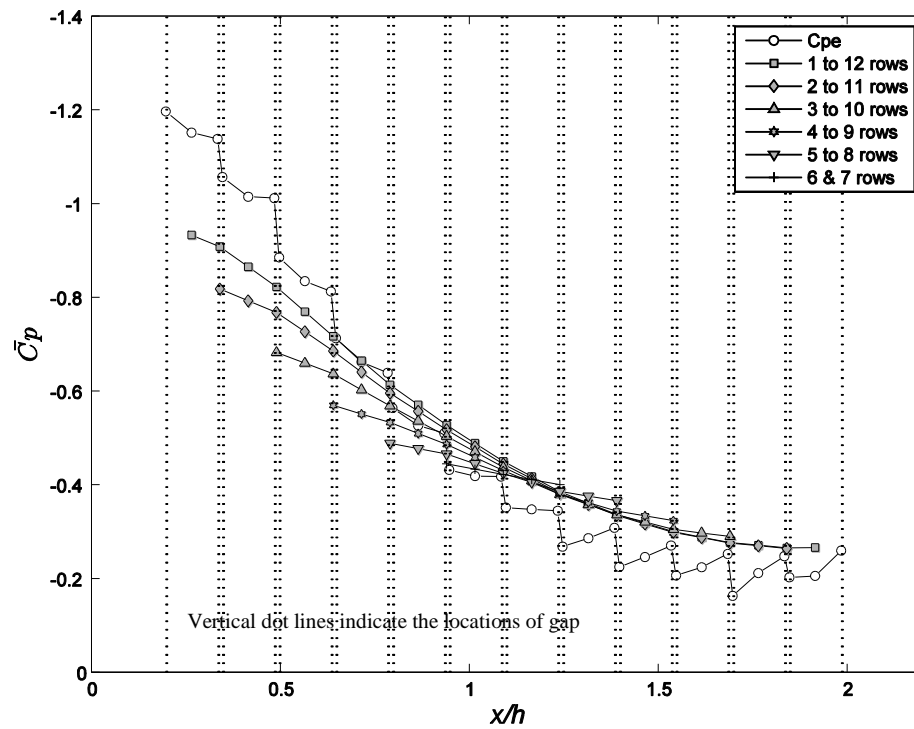


Figure 4.10 Effects of compartmentalization of cavity in different number of rows, as shown in Figure 4.9, on mean cavity pressures for 180° wind.

#### 4.5.2 Compartmentalization of cavity in different locations of the roof

The mean cavity pressure coefficients,  $\bar{C}_{p_i}$ , for the compartment configuration of the two panel array beneath rows 6 and 7 were nearly uniform, compared to that for the 12 panel arrays as shown in 4.10a. The compartmentalization on the two panel arrays are further investigated with four additional locations on the roof such as rows 2 and 3, rows 4 and 5, rows 6 and 7, rows 8 and 9, and rows 10 and 11, as depicted in Figure 4.11. The numerical results of mean cavity pressure distributions on the two panel array for five different locations for 180° wind are shown in Figure 4.12, comparing with the 12 panel array. It is clearly seen that the mean pressure distributions in the cavity for the two panel arrays are significantly reduced, while the two panel array yields lower net loads, depending on locations. The gradient change of cavity pressures in two panel arrays reduces the upward net loads on rows 2 and 3, while it increases the net loads on rows 4 and 5. For the rest of rows, the two panel array yields slightly lower net loads.

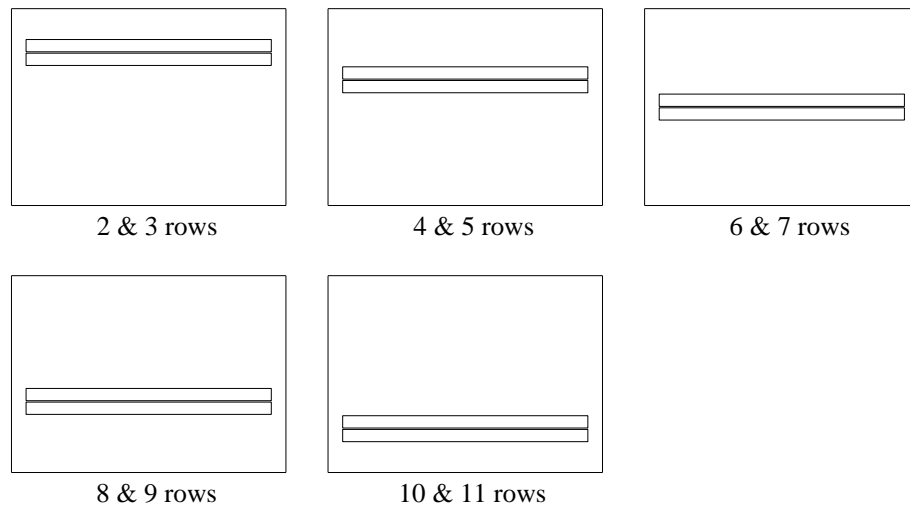


Figure 4.11 Configurations examined numerically to investigate cavity pressures on a two panel array for different locations.

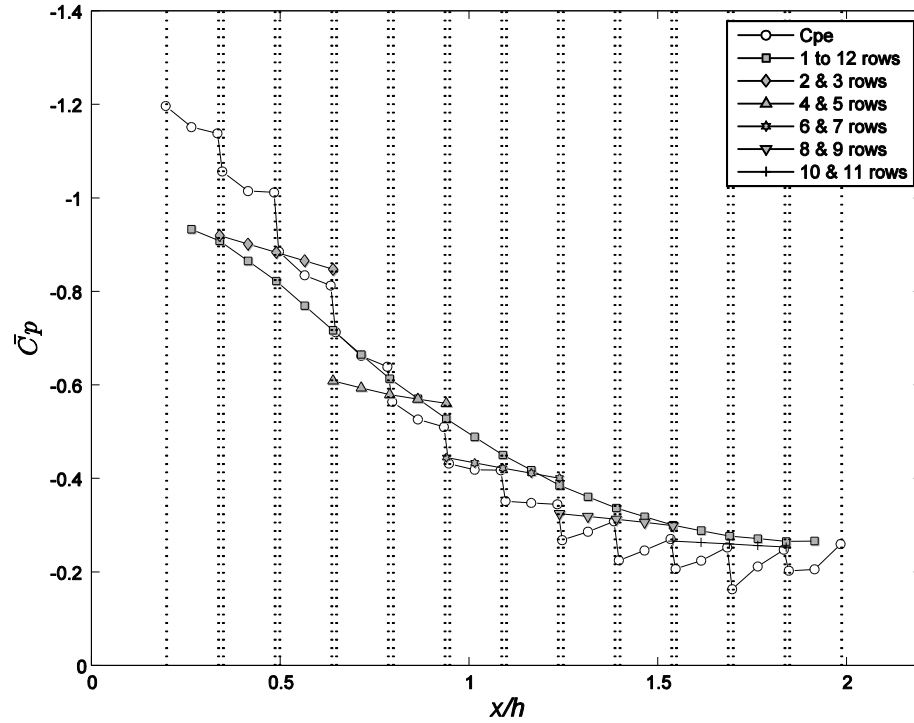


Figure 4.12 Effects of compartmentalization of cavity in different locations of the roof, as shown in Figure 4.11, on mean cavity pressures for 180° wind

#### 4.5.3 Compartmentalization of cavity between edge and intermediate rows

Since mean cavity pressures for the compartment configuration of the rows 2 and 3 in the leading edge of roof are more equalizing to external pressures than those for the 12 panel array, it is suggested to have the cavity compartmentalized between the edge and intermediate rows (i.e., between rows 3 and 4, and between rows 9 and 10), as illustrated in Figure 4.12. Thus, the cavity pressures on panels in leading edge zone with rows 1 to 3, in the intermediate zone with rows 4 to 9, and the trailing edge zone with rows 10 to 12 are all independent. The numerical results of pressure distributions in the compartmentalized cavities are presented in Figure 4.14, comparing with the non-compartmentalization case. It is clearly observed that the compartmentalization plays a significant role in pressure distributions in the cavity, in particular, for panels in the leading edge of roof. The mean cavity pressures ( $\bar{Cp}_i$ ) on panels in rows 1 to 3 are more equalizing to external pressures by the compartmentalization, which is a critical zone for

the design of photovoltaic panels, as shown in Figure 4.14a. The resulting, net mean pressures ( $\bar{C}p_n$ ) are significantly altered by the compartmentalization on rows 1-5, i.e.,  $x/h < 1$ . While the mean net loads tend to decrease on rows 1-3 and increase on rows 4-5, the maximum, mean net load on row 1 is reduced. The RMS and peak pressure distributions, as shown in Figures 4.14a and 1.14b, show a similar trend as the mean values. The compartment-induced reductions of the uplift net loads on the row 1 are approximately 60 % and 85 % for mean and peak values, respectively. The numerical results show that the compartment effects between rows are significant when  $x/h < 1$ , in which  $\Delta Cp_e$  are greater than those on the rows for  $x/h > 1$ . This indicates that  $\Delta Cp_e$  is important on the effect of the compartmentalization. Because  $\Delta Cp_e$  is greater on the rows for  $x/h < 1$ , the amount of the cavity flow induced by the  $\Delta Cp_e$  should be larger. Thus, the compartment effect is greater when  $x/h < 1$ , since the significant cavity flows are resisted by the compartmentalization.

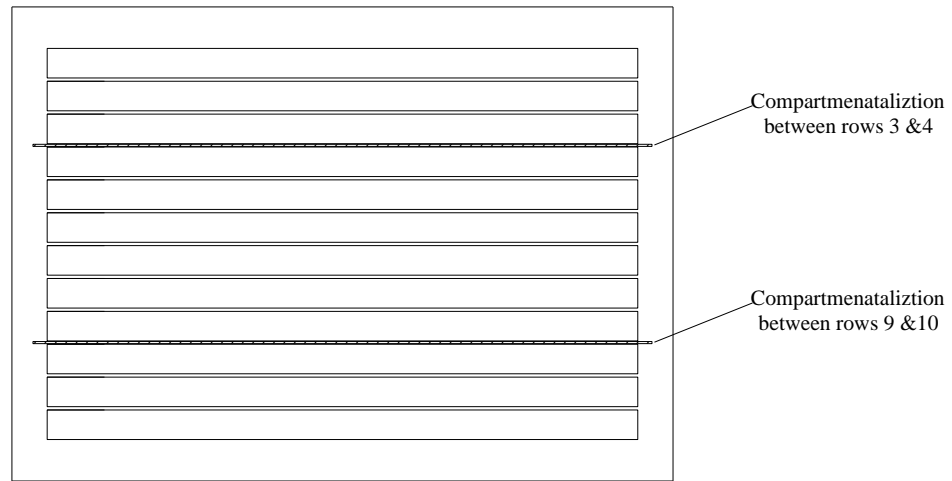


Figure 4.13 Compartmentalization between rows 3 & 4 and between 9 & 10 to numerically investigate cavity pressures.



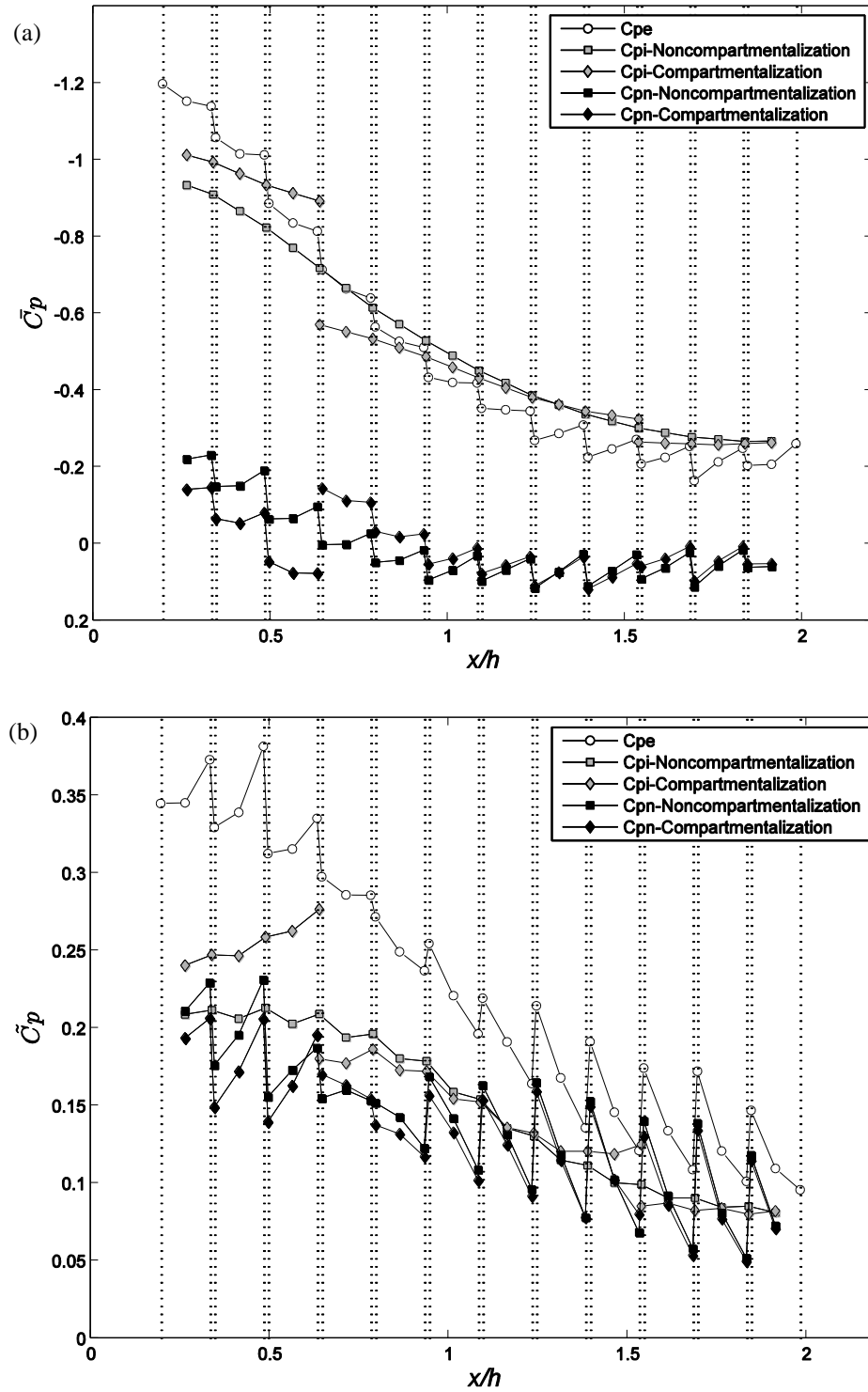


Figure 4.14 External, cavity and net pressure distributions from compartmentalization of cavities as shown in Figure 4.13, for 180° wind: (a) mean; (b) RMS; (c) peak values.

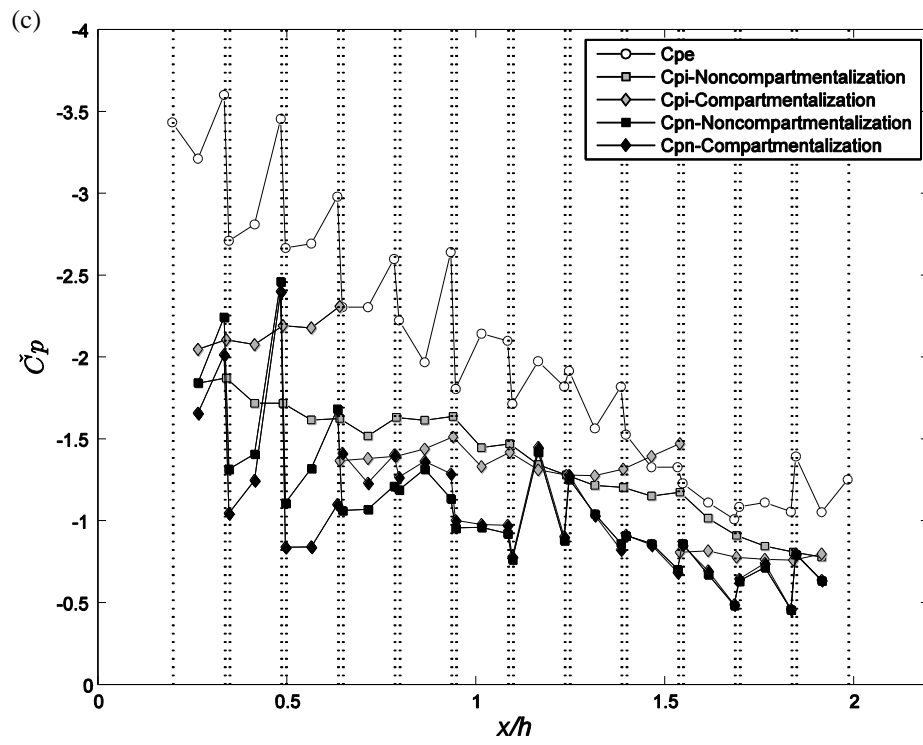


Figure 4.14: continued.

#### 4.5.4 Compartmentalization of cavity between modules

Local cavity flow along the span of rows (in the y-direction) can be also resisted by compartment between modules, as illustrated in Figure 4.15. The pressure distributions in the compartmentalized cavity beneath the module 6 are obtained numerically from input time histories of  $Cp_e$  measured at pressure taps located along the module 6. The cavity pressure coefficients,  $Cp_i$ , and the net pressure coefficients,  $Cp_n$ , on the module 6 are compared between compartmentalization and non-compartmentalization, as depicted in Figure 4.16. The cavity pressures for non-compartmentalization are calculated from the spanwise-averaged  $Cp_e$  since it is the basic concept that there is continuity of the cavity flow along the span in the spanwise-averaging.

The mean pressure distributions do not show significant changes, as depicted in Figure 4.16a, because mean flow is approximately two-dimensional. However, the RMS and peak pressures in the compartmentalized cavity are significant increased, resulting in a significant reduction on uplift net loads, as shown in Figures 4.16b and 4.16c. Hence, it is concluded that uplift net loads are significantly reduced by restricting local flow by compartmentalization of the cavity between rows and between modules. Since the cavity pressures for compartmentalization are not available in the current wind tunnel test data, the numerical results cannot be validated with experimental data. However, the numerical simulations show how the analytical model can be used in design as a tool to set compartments for reducing the wind loads.

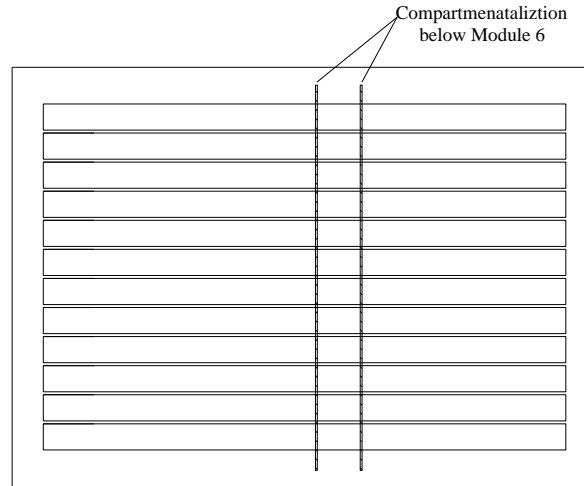


Figure 4.15 Compartmentalization below Module 6 to numerically investigate cavity pressures.

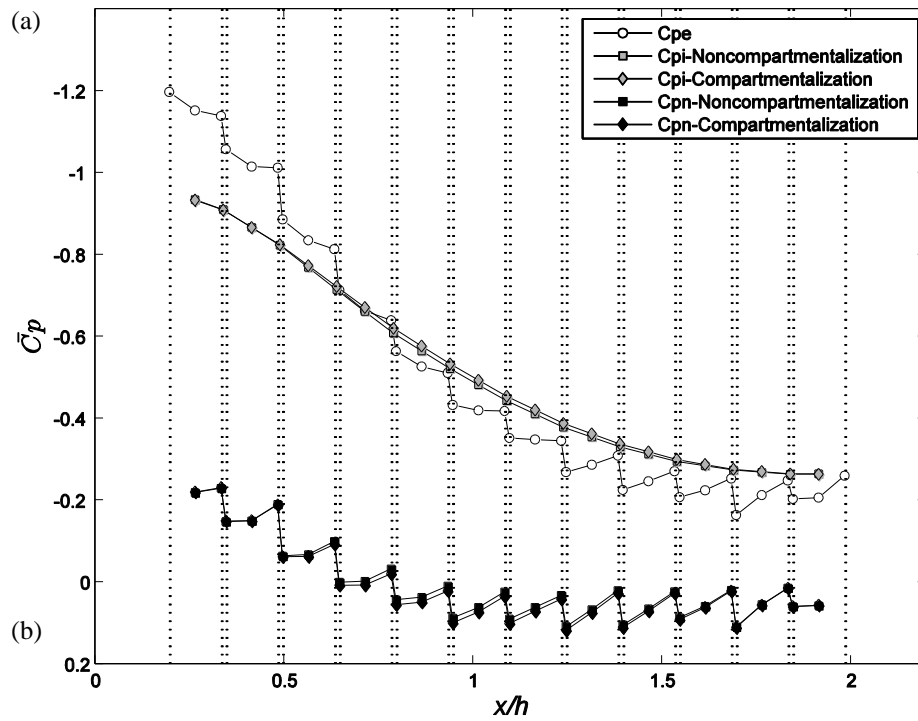


Figure 4.16 External, cavity and net pressure distributions from compartmentalization of cavities as shown in Figure 4.15, for 180° wind: (a) mean; (b) RMS; (c) peak values.

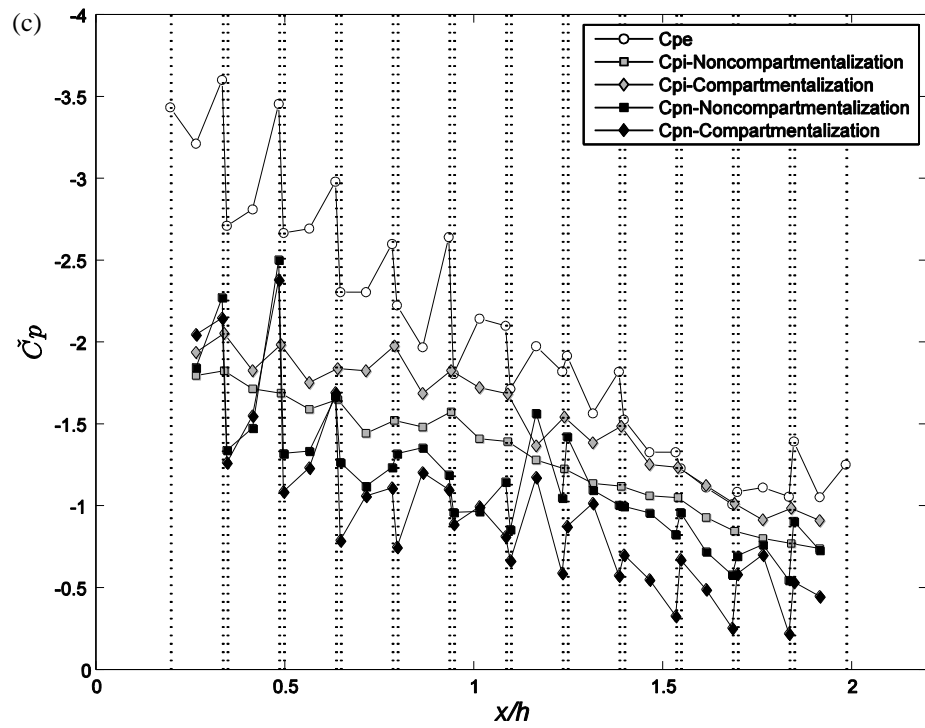
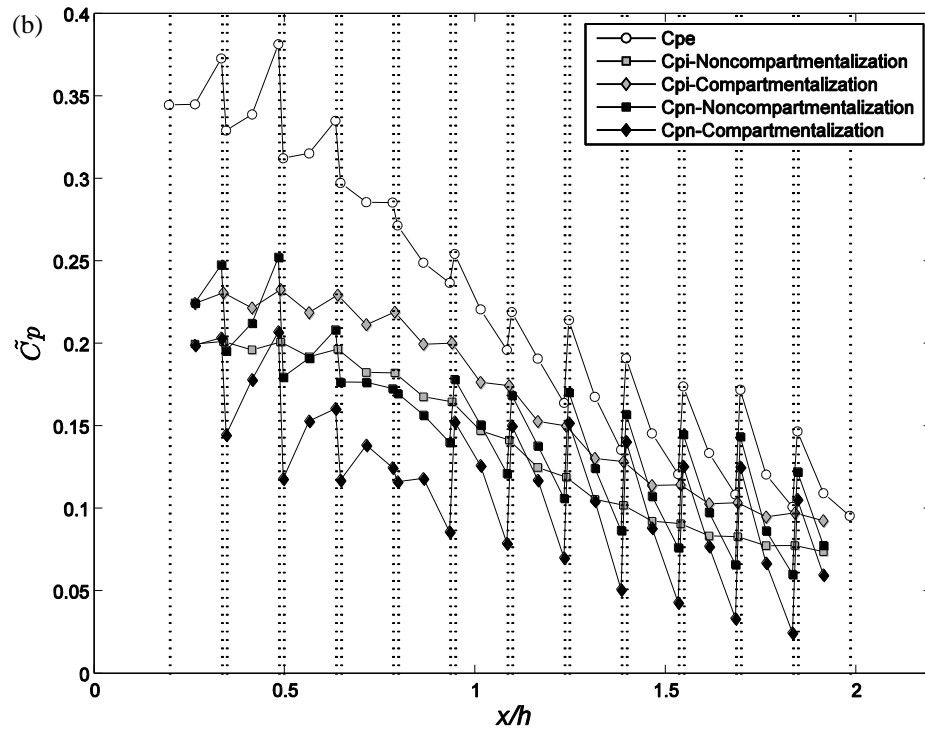


Figure 4.16: continued.

## 4.6 Summary and Conclusions

A set of existing experimental data are investigated numerically by using the analytical model developed in Chapter 3. The analytical model was validated by applying it to a practical problem which consisted of 12 photovoltaic rows covering the roof. In addition, the study examined how the model can be used as a tool to design compartments for pressure equalizing, double-layer systems. The current study focuses only on winds ( $0^\circ$  and  $180^\circ$ ) perpendicular to the photovoltaic panel array and building edges so that the mean pressure in the cavity between photovoltaic panels and the roof is approximately one-dimensional. The main conclusions are summarized below.

Mean, RMS and peak values of area-averaged time histories of cavity pressure coefficients are investigated experimentally and numerically, comparing with those of external pressures. It is observed that the cavity pressure coefficients are localized, following the external pressure coefficients for this photovoltaic panel arrays, although the RMS interior pressure coefficients are significantly attenuated. The numerical model can estimate the attenuations of fluctuating pressures with considerable accuracy, while the numerical results from different spanwise-averaged  $C_{pe}$  are altered for the RMS and peak cavity pressure coefficients. This indicates that unsteady effects on the loss coefficients of the gap flows may not be fully accounted for; a point which merits further investigation.

The numerical model captures fluctuations of the area-averaged cavity pressure coefficients presented in time history plots. However, the magnitudes of the predicted temporal cavity pressure coefficients tend to be lower beneath row 1 (i.e., the panel at the leading edge) and greater beneath rows 5 and 6 (i.e., the panels in regions of the reattachment point), compared with experimental data.

Mean, RMS and peak (minimum) point pressure coefficients along the midplane were investigated, comparing the measured external and cavity pressure coefficients and numerical cavity pressure coefficients. It is observed that the external pressures are altered by the local flows generated by gaps between panels, as discussed in Chapter 2 and by Pratt and Kopp (2013). It seems that secondary flow separations occur at the

trailing edge of photovoltaic panels within the reattachment point (i.e.,  $x/h < 1$ ) and at the leading edge of photovoltaic panels beyond the reattachment point (i.e.,  $x/h > 1$ ). As a result, the external pressures as input should be carefully selected, since the local flow-driven aspects of external pressures are not transmitted into the cavity. In this study, the lower value of RMS external pressures between two adjacent pressure taps at gaps (i.e., pressure taps at the trailing edge of photovoltaic panels before reattachment point and pressure taps at the leading edge of photovoltaic panels after reattachment point) are used for  $Cp_e$  as input. They are expected to represent more reliable pressures at the gaps between panels for modelling the cavity pressures. The pressure gradient of mean cavity pressure coefficients is fairly similar to the external pressures, while RMS interior pressure coefficients are significantly attenuated. This implies that the mean cavity flow dominates the mean pressure drop, while fluctuating pressures are attenuated by flow through gaps between panels, for this photovoltaic panel array. The numerical model predicts the shape of the mean and RMS cavity pressure distributions with considerable accuracy, even though there are some differences, in particular, on panels in the region of the leading edge and the reattachment point on the roof.

Effects of compartmentalization of the cavity in different number of rows are investigated numerically by using the analytical model. It is observed that the cavity pressure coefficients are found to vary significantly with the compartmentalization in different number of rows, for this photovoltaic panel array. For a given gap-to-cavity ratio,  $G/H$ , the mean cavity pressure gradients decrease with decreasing number of rows in the compartment. This should be due to the smaller  $\Delta\bar{Cp}_e$  and the shorter length of the cavity ( $L$ ) for fewer numbers of rows.

Compartmentalization between the edge and intermediate rows (i.e., between rows 3 and 4, and between rows 9 and 10) play a significant role in reducing the uplift net loads on the photovoltaic array, in particular, at the compartmentalized cavity in the leading edge of the roof (e.g., approximately 60 % mean and 85 % peak reductions for the row 1). This indicates that the compartment effect is greater in regions of separated flow, since the significant cavity flows induced by the large magnitude of external pressure gradient,  $\Delta Cp_e$ , are resisted by the compartmentalization.

Effects of compartmentalization between modules are also investigated numerically and compared with results from non-compartmentalization. The single module beneath which the underside (cavity) is compartmentalized shows reductions on the RMS and peak uplift net loads by restricting local flow along the span between modules.

The numerical results show how the analytical model can be used in design as a tool to set compartments for reducing the wind loads on pressure equalizing, double-layer systems.

## References

- ASCE 7 -10. (2010). Minimum design loads for buildings and other structures. *American Society of Civil Engineers*, 2010.
- AS/NZS 5033:2012. (2012). Installation and safety requirements for photovoltaic (PV) arrays. *Australian/New Zealand Standard*, 2012
- Banks, D. (2013). The role of corner vortices in dictating peak wind loads on tilted flat solar panels mounted on large, flat roofs. *Journal of Wind Engineering and Industrial Aerodynamics*, 123: 192-201.
- Barkaszi, S. and O'Brien, C. (2010). Wind load calculations for PV arrays. *Solar American Board for Codes and Standards Report*, June, 2010.
- Chapra, S.C. and Canale, R.P. (2006). Numerical methods for engineers: 5<sup>th</sup> Edition. *McGraw-Hill*, pp. 632-634.
- Farquhar, S. and Kopp, G.A. (2009). Wind loads on SunLink roof-mounted solar arrays: BLWT-SS4-2009. *Boundary Layer Wind Tunnel Laboratory Report*, University of Western Ontario.
- Kopp, G.A. (2014). Wind loads on Low-Profile, Tilted, Solar Arrays Placed on Large, Flat, Low-Rise Building Roofs. *Journal of Structural Engineering*, 140 (2): 04013057.



- Kopp, G.A., Farquhar, S. and Morrison, M.J. (2012). Aerodynamic mechanisms for wind load on tilted, roof-mounted solar arrays. *Journal of Wind Engineering and Industrial Aerodynamics*, 111: 40-52.
- Matsumoto, M., Shirato, H., Araki, K., Haramura, T. and Hashimoto, T. (2003). Spanwise coherence characteristics of surface pressure field on 2-D bluff bodies. *Journal of Wind Engineering and Industrial Aerodynamics*, 91: 155-163.
- NEN (2014). NEN 7250: Solar energy systems - Integration in roofs and facades - Building aspects. *The Netherlands Standardization Institute*, 2014.
- Potter, M.C., Wiggert, D.C. and Rmadan, B.H. (2012). Mechanics of fluids: 4<sup>th</sup> Edition. *Cengage Learning*, 2012.
- Pratt, R. and Kopp, G. (2013). Velocity measurements around low-profile, tilted, solar arrays mounted on large flat-roofs, for wall normal wind directions. *Journal of Wind Engineering and Industrial Aerodynamics*, Online published in October 2013.
- Razykov, T.M., Ferekides, C.S., Morel, D., Stefanakos, E., Ullal, H.S., and Upadhyaya, H.M. (2011). Solar photovoltaic electricity: Current status and future prospects. *Solar Energy*, 85: 1580-1608.
- SEAOC PV2-2012. (2012). Wind design for low-profile solar photovoltaic arrays on flat roofs. *Structural Engineers Association of California*, 2012

## **Chapter 5 Summary, Conclusions and Recommendations**

### **5.1 General**

The most important goal of this study was to investigate the cavity pressure beneath the outer layer for air permeable, double-layer systems, and its correlation with external pressure above the outer layer, so that the effects of pressure equalization (between the external and cavity) on net wind loads is characterized and modeled. Investigations on these were carried out both experimentally and numerically. Experimental results did provide with a necessary basis on mechanisms of flows and pressures in the cavity, while the theoretical framework has been built up through the development of the analytical model for numerical simulations. Major conclusions drawn from the study and recommendations for future research are highlighted below.

### **5.2 Pressure Distributions within a Double-Layer Roof System in Regions of Separated Flow**

A wind tunnel model of double-layer roof systems placed on a low-rise building was carefully designed with knowledge gained from the literature, in order to simulate the cavity pressures for various geometric parameters. In total, 39 configurations consisting of six different gaps ( $G$ ) between panels, six different heights ( $H$ ) of the cavity between layers and three additional configurations with different panel sizes ( $L$ ) were examined. In this study, wind perpendicular to the building edge is investigated so that the mean flow on the double-layer roof system is approximately two-dimensional. The objectives of this experimental research work were to investigate the detailed cavity pressure distributions for an air permeable, double-layer roof system, with a fine resolution of the pressure taps, examining effects of the gap ( $G$ ) between panels and the height ( $H$ ) of the cavity between layers on the cavity pressures, and characterize the mechanisms of flows and pressures in the double-layer system. The main conclusions are as follows.

1. External pressure: The presence of gaps between the panels alters the pressure distribution on the external surface ( $Cp_e$ ) near the locations of the gaps. This is likely due to the local flow through the gap, including “secondary” flow separations at the edge of the gaps of the panel.
2. Cavity pressure and effects of  $G/H$ :
  - Mean pressure: The mean pressure distribution on the internal surface ( $Cp_i$ ) of the panel is significantly altered by  $G/H$  and  $\frac{fL/H}{c_L}$ . It is fairly uniform for smaller  $G/H$  ratios but varies linearly along the panel for larger  $G/H$  ratios. The uniform cases result from the significant pressure drop through the gaps ( $G$ ), which is comparable to the (building) internal pressure problem where there is insignificant net flow through the cavity between the panel and the roof surface. The linear case is caused by the friction losses in the flow in the cavity. The boundary for the change in phenomena is about  $G/H = 0.2$  to  $0.4$  for the current building size, panel size and shape, and wind direction.
  - RMS pressure: The RMS pressure coefficients,  $\tilde{Cp}_i$ , are relatively uniform in the cavity compared to  $\bar{Cp}_i$ . The magnitude of  $\tilde{Cp}_i$  increases with larger  $G/H$  and with shorter panels. This helps PE by allowing fluctuations into the cavity flow region.
  - Instantaneous pressure: the instantaneous  $Cp_i$  do not respond locally or immediately to  $Cp_e$  during strong peak events. This would be an “unsteady” effect so that models based on quasi-steady theory would be challenged in such computations.
  - Peak pressure: The peak internal pressures,  $\check{Cp}_i$ , also increase with larger  $G/H$  but they are relatively independent of the effects of  $G/H$  at the panels nearer the reattachment point, implying that the effects of  $G$  and  $H$  on pressure equalization is not consistent across all panels. This is due to relative differences in the external and internal pressures causing the presence of adjacent upward and downward net loads.
3. Mechanisms of flows and pressures: With external and cavity pressure distributions, the orifice (discharge) flows through gaps between panels and the

cavity (Couette) flows between layers are generated and these sequential flows are controlled by geometric parameters ( $G$ ,  $H$  and  $L$ ), friction factor,  $f$ , and loss coefficient,  $C_L$ . Based on dimensional analysis of the flows involved in a double-layer system (i.e., the discharge equation and one-dimensional Couette flow), we found that the mean pressure distribution in the cavity depends on two dimensionless parameters,  $G/H$  and  $\frac{fL/H}{C_L}$ . The smaller the parameters the more uniform the cavity pressure distribution is (e.g., the cavity pressure is uniform with  $G/H = 0.2$  for the current building size, panel size and shape, and wind direction). The non-dimensional parameter controlling this is  $\left[\frac{G}{H}\right]^2 \left[\frac{fL/H}{C_L}\right]$ , given external pressure gradient,  $\Delta P_e$ , and the panel thickness,  $l_o$ .

### 5.3 Development of One-Dimensional Modelling of Flows in Double-Layer Systems

The objective of this research work was to develop a numerical model to predict the unsteady pressure distribution in the cavity within an air permeable, double-layer roof system. The analytical model was developed considering the flows involved in a double-layer system, i.e., the orifice (i.e., gap) flow and the cavity flow. The gap flow between panels is modeled by the discharge equation, while the cavity flow between layers is modeled by the one-dimensional equation for Couette flow. Since the flows are continuous, this problem can be solved simultaneously by combining the discharge equation and the equation for the cavity flow (i.e., Couette flow), and applying the continuity equations. The approach for the numerical model requires as input the external pressure time histories at the openings so that the cavity (interior) pressure time histories can be obtained. The numerical simulations were conducted with two different approaches using the external pressure coefficients time histories,  $Cp_e(t)$ , at the gaps as the input: (i)  $Cp_e(t)$  from point pressure taps along the middle row, and (ii) spanwise-averaged  $Cp_e(t)$ . The numerical results simulated by the analytical model are validated by comparing with wind tunnel data. The main conclusions are summarized below:

1. Numerical  $Cp_i(t)$  from point external pressures: The numerical results obtained by using the point pressure  $Cp_e(t)$  are compared with  $Cp_i(t)$  obtained from experiments in plots of time history, spectra and distributions of mean and RMS pressure coefficients. The results indicate that the numerical model captures the variations and shapes of the pressure distribution of  $Cp_i$ , although there are some discrepancies (i.e., about  $\pm 5$  % for mean and  $+5 \sim +15$  % for RMS) in magnitude. The bias in RMS values was found to be due to the use of point external pressures as the input, which may not perfectly represent the driving force for the cavity flow in the numerical computations.
2. Numerical  $Cp_i(t)$  from spanwise-averaged external pressures:
  - Spanwise correlation: The analysis of the spanwise correlation of pressure data shows that, depending on  $G/H$ , the spanwise  $Cp_i$  are closely correlated, indicating that  $Cp_i$  depends on the spanwise-averaged  $Cp_e$  values, instead of following a single  $Cp_e$ .
  - Mean and RMS pressure distribution: Results from numerical simulation by employing the spanwise-averaged  $Cp_e$  indicate that the pressure distributions of both the mean and RMS  $Cp_i$  are within a range of numerical error of about  $\pm 5$  % (when  $G/H < \sim 2$  for the panel size examined herein). This implies that the spanwise-averaged  $Cp_e$  does not alter the mean  $Cp_i$  due to the fact that mean flow is one-dimensional. However, the numerical RMS values are decreased and much closer to the experimental results, which means that fluctuating components of the local  $Cp_e$  are attenuated during area-averaging and that the simulated cavity pressures are not affected by the highly fluctuating, but localized, external pressures. As a result, the numerical model better captures  $\tilde{Cp}_i$ , especially for larger  $H$  (or smaller  $G/H$  values).
  - Peak pressure distribution: Minimum peak distributions of the cavity pressure coefficients are compared between the numerical and experimental results, as well as instantaneous local pressure coefficient distributions. The numerical simulation results using the spanwise-averaged  $Cp_e$  for the input indicate that the numerical model is able to predict the shape of peak and instantaneous pressure distributions to a great extent, while the magnitudes of peak pressures

gradually increase as  $G/H$  increases. However, with larger  $G/H$  values, the accuracy of the numerical prediction is not as good as that for smaller  $G/H$ . The current work indicates that the spanwise averaging works well for these one-dimensional flow fields when  $G/H < \sim 2$  (for this particular panel size).

3. Numerical  $Cp_i(t)$  from external pressures using bare roof data: The numerical computations from two different  $Cp_e$  data sets were compared, one with and the other without the presence of the gaps and cavities. The numerical predictions were found to be very similar, indicating that experiments conducted without panels may be used to estimate the cavity pressures and net panel wind loads.
4. Contributions of terms in the analytical model: Variations of the unsteady, discharge and friction terms in the analytical model to pressure drops through the second gap ( $G_2$ ) and in the cavity underneath the second panel were investigated with the mean and RMS values and the time history plots for  $G = 1.5$  mm,  $H = 1.2$  mm. The results indicate that the discharge effect at the gap flow and the friction in the cavity flow are the main cause of the pressure drop. However, the unsteady term plays a role in determining fluctuating and peak pressures.

## 5.4 Pressure Distributions on Roof-Mounted Photovoltaic Arrays

The purpose of this work was to (i) determine whether the analytical model developed in Chapter 3 is applicable to a practical problem which consists of 12 photovoltaic rows placed at the entire roof zones from the separation, the reattachment point, up to the leeward zone, and (ii) discuss how this analytical model can be used as a tool to design compartments for pressure equalizing, double-layer systems. One set of existing wind tunnel test data was used for this study. The current author did not contribute to the experimental modelling and wind tunnel testing. As in Chapters 2 and 3, this study again focuses on winds ( $0^\circ$  and  $180^\circ$ ) perpendicular to the photovoltaic panel array and building edges so that the mean pressure in the cavity between photovoltaic panels and roof is approximately one-dimensional. The main conclusions are as follows:

1. Area-averaged cavity pressures on panels
  - Mean, RMS and peak values: The experimental and numerical results show that the cavity pressure coefficients are localized, following the external pressure coefficients for this photovoltaic panel arrays, although the RMS interior pressure coefficients are significantly attenuated. The numerical model can estimate the attenuations of fluctuating pressures to a great extent, while the numerical results from different spanwise-averaged  $C_{pe}$  are altered for the RMS and peak cavity pressure coefficients. This indicates that unsteady effects on the loss coefficients of the gap flows may not be fully accounted for.
  - Time histories and spectra: The numerical model captures fluctuations of the area-averaged cavity pressure coefficients presented in time history plots. However, the magnitudes of the predicted temporal cavity pressure coefficients tend to be lower beneath row 1 (i.e., the panel at the leading edge) and greater beneath rows 5 and 6 (i.e., the panels in regions of the reattachment point), compared with experimental data.
2. Point pressure distributions: Mean, RMS and peak (minimum) point pressure coefficients along the midplane are investigated, comparing the measured external and cavity pressure coefficients and numerical cavity pressure coefficients. It is observed that the external pressures are altered by the local flows generated by gaps between panels, as discussed in Chapter 2 and by Pratt and Kopp (2013). It seems that secondary flow separations occur at the trailing edge of photovoltaic panels within the reattachment point (i.e.,  $x/h < 1$ ) and at the leading edge of photovoltaic panels beyond the reattachment point (i.e.,  $x/h > 1$ ). As a result, the external pressures as input should be carefully selected, since the local flow-driven aspects of external pressures are not transmitted into the cavity. In this study, the lower value of RMS external pressures between two adjacent pressure taps at gaps (i.e., pressure taps at the trailing edge of photovoltaic panels before reattachment point and pressure taps at the leading edge of photovoltaic panels after reattachment point) are used for  $C_{pe}$  as input. They are expected to represent more reliable pressures at the gaps between panels for modelling the cavity pressures. The pressure gradient of mean cavity

pressure coefficients is fairly similar to the external pressures, while RMS interior pressure coefficients are significantly attenuated. This implies that the mean cavity flow dominates the mean pressure drop, while fluctuating pressures are attenuated by flow through gaps between panels, for this photovoltaic panel array. The numerical model predicts the shape of the mean and RMS cavity pressure distributions with considerable accuracy, even though there are some differences, in particular, on panels in the region of the leading edge and the reattachment point on the roof.

### 3. Numerical investigations on compartmentalization

- Compartmentalization in different number of rows: The numerical simulation shows that the cavity pressure coefficients are found to vary significantly with the compartmentalization in different number of rows, for this photovoltaic panel array. For a given gap-to-cavity ratio,  $G/H$ , the mean cavity pressure gradients decrease while the number of rows within the compartment decreases. This should be due to the smaller  $\Delta\bar{C}p_e$  and the shorter length of the cavity ( $L$ ) when decreasing the number of rows.
- Compartmentalization between the edge and intermediate rows: Compartmentalization between the edge and intermediate rows (i.e., between rows 3 and 4, and between rows 9 and 10) play a significant role in reducing the uplift net loads on the photovoltaic array, in particular, at the compartmentalized cavity in the leading edge of the roof. The compartment-induced reductions of the uplift net loads on the row 1 are approximately 60 % and 85 % for mean and peak values, respectively. This indicates that the compartment effect is greater in regions of separated flow, since the significant cavity flows induced by the large magnitude of external pressure gradient,  $\Delta Cp_e$ , are resisted by the compartmentalization.
- Compartmentalization between modules: The single module beneath which the underside (cavity) is compartmentalized shows reductions on the RMS and peak uplift net loads by restricting local flow along the span between modules. Although these numerical simulations for the effects of compartmentalization were not validated with experimental data, the numerical results show how the



analytical model can be used in design as a tool to set compartments for reducing the wind loads on pressure equalizing, double-layer systems.

## 5.5 Recommendations for Future Research

A number of additional issues need further study to complement the results presented in this thesis and to fully complete the analytical model developed in Chapter 3. The following recommendations are outlined for future research.

1. The thickness of the outer layer should be an important geometric parameter, in particular, for small gaps between panels. The thickness appears in the numerical model as  $l_o$ . This should be validated with experimental data.
2. The “sudden” pressure drop during a peak of the external pressure for large gap-to-cavity ratio (i.e.,  $G/H$ ) should be investigated more fully, perhaps, by either the spanwise-averaging with higher external pressure tap resolution or the investigation on the loss coefficient for unsteady flows.
3. More research on the effects of the Reynolds number and the friction factor,  $f$ , for the turbulent flows (if possible, with an experimental study in full-scale) are required to understand differences in results between laminar flow in model-scale and turbulent flow in full-scale.
4. The analytical model needs to be extended to simulate two-dimensional pressure distribution in the cavity. A possible idea of the two-dimensional modelling of the cavity pressure is that the interior volume within a cavity is divided into a finite number of “control volumes” in which the equation of the Couette flow is applied to two-directions. Thus, the two-dimensional model allows two-dimensional flows in the cavity. A preliminary study on the two-dimensional modelling of the flow in the cavity is presented in Appendix D.

## Appendix A

### Numerical Method

To solve the simultaneous ordinary differential equations, a 2<sup>nd</sup> order, backward differencing, numerical approximation of the derivatives (Chapra and Canale, 2006) were used as follows,

$$\dot{U}(t) = \frac{3U(t) - 4U(t-1) + U(t-2)}{2d} \quad (\text{A.1})$$

where  $t = 1, 2, \dots, n$  is the time index,  $d$  is the time step between  $t$  and  $t-1$ . Substituting the derivative terms with Eq. (A.1), the first-order differential equation, Eq. (3.12) can be expressed as:

$$a_{11} \frac{3U_1(t) - 4U_1(t-1) + U_1(t-2)}{2d} + a_{12}U_1(t)|U_1(t)| + a_{13}U_1(t) = P_{e1}(t) - P_{i1}(t) \quad (\text{A.2a})$$

$$b_{11} \frac{3U_1(t) - 4U_1(t-1) + U_1(t-2)}{2d} + b_{12}U_1(t) = P_{i1}(t) - P_{i2}(t) \quad (\text{A.2b})$$

$$a_{21} \frac{3U_1(t) - 4U_1(t-1) + U_1(t-2)}{2d} + a_{22}U_1(t)|U_1(t)| + a_{23}U_1(t) = P_{e2}(t) - P_{i2}(t) \quad (\text{A.2c})$$

where  $a_{i1} = \rho l_{ei} \frac{H}{G_i}$ ,  $a_{i2} = C_{Li} \frac{\rho}{2} \left( \frac{H}{G_i} \right)^2$ ,  $a_{i3} = \frac{12\mu l_{oi}H}{G_i^3}$ ,  $b_{i1} = \rho L_i$  and  $b_{i2} = \frac{12\mu L_i}{H^2}$ .

To solve the non-linear simultaneous equations in Eq. (A.2), the non-linear term,  $U_1(t)|U_1(t)|$  is linearized by defining an approximate value for  $|U_1(t)|$  so that Eq. (A.2) become simultaneous linear equations with three unknowns of  $U_1$ ,  $P_{i1}$  and  $P_{i2}$ . Then, the simultaneous linear equations can be solved explicitly for given external pressure data,  $P_{e1}(t)$  and  $P_{e2}(t)$ , and the initial values for  $U_1(t-1)$  and  $U_1(t-2)$ . Now, the solution of  $U_1$  should be identical to the approximate value for  $|U_1|$ . If not, a new approximate value,  $|U_1(t)|_{new}$ , is defined by  $0.5U_1 + 0.5|U_1|_{old}$  and the equations are solved repeatedly. This computation process is iterated until the solution of  $U_1$  and the approximate value of  $|U_1|$  are converged. Further details of the iteration method can be found in Oh (2004). A computational code programed in Matlab is used to repeat all the time steps. The numerical simulation was similar to the computation by a 4<sup>th</sup>-order Runge-Kutta method, within an error of 1 %, while being faster.

**Appendix B**  
**Spanwise Correlation and Area-Averaged Pressures on**  
**Photovoltaic Arrays for 0° wind**

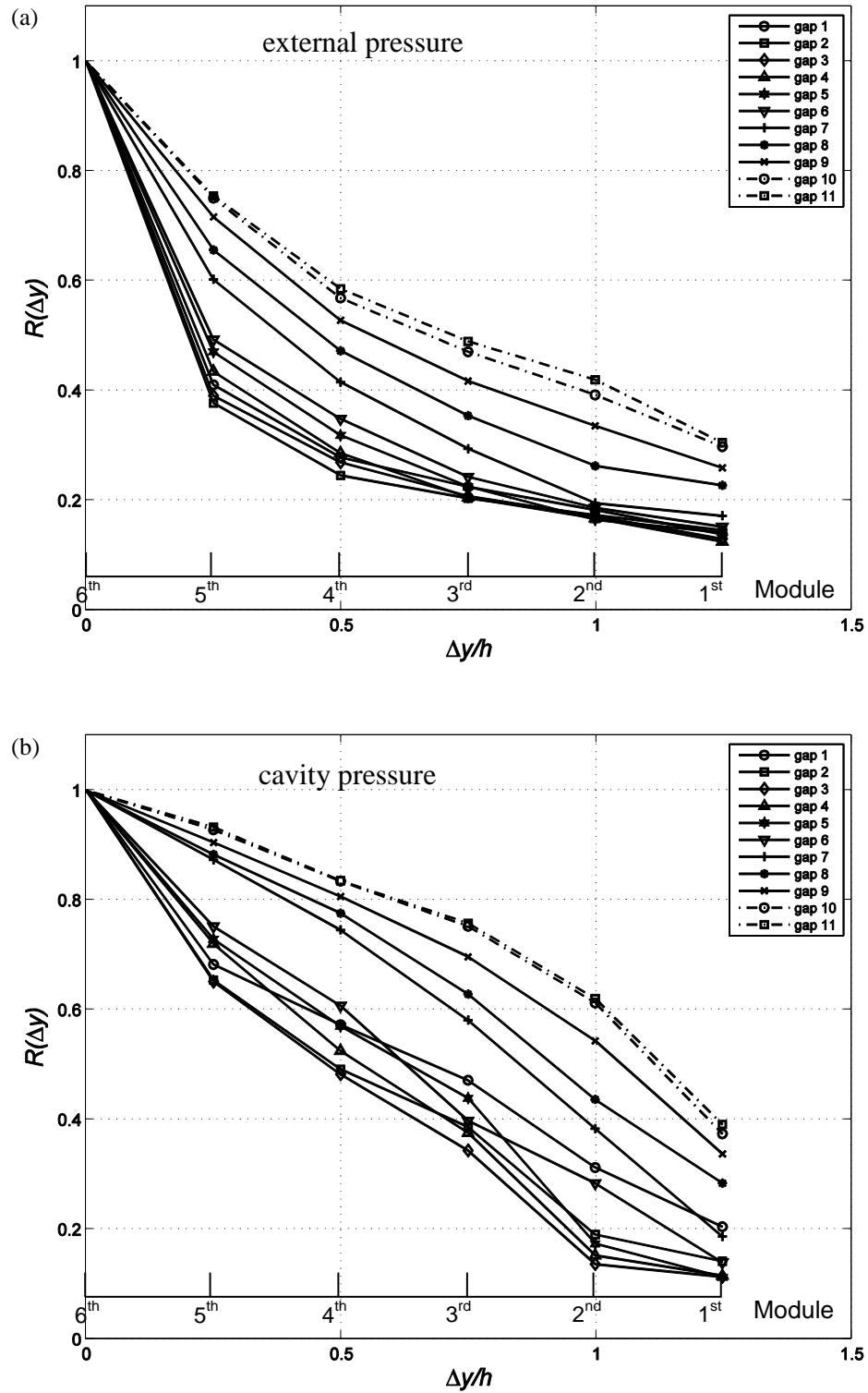


Figure B.1 Correlation of pressure data in the y-direction with respect to the pressure taps in the midplane (i.e., Module 6), for 0° wind: (a)  $C_{p_e}$ ; (b)  $C_{p_i}$ . Straight lines are used to connect data points, for clarity only.

Table B.1 Mean area-averaged pressures on Module 6 for 0° wind

| Row | Measured     |              | Numerical                                     |       |       |       |       |       |
|-----|--------------|--------------|---|-------|-------|-------|-------|-------|
|     | $\bar{C}p_e$ | $\bar{C}p_i$ | $\bar{C}p_i^*$                                |       |       |       |       |       |
|     |              |              | No. of taps for spanwise-averaged $Cp_e^{**}$ |       |       |       |       |       |
|     |              |              | 1   | 3     | 5     | 7     | 9     | 12    |
| 1   | -0.22        | -0.19        | -0.23   | -0.22 | -0.22 | -0.22 | -0.22 | -0.22 |
| 2   | -0.24        | -0.18        | -0.23   | -0.23 | -0.23 | -0.23 | -0.22 | -0.22 |
| 3   | -0.24        | -0.18        | -0.25   | -0.25 | -0.25 | -0.24 | -0.24 | -0.24 |
| 4   | -0.26        | -0.21        | -0.29   | -0.28 | -0.28 | -0.27 | -0.27 | -0.26 |
| 5   | -0.3         | -0.26        | -0.33   | -0.33 | -0.32 | -0.32 | -0.31 | -0.31 |
| 6   | -0.35        | -0.33        | -0.4  | -0.39 | -0.38 | -0.38 | -0.37 | -0.36 |
| 7   | -0.42        | -0.41        | -0.47   | -0.46 | -0.45 | -0.45 | -0.44 | -0.43 |
| 8   | -0.52        | -0.53        | -0.55   | -0.55 | -0.54 | -0.54 | -0.53 | -0.51 |
| 9   | -0.66        | -0.67        | -0.65   | -0.65 | -0.64 | -0.64 | -0.63 | -0.61 |
| 10  | -0.81        | -0.82        | -0.75   | -0.75 | -0.75 | -0.75 | -0.74 | -0.72 |
| 11  | -0.98        | -0.94        | -0.84   | -0.85 | -0.84 | -0.84 | -0.84 | -0.82 |
| 12  | -1.1         | -1.04        | -0.89   | -0.9  | -0.9  | -0.9  | -0.89 | -0.88 |

\*: Numerical  $Cp_i$  are calculated from six different cases of spanwise-averaged  $Cp_e$ .

\*\*: The numbers indicate the number of pressure taps used to obtain spanwise-averaged  $Cp_e$  which are input for numerical computations. (e.g., 1: tap from Module 6 only, 3: taps from Modules 5, 6 & 7, and 12: taps from all Modules from 1 to 12)

Table B.2 RMS area-averaged pressures on Module 6 for 0° wind

| Row | Measured       |                | Numerical                                     |      |      |      |      |      |
|-----|----------------|----------------|---|------|------|------|------|------|
|     | $\tilde{C}p_e$ | $\tilde{C}p_i$ | $\tilde{C}p_i^*$                              |      |      |      |      |      |
|     |                |                | No. of taps for spanwise-averaged $Cp_e^{**}$ |      |      |      |      |      |
|     |                |                | 1   | 3    | 5    | 7    | 9    | 12   |
| 1   | 0.11           | 0.09           | 0.1   | 0.09 | 0.08 | 0.07 | 0.07 | 0.06 |
| 2   | 0.12           | 0.09           | 0.1   | 0.09 | 0.08 | 0.08 | 0.07 | 0.07 |
| 3   | 0.13           | 0.11           | 0.12  | 0.1  | 0.09 | 0.08 | 0.08 | 0.07 |
| 4   | 0.14           | 0.13           | 0.13  | 0.11 | 0.1  | 0.09 | 0.09 | 0.08 |
| 5   | 0.16           | 0.15           | 0.14  | 0.12 | 0.11 | 0.1  | 0.09 | 0.09 |
| 6   | 0.18           | 0.17           | 0.15  | 0.13 | 0.12 | 0.11 | 0.1  | 0.09 |
| 7   | 0.2            | 0.18           | 0.17  | 0.15 | 0.14 | 0.13 | 0.12 | 0.11 |
| 8   | 0.24           | 0.2            | 0.19  | 0.17 | 0.16 | 0.15 | 0.14 | 0.13 |
| 9   | 0.27           | 0.23           | 0.21  | 0.19 | 0.18 | 0.17 | 0.16 | 0.15 |
| 10  | 0.3            | 0.24           | 0.22  | 0.2  | 0.19 | 0.18 | 0.18 | 0.16 |
| 11  | 0.32           | 0.25           | 0.22  | 0.21 | 0.2  | 0.19 | 0.18 | 0.17 |
| 12  | 0.32           | 0.27           | 0.23  | 0.21 | 0.2  | 0.2  | 0.19 | 0.18 |

\*: Numerical  $Cp_i$  are calculated from six different cases of spanwise-averaged  $Cp_e$ .

\*\*: The numbers indicate the number of pressure taps used to obtain spanwise-averaged  $Cp_e$  which are input for numerical computations.

■ : indicate that numerical  $Cp_i$  are within  $\pm 5\%$  of the measured  $Cp_i$ .

Table B.3 Peak (minimum) area-averaged pressures on Module 6 for 0° wind

| Row | Measured       |                | Numerical                                     |       |       |       |       |       |
|-----|----------------|----------------|---|-------|-------|-------|-------|-------|
|     | $\check{C}p_e$ | $\check{C}p_i$ | $\check{C}p_i^*$                              |       |       |       |       |       |
|     |                |                | No. of taps for spanwise-averaged $Cp_e^{**}$ |       |       |       |       |       |
|     |                |                | 1   | 3     | 5     | 7     | 9     | 12    |
| 1   | -1.24          | -0.7           | -1.1  | -0.97 | -0.95 | -0.9  | -0.8  | -0.68 |
| 2   | -1.22          | -0.77          | -1.16   | -0.94 | -0.93 | -0.89 | -0.81 | -0.7  |
| 3   | -1.1           | -0.94          | -1.17   | -1    | -0.94 | -0.87 | -0.8  | -0.7  |
| 4   | -1.32          | -1.13          | -1.45   | -1.21 | -1.12 | -1.01 | -0.92 | -0.8  |
| 5   | -1.73          | -1.32          | -1.46   | -1.33 | -1.21 | -1.08 | -0.94 | -0.84 |
| 6   | -2.07          | -1.27          | -1.57   | -1.39 | -1.27 | -1.16 | -1.03 | -0.91 |
| 7   | -2.06          | -1.32          | -1.61   | -1.42 | -1.32 | -1.22 | -1.13 | -1.07 |
| 8   | -2.18          | -1.56          | -1.63   | -1.5  | -1.46 | -1.34 | -1.3  | -1.25 |
| 9   | -2.48          | -1.81          | -1.77   | -1.72 | -1.6  | -1.49 | -1.43 | -1.36 |
| 10  | -2.69          | -2.14          | -1.78   | -1.83 | -1.74 | -1.66 | -1.58 | -1.52 |
| 11  | -2.96          | -2.25          | -1.95   | -1.83 | -1.74 | -1.71 | -1.65 | -1.6  |
| 12  | -2.86          | -2.51          | -2.06   | -1.94 | -1.84 | -1.78 | -1.76 | -1.7  |

\*: Numerical  $Cp_i$  are calculated from six different cases of spanwise-averaged  $Cp_e$ .

\*\*: The numbers indicate the number of pressure taps used to obtain spanwise-averaged  $Cp_e$  which are input for numerical computations.

■ : indicate that numerical  $Cp_i$  are within  $\pm 5\%$  of the the measured  $Cp_i$ .

**Appendix C**  
**Point Pressures on Photovoltaic Arrays for All Spanwise-**  
**Averaged  $C_{p_e}$**

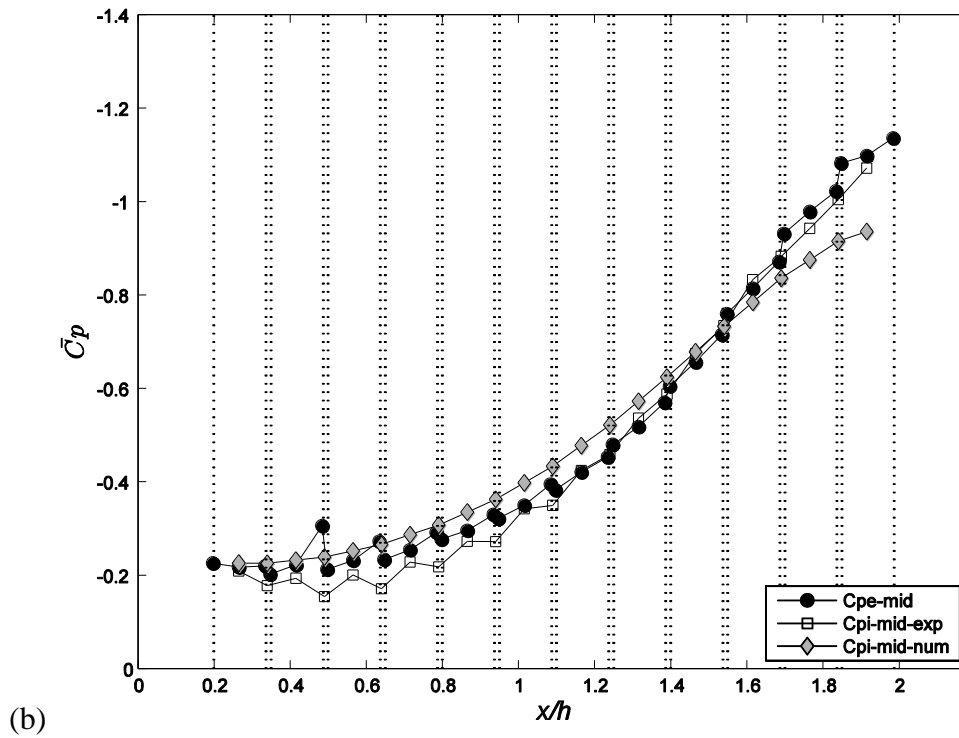
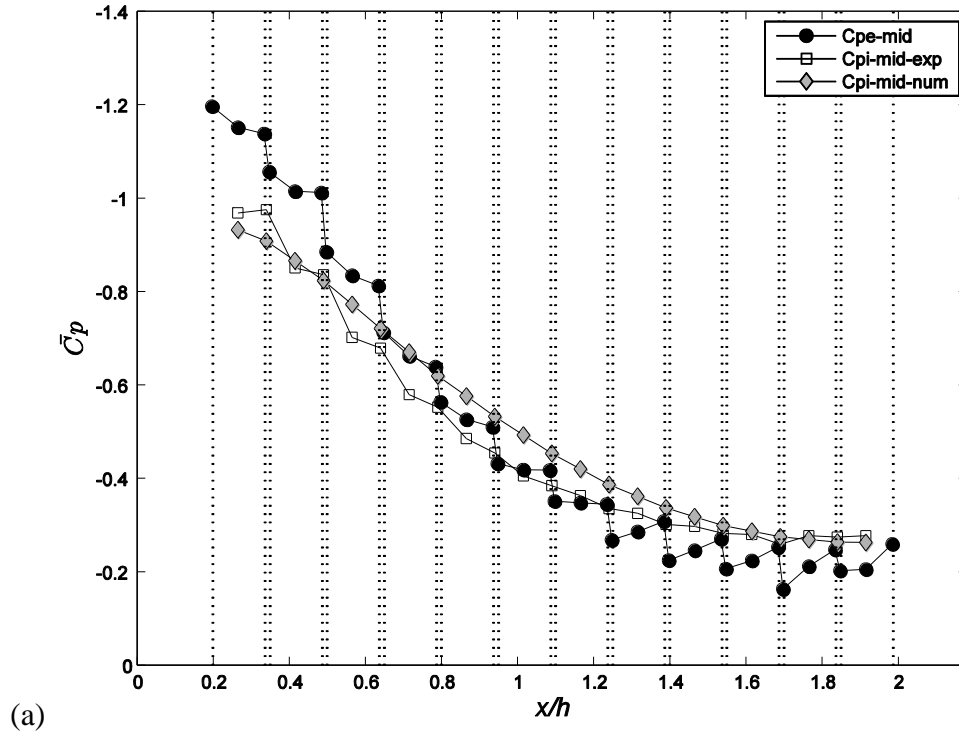


Figure C.1 Mean point pressure distributions for the pressure taps along the midplane (Module 6): (a) for 180°; (b) for 0° wind. – single tap for spanwise-averaged  $C_{p_e}$  –



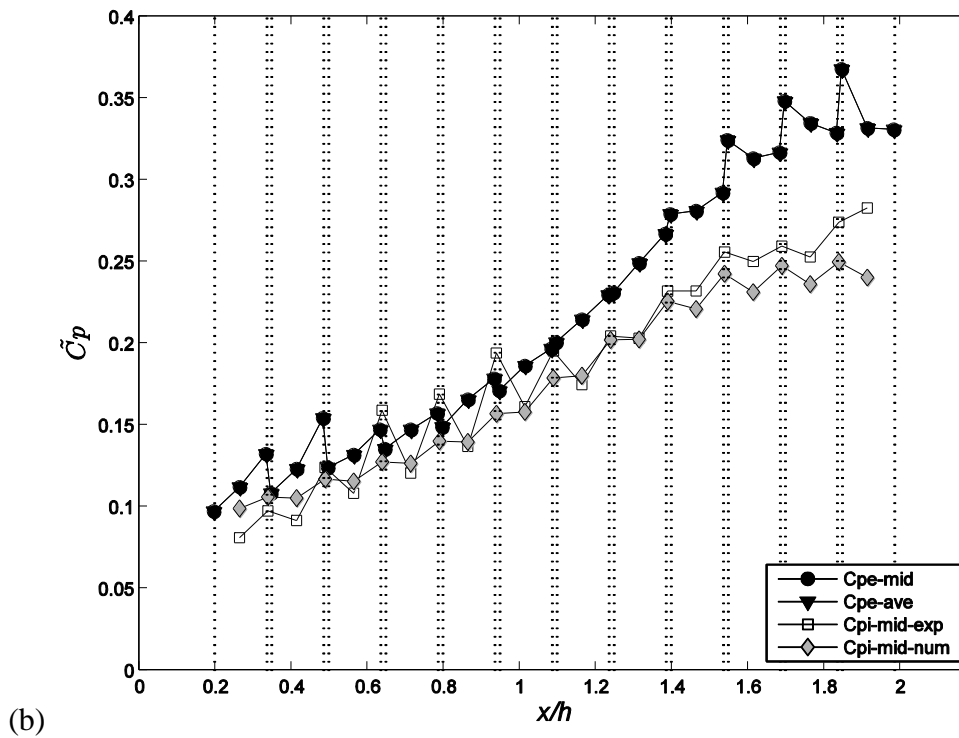
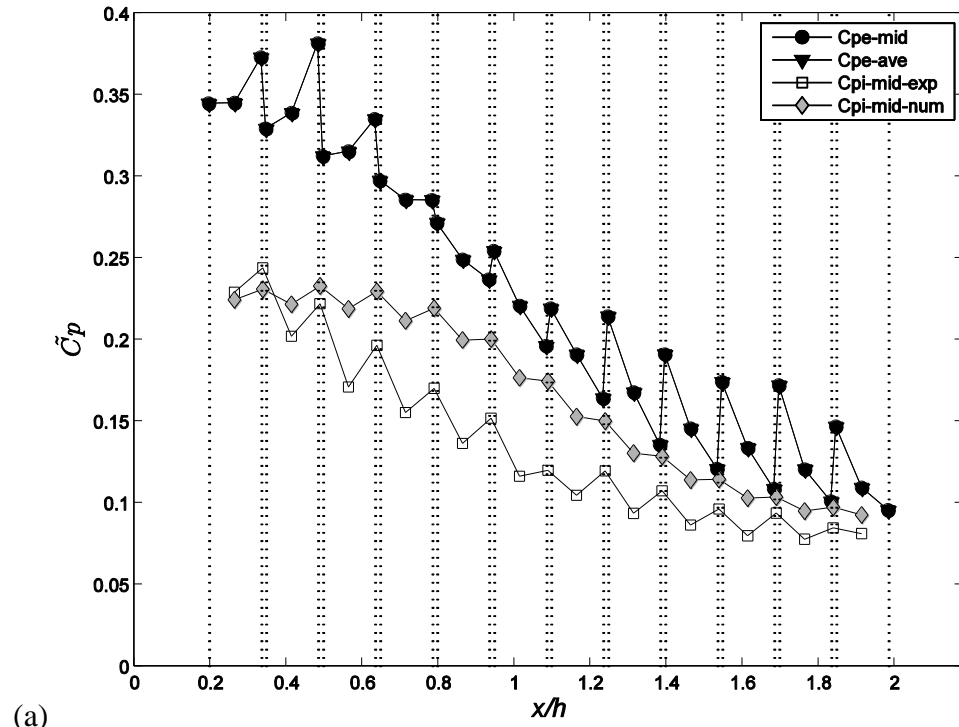


Figure C.2 RMS point pressure distributions for the pressure taps in the midplane (Module 6): (a) for 180°; (b) for 0° wind. – single tap for spanwise-averaged  $C_{p_e}$  –

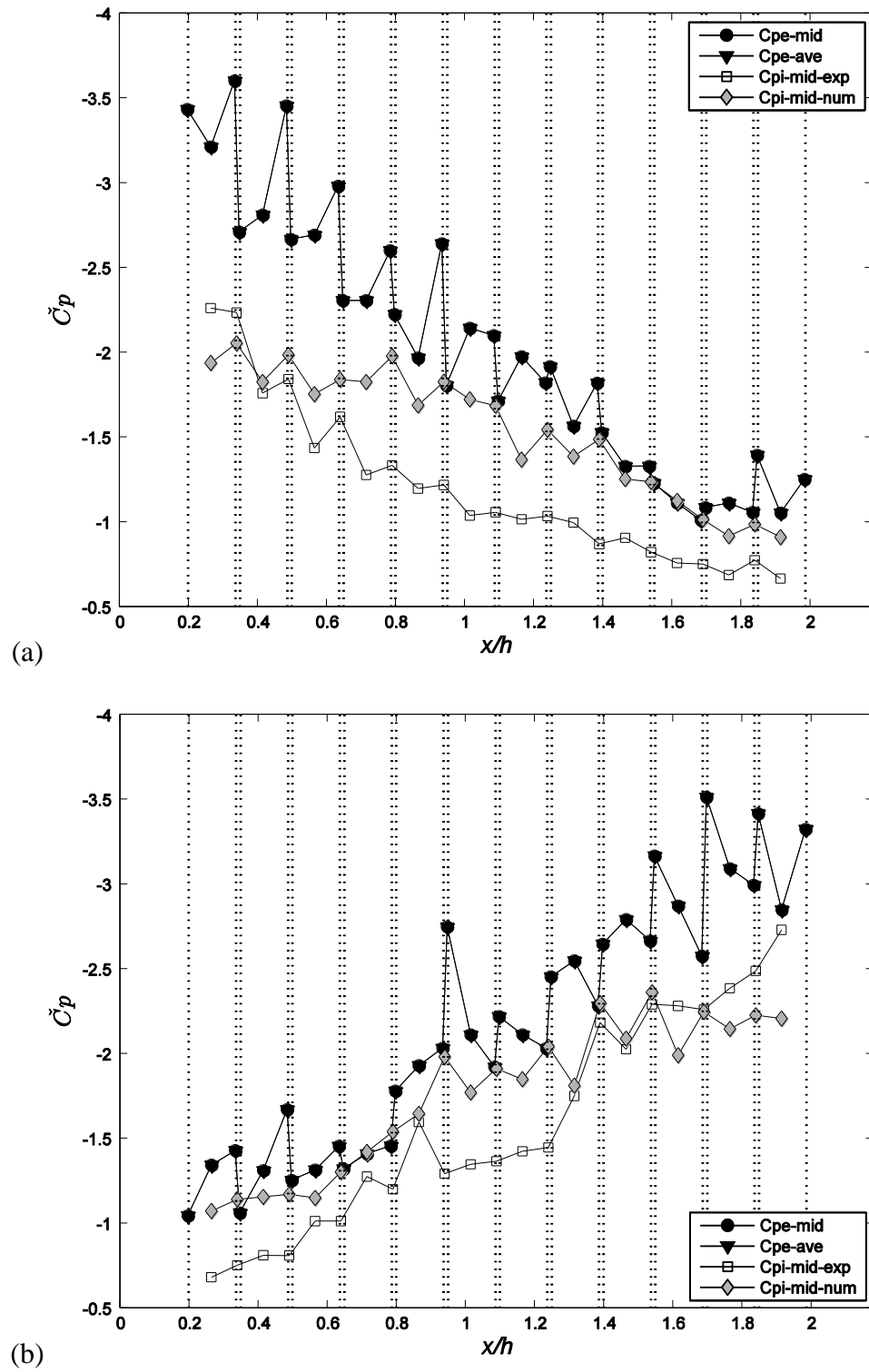


Figure C.3 Peak (minimum) point pressure distributions for the pressure taps in the midplane (Module 6): (a) for  $180^\circ$ ; (b) for  $0^\circ$  wind. – single tap for spanwise-averaged  $C_{p_e}$  –

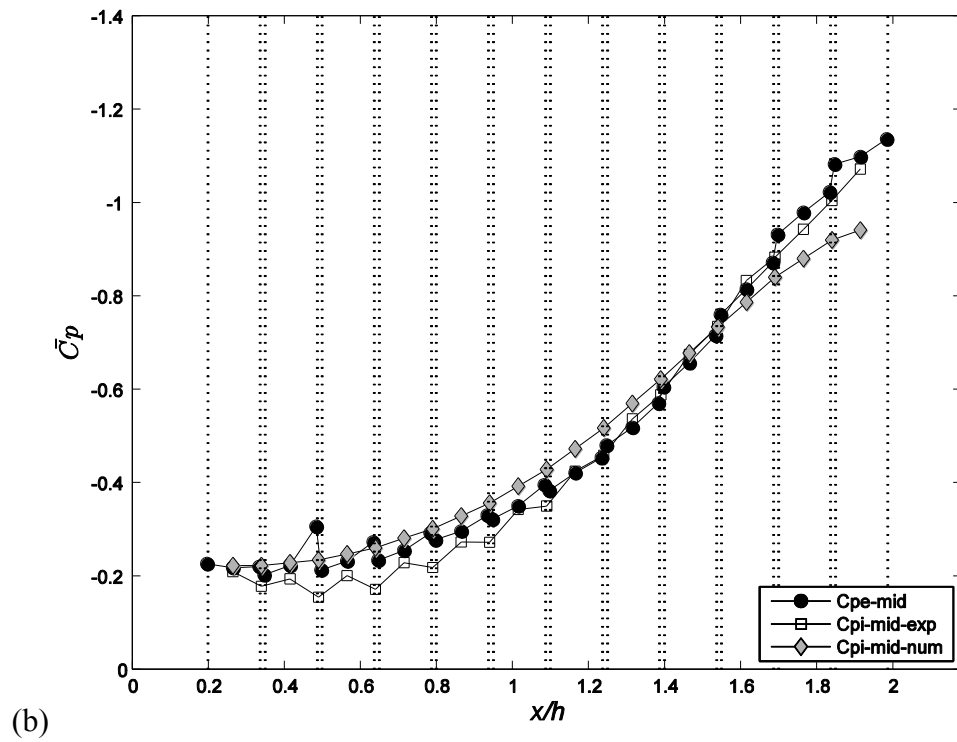
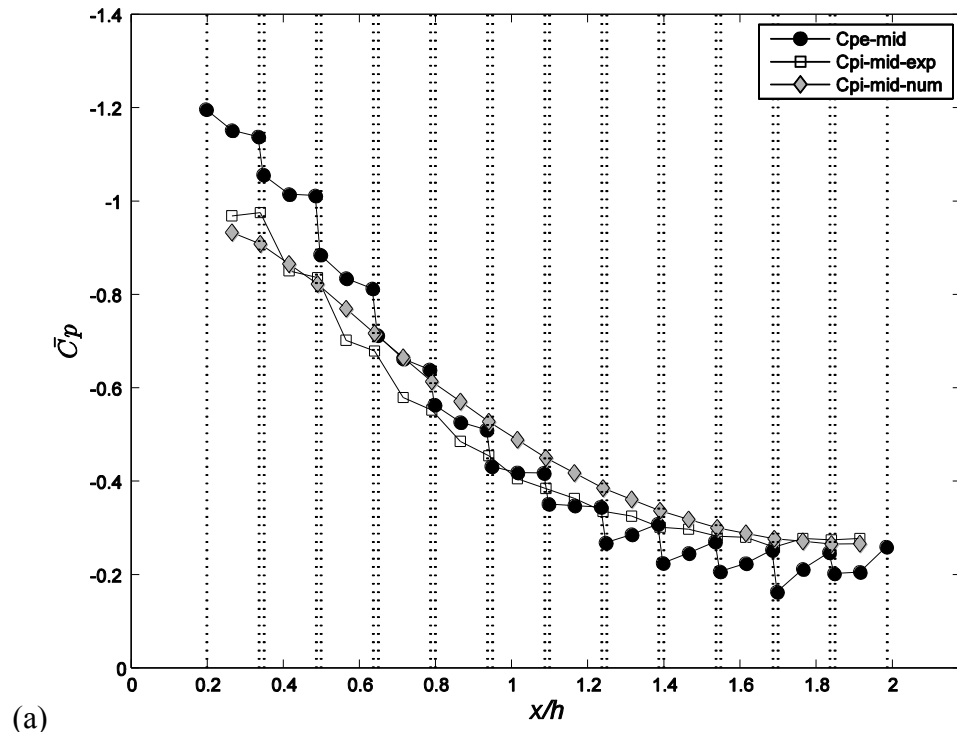


Figure C.4 Mean point pressure distributions for the pressure taps along the midplane (Module 6): (a) for 180°; (b) for 0° wind. – three taps for spanwise-averaged  $C_{p_e}$  –

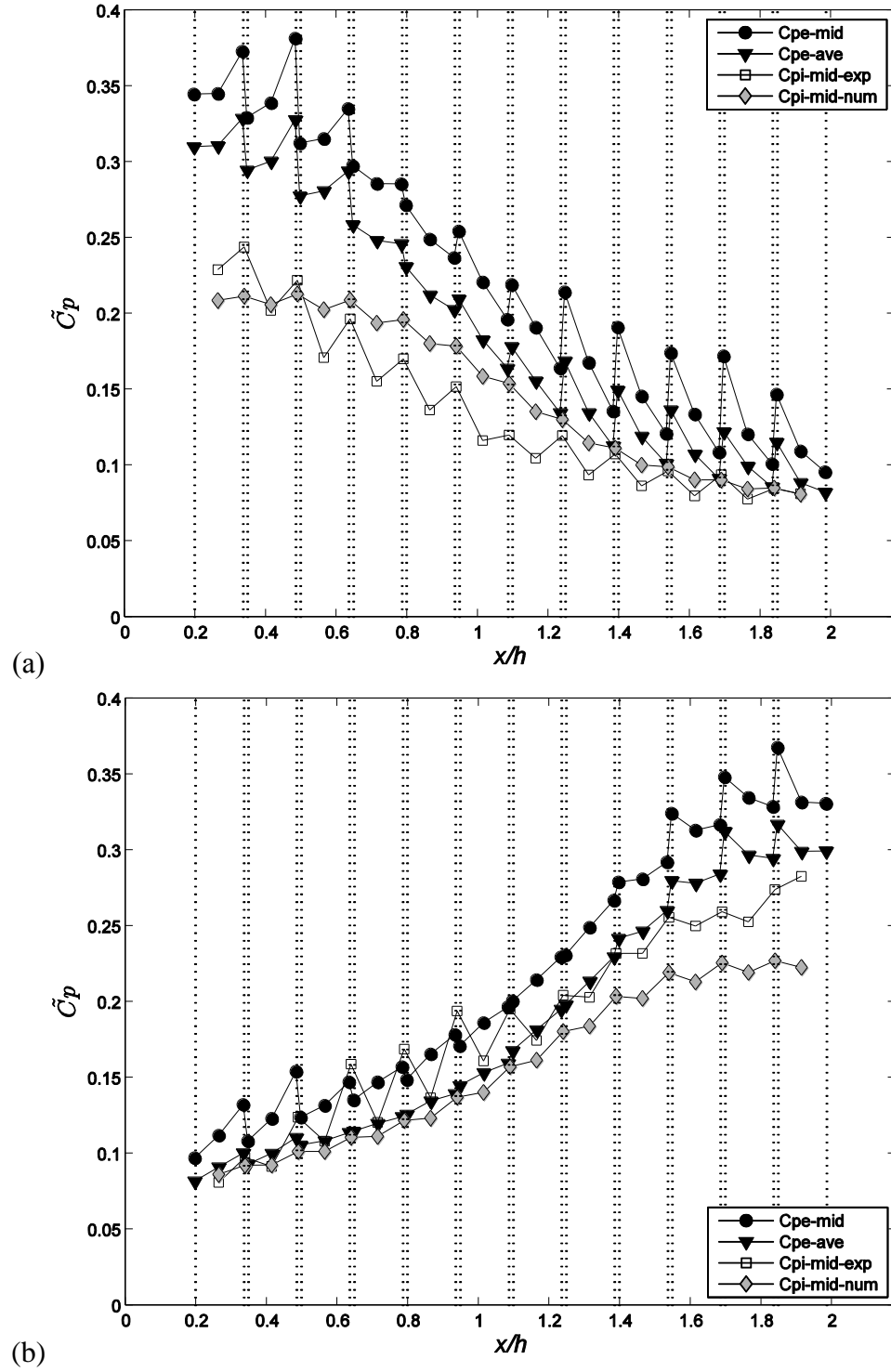


Figure C.5 RMS point pressure distributions for the pressure taps in the midplane (Module 6): (a) for 180°; (b) for 0° wind. – three taps for spanwise-averaged  $C_{p_e}$  –

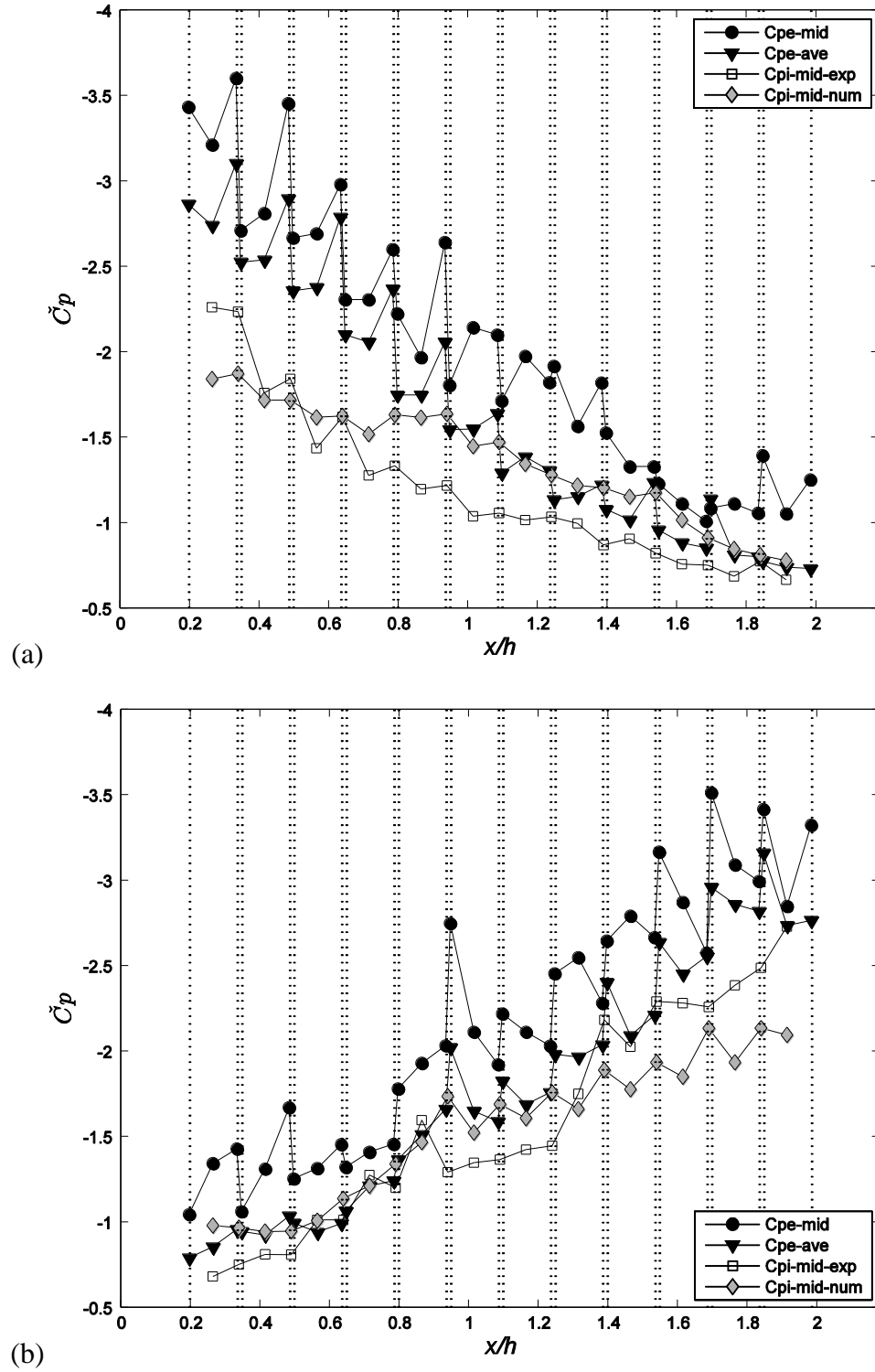


Figure C.6 Peak (minimum) point pressure distributions for the pressure taps in the midplane (Module 6): (a) for 180°; (b) for 0° wind. – three taps for spanwise-averaged  $C_{pe}$  –

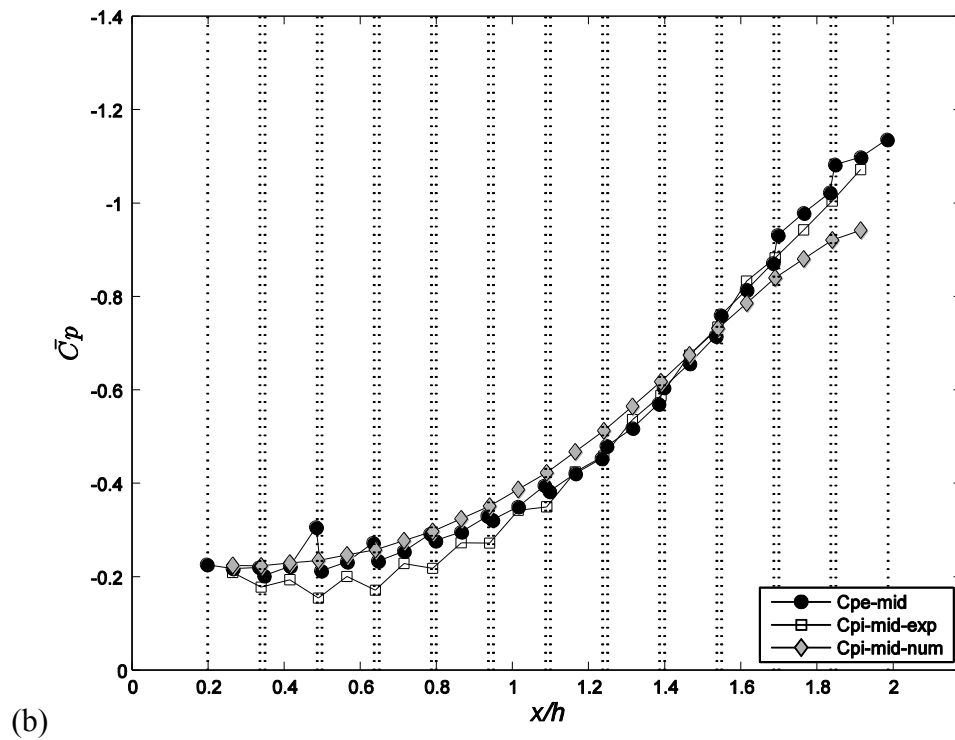
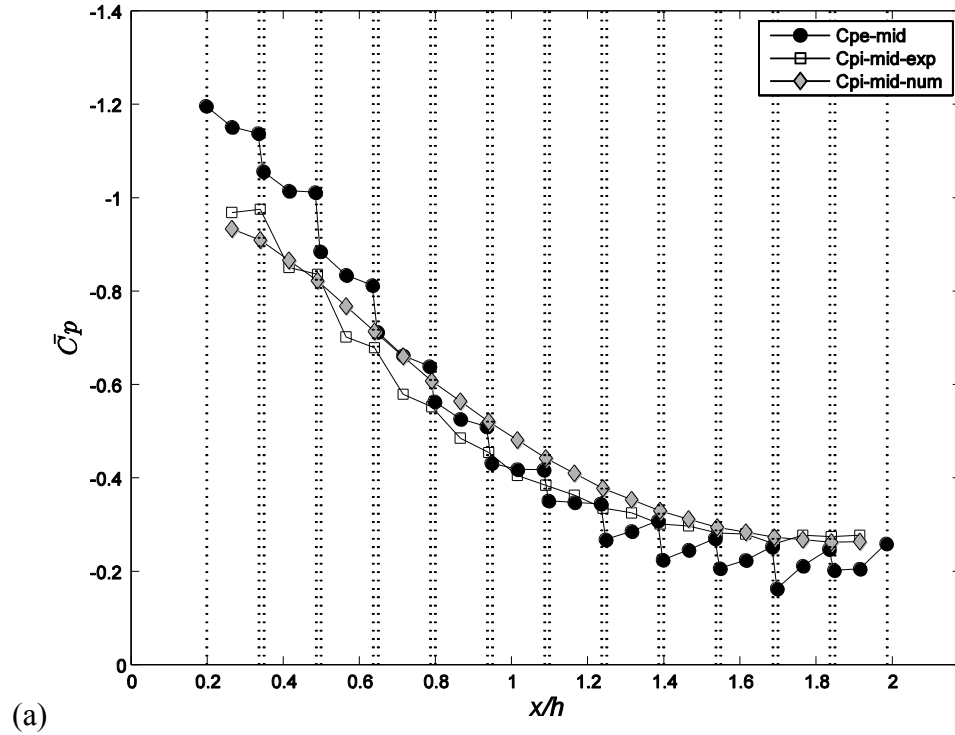


Figure C.7 Mean point pressure distributions for the pressure taps along the midplane (Module 6): (a) for  $180^\circ$ ; (b) for  $0^\circ$  wind. – five taps for spanwise-averaged  $C_{p_e}$  –

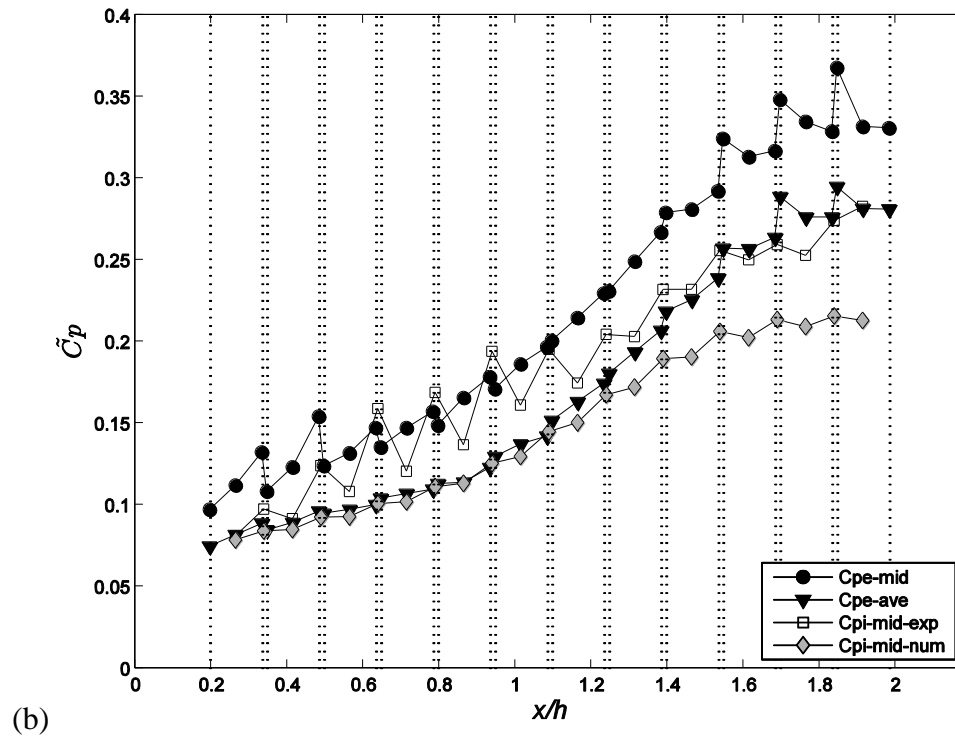
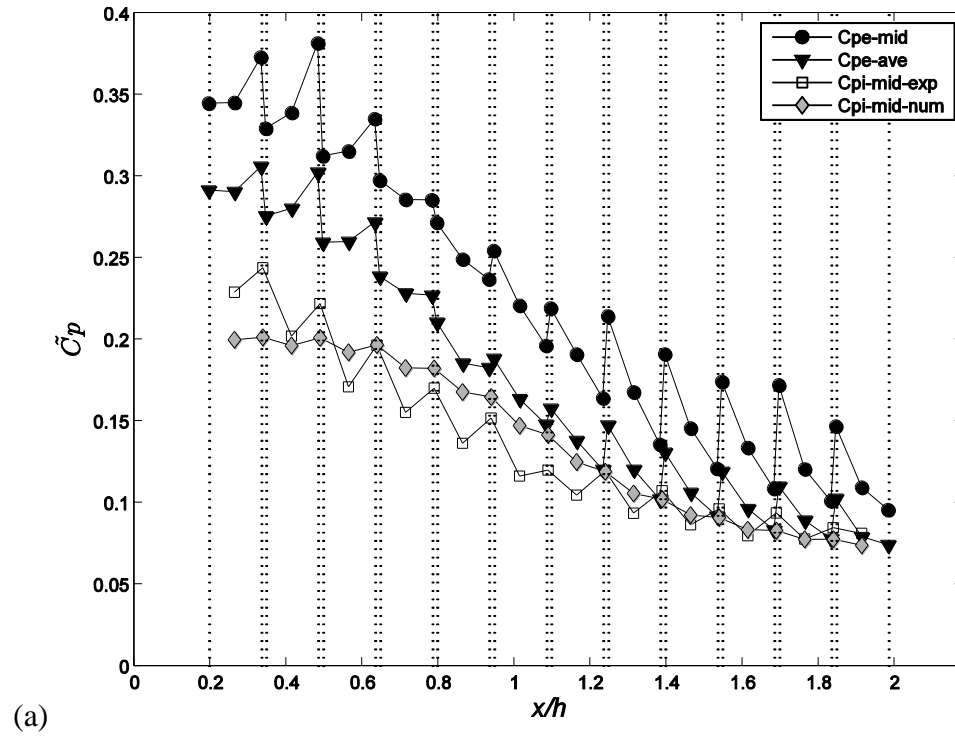


Figure C.8 RMS point pressure distributions for the pressure taps in the midplane (Module 6): (a) for 180°; (b) for 0° wind. – five taps for spanwise-averaged  $C_{pe}$  –

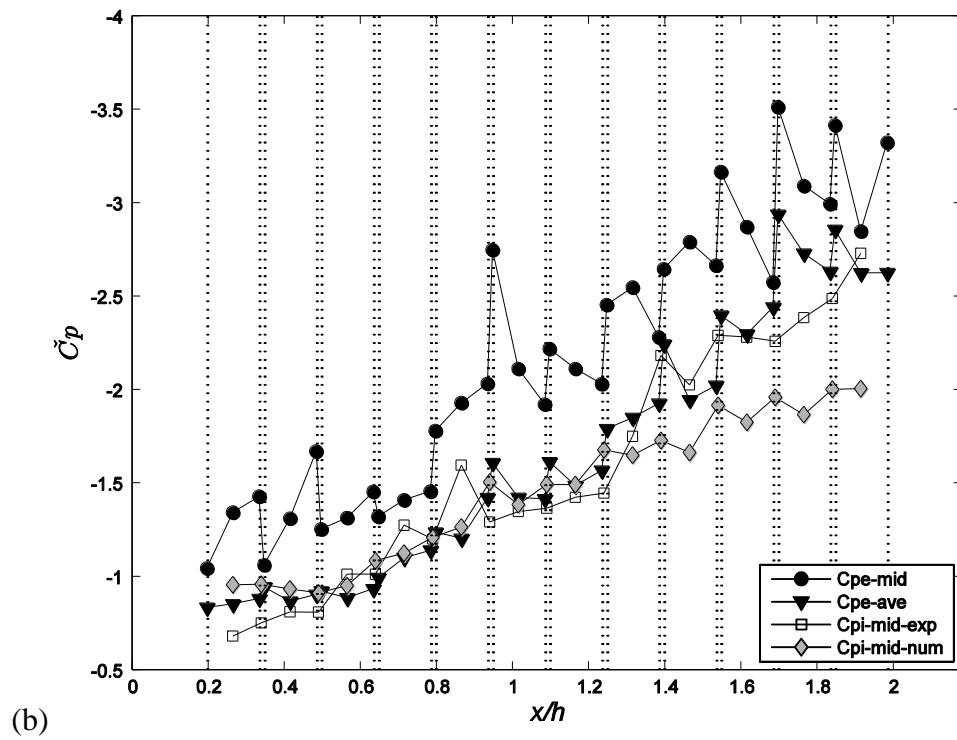
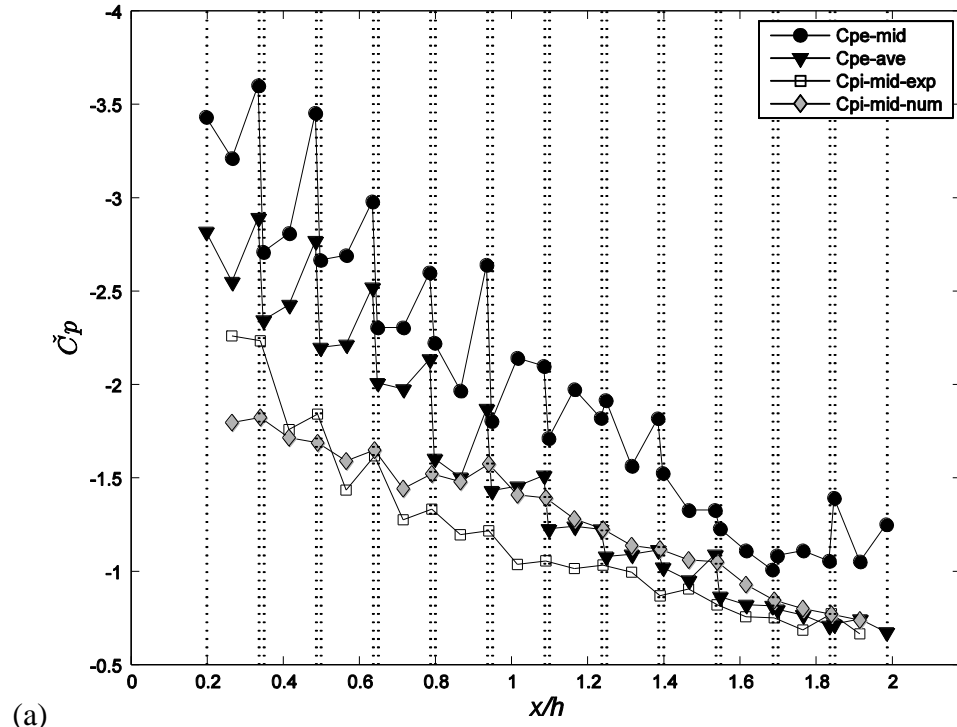


Figure C.9 Peak (minimum) point pressure distributions for the pressure taps in the midplane (Module 6): (a) for 180°; (b) for 0° wind. – five taps for spanwise-averaged  $C_{p_e}$



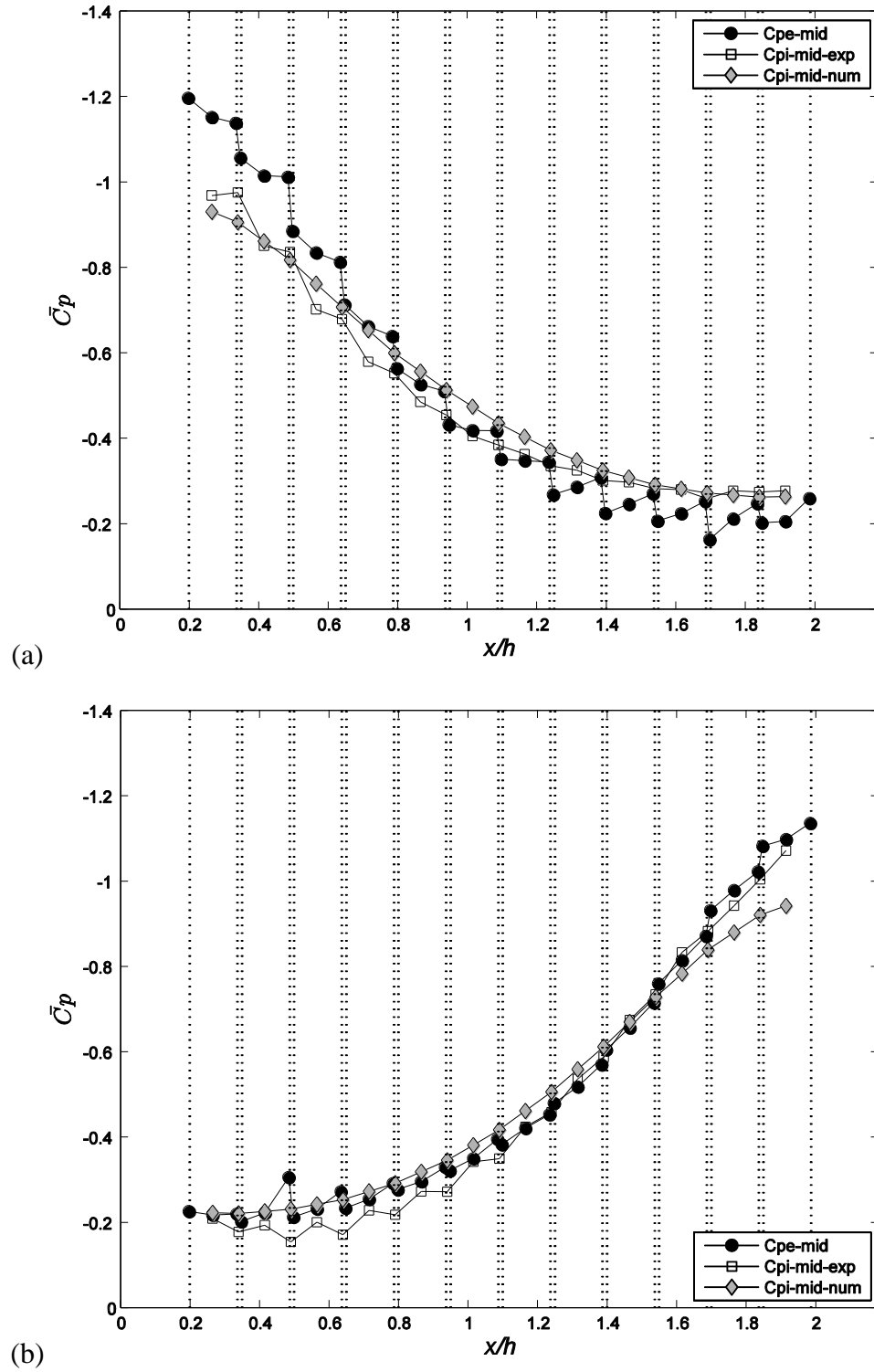


Figure C.10 Mean point pressure distributions for the pressure taps along the midplane (Module 6): (a) for 180°; (b) for 0° wind. – seven taps for spanwise-averaged  $C_{pe}$  –

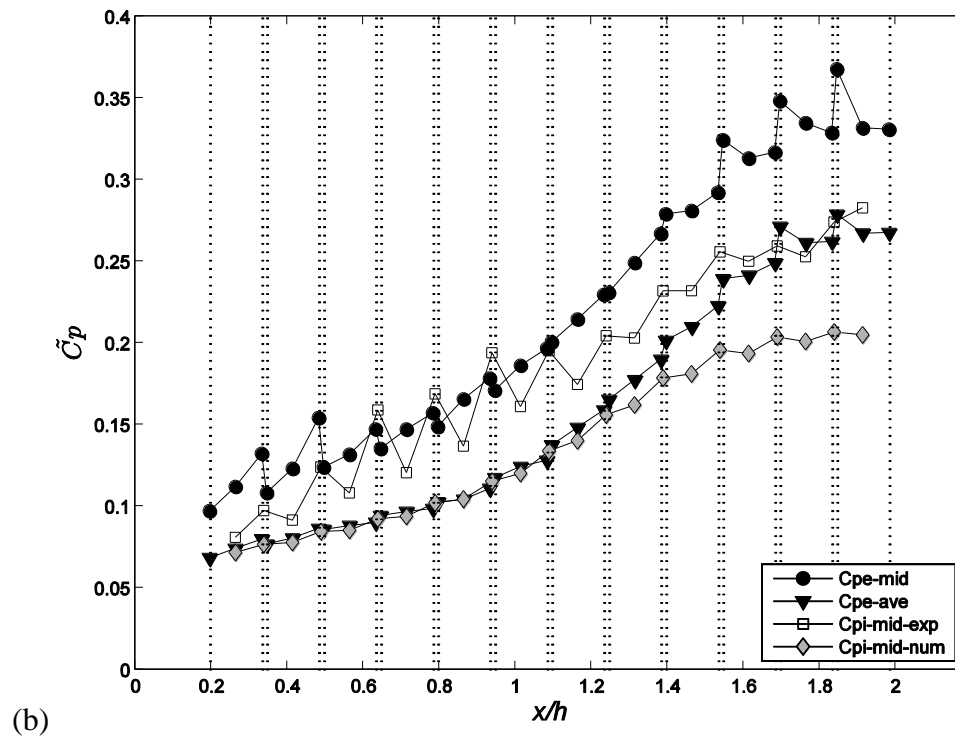
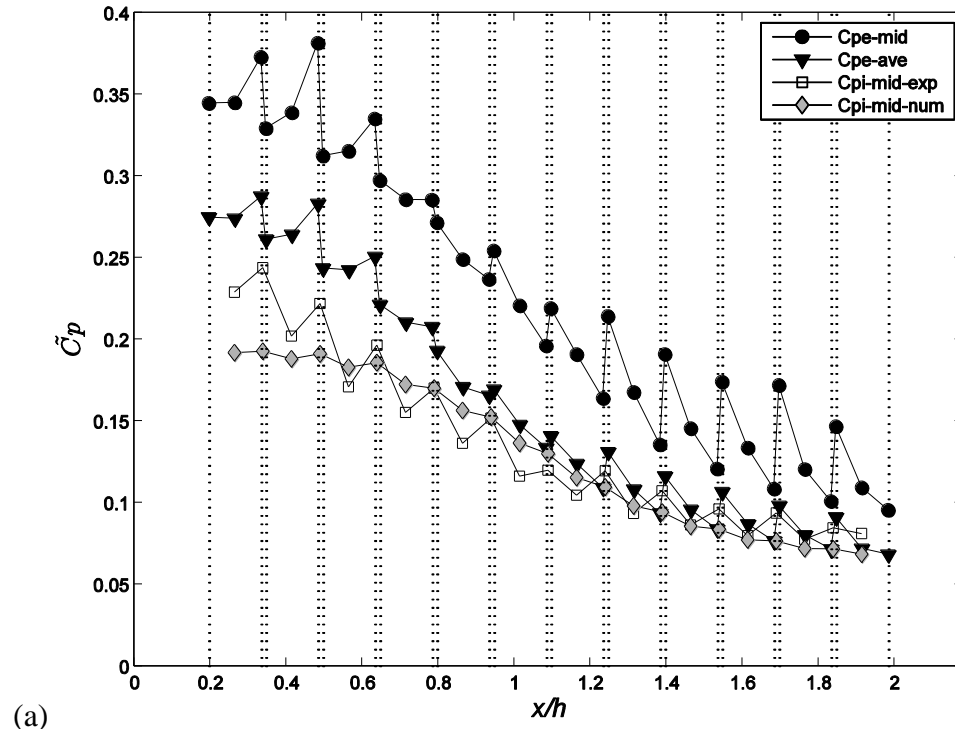


Figure C.11 RMS point pressure distributions for the pressure taps in the midplane (Module 6): (a) for 180°; (b) for 0° wind. – seven taps for spanwise-averaged  $Cp_e$  –

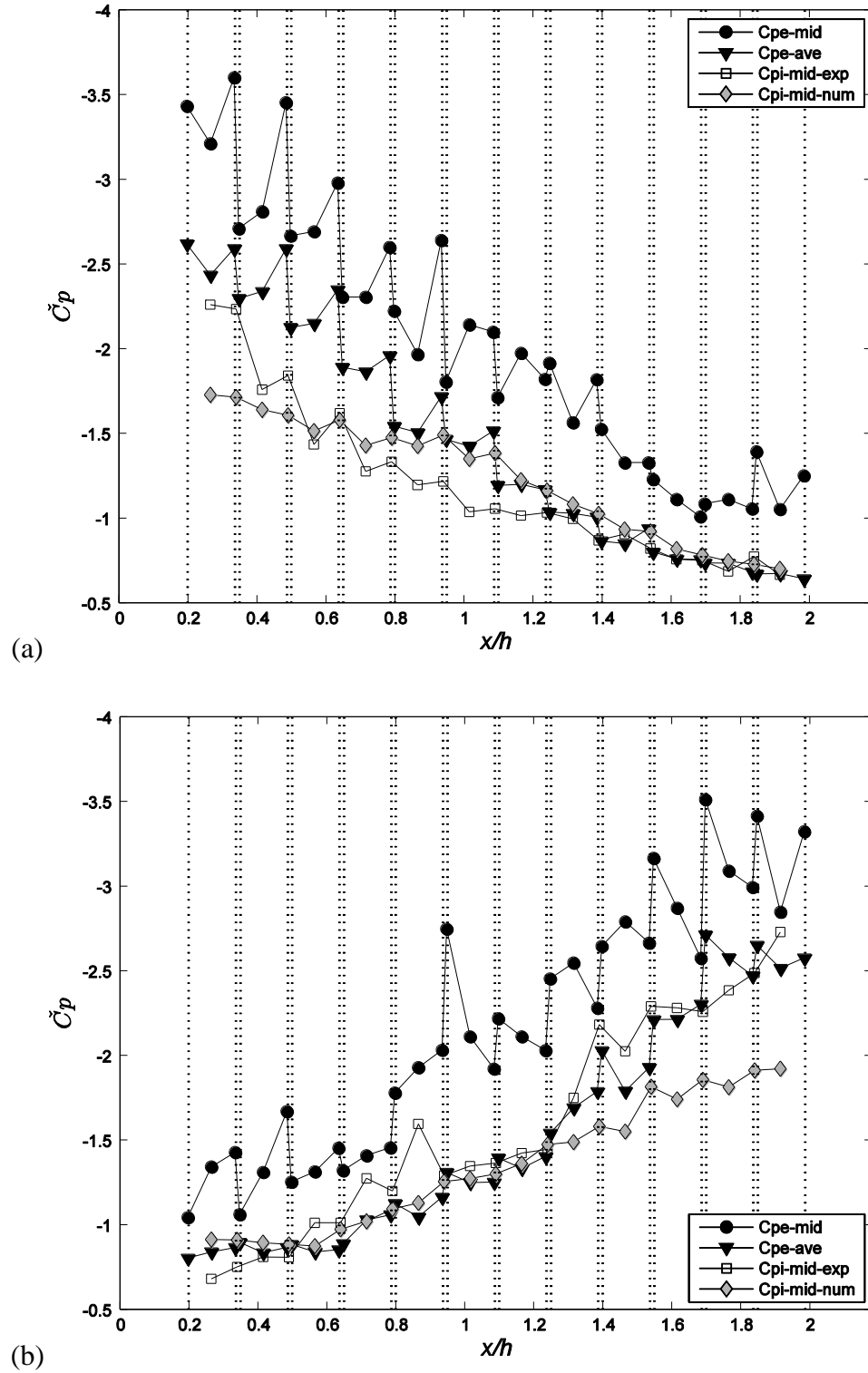


Figure C.12 Peak (minimum) point pressure distributions for the pressure taps in the midplane (Module 6): (a) for 180°; (b) for 0° wind. – seven taps for spanwise-averaged  $C_{pe}$  –

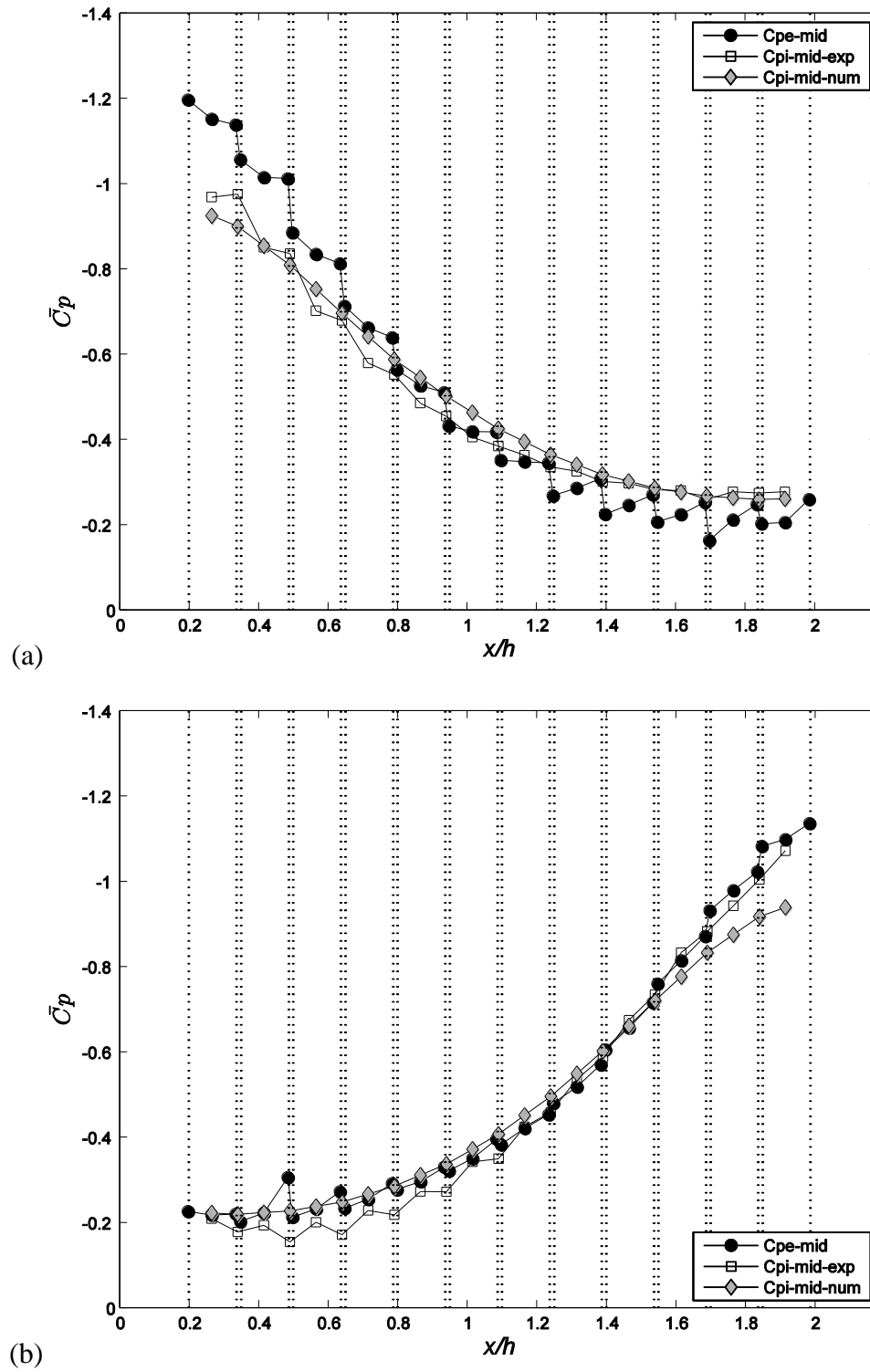


Figure C.13 Mean point pressure distributions for the pressure taps along the midplane (Module 6): (a) for 180°; (b) for 0° wind. – nine taps for spanwise-averaged  $C_{pe}$  –

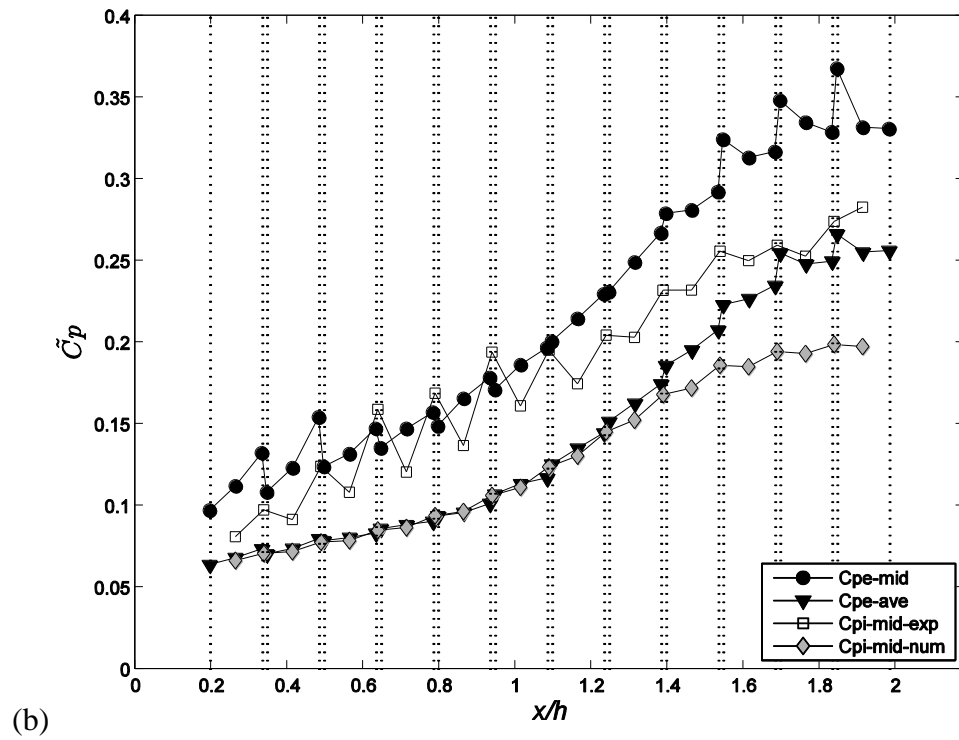
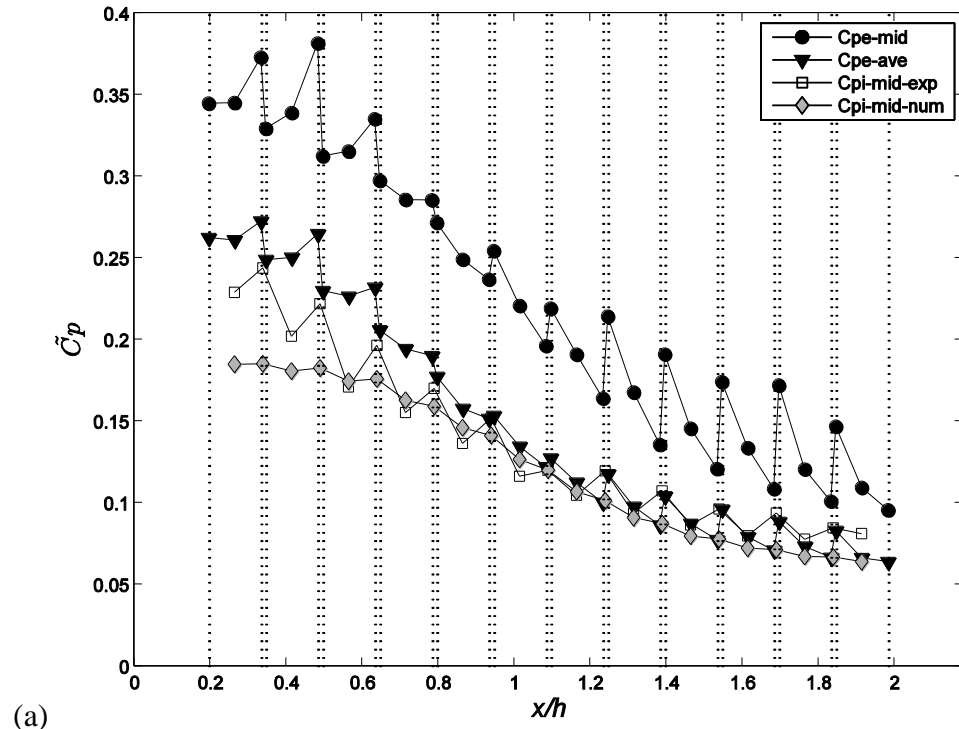


Figure C.14 RMS point pressure distributions for the pressure taps in the midplane (Module 6): (a) for 180°; (b) for 0° wind. – nine taps for spanwise-averaged  $Cp_e$  –

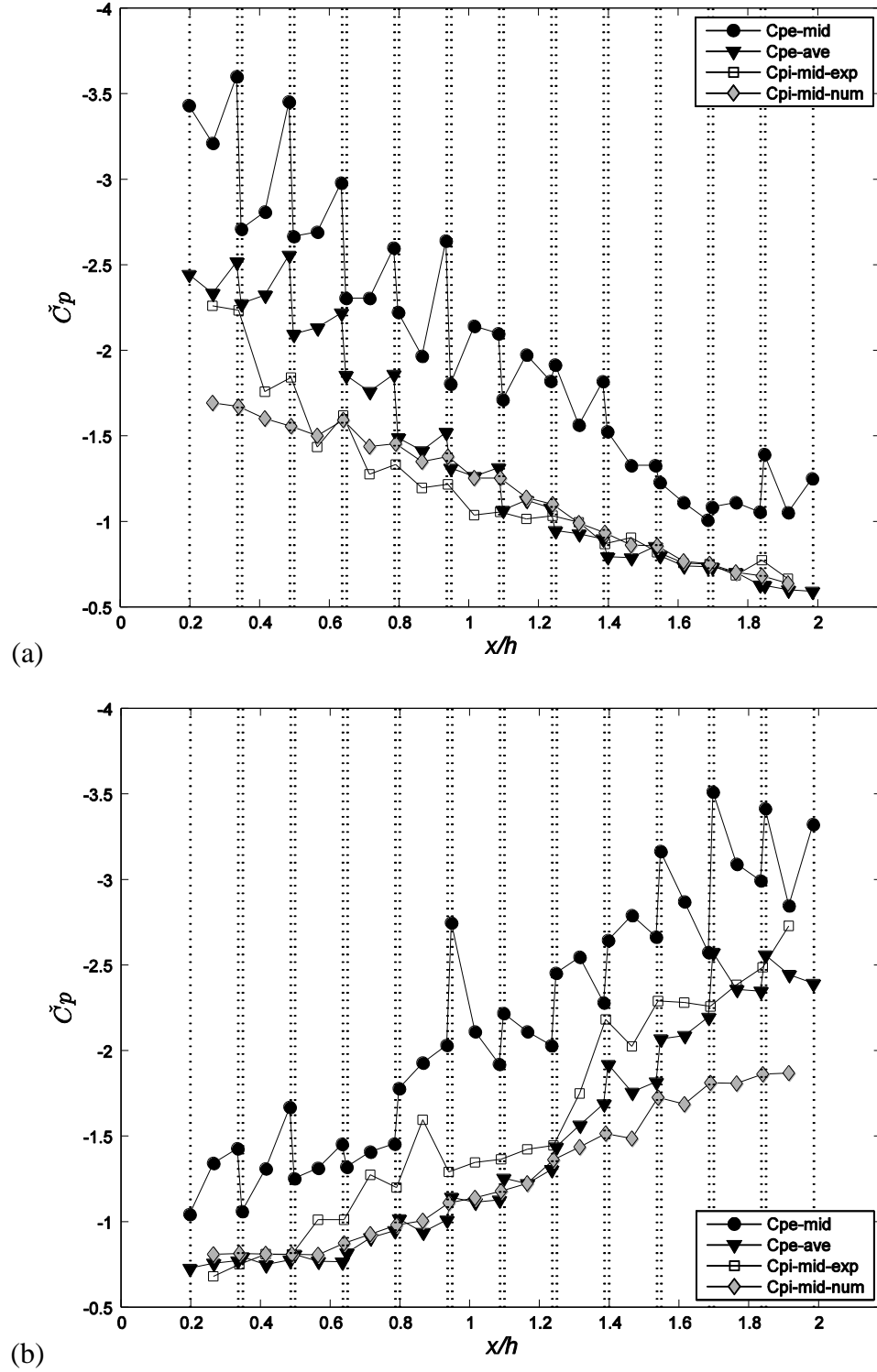


Figure C.15 Peak (minimum) point pressure distributions for the pressure taps in the midplane (Module 6): (a) for 180°; (b) for 0° wind. – nine taps for spanwise-averaged  $C_{pe}$

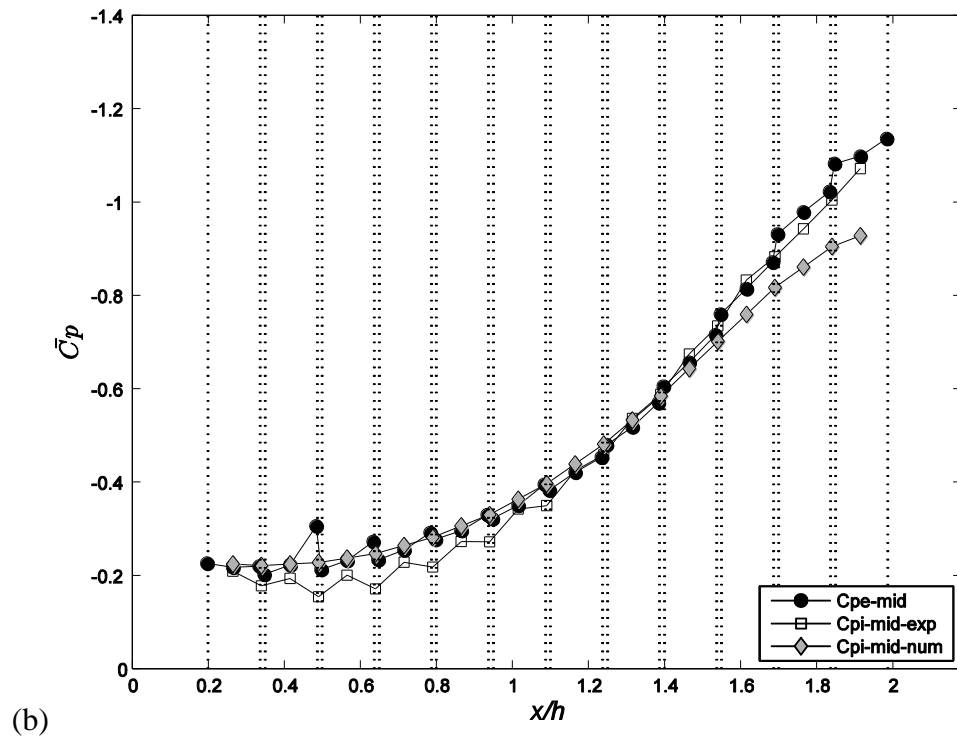
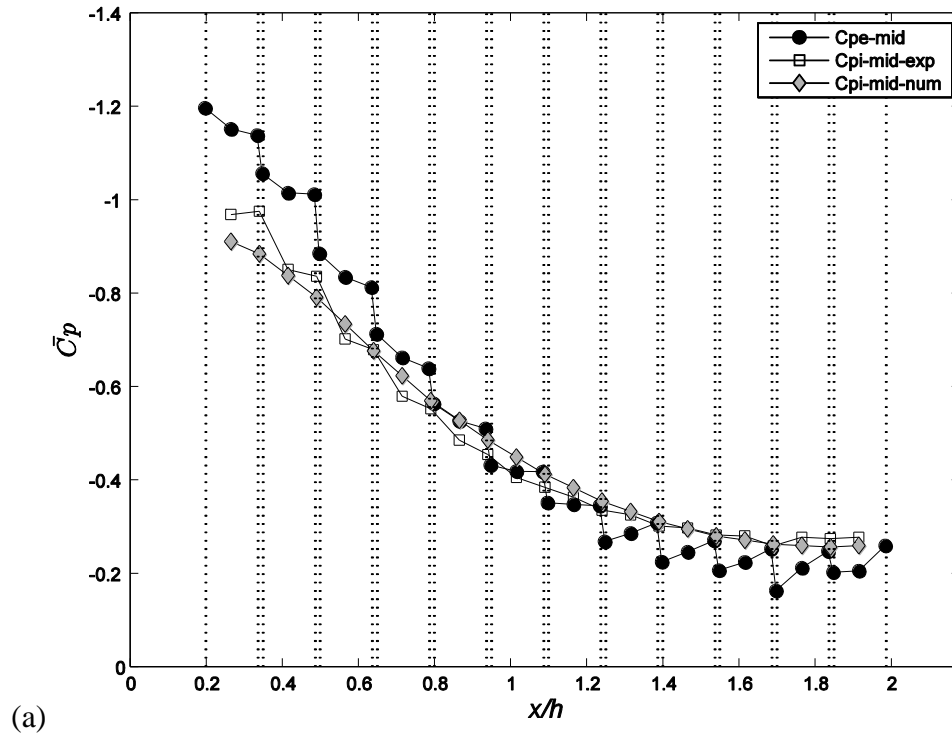


Figure C.16 Mean point pressure distributions for the pressure taps along the midplane (Module 6): (a) for 180°; (b) for 0° wind. – 12 taps for spanwise-averaged  $C_{p_e}$  –

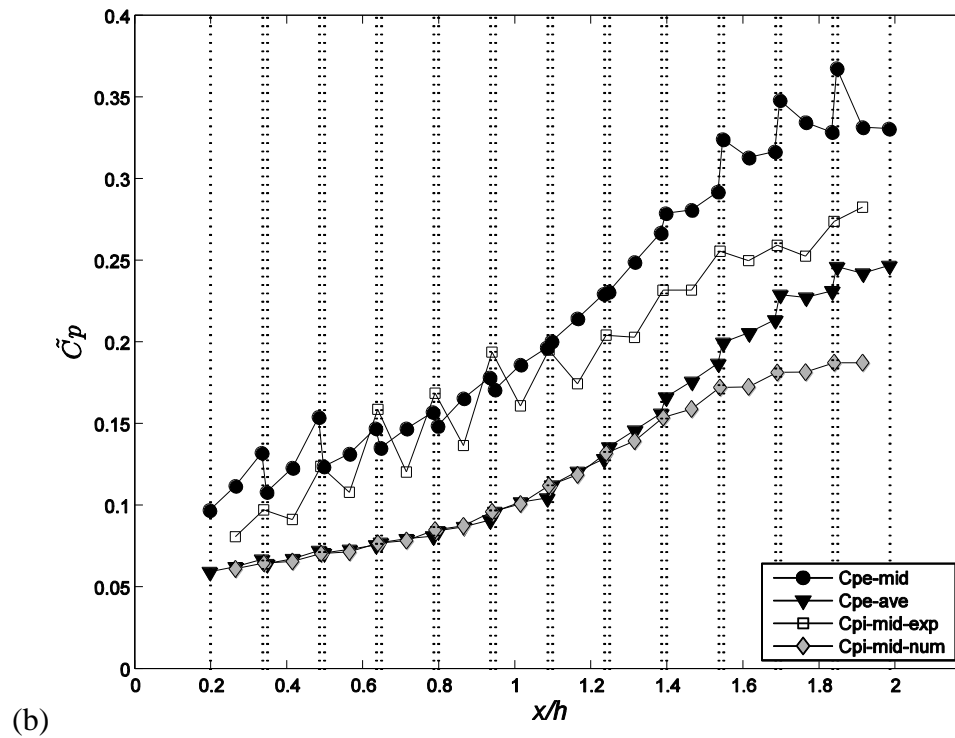
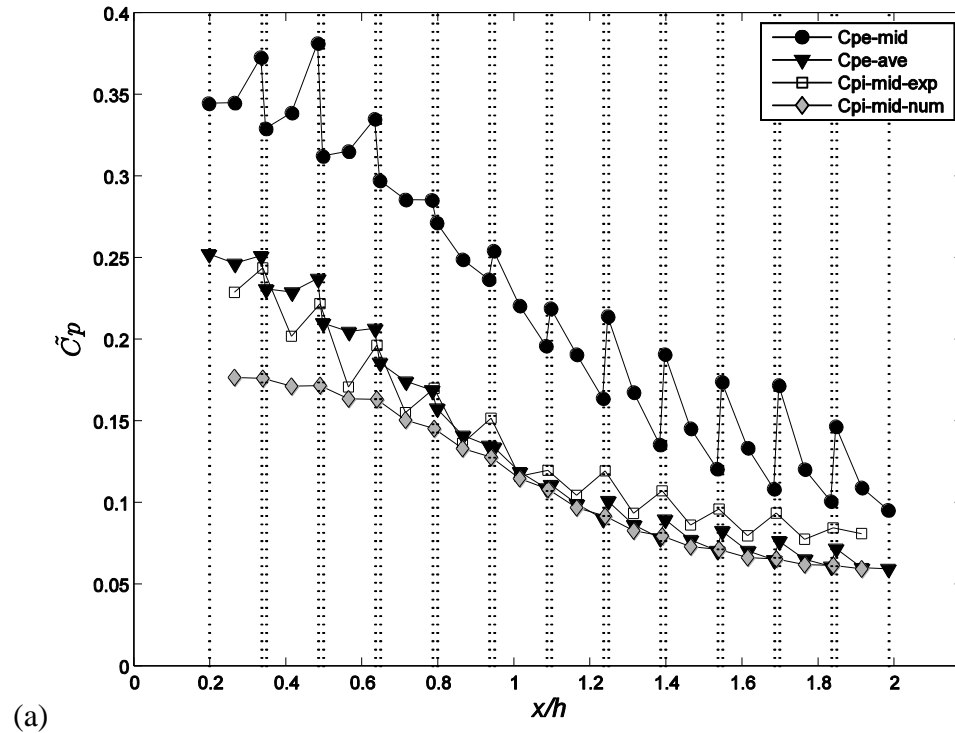


Figure C.17 RMS point pressure distributions for the pressure taps in the midplane (Module 6): (a) for 180°; (b) for 0° wind. – 12taps for spanwise-averaged  $Cp_e$  –



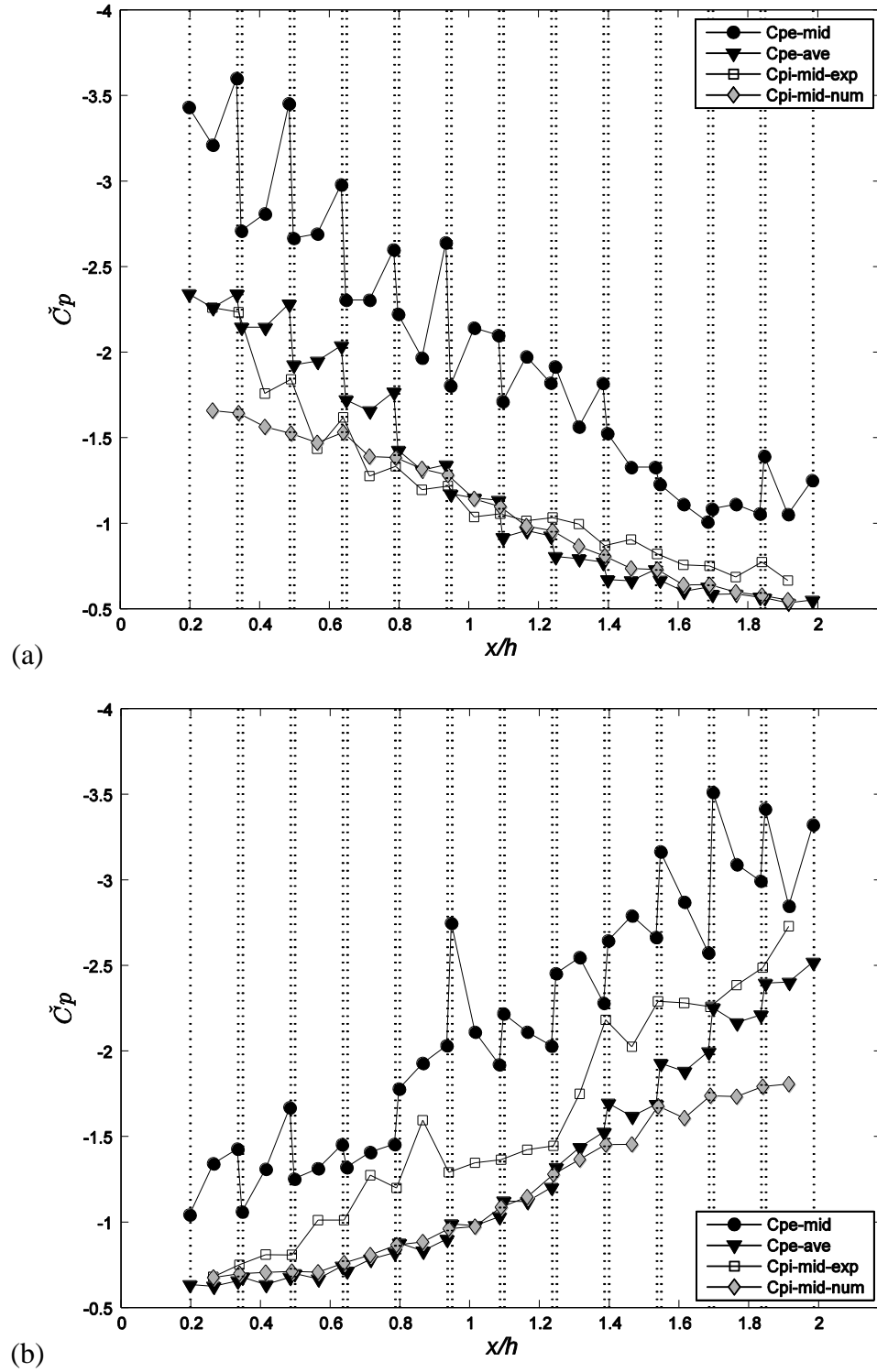


Figure C.18 Peak (minimum) point pressure distributions for the pressure taps in the midplane (Module 6): (a) for 180°; (b) for 0° wind. – 12taps for spanwise-averaged  $C_{pe}$  –

## Appendix D

### Preliminary Study on Two-Dimensional Modelling of the Flow in the Cavity

A possible idea of the two-dimensional modelling of the cavity pressure is that the interior volume within a cavity is divided into a finite number of “control volumes” as illustrated in Figure D.1, and thereby the flows between adjacent control volumes are modeled by the equation of the Couette flow in two-directions, as depicted in Figure D.2.

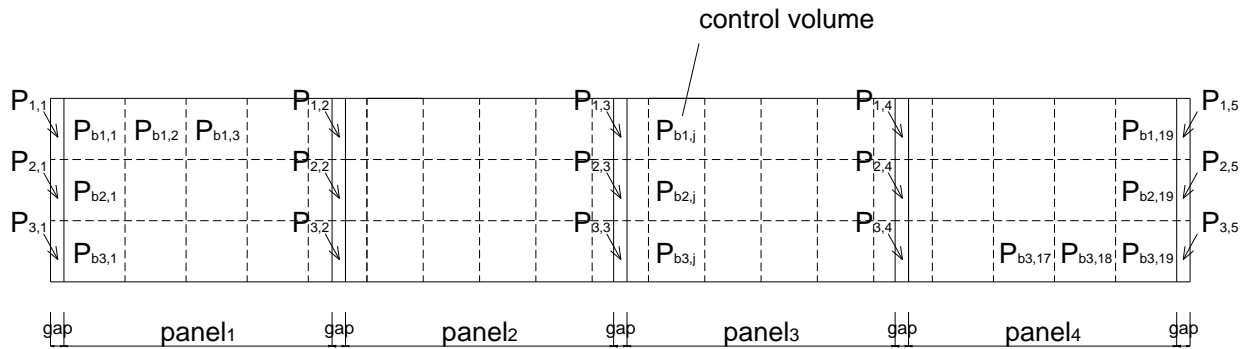


Figure D.1 Plan view of panels with pressures at the gaps and in the cavity beneath the panels.

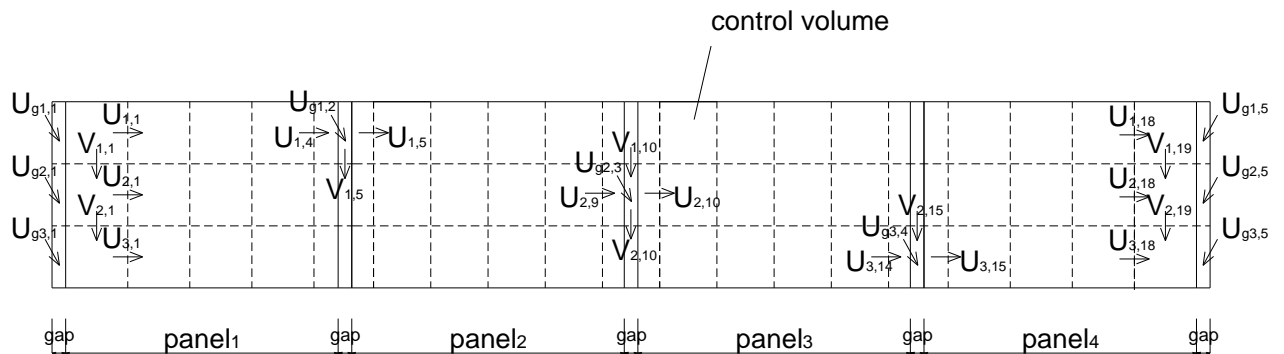


Figure D.2 Plan view of panels with flow velocities at the gaps and in the cavity beneath the panels.

The number of unknown variables identified from the model described in Figures D.1 and D.2 is:

- 19 x 3 for the cavity pressures,  $P_{bi,j}$
- 5 x 3 for the gap flow velocities,  $U_{gi,j}$
- 18 x 3 for the  $u$ -component cavity velocities,  $U_{i,j}$
- 19 x 2 for the  $v$ -component cavity velocities,  $V_{i,j}$ .

Thus, the total number of unknown variables is 164. To solve this problem, the same number of independent equations is required. The number of equations involved in flows at the gaps and in the cavities is:

- 15 discharge equations for the gap flows
- 92 equations of the Couette flow for the cavity flows
- 57 continuity equations.

The analytical model containing the 15 discharge equations and the 92 equations for the cavity flows can be expressed as follows:

$$\rho l_{e1,1} \dot{U}_{g1,1} + C_{L1,1} \frac{\rho}{2} U_{g1,1} |U_{g1,1}| + \frac{12\mu l_{o1,1}}{G_{1,1}^2} U_{g1,1} = P_{1,1} - P_{b1,1} \quad (\text{D.1a})$$

$$\rho l_{e1,2} \dot{U}_{g1,2} + C_{L1,2} \frac{\rho}{2} U_{g1,2} |U_{g1,2}| + \frac{12\mu l_{o1,2}}{G_{1,2}^2} U_{g1,2} = P_{1,2} - P_{b1,5} \quad (\text{D.1b})$$

$\vdots$

$$\rho l_{e3,4} \dot{U}_{g3,4} + C_{L3,4} \frac{\rho}{2} U_{g3,4} |U_{g3,4}| + \frac{12\mu l_{o3,4}}{G_{3,4}^2} U_{g3,4} = P_{3,4} - P_{b3,15} \quad (\text{D.1c})$$

$$\rho l_{e3,5} \dot{U}_{g3,5} + C_{L3,5} \frac{\rho}{2} U_{g3,5} |U_{g3,5}| + \frac{12\mu l_{o3,5}}{G_{3,5}^2} U_{g3,5} = P_{3,5} - P_{b3,19} \quad (\text{D.1d})$$

$$\rho L_{x1,1} \dot{U}_{1,1} + \frac{12\mu L_{x1,1}}{H^2} U_{1,1} = P_{b1,1} - P_{b1,2} \quad (\text{D.1e})$$

$$\rho L_{x1,2} \dot{U}_{1,2} + \frac{12\mu L_{x1,2}}{H^2} U_{1,2} = P_{b1,2} - P_{b1,3} \quad (\text{D.1f})$$

$\vdots$

$$\rho L_{x3,17} \dot{U}_{3,17} + \frac{12\mu L_{x3,17}}{H^2} U_{3,17} = P_{b3,17} - P_{b3,18} \quad (\text{D.1g})$$

$$\rho L_{x3,18} \dot{U}_{3,18} + \frac{12\mu L_{x3,18}}{H^2} U_{3,18} = P_{b3,18} - P_{b3,19} \quad (\text{D.1h})$$

$$\rho L_{y1,1} \dot{V}_{1,1} + \frac{12\mu L_{y1,1}}{H^2} V_{1,1} = P_{b1,1} - P_{b2,1} \quad (\text{D.1i})$$

$$\rho L_{y1,2} \dot{V}_{1,2} + \frac{12\mu L_{y1,2}}{H^2} V_{1,2} = P_{b1,2} - P_{b2,2} \quad (\text{D.1j})$$

$$\vdots$$

$$\rho L_{y2,18} \dot{V}_{2,18} + \frac{12\mu L_{y2,18}}{H^2} V_{2,18} = P_{b2,18} - P_{b3,18} \quad (\text{D.1k})$$

$$\rho L_{y2,19} \dot{V}_{2,19} + \frac{12\mu L_{y2,19}}{H^2} V_{2,19} = P_{b2,19} - P_{b3,19} \quad (\text{D.1l})$$

The 57 continuity equations are as follows:

$$G_{1,1} U_{g1,1} = H(U_{1,1} + V_{1,1}) \quad (\text{D.2a})$$

$$U_{1,1} = U_{1,2} + V_{1,2} \quad (\text{D.2b})$$

$$U_{1,2} = U_{1,3} + V_{1,3} \quad (\text{D.2c})$$

$$U_{1,3} = U_{1,4} + V_{1,4} \quad (\text{D.2d})$$

$$G_{1,2} U_{g1,2} = H(U_{1,5} + V_{1,5} - U_{1,4}) \quad (\text{D.2e})$$

$$U_{1,5} = U_{1,6} + V_{1,6} \quad (\text{D.2f})$$

$$U_{1,6} = U_{1,7} + V_{1,7} \quad (\text{D.2g})$$

$$U_{1,7} = U_{1,8} + V_{1,8} \quad (\text{D.2h})$$

$$U_{1,8} = U_{1,9} + V_{1,9} \quad (\text{D.2i})$$

$$G_{1,3} U_{g1,3} = H(U_{1,10} + V_{1,10} - U_{1,9}) \quad (\text{D.2j})$$

$$\vdots$$

$$G_{1,5}U_{g1,5} = H(V_{1,19} - U_{1,18}) \quad (\text{D.2k})$$

$$G_{2,1}U_{g2,1} = H(U_{2,1} + V_{2,1} - V_{1,1}) \quad (\text{D.2l})$$

$$U_{2,1} = U_{2,2} + V_{2,2} - V_{1,2} \quad (\text{D.2m})$$

$$U_{2,2} = U_{2,3} + V_{2,3} - V_{1,3} \quad (\text{D.2n})$$

$$\vdots$$

$$G_{2,3}U_{g2,3} = H(U_{2,10} + V_{2,10} - U_{2,9} - V_{1,10}) \quad (\text{D.2o})$$

$$\vdots$$

$$G_{2,5}U_{g2,5} = H(V_{2,19} - U_{2,18} - V_{1,19}) \quad (\text{D.2p})$$

$$\vdots$$

$$G_{3,4}U_{g3,4} = H(U_{3,15} - V_{2,15} - U_{3,14}) \quad (\text{D.2q})$$

$$U_{3,15} = U_{3,16} - V_{2,16} \quad (\text{D.2r})$$

$$U_{3,16} = U_{3,17} - V_{2,17} \quad (\text{D.2s})$$

$$U_{3,17} = U_{3,18} - V_{2,18} \quad (\text{D.2t})$$

$$G_{3,5}U_{g3,5} = H(-U_{3,18} - V_{2,19}) \quad (\text{D.2u})$$

## Curriculum Vitae

|  |  |
|--|--|
| <b>Name:</b>                                 | Jeong Hee Oh   |
| <b>Post-secondary Education and Degrees:</b> | <p>The University of Western Ontario, London, Ontario, Canada<br/>2010-2014 Ph.D.</p> <p>The University of Western Ontario, London, Ontario, Canada<br/>2003-2004 M.E.Sc</p> <p>Korea University, Seoul, Korea<br/>1987-1993 B.E.</p>  |
| <b>Honours and Awards:</b>                   | <p>NSERC Alexander Graham Bell Canada Graduate Scholarship<br/>2011 to 2014</p> <p>Ontario Graduate Scholarship, 2011</p> <p>Samsung University Student Construction Thesis Award, 1992</p>  |
| <b>Related Work Experience</b>               | <p>Research Associate / Project Manager / Engineering Assistant<br/>Boundary Layer Wind Tunnel Laboratory<br/>London, Ontario, Canada<br/>2005-2014</p> <p>Teaching Assistants<br/>The University of Western Ontario, London, Ontario, Canada<br/>2003-2004, 2010-2014</p> <p>Construction Engineer / Structural Engineer / Assistant Manager<br/>Samsung Engineering &amp; Construction, Seoul, Korea<br/>1994-2001</p>   |
| <b>Publications:</b>                         | <ol style="list-style-type: none"> <li>1. <b>Oh, J.H.</b>, Kopp, G.A., Inculet, D.R. (2004). Wind-induced internal pressures in low-rise buildings. <i>Proceedings of CSME Forum 2004</i>, University of Western Ontario, Canada, 634-642.</li> <li>2. <b>Jeong Hee Oh</b>, Gregory A. Kopp, and Diana R. Inculet (2007). The UWO contribution to the NIST aerodynamic database for wind loads on low buildings: Part 3. Internal Pressures. <i>Journal of Wind Engineering and Industrial Aerodynamics</i>, 95, 755-779.</li> </ol> |

3. Gregory A. Kopp, **Jeong Hee Oh**, Diana R. Inculet (2008). Wind-induced internal pressures in houses. *Journal of Structural Engineering*, 134, 1129-1138.
4. Gregory A. Kopp, Jon Galsworthy, **Jeong Hee Oh** (2008). Wind loads on open-frame buildings. *Proceedings of 4<sup>th</sup> International Conference on Advances in Wind Structures*, Jeju, Korea, 294-309.
5. Gregory A. Kopp, Jon Galsworthy, **Jeong Hee Oh** (2010). Horizontal wind loads on open-frame. low-rise buildings. *Journal of Structural Engineering*, 136, 98-105.
6. **Jeong Hee Oh**, and Gregory A. Kopp (2012). Pressure equalization and analytical solutions for pressures between double-layer envelopes. *3<sup>rd</sup> AAWE Workshop*, Hyannis, USA.
7. **Jeong Hee Oh**, and Gregory A. Kopp (2014). An experimental study of pressure equalization on double-layered roof system of low-rise buildings. *6<sup>th</sup> International Symposium on Computational Wind Engineering*, Hamburg, Germany.
8. **Jeong Hee Oh**, and Gregory A. Kopp (2014). An experimental study of pressure distributions within a double-layered roof system in a region of separated flow. Submitted to *Journal of Wind Engineering and Industrial Aerodynamics*, March 8, 2014.
9. **Jeong Hee Oh**, and Gregory A. Kopp (2014). One-dimensional modelling of the flow in pressure equalizing, double-layer, roof systems in regions of separated flow. Submitted to *Building and Environment*, June 2, 2014.

#### Technical Reports:

1. **J.H. Oh** and J.K. Galsworthy (2006). A study of wind effects for One River Terrace in New York, NY. *BLWT-SS10-2006*.
2. **J.H. Oh**, R.T. Edey and T.C.E. Ho (2006). A study of wind effects for Mansion on Peachtree Hotel Tower in Atlanta, Georgia. *BLWT-SS20-2006*.
3. **J.H. Oh** and J.K. Galsworthy (2006). A study of wind effects for Oryukdo SK View Project in Busan, Korea. *BLWT-SS24-2006*.
4. G.R. Lythe, T.C.E. Ho and **J.H. Oh** (2006). A study of wind effects for Whasung Dongtan Metaplois in Korea – based on TE experiments. *BLWT-SS59-2006*.
5. **J.H. Oh**, T.C.E. Ho and G.R. Lythe (2006). A study of wind effects for Whasung Dongtan Metaplois in Korea – based on BLWTL experiments. *BLWT-SS60-2006*.
6. **J.H. Oh** and T.C.E. Ho (2006). A study of wind effects for Gupo Dongwon Royal Palace in Busan, Korea. *BLWT-SS63-2006*.

7. **J.H. Oh** and T.C.E. Ho (2006). A study of wind effects for MBC Building Project in Ilsan, Korea. *BLWT-SS70-2006*.
8. **J.H. Oh** and J.K. Galsworthy (2006). A study of wind effects for Cheongju Daenong Project in Korea. *BLWT-SS77-2006*.
9. **J.H. Oh** and T.C.E. Ho (2007). A study of wind effects for DeKalb Avenue in Brooklyn, New York. *BLWT-SS2-2007*.
10. **J.H. Oh** and T.C.E. Ho (2007). A study of wind effects for West End Summit in Nashville, Tennessee. *BLWT-SS21-2007*.
11. **J.H. Oh** and T.C.E. Ho (2007). A study of wind effects for Myrtle Avenue in Brooklyn, New York. *BLWT-SS53-2007*.
12. **J.H. Oh** and T.C.E. Ho (2007). A study of wind effects for Posco E&C Songdo Headquarters in Korea. *BLWT-SS61-2007*.
13. G.A. Kopp, J.K. Galsworthy and **J.H. Oh** (2008). Wind loads on open-frame buildings. *BLWT-SS4-2008*.
14. **J.H. Oh**, A. Welburn and J.K. Galsworthy (2008). A study of wind effects for Site 23 & 24 Battery Park City in New York, NY. *BLWT-SS13-2008*.
15. S. Farquhar, **J.H. Oh** and T.C.E. Ho (2009). A study of wind effects for Planetarium Tower in Panama City, Panama. *BLWT-SS46-2008*.
16. **J.H. Oh** and T.C.E. Ho (2009). A study of wind effects for Phnom Penh Residence & Commercial Complex in Cambodia. *BLWT-SS1-2009*.
17. **J.H. Oh** and T.C.E. Ho (2009). A study of wind effects for Clarence E Lightner Public Safety Center in Raleigh, North Carolina. *BLWT-SS24-2009*.
18. **J.H. Oh**, D. Inculet and T.C.E. Ho (2009). A study of wind effects for Torre Paulista in Sao Paulo, Brazil. *BLWT-SS25-2009*.
19. T.C.E. Ho and **J.H. Oh** (2011). A study of wind effects for No. 1 Sai Wan Terrace, S.I.L. 761 in Quarry Bay, Hong Kong. *September, 2011*.
20. **J.H. Oh** and G.A. Kopp (2012). A study of wind effects for Rehabilitation Institute in Chicago, IL. *BLWT-SS26-2012*.
21. **J.H. Oh** G.A. Kopp and T.C.E. Ho (2012). A study of wind effects for 20 West 53rd Street Tower in New York, NY. *BLWT-SS36-2012*.
22. **J.H. Oh** and G.A. Kopp (2013). A study of wind effects for BAM in Brooklyn, NY. *July, 2013*.
23. **J.H. Oh** and G.A. Kopp (2014). Wind loads on equipment elevated above the roof of a low-rise building. *BLWT-1-2014*.